Modelling Wall Deformation and Fluid-Structure Interaction in Fluid-Conveying Elastic-Walled Tubes

A thesis submitted to the School of Mathematics at the University of East Anglia in partial fulfilment of the requirements for the degree of Doctor of Philosophy

Daniel J. Netherwood

Supervised by Robert J. Whittaker

February 24, 2024

UEA School of Mathematics

Norwich Research Park

In loving memory of my grandparents Patricia and Janet

Modelling Wall Deformation and Fluid-Structure Interaction in Fluid-Conveying Elastic-Walled Tubes

by Daniel J. Netherwood

The fluid-structure interaction arising from the flow through collapsible tubes plays an important biological role in the transportation and delivery of nutrients to tissues and organs. In this thesis, we focus on developing mathematical models for the wall deformation and fluid-structure interaction arising from the flow through an elastic-walled tube.

Whittaker et al. (2010; *Q. J. Mech. Appl. Math.* **63**(4): 465-496) developed a mathematical model for the wall deformations of an initially elliptical elastic-walled tube, which are induced by an azimuthally uniform transmural pressure. In Chapter 2, we expand on this model to allow arbitrary initial cross-sectional shapes and azimuthally non-uniform pressures.

In Chapter 3, we re-visit the problem for the deformations of an initially

elliptical tube and produce the first formal solution for the wall motion using an eigenfunction expansion method, which overcomes the need to invoke ad-hoc assumptions made by Whittaker et al. (2010; *Q. J. Mech. Appl. Math.* **63**(4): 465-496) in order to obtain their solution. In Chapter 4, we couple our results for the wall deformation from Chapter 3 to the asymptotic model for the flow through a rapidly oscillating elastic tube derived by Whittaker et al. (2010, *J. Fluid. Mech.* **648**, 83–121). Our results provide a three-dimensional description of the fluid-structure interaction that arises from the flow through an initially elliptical elastic tube.

In Chapter 5, we produce a formal solution for the wall deformation of an elastic-walled tube with an arbitrary initial cross-sectional shape. We then use this model to compute a family of initial cross-sectional shapes with the property that an azimuthally uniform transmural pressure will excite only a single deformation mode.

Contents

List of Figures

List of Tables

Preface

Copyright

Published work

A paper based on the work in Chapter 3 has been published in the Quarterly Journal of Mechanics and Applied Mathematics (Netherwood and Whittaker, 2023). I have had the benefit of suggestions and comments from the referees.

Acknowledgements

First and foremost, I'd like to thank my supervisor, Dr. Robert Whittaker for his amazing support, feedback, guidance and general expertise during my Ph.D. project. I have not taken the incredible education that I have received for granted, and I am both thankful and proud to have been able to learn from you over the years.

I would like to thank the University of East Anglia for funding my Ph.D. project and also for providing me with a fantastic academic home for the last eight years. In particular, I'd like to acknowledge my secondary supervisor, Dr. Paul Hammerton's support and consistent interest in my professional development. I also wish to acknowledge the generous help of Prof Rick Laugesen for his suggestions surrounding Appendix A.

I wish to thank my Mum, Dad and sister for their unconditional support and patience during my project. In what has been difficult circumstances, your support has helped me make it to the end. I also wish to acknowledge the generous contributions made by Levi.

I wish to thank the boys: Ash, Hartley, Joe, Max, Tom, Matty, Filby, Soc, and Marcus for always having my best interests at heart and for the support you have shown me during my time in Norwich. I'd also like to thank the UEA PGR office and Fred Scruntley for the memories over the last four years.

Chapter 1

Introduction

1.1 Background

1.1.1 Biological motivation

The fluid-structure interaction between elastic-walled tubes and biological fluids can be observed throughout the biological and medicinal sciences. Examples include the circulatory, respiratory, lymphatic and central nervous systems. Of the most important is the transportation and delivery of nutrients to tissues and organs, which is facilitated by blood flow through the blood vessels. These vessels are deformable, and will often experience forces both internally and externally. Consequently, the mathematical modelling of the wall deformation and fluid-structure interaction is vital in gaining a better understanding of the mechanisms that lead to various physiological phenomena.

In the circulatory system, the deformability of the vasculature has a significant impact on pulse-wave propagation (Pedley, 1980), which allows for the transportation of nutrients to tissues and organs within the body. Furthermore, flow-induced deformations are a mechanism for the rupture of cholesterol deposits (plaques) inside of the arteries, which can lead to potentially fatal vessel occlusion (Binns and Ku, 1989; Ku, 1997). For veins located above the heart and outside of the skull, the reduction in hydrostatic pressure can

be sufficient to induce the blood vessel to collapse (Lokossou et al., 2020; Moreno et al., 1970; Wild et al., 1977). Fluid-filled elastic-walled tubes play a key role in maintaining a constant flux of blood to systemic organs, known as blood-flow autoregulation (Rodbard and Takacs, 1966; Rodbard, 1966). In the medical industry, a device known as a sphygmomanometer can be used to measure blood pressure. Sphygmomanometry is then the process of measuring the pressure. This involves controlling the collapse of the brachial artery by wrapping the cuff of the device around the arm of the patient and inflating/deflating. This collapse generates Korotkoff sounds (Bertram et al., 1989; Ur and Gordon, 1970), from which a medical professional can obtain the measurements non-invasively. To aid blood-flow circulation, intra-aortic balloon counter pulsation has been used on critically ill patients with cardiac disease for several decades (Trost and Hillis, 2006). This process involves a thin-walled flexible tube known as a catheter, which has had one end attached to a long balloon (known as the intra-aortic balloon), and the other end attached to a console. The console has a mechanism to inflate and deflate the balloon in phase with the heart's contractions. The device is inserted into the body (usually in the leg) and then guided to the aorta to aid blood pumping.

In the respiratory system, there is a strong interaction between air flow and the elasticity of the airway walls. For example, forced expiration of air from the lungs can cause the airways to collapse (Macklem, 1971; Skalak et al., 1989), which results in a reduction in the air flow-rate (Grotberg and Gavriely, 1989). This phenomena is known as flow-rate limitation. Airway collapse can also be attributed to certain pulmonary diseases (Pride and

Milic-Emili, 1995; Macklem et al., 1970), which again can result in airway collapse, as well as occlusion with viscous fluid. If persistent, this occlusion can be fatal (Rafieian-Kopaei et al., 2014). The re-opening of the airways has also been of scientific interest, and can be modelled by assuming that the opening occurs via the propagation of an air finger into the collapsed fluid-filled part of the airway (Heil, 2000; Baroud et al., 2006; White and Heil, 2005).

In relatively recent history, considerable research has been focused on flow-induced instabilities associated with the fluid-structure interaction of fluid-conveying elastic-walled tubes (Grotberg and Jensen, 2004; Heil and Hazel, 2011). Many physiological phenomena can be attributed to such instabilities. Examples include: wheezing during forced expiration, Korotkoff sounds during sphygmomanometry, and cervical venous hum (Danahy and Ronan Jr, 1974). For more details associated with the biological applications see the reviews by Pedley and Luo (1998), Grotberg and Jensen (2004), Heil and Jensen (2003) and Heil and Hazel (2011).

1.1.2 Experimental investigations: The Starling resistor

Many theoretical models that describe the relationship between the deformation of elastic-walled tubes and the fluid conveyed within them are based on experimental investigations (see, e.g. the review Bertram, 2003). Such experimental investigations are typically performed in a 'Starling resistor' (Knowlton and Starling, 1912). As shown in figure 1.1, the set-up consists of a thin-walled finite-length (but not necessarily axially uniform) elastic tube.

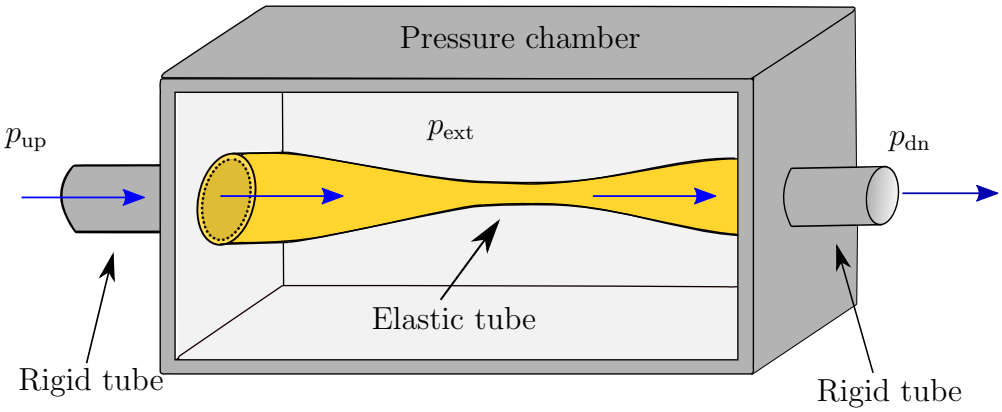

Figure 1.1: The typical set-up of the Starling resistor comprising a thin-walled elastic tube section pinned between two rigid tubes. The elastic section is placed inside a pressure chamber and fluid is driven through the system by either imposing a pressure difference between the ends of the tube or by imposing a flow rate at one end using a volumetric pump.

The tube is pre-stretched and clamped (at both ends) to two rigid tubes. Fluid is driven through the system by either imposing a pressure difference between the ends of the tube, or by imposing a flow rate at one end through a volumetric pump. By enclosing the collapsible section of the tube inside a pressure chamber, we are given the freedom to subject the exterior of the tube to an external pressure p_{ext} (Bertram, 1986; Bertram et al., 1990). Deformations in the tube wall then occur due to the combined effect of the fluid traction (i.e., the internal hydrodynamic pressure p_{int} and viscous shear forces) and the applied external pressure p_{ext}. For large Reynolds number flows, contributions from the viscous shear stresses are dominated by inertial effects, and are often neglected. Deformations are then said to occur due to the transmural pressure $p_{\text{tm}} = p_{\text{int}} - p_{\text{ext}}$, which is the pressure difference between the inside and outside of the tube.

Depending on both the sign and magnitude of the transmural pressure, the tube will deform in different ways. For sufficiently large and positive

transmural pressures, the tube will inflate, and adopt an almost axisymmetric configuration. In this state, the transmural pressure will mainly be balanced by an azimuthal hoop stress, and the dominant physical mechanism associated with the deformations is that of azimuthal stretching. For small values of the transmural pressure (either positive or negative), the tube will be approximately axisymmetric. Once the transmural pressure becomes sufficiently negative, (i.e., the external pressure p_{ext} becomes larger than the interior fluid pressure p_{int} by a suitable amount), the tube will buckle into an elliptical-like configuration, in which the primary mode of deformation is that of azimuthal bending. Decreasing the transmural pressure further causes the tube's cross-section to adopt a 'two lobed' state (see figure 1.2), before the opposite sides finally come into contact (Shapiro, 1977).

In its deformed and compliant state, small changes in the transmural pressure yield large changes in the cross-sectional area of the tube. Provided that the mean axial flow rate is sufficient to over come viscous losses, the system can exhibit high and low frequency self-excited oscillations (of large and small amplitude) associated with a number of different instability mechanisms.

1.1.3 Modelling fluid-structure interaction

In the last 50 years significant efforts have been made in producing accurate theoretical descriptions of the fluid-structure interaction observed experimentally within a Starling resistor. In this thesis, we will concentrate our attention on theoretical models that can be used to predict the onset of self-excited oscillations. In order to produce such a theoretical description,

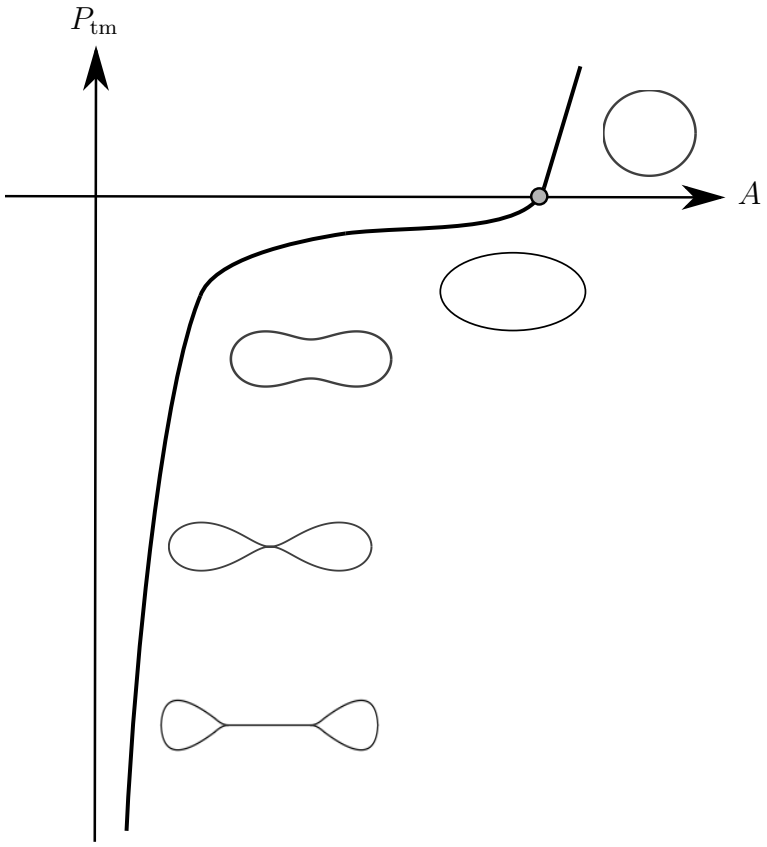

Figure 1.2: Illustration of the typical relationship between the transmural pressure P_{tm} and cross-sectional area A of a collapsible tube. Sketches of the corresponding cross-sectional shapes are included.

independent mechanistic models for the wall and internal fluid are typically established, and then coupled via the hydrodynamic pressure. In a general three-dimensional set-up, the model for the wall mechanics will involve a system of three equations relating four dependent variables, namely the transmural pressure (involving the unknown fluid pressure and imposed external pressure) and three unknown displacement functions measuring the deformations of the tube in the normal, azimuthal and axial directions. The model for the fluid mechanics provides an additional four equations, relating four unknown dependent variables, namely the fluid pressure as well as

two transverse fluid velocity components and an axial fluid velocity component. In total this yields a system of seven equations, relating seven distinct unknowns. In principle, a solution of this fully coupled system can be obtained. However, this is beyond analytical treatment, and would require vast amounts of computational power. As an alternative approach, many authors have used a variety of techniques such as cross-sectional averaging, asymptotic analysis and/or shell theory to simplify this system (Heil and Hazel, 2011). We will discuss some of these approaches in the following sections.

1.1.4 One-dimensional models and the tube law

Some of the simplest theoretical descriptions of physiological flows in elastic vessels are based on spatially one-dimensional models (Conrad, 1969; Katz et al., 1969; Bertram and Pedley, 1982). Within these models, the system is represented by three variables, namely the cross-sectionally averaged fluid pressure, p and velocity, w, as well as the cross-sectional area, A, which each depend on the axial co-ordinate z and time t. Cross-sectionally averaged conservation of mass and axial momentum provides two equations, e.g.,

$$\frac{\partial A}{\partial t} + \frac{\partial}{\partial z}(wA) = 0, \tag{1.1}$$

$$\rho\left(\frac{\partial w}{\partial t} + w\frac{\partial w}{\partial z}\right) = -\frac{\partial p}{\partial z}, \tag{1.2}$$

where ρ is fluid density. To close the system, a third equation — known as a tube law — is required to capture the wall mechanics. The tube law, which usually takes the form

$$p - p_{\text{ext}} = P(A), \tag{1.3}$$

for some function P, is often chosen to fit experimental results (see Shapiro, 1977; Kececioglu et al., 1981).

Flaherty et al. (1972) was one of the first to propose a theoretical tube law, based on the post-buckling behaviour of an inextensible elastic ring. However, this local analysis fails to capture axial tension and axial bending effects that are induced by the interaction between neighbouring cross-sections (Heil and Pedley, 1996).

In an attempt to improve the tube law of Flaherty et al. (1972), Mcclurken et al. (1981) assumed that effects due to axial tension and bending contribute additively to the tube law, so that

$$p - p_{\text{ext}} = P(A) + P_T + P_B. \tag{1.4}$$

Expressions for P_T and P_B were then derived in terms of the respective second and fourth axial derivatives of the tube's cross-sectional area, A. However, these derivations were based on the assumption that the deformed tube would adopt an idealised geometry, which is a significant limitation. Many other authors have proposed ways of incorporating contributions from axial forces and bending moments. We refer the reader to the studies of Reyn (1987), Jensen and Pedley (1989) and Whittaker et al. (2010b) as additional examples.

The canonical example of a one-dimensional model of the fluid-structure interaction observed in a Starling resistor takes the form (Pedley, 1980)

$$\frac{\partial A}{\partial t} + \frac{\partial}{\partial z}\left(wA\right) = 0, \tag{1.5}$$

$$\rho\left(\frac{\partial w}{\partial t} + w\frac{\partial w}{\partial z}\right) = -\frac{\partial p}{\partial z} - F, \tag{1.6}$$

$$p - p_{\text{ext}} = P(A) - T\frac{\partial^2 A}{\partial z^2}. \tag{1.7}$$

Here z is the axial co-ordinate of the tube, t is time, $A(z,t)$ is the tube's cross-sectional area, p_{ext} is an applied external pressure, and $w(z,t)$ and $p(z,t)$ are the respective cross-sectionally integrated axial fluid velocity and pressure. The function P measures the local relationship between the tube's cross-sectional area and the transmural pressure $p - p_{\text{ext}}$ in the absence of axial effects. The function F (which typically depends on the model variables) represents viscous losses and T approximates an axial tension force applied at the tube ends. The inclusion of the final term in (1.7) is therefore an attempt to include axial tension-curvature effects between neighbouring cross-sections into the model. Many authors have had success in demonstrating that the system (1.5)–(1.7) exhibits some of the physiological phenomena observed in experiments. Examples include: full vessel occlusion in finite time, (Cancelli and Pedley, 1985), pulse wave propagation (Pedley, 1980), and self-excited oscillations (Cancelli and Pedley, 1985; Hayashi et al., 1998; Matsuzaki et al., 1994).

1.1.5 Two-dimensional models

Fully three-dimensional models capturing the fluid-structure interaction arising from flow through collapsible vessels are both difficult to produce theoretically and computationally expensive to simulate numerically. Instead, two-dimensional models have been produced. Developments have been made in producing theoretical and numerical models of the Starling resistor that

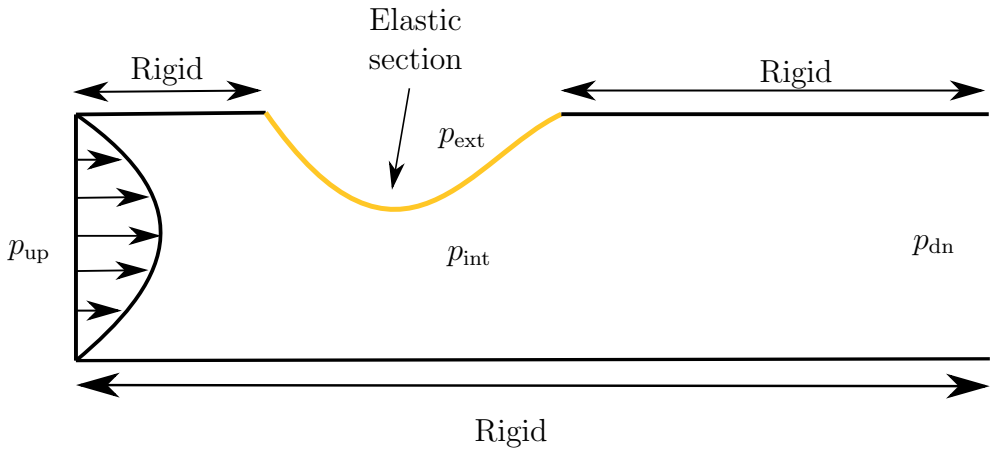

Figure 1.3: Visual representation of the Pedley (1992) model, which involves a finite length two-dimensional channel with one section of the upper wall replaced with a collapsible section of elastic membrane held under longitudinal tension. Fluid is driven through the system by an imposed pressure difference $p_{\text{up}} - p_{\text{dn}} > 0$ between the upstream and downstream ends of the channel.

predict self-excited oscillations. The first model that gathered considerable traction was that of Pedley (1992), who formulated the problem of fluid flow (driven by an imposed pressure drop) through a two-dimensional planar channel in which one wall has a section replaced by an elastic membrane under longitudinal tension (see figure 1.3). This problem is the two-dimensional analogue of the problem considered throughout this thesis. Provided that the mean-flow Reynolds number is large, it is well known that this system exhibits a rich variety of flow-induced instabilities (see numerical studies by Rast, 1994; Luo and Pedley, 1995, 1996, 2000). The frequency and amplitude of the resulting self-excited oscillations is heavily dependent on the magnitude of the membrane tension. For a low membrane tension regime, the viscous pressure drop along the length of the tube induces large-amplitude

steady wall deformations. Numerical simulations conducted (for the case of flux-driven flow) by Luo et al. (2008) and Liu et al. (2009) reveal that these steady states are susceptible to relatively low-frequency oscillations. However, capturing this behaviour from a theoretical standpoint remains a significant challenge, due to the large-amplitude nature of the oscillations. Conversely, in the large membrane tension regime, the steady viscous pressure drop induces only small-amplitude wall deflections, and the system is susceptible to small-amplitude high-frequency self-excited oscillations. For the case of pressure-driven flow, Jensen and Heil (2003) were the first to produce a theoretical description of these oscillations. For a regime in which the membrane tension, mean-flow Reynolds number and axial lengthscales were all large, Jensen and Heil (2003) formally identified a 'sloshing' mechanism that drives self-excited oscillations, and deduced a stability threshold which can be used to predict their onset. It is this regime and mechanism that we focus on in this thesis.

1.1.6 The sloshing mechanism

We now give a brief description of how the sloshing mechanism identified by Jensen and Heil (2003) can result in the onset of self-excited oscillations. Owing to the large longitudinal tension within the membrane, the deflections in the compliant wall are small, and large elastic restoring forces are exerted on the internal fluid. The small-amplitude displacements in the flexible wall change the volume of the channel and displace fluid particles (periodically) towards the upstream and downstream ends of the tube, resulting in oscillatory 'axial sloshing' flows in the rigid sections. By virtue of a non-zero

time-mean-square, any oscillatory flow at the upstream end increases the kinetic energy influx and any oscillatory flow at the downstream end increases the kinetic energy outflux. Hence, if the amplitude of the oscillations is greater in the upstream section of the tube, then there will be a net influx of kinetic energy into the system. Provided that this input exceeds additional losses (e.g., the dissipation due to the viscosity in the fluid and work done by the pressure at the tube ends), then this additional kinetic energy can be sufficient to drive the instability (Jensen and Heil, 2003; Heil and Waters, 2008). Typical ways of achieving larger amplitude sloshing flows in the upstream region include having a shorter upstream rigid section than downstream section, or to prescribe the volume flux at the downstream end. Alternative instability mechanisms, which do not necessarily rely on an increase in kinetic energy flux over time, also exist. For instance, Stewart et al. (2009) developed a spatially one-dimensional long-wavelength model, based on integrating the Jensen and Heil (2003) model over the channel width. This work determined fundamentally different instability mechanisms that rely on either a minimisation of viscous losses or alternatively a reduction of the work done by the pressure at the tube ends.

1.1.7 Three-dimensional models

Whittaker et al. (2010c) showed that the sloshing mechanism identified by Jensen and Heil (2003) in two dimensions can also exist in a three-dimensional set up. They considered oscillations about a non-axisymmetric base configuration. This is because area changes associated with the small-amplitude deformations of a circular cross-section are an order of magnitude smaller

than for the case of a non-axisymmetric cross-section. Since the axial sloshing flows are driven by the area changes, a non-axisymmetric base-state is significantly more likely to become unstable. To obtain a model that predicts the oscillations, independent asymptotic descriptions of the wall mechanics (Whittaker et al., 2010b) and fluid mechanics (Whittaker et al., 2010d) were first established. For the wall mechanics, Whittaker et al. (2010b) systematically derived a tube law using Kirchhoff–Love shell theory, which is valid within a small-amplitude long-wavelength, thin-walled regime and takes the form

$$\tilde{P} = k_0\alpha - k_2\tilde{F}\frac{\mathrm{d}^2\alpha}{\mathrm{d}z^2}, \tag{1.8}$$

where α is the relative area change of the tube's cross-section and k_0 and k_2 are constants. For the fluid mechanics, they used the Navier–Stokes equations, which were shown to simplify significantly due to the high-frequency small-amplitude nature of the oscillations (Whittaker et al., 2010d). Whittaker et al. (2010c) then combined these models and determined the normal modes of the resulting system. After an assessment of the systems energy budget, they used these normal mode solutions to demonstrate that their model exhibits self-excited oscillations, induced by the sloshing instability. On computing the growth rates, frequencies and mode shapes of the oscillations, they compared their work directly with numerical simulations and obtained good agreement. The model of Whittaker et al. (2010c) was then extended by Walters et al. (2018) to include effects due to the inertia of the tube wall. It was found that the addition of wall inertia has a stabilising effect on the system.

Other three-dimensional studies involving collapsible tube flow have also

been conducted. Both Hazel and Heil (2003) and Heil and Boyle (2010) computed full numerical simulations of a model similar to that of Whittaker et al. (2010c) in the large-amplitude regime, while Zhang et al. (2018) considered the three-dimensional deformations of a hyperelastic cylindrical tube.

1.2 Overview

In this thesis, we will focus on the mechanistic modelling of the wall deformations of fluid-filled elastic-walled tubes, and also how these results can be coupled to the mechanics of the internal fluid. In Chapter 2, we re-examine the model used by Whittaker et al. (2010b) to derive a tube law for an initially elliptical elastic-walled tube. We extend the modelling to allow for arbitrary initial cross-sectional shapes and azimuthally varying transmural pressures. These formulations will then be used in the following chapters. In Chapter 3, we use an eigenfunction expansion method to derive the first formal solution for the small-amplitude deformations of a long thin-walled elastic tube having an initially elliptical cross-section. In Chapter 4, we couple this new model for the wall mechanics to the mechanics of an internal fluid. We compute the normal modes of the system, and use these solutions to compute a stability threshold for the onset of self-excited oscillations. In Chapter 5, we derive a model for the wall deformations of a tube with an arbitrary initial cross-sectional shape. We then use this model to compute a family of initial cross-sectional shapes with the property that an azimuthally uniform transmural pressure will excite only a single azimuthal deformation mode, resulting in a semi-analytical solution of the solid mechanics problem. Finally in Chapter 6, we present our final discussions and conclusions.

Chapter 2

Problem formulation

Synopsis

In this chapter, we formally present the problem that is to be considered throughout this thesis by generalising the initial set-up of Whittaker et al. (2010b) to include elastic-walled tubes with arbitrary initial cross-sections. We begin by re-formulating the physical set-up of Whittaker et al. (2010b) in terms of an arbitrary azimuthal co-ordinate system and introduce notation used to describe the tube wall and its deformation. We then derive a revised set of governing equations measuring the wall deformation, which now permit arbitrary initial cross-sections and allow the transmural pressure to be azimuthally non-uniform. Finally, we express the system using two specific co-ordinate systems that will be used in later chapters.

2.1 Introduction

Whittaker et al. (2010b) investigated the small-amplitude deformations of a long thin-walled elastic tube having an initially axially uniform elliptical cross-section. The deformations of the tube were assumed to be induced by an applied transmural pressure, and contributions from the inertia of the

tube wall were ignored. Whittaker et al. (2010b) formally derived governing equations using Kirchhoff–Love shell theory within a long wavelength thin-walled regime, and then used these to obtain a tube law.

By considering the equilibrium of forces in the normal, azimuthal and axial directions, together with linear constitutive laws, Whittaker et al. (2010b) derived a system of equilibrium equations that measure the small-amplitude deformations of the tube. The deformations are expressed in terms of four deformation functions: $\xi(\tau, z), \eta(\tau, z), \zeta(\tau, z)$ and $\zeta_a(z)$, which describe the normal, azimuthal, averaged axial, and residual axial displacements respectively. The displacements are functions of τ and z, which are dimensionless azimuthal and axial co-ordinates respectively. The equilibrium equations obtained are leading order in the deformation magnitude $\epsilon \ll 1$, the reciprocal of the dimensionless tube length $\ell^{-1} \ll 1$, and the dimensionless wall thickness $\delta \ll 1$.

By exploiting the fact that for a long thin-walled tube there is negligible azimuthal extension and in-plane shear at leading order, Whittaker et al. (2010b) obtained relationships between the deformation functions which meant that the entire problem could be formulated in terms of only the azimuthal displacement, $\eta(\tau, z)$. The governing partial differential equation (PDE) for η was shown to be of the form

$$\mathscr{L}\left(\mathscr{K}(\eta)\right) - \tilde{F}\frac{\partial^2}{\partial z^2}\mathscr{J}(\eta) = -\tilde{P}(z)\frac{\mathrm{d}}{\mathrm{d}\tau}\left(\frac{1}{\bar{B}(\tau)}\right), \tag{2.1}$$

where $\mathscr{L}, \mathscr{K}$ and $\mathscr{J}$ are linear differential operators in τ, $\tilde{F}$ is the dimensionless axial tension, $\bar{B}$ is the (known) base-state azimuthal curvature and $\tilde{P}(z)$ is the dimensionless (azimuthally uniform) transmural pressure.

Walters et al. (2018) expanded on the work of Whittaker et al. (2010b) by including effects due to the inertia of the tube wall. Walters et al. (2018) showed that the size of the inertial effects could be captured by a single dimensionless parameter, M. It was found that wall inertia contributed additively to the governing PDE (2.1) through a new term proportional to M. The governing equation becomes

$$\mathscr{L}\left(\mathscr{K}(\eta)\right) - \tilde{F}\frac{\partial^2}{\partial z^2}\mathscr{J}(\eta) + M\frac{\partial^2}{\partial t^2}\mathscr{J}(\eta) = -\tilde{P}(z,t)\frac{\mathrm{d}}{\mathrm{d}\tau}\left(\frac{1}{\bar{B}(\tau)}\right). \qquad (2.2)$$

In this chapter, we generalise the model described above for the case in which the tube has an arbitrary initial cross-sectional shape and the transmural pressure is azimuthally non-uniform. In §2.2, we describe the initial geometry of the tube and its subsequent deformation in terms of an arbitrary azimuthal co-ordinate system. In §2.3, the parameter regime in which the model is valid is presented, and a system of force-balance equations are derived measuring the deformations in the tube wall. By following the methodology set out in Whittaker et al. (2010b), the entire problem is formulated in terms of the azimuthal displacement function, η. The governing equation for η takes a similar form to (2.2), but differs in that $\bar{B}$ is now arbitrary, and the forcing term takes a different form due to the pressure no longer being azimuthally uniform. In §2.4 we recover the set-up of Whittaker et al. (2010b) for the case of an elliptical tube, and also consider the case in which the tube's initial cross-sectional shape is described using intrinsic co-ordinates.

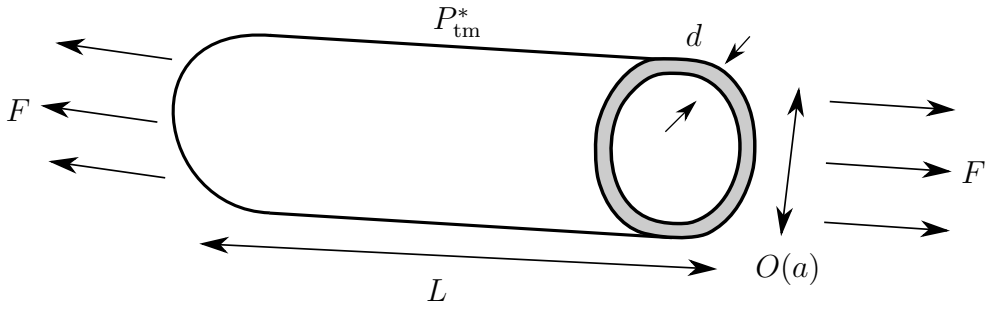

Figure 2.1: The typical set-up showing the initial configuration of a long thin-walled tube of dimensional length L and wall thickness d. The tube has an initially axially uniform arbitrary cross-sectional shape of $O(a)$ radial scale, and is subject to a dimensional axial tension force F at both ends. The tube will undergo deformations about this pre-stressed state due to an applied dimensional transmural pressure P^*_{tm}.

2.2 Set-up

2.2.1 Physical set-up

We adopt a similar set-up to Whittaker et al. (2010b) and Walters et al. (2018) by considering a long thin-walled elastic tube of dimensional length L, with mass per unit area m and dimensional wall thickness d (see figure 2.1). In what we shall term the undeformed configuration, the tube is subject to a dimensional axial pre-stress of magnitude $F/(2\pi ad)$ at both ends and is axially uniform with an arbitrary cross-sectional shape of perimeter $2\pi a$. Hence F is the extensional force applied at the ends of the undeformed tube, and a is the length scale of the tube's cross-section. The tube is aligned with dimensional Cartesian coordinates (ax, ay, Lz), where z is aligned with the tube's central axis. We assume that at the dimensionless endpoints $z = 0, 1$ the tube is pinned to rigid extensions. We introduce $\tau \in (0, \pi/2)$ as an arbitrary dimensionless Lagrangian azimuthal co-ordinate around the tube

midplane.

Assuming that the tube wall is linearly elastic with Young's modulus E and Poisson ratio ν, we define the extensional stiffness D and bending stiffness K respectively as

$$D = \frac{Ed}{1-\nu^2}, \qquad K = \frac{Ed^3}{12(1-\nu^2)}. \tag{2.3}$$

We suppose that changes to the deformation of the tube wall occur over a typical time scale T, and are induced by an applied transmural pressure $P^*_{\mathrm{tm}}(\tau, z, t)$, with dimensional scale $\mathscr{P}$, where t is dimensionless time. We note that in contrast to previous work we allow for azimuthal variation in P^*_{tm}. For simplicity, we assume that P^*_{tm} is even and π-periodic in τ. This corresponds to mirror symmetry in the x and y axes.

2.2.2 Dimensionless parameters and asymptotic regime

We will work within an asymptotic regime in which the tube is long and the wall is thin. Defining dimensionless parameters ℓ and δ for the respective aspect ratios, we have

$$\ell = \frac{L}{a} \gg 1 \qquad \text{and} \qquad \delta = \frac{d}{a} \ll 1. \tag{2.4}$$

We introduce the dimensionless transmural pressure as

$$\tilde{P}(\tau, z, t) = \frac{P^*_{\mathrm{tm}}(\tau, z, t)}{\mathscr{P}}. \tag{2.5}$$

Whittaker et al. (2010b) showed that the dominant mechanisms that bal-

ance the transmural pressure (at leading order) within this regime are those of azimuthal bending and/or the action of axial tension through axial curvature. For the case of Walters et al. (2018) the pressure may also be balanced by contributions due to wall inertia. To describe the relative magnitudes of the transmural pressure scale $\mathscr{P}$, the bending stiffness K, the axial tension F, and the mass m, we introduce the dimensionless parameters:

$$\tilde{F} = \frac{aF}{2\pi K\ell^2} = O(1), \qquad M = \frac{ma^4}{KT^2} \lesssim 1, \qquad \epsilon = \frac{a^3\mathscr{P}}{K} \ll 1. \tag{2.6}$$

The parameter $\tilde{F}$ gives the ratio between axial tension–curvature effects and azimuthal bending, and can be thought of as a dimensionless axial tension. The parameter M gives the ratio between wall inertia and azimuthal bending and can be thought of as a dimensionless mass. Taking $\tilde{F} = O(1)$ and $M \lesssim O(1)$ enables effects due to axial tension–curvature, wall inertia and azimuthal bending all to be present at leading order. The parameter ϵ is the ratio of the pressure forcing to the resistance from azimuthal bending. It gives an estimate of the dimensionless amplitude of the deformations (ϵa in dimensional terms). Taking $\epsilon \ll 1$ ensures that we have small-amplitude deformations, and that we can linearise the problem about the base state.

2.2.3 Description of the shape of the undeformed tube

The tube wall's midplane is parametrised by the dimensionless co-ordinates $\tau \in (0, 2\pi)$ and $z \in (0, 1)$. As depicted in figure 2.2, the co-ordinate τ varies along the midplane of the tube and z is the distance along the tube's central axis. In its undeformed configuration, the Cartesian position vector of the

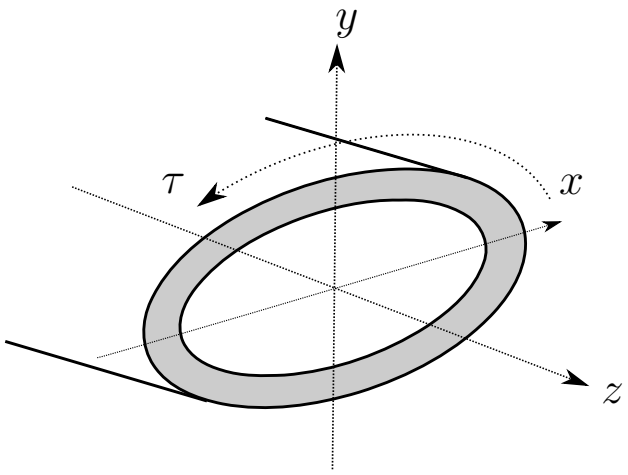

Figure 2.2: Schematic of a shell segment illustrating the dimensionless co-ordinate system (τ, z). Here, τ is the azimuthal co-ordinate oriented around the circumference of the tube's cross-section. The co-ordinate z represents the distance along the tube's central axis.

tube wall is written as

$$\bar{\boldsymbol{r}}(\tau, z) = a \begin{pmatrix} \bar{x}(\tau) \\ \bar{y}(\tau) \\ \ell z \end{pmatrix}, \tag{2.7}$$

where $(x, y) = (\bar{x}(\tau), \bar{y}(\tau))$ gives a dimensionless parametric representation of the tube's initial cross-section.

For simplicity, we assume that the initial cross-sectional shape exhibits two-fold symmetry in the x and y axis, and that the domain $\tau \in (0, \pi/2)$ covers precisely the first quadrant of the tube's midplane. This symmetry can be imposed by requiring $\bar{x}$ to be even about $\tau = 0$, odd about $\tau = \pi/2$, and 2π-periodic, as well as $\bar{y}$ being odd about $\tau = 0$, even about $\tau = \pi/2$, and 2π-periodic. Overall, these symmetries mean that we can restrict the azimuthal domain to the first quadrant $\tau \in (0, \pi/2)$.

We define unit vectors $\hat{\boldsymbol{t}}, \hat{\boldsymbol{z}}$ and $\hat{\boldsymbol{n}}$, which are oriented in the azimuthal, axial and normal directions respectively. They are given by

$$\hat{\boldsymbol{t}} = \frac{1}{h}\begin{pmatrix} \bar{x}'(\tau) \\ \bar{y}'(\tau) \\ 0 \end{pmatrix}, \qquad \hat{\boldsymbol{z}} = \begin{pmatrix} 0 \\ 0 \\ 1 \end{pmatrix}, \qquad \hat{\boldsymbol{n}} = \frac{1}{h}\begin{pmatrix} \bar{y}'(\tau) \\ -\bar{x}'(\tau) \\ 0 \end{pmatrix}, \tag{2.8}$$

where the dash represents a derivative with respect to τ, and the scale factor $h(\tau)$ is given by

$$h(\tau) = \sqrt{\left(\frac{\mathrm{d}\bar{x}}{\mathrm{d}\tau}\right)^2 + \left(\frac{\mathrm{d}\bar{y}}{\mathrm{d}\tau}\right)^2} > 0. \tag{2.9}$$

The imposed symmetry on $\bar{x}$ and $\bar{y}$ then results in $h(\tau)$ being both even and π-periodic. We introduce a dimensional arclength parameter as that is measured around the tube's midplane, and let A and B be points corresponding to $\tau = 0$ and $\tau = \pi/2$ respectively. Using figure 2.3 for reference, the dimensional circumference $\bar{C}$ of the tube is given by

$$\begin{aligned} \bar{C} &= 4a\int_A^B \mathrm{d}s, \\ &= 4a\int_0^{\pi/2} h(\tau)\,\mathrm{d}\tau, \end{aligned} \tag{2.10}$$

Since the perimeter of the tube's cross-section is fixed as $2\pi a$, we require

$$\int_0^{\pi/2} h(\tau)\,\mathrm{d}\tau = \frac{\pi}{2}. \tag{2.11}$$

The dimensional base-state cross-sectional area $\bar{A}$ of the tube is given by

$$\bar{A} = 4a^2\int_B^A \bar{y}\,\mathrm{d}x,$$

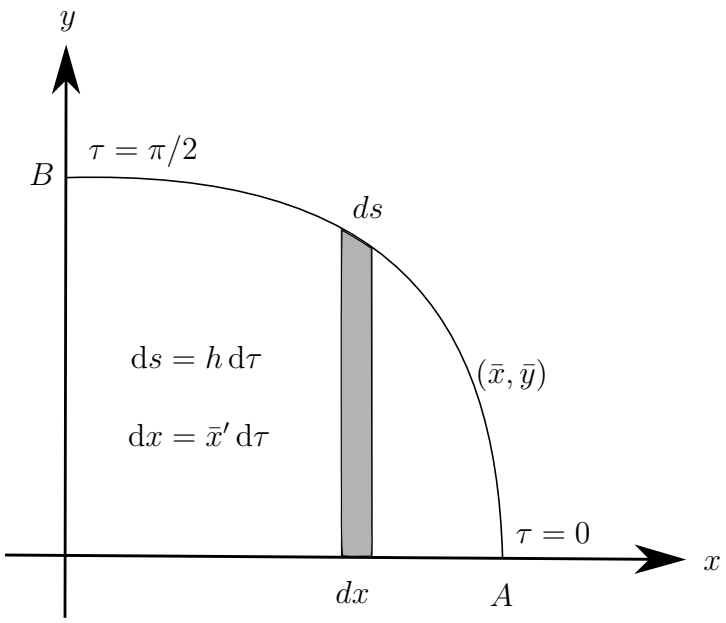

Figure 2.3: One quarter of an initial cross-sectional shape that is parametrised by $(x, y) = (\bar{x}, \bar{y})$. The grey shaded region is a thin area element with an approximate area of $\bar{y}\,\mathrm{d}x$. The schematic illustrates the relationship between the Cartesian co-ordinate x and the dimensionless arclength parameter s to the azimuthal co-ordinate τ.

$$= 4a^2 \int_{\pi/2}^{0} \bar{y}(\tau)\bar{x}'(\tau)\,\mathrm{d}\tau. \tag{2.12}$$

The base-state azimuthal curvature $\bar{B}(\tau)$ of the undeformed tube is given by

$$\begin{aligned} \bar{B}(\tau) &= \hat{\boldsymbol{n}} \cdot \frac{\mathrm{d}\hat{\boldsymbol{t}}}{\mathrm{d}s}, \\ &= \hat{\boldsymbol{n}} \cdot \frac{1}{h}\frac{\mathrm{d}\hat{\boldsymbol{t}}}{\mathrm{d}\tau}, \\ &= \frac{\bar{y}'}{h^2}\left(\frac{\bar{x}'}{h}\right)' - \frac{\bar{x}'}{h^2}\left(\frac{\bar{y}'}{h}\right)'. \end{aligned} \tag{2.13}$$

The symmetries of $\bar{x}$, $\bar{y}$ and h result in $\bar{B}$ being both even and π-periodic.

2.2.4 Description of the deformations

We now introduce variables to describe the deformation of the tube from its undeformed configuration. We follow Whittaker et al. (2010b) who used the four deformation functions: $\xi(\tau, z, t), \eta(\tau, z, t), \zeta(\tau, z, t)$ and $\zeta_a(z, t)$. The function $\xi(\tau, z, t)$ describes the component of displacement normal to the tube wall, $\eta(\tau, z, t)$ describes the displacement in the azimuthal direction, and the functions $\zeta(\tau, z, t)$ and $\zeta_a(z, t)$ represent the axial displacements. The two functions are used here to distinguish between the azimuthal-mean axial displacement $\zeta_a(z, t)$, and the azimuthally varying component $\zeta(\tau, z, t)$, which have different scales. The deformed position of the part of the tube wall which was at $\bar{\boldsymbol{r}}(\tau, z)$ in the undeformed configuration is then written as

$$\begin{aligned}\boldsymbol{r}(\tau, z, t) = \bar{\boldsymbol{r}}(\tau, z) + \frac{\epsilon a}{h(\tau)}\left(\xi(\tau, z, t)\hat{\boldsymbol{n}} + \eta(\tau, z, t)\hat{\boldsymbol{t}}\right) \\ + \epsilon a \ell \left(\frac{1}{\ell^2}\zeta(\tau, z, t) + \delta^2 \zeta_a(z, t)\right)\hat{\boldsymbol{z}},\end{aligned} \tag{2.14}$$

where

$$\int_0^{2\pi} \zeta(\tau, z, t) h(\tau)\, \mathrm{d}\tau = 0. \tag{2.15}$$

The pre-factors present in (2.14) ensure that the dimensional scales are consistent whilst rendering the deformation functions $\xi, \eta, \zeta, \zeta_a$ all $O(1)$.

2.3 Asymptotic model for the deformations

Using the set-up of Whittaker et al. (2010b), we consider an asymptotic model in the multiple limits $\delta \ll 1, \ell \gg 1$ and $\epsilon \ll 1$, that is zeroth order in δ, and ℓ^{-1}, and first order in ϵ. There is one constraint on the relative

magnitudes of δ and ℓ^{-1}, which ensures that boundary layers in the axial co-ordinate (containing unwanted shear effects) are passive, and have a negligible effect on the bulk solution:

$$\delta\ell^2 \gg 1. \tag{2.16}$$

We refer readers to Whittaker (2015) and Walters et al. (2018) for a comprehensive discussion on this topic. But briefly, Whittaker (2015) and Walters et al. (2018) introduce the dimensionless parameter

$$\mathscr{F} = \frac{\tilde{F}\delta^2\ell^2}{12(1-\nu^2)} \tag{2.17}$$

to characterize boundary layer thickness for the asymptotic regimes considered here. For $\mathscr{F} \gg 1$, an axial boundary layer of dimensional thickness $O(a\delta\ell)$ is present, which is necessarily passive when $\delta \ll 1$. On the other hand, when $\mathscr{F} \ll 1$, an outer shear layer of dimensional thickness $O(a\mathscr{F}^{-1/2})$ is present. For this layer to have negligible affect on the bulk solution, we require $a\mathscr{F}^{-1/2} \ll L$. Overall, this leads to the constraint (2.16).

2.3.1 Leading-order force balance

For the case of an initially elliptical tube, Whittaker et al. (2010b) and Walters et al. (2018) derived a system of equations of motion measuring the deformations in the tube wall. The derivation starts with linear constitutive laws (Flügge, 1972) for the elastic wall and the Kirchhoff–Love shell equations (Love, 1888). On substituting the deformation (2.14) for the case of an ellipse into these equations and neglecting terms of $O(\epsilon, \ell^{-1}, \delta)$, a set of

three equations of motion in the normal, azimuthal and axial directions is obtained. The unknowns in these equations are the displacement functions $\xi, \eta, \zeta, \zeta_a$ and a hoop stress $\tilde{N}$ (the latter is effectively a Lagrange multiplier for the constraint of no azimuthal stretching).

We now replicate the methodology set out in Whittaker et al. (2010b) and Walters et al. (2018) for the more general set-up stated above. Omitting the detailed calculations for brevity, we obtain the following leading-order system of three force-balance equations that describe the deformations of a tube with an arbitrary initial cross-sectional shape

$$\bar{B}\tilde{N} + \frac{\tilde{F}}{h}\frac{\partial^2 \xi}{\partial z^2} - \frac{1}{h}\frac{\partial}{\partial \tau}\left(\frac{1}{h}\frac{\partial}{\partial \tau}\left(\frac{\beta}{h}\right)\right) + \frac{M}{h}\frac{\partial^2 \xi}{\partial t^2} + \tilde{P}(\tau, z, t) = 0, \tag{2.18}$$

$$\frac{\partial \tilde{N}}{\partial \tau} + \frac{12(1-\nu)}{\delta^2 \ell^2}\frac{\mathrm{d}}{\mathrm{d}z}\left(\frac{\partial \eta}{\partial z} + \frac{\partial \zeta}{\partial \tau}\right) + \tilde{F}\frac{\partial^2 \eta}{\partial z^2} + \bar{B}\frac{\partial}{\partial \tau}\left(\frac{\beta}{h}\right) + M\frac{\partial^2 \eta}{\partial t^2} = 0, \tag{2.19}$$

$$\begin{aligned}\frac{1}{\ell}\frac{\partial}{\partial z}\left(\nu\tilde{N} + 12(1-\nu^2)\left(\frac{1}{\delta^2\ell^2}\frac{\partial \zeta}{\partial z} + \frac{\partial \zeta_a}{\partial z}\right)\right) + \frac{\tilde{F}\ell\delta^2}{12}\frac{\partial \tilde{N}}{\partial z} \\ \tilde{F}\ell(2-\nu)\left(\frac{1}{\ell^2}\frac{\partial^2 \zeta}{\partial z^2} + \delta^2\frac{\partial^2 \zeta_a}{\partial z^2}\right) + M\ell\left(\frac{1}{\ell^2}\frac{\partial^2 \zeta}{\partial t^2} + \delta^2\frac{\partial^2 \zeta_a}{\partial t^2}\right) = 0,\end{aligned} \tag{2.20}$$

where

$$\beta = \frac{\partial}{\partial \tau}\left[\frac{\eta \bar{B}}{h} + \frac{1}{h}\frac{\partial}{\partial \tau}\left(\frac{\xi}{h}\right)\right] \tag{2.21}$$

and $\tilde{N}$ is the azimuthal hoop stress. We choose not to give an explicit expression for $\tilde{N}$ as it will later be eliminated. Equations (2.18)–(2.21) are identical to those presented in Walters et al. (2018), with the exceptions that h and $\bar{B}$ are now arbitrary, β is no longer defined in terms of elliptical

co-ordinates, and $\tilde{P}$ can vary in τ.[1]

2.3.2 Asymptotic constraints

For the thin-walled regime considered here, the tube is much more susceptible to bending than it is to stretching and shearing. Whittaker et al. (2010b) argued that at leading order in ϵ there is negligible azimuthal stretching and that the in-plane shear is uniform within each cross-section. They showed that these physical constraints result in the following leading-order relationships

$$-\xi\bar{B} + \frac{\partial}{\partial\tau}\left(\frac{\eta}{h}\right) = 0, \tag{2.22}$$

$$\frac{\partial\eta}{\partial z} + \frac{\partial\zeta}{\partial\tau} = \frac{h(\tau)}{2\pi}\frac{\mathrm{d}}{\mathrm{d}z}\int_0^{2\pi}\eta\,\mathrm{d}\tau. \tag{2.23}$$

Equations (2.22)–(2.23) provide useful relationships between the deformation functions ξ, η and ζ. In the following section, they will be used to eliminate ξ and ζ, in favour of η. The remaining displacement function ζ_a decouples automatically, and can be obtained by averaging (2.20) over the azimuthal co-ordinate τ and applying appropriate boundary conditions at $z = 0, 1$ (see §2.3.4). Overall, this means the entire problem can be formulated in terms of the azimuthal deformation, η.

[1]Note: there is an erroneous factor of h in the second term of eq. (2.51) in Walters et al. (2018).

2.3.3 The governing equation for the azimuthal displacements

Eliminating $\tilde{N}$ between equations (2.18) and (2.19) and using (2.22)–(2.23) to write the resulting equation in terms of only η, we arrive at the following partial integro-differential equation for η

$$\mathscr{L}(\mathscr{K}(\eta)) - h\frac{\partial^2}{\partial z^2}\mathscr{R}(\eta) - \tilde{F}\frac{\partial^2}{\partial z^2}\mathscr{J}(\eta) + M\frac{\partial^2}{\partial t^2}\mathscr{J}(\eta) = -\frac{\partial}{\partial \tau}\left(\frac{\tilde{P}(\tau, z, t)}{\bar{B}(\tau)}\right), \tag{2.24}$$

where the linear differential operators $\mathscr{L}, \mathscr{K}$ and $\mathscr{J}$, are given explicitly by

$$\mathscr{L}(\eta) = -\bar{B}\frac{\partial}{\partial \tau}\left(\frac{\eta}{h}\right) - \frac{\partial}{\partial \tau}\left(\frac{1}{\bar{B}h}\frac{\partial}{\partial \tau}\left(\frac{1}{h}\frac{\partial}{\partial \tau}\left(\frac{\eta}{h}\right)\right)\right), \tag{2.25}$$

$$\mathscr{J}(\eta) = \eta - \frac{\partial}{\partial \tau}\left(\frac{1}{\bar{B}^2 h}\frac{\partial}{\partial \tau}\left(\frac{\eta}{h}\right)\right), \tag{2.26}$$

$$\mathscr{K}(\eta) = \frac{\partial}{\partial \tau}\left(\frac{\bar{B}\eta}{h} + \frac{1}{h}\frac{\partial}{\partial \tau}\left(\frac{1}{\bar{B}h}\frac{\partial}{\partial \tau}\left(\frac{\eta}{h}\right)\right)\right), \tag{2.27}$$

and the integral operator $\mathscr{R}(\eta)$ is defined as

$$\mathscr{R}(\eta) = \frac{12(1-\nu)}{\delta^2 \ell^2}\frac{1}{2\pi}\int_0^{2\pi} \eta \, \mathrm{d}\tau. \tag{2.28}$$

The transmural pressure $\tilde{P}$, the base-state curvature $\bar{B}$, and the scale factor h are all assumed to be even and π-periodic in τ. Noting the even symmetry of the operators $\mathscr{L}\mathscr{K}$ and $\mathscr{J}$ in (2.24) we can see that the only component of η that is forced by the transmural pressure will be both odd and π-periodic. For the case in which wall inertia is neglected ($M = 0$), Whittaker et al. (2010b) showed that solutions for η must be both odd and π-periodic. We note that for the general set-up considered here this result still

holds true. For the case in which wall inertia is present ($M \neq 0$), solutions for η exist involving free oscillatory modes that do not exhibit this symmetry. Since these are unforced, we neglect these components and proceed by seeking solutions for η that are odd and π-periodic. This results in $\hat{\mathscr{R}}(\eta) \equiv 0$, and the governing equation (2.24) becomes a PDE

$$\mathscr{L}(\mathscr{K}(\eta)) - \tilde{F}\frac{\partial^2}{\partial z^2}\mathscr{J}(\eta) + M\frac{\partial^2}{\partial t^2}\mathscr{J}(\eta) = -\frac{\partial}{\partial \tau}\left(\frac{\tilde{P}(\tau, z, t)}{\bar{B}(\tau)}\right). \tag{2.29}$$

Equation (2.29) is a generalisation of the governing PDE derived by Walters et al. (2018), and differs in that the base-state curvature $\bar{B}$, and the azimuthal co-ordinate τ are both arbitrary. The form of the pressure term also differs and now involves an azimuthal derivative, which is present because the pressure is no longer assumed to be azimuthally uniform.

2.3.4 Boundary conditions

There are two sets of boundary conditions that accompany (2.29). The first applies at $\tau = 0, \pi/2$, and arise due to the symmetries of the problem. Since we are assuming that η is both odd and π periodic in τ we can restrict our attention to the quarter domain $\tau \in (0, \pi/2)$ and reconstruct the global solution for η using symmetry. To ensure that this global solution is smooth everywhere, we need to impose

$$\eta = \frac{\partial^2 \eta}{\partial \tau^2} = \frac{\partial^4 \eta}{\partial \tau^4} = 0 \qquad \text{on} \qquad \tau = 0, \frac{\pi}{2}. \tag{2.30}$$

The second set of boundary conditions apply at the dimensionless tube ends $z = 0$ and $z = 1$, and encapsulate the requirement that the elastic tube

is pinned to rigid supports. The conditions are given explicitly by

$$\eta = 0 \qquad \text{on} \qquad z = 0, 1. \tag{2.31}$$

As discussed by Whittaker et al. (2010b), the pinned-end boundary conditions (2.31) combined with the inextensibility constraints (2.22)–(2.23) imply that we require $\xi = 0$ at $z = 0, 1$, however that we shall not, in general, obtain either $\zeta = 0$ or $\partial\xi/\partial z = 0$ at $z = 0, 1$. The inability to fix the axial displacements and normal gradient at the tube ends is a result of losing degrees of freedom by neglecting in-plane shear and axial bending effects. These effects are contained within boundary layers adjacent to the tube ends, which are passive for the asymptotic regime considered here. For a detailed discussion on this topic see Whittaker (2015) and Walters et al. (2023).

Equations (2.29)–(3.20) define a sixth-order linear boundary value problem for the azimuthal displacement function, η. Once a solution for η has been obtained, the inextensibility conditions (2.22)–(2.23) can then be used to determine ξ and ζ. The final displacement function ζ_a can be obtained by averaging (2.20) over the cross-section and imposing $\zeta_a = 0$ at $z = 0, 1$.

2.4 Specific co-ordinate systems

We now consider two special cases of the above system, which we shall use in later chapters of this thesis: First, the case of an elliptical cross-section (previously used by Whittaker et al. (2010b) and Walters et al. (2018)) and secondly the case where the cross-sectional shape is defined using intrinsic co-ordinates.

2.4.1 Elliptical co-ordinates

For the case of an initially elliptical tube, we introduce the constant ellipticity parameter σ_0 such that the tube's initial cross-section is parametrised by

$$\bar{x}(\tau) = c\cosh(\sigma_0)\cos(\tau), \qquad \bar{y}(\tau) = c\sinh(\sigma_0)\sin(\tau). \tag{2.32}$$

Here, the constant $c(\sigma_0)$ is a normalisation factor that is chosen to set the initial circumference of the tube's cross-section to be $2\pi a$. The dimensional Cartesian position vector of the tube in its undeformed configuration is given by

$$\bar{\boldsymbol{r}}(\tau, z) = a\begin{pmatrix} c\cosh(\sigma_0)\cos(\tau) \\ c\sinh(\sigma_0)\sin(\tau) \\ \ell z \end{pmatrix}. \tag{2.33}$$

From (2.9), the scale factor $h(\tau)$ is given by

$$h(\tau) = c\left(\frac{1}{2}\cosh(2\sigma_0) - \frac{1}{2}\cos(2\tau)\right)^{\frac{1}{2}} > 0. \tag{2.34}$$

Using (2.10) the circumference of the tube is then given by

$$\bar{C} = 2\pi a\frac{2cE(\operatorname{sech}(\sigma_0))}{\pi\operatorname{sech}(\sigma_0)}, \tag{2.35}$$

where $E(k) = \int_0^{\pi/2}\sqrt{1-k^2\sin^2(\theta)}\mathrm{d}\theta$ is the complete elliptic integral of the second kind. Hence, to obtain $\bar{C} = 2\pi a$, we require

$$c = \frac{\pi\operatorname{sech}(\sigma_0)}{2E(\operatorname{sech}(\sigma_0))}. \tag{2.36}$$

Using (2.12) and (2.13), expressions for the undisturbed area $\bar{A}$ and the base-state azimuthal curvature are then given by

$$\bar{A} = \pi a^2 \frac{c^2 \sinh(2\sigma_0)}{2}, \qquad \bar{B}(\tau) = -\frac{c^2 \sinh(2\sigma_0)}{2h^3}. \tag{2.37}$$

Finally, from (2.8), the unit vectors $\hat{\boldsymbol{t}}, \hat{\boldsymbol{z}}$ and $\hat{\boldsymbol{n}}$ are given by

$$\hat{\boldsymbol{t}} = \frac{c}{h}\begin{pmatrix} -\cosh(\sigma_0)\sin(\tau) \\ \sinh(\sigma_0)\cos(\tau) \\ 0 \end{pmatrix}, \qquad \hat{\boldsymbol{z}} = \begin{pmatrix} 0 \\ 0 \\ 1 \end{pmatrix}, \qquad \hat{\boldsymbol{n}} = \frac{c}{h}\begin{pmatrix} \sinh(\sigma_0)\cos(\tau) \\ \cosh(\sigma_0)\sin(\tau) \\ 0 \end{pmatrix}. \tag{2.38}$$

These results match those obtained by Whittaker et al. (2010b).

2.4.2 Intrinsic arclength co-ordinates

For the case where the tube's initial cross-section is arbitrary, we can parametrise the tube's cross-section using a dimensionless arclength co-ordinate, s, which is measured around the tube's midplane. To describe the cross-sectional shape, we can introduce $\theta(s)$, which represents the angle made between the y axis and the tangent to the tube midplane (see figure 2.4).

The components $\bar{x}$ and $\bar{y}$ of the Cartesian position vector of the tube in its undeformed configuration are then given by:

$$\bar{x} = -\int_s^{\pi/2} \sin\theta(s')\,\mathrm{d}s', \qquad \bar{y} = \int_0^s \cos\theta(s')\,\mathrm{d}s'. \tag{2.39}$$

The scale factor for the arclength co-ordinate system is given by $h = 1$. Using (2.8)–(2.13), we obtain the following expressions for the unit vectors

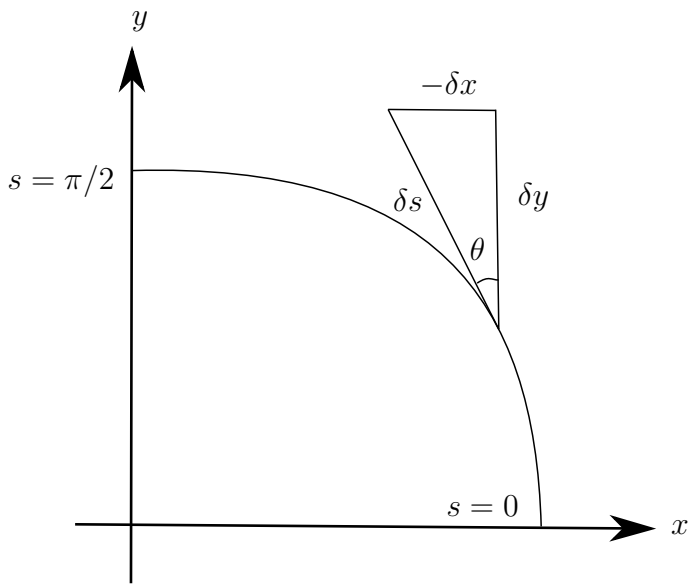

Figure 2.4: Schematic of a shell segment illustrating the relationship between the dimensionless intrinsic co-ordinate, $\theta(s)$ and the co-ordinates x, y and s. Here s is a measure of arclength around the tube's midplane.

and base-state curvature

$$\hat{\boldsymbol{n}} = \begin{pmatrix} \cos\theta(s) \\ \sin\theta(s) \\ 0 \end{pmatrix}, \qquad \hat{\boldsymbol{t}} = \begin{pmatrix} -\sin\theta(s) \\ \cos\theta(s) \\ 0 \end{pmatrix}, \qquad \hat{\boldsymbol{z}} = \begin{pmatrix} 0 \\ 0 \\ 1 \end{pmatrix}, \tag{2.40}$$

and

$$\bar{B}(s) = -\frac{\mathrm{d}\theta}{\mathrm{d}s}. \tag{2.41}$$

By symmetry in the cross-sectional shape, we require θ to satisfy

$$\theta(0) = 0, \qquad \theta(\pi/2) = \frac{\pi}{2}. \tag{2.42}$$

2.5 Conclusions

In this chapter, we have generalised the set-up and initial modelling of Whittaker et al. (2010b) to permit arbitrary initial cross-sectional shapes and azimuthally varying transmural pressures. To do this, we re-formulated the physical set-up outlined by Whittaker et al. (2010b) in terms of an arbitrary azimuthal co-ordinate system. Following the methodology set out by Whittaker et al. (2010b), we then derived a generalised governing equation for the azimuthal displacement function η, which now permits arbitrary initial cross-sections and an azimuthally non-uniform transmural pressure.

The problem formulated in this chapter will be considered throughout the remainder of this thesis. In Chapter 3, we consider the case of an initially elliptical tube by adopting the set-up here in terms of the elliptical co-ordinates set out in §2.4.1. In Chapter 5, we investigate the deformations of tubes with different initial cross-sectional shapes by adopting the set up here in terms of the intrinsic arclength co-ordinate system set-out in §2.4.2.

Chapter 3

Formal series solution for the deformations of an initially elliptical elastic-walled tube

Synopsis

We derive a formal series solution to the PDE obtained in Chapter 2 that models the deformations of an initially elliptical elastic-walled tube. The tube is deformed by a (possibly non-uniform) transmural pressure. To obtain the solution, we write the azimuthal displacement as a sum over the azimuthal eigenfunctions of a generalised eigenvalue problem, and show that we are able to derive an uncoupled system of linear PDEs with constant coefficients for the amplitude of the azimuthal modes as a function of the axial co-ordinate and time. This results in a formal solution of the whole system being found as a sum over the azimuthal modes. We show that the nth mode's contribution to the tube's relative area change is governed by a simplified second-order PDE, and examine the case in which the tube's deformations are driven by a uniform transmural pressure. The relative errors induced by truncating the series solution after the

first and second term are then evaluated as a function of both the ellipticity and pre-stress of the tube. After comparing our results with Whittaker et al. (2010b), we find that this new method leads to a significant simplification when calculating contributions from the higher-order azimuthal modes, which in turn makes a more accurate solution easier to obtain.

3.1 Introduction

When modelling fluid-structure interaction in elastic-walled tubes, the wall mechanics are often captured using a so-called 'tube law' — a relationship between the transmural pressure and the cross-sectional area. As part of a series of papers developing a model for self-excited oscillations in a Starling resistor set up, Whittaker et al. (2010c) needed to obtain a tube law for an initially elliptical elastic-walled tube under axial tension. Whittaker et al. (2010b) used the modelling described here in Chapter 2 to obtain the PDE

$$\mathscr{L}\left(\mathscr{K}(\eta)\right) - \tilde{F}\frac{\partial^2}{\partial z^2}\mathscr{J}(\eta) = -\tilde{P}(z)\frac{\mathrm{d}}{\mathrm{d}\tau}\left(\frac{1}{\bar{B}(\tau)}\right), \tag{3.1}$$

which governs the leading-order azimuthal displacements of a long thin-walled initially elliptical elastic-walled tube, with dimensionless axial tension $\tilde{F}$ under dimensionless axially varying transmural pressure $\tilde{P}$. (Here τ and z are the azimuthal and axial co-ordinates, $\bar{B}$ is the base-state azimuthal curvature, and $\mathscr{L}, \mathscr{K}$ and $\mathscr{J}$ are linear differential operators in τ.)

Whittaker et al. (2010b) opted to solve the governing equation (3.1) via Fourier decomposition, by seeking a solution of the form

$$\eta(\tau, z) = \sum_{n=1}^{\infty} e_n(z) \sin(2n\tau). \tag{3.2}$$

Whittaker et al. (2010b) argued that just the first term in (3.2) would provide a good approximation to η. After truncating (3.2) after mode $n = 1$ and introducing $\alpha(z)$, the relative change in cross-sectional area, Whittaker et al. (2010b) deduced the tube law

$$\tilde{P} = k_0 \alpha - k_2 \tilde{F} \frac{\mathrm{d}^2 \alpha}{\mathrm{d}z^2}, \tag{3.3}$$

where k_0 and k_2 are constants, which are computed using numerical solutions for the leading Fourier modes of the particular integral and complementary function of (3.1).

By adopting the same solution method as Whittaker et al. (2010b), Walters et al. (2018) extended the work of Whittaker et al. (2010b) by including contributions due to the inertia of the tube wall. Walters et al. (2018) showed that such contributions could be captured via an additional term in the PDE containing a new dimensionless parameter, M, which is a dimensionless measure of the inertia in the tube wall. The governing PDE becomes

$$\mathscr{L}\left(\mathscr{K}(\eta)\right) - \tilde{F} \frac{\partial^2}{\partial z^2} \mathscr{J}(\eta) + M \frac{\partial^2}{\partial t^2} \mathscr{J}(\eta) = -\tilde{P}(z,t) \frac{\mathrm{d}}{\mathrm{d}\tau} \left(\frac{1}{\bar{B}(\tau)} \right). \tag{3.4}$$

and the corresponding tube law is

$$\tilde{P} = k_0\alpha - k_2\tilde{F}\frac{\partial^2\alpha}{\partial z^2} + k_2 M\frac{\partial^2\alpha}{\partial t^2}. \tag{3.5}$$

Whilst the approach of Whittaker et al. (2010b) and Walters et al. (2018) appeared to give good results, an ad hoc approximation was used to truncate the Fourier series (3.2). The correction to the first mode, which is induced by the (coupled) higher-order modes is then difficult to calculate. In particular, higher-order modes in the expansion (3.2) will affect the system for e_1, meaning it has to be re-solved when additional terms are added.

In the present work, we will instead use an eigenfunction expansion method that allows the equations for the modes to fully decouple. We derive a formal solution of the whole system, which allows us to calculate the order of magnitude of the error induced after truncation at any mode.

We begin by adopting the setup and governing equations from Chapter 2 in terms of the elliptical azimuthal co-ordinates system introduced in §2.4.1. In §3.3 we then introduce a generalised eigenvalue problem, which will later be used to decouple the governing equation for the azimuthal deformation. The generalised eigenvalue problem is solved numerically using a collocation method (`bvp4c`) and solutions for a variety of elliptical cross-sections are presented. In §3.4 we show that the relative area change α can be decomposed as $\alpha(z,t) = \sum_{n=1}^{\infty}\alpha_n(z,t)$, where each $\alpha_n(z,t)$ satisfies a tube-law like equation

$$\tilde{F}\frac{\partial^2\alpha_n}{\partial z^2} - M\frac{\partial^2\alpha_n}{\partial t^2} - \lambda_n\alpha_n = -Q_n(z,t)t_n. \tag{3.6}$$

Here α_n is the component of the relative area change corresponding to the

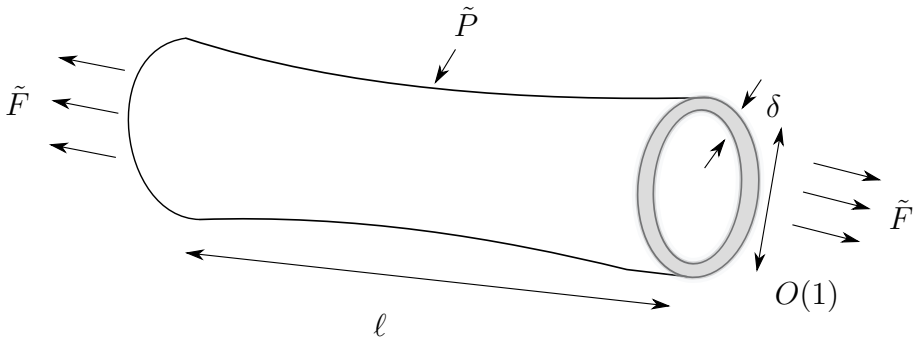

Figure 3.1: The typical setup showing a long thin-walled tube of dimensionless length ℓ, dimensionless mass M, and dimensionless wall thickness δ, with an initially axially uniform elliptical cross-section. The tube is subject to a dimensionless axial tension $\tilde{F}$ at both ends and is exhibiting deformations in response to an applied dimensionless transmural pressure $\tilde{P}$.

nth azimuthal deformation eigenmode, λ_n and t_n are positive constants that arise from the solutions of the generalised eigenvalue problem, and $Q_n(z,t)$ measures forcing from the transmural pressure on the nth eigenmode. In §3.5 we examine the case where the deformations of the tube wall are induced by a steady uniform transmural pressure. In this case, the components $\alpha_n(z)$ are governed by a system of ordinary differential equations (ODEs). We present results for the first four modes of the relative area change, comparing directly with the work of Whittaker et al. (2010b), and evaluate the relative error after truncation after $n = 1$ and $n = 2$. Finally, in §3.6 we present our final discussions and conclusions, whilst also commenting on future work.

3.2 Setup

3.2.1 Physical setup

We adopt the setup of Chapter 2 in dimensionless form and consider a long thin-walled elastic tube of dimensionless length $\ell \gg 1$, dimensionless wall

thickness $\delta \ll 1$ and dimensionless mass $M \lesssim 1$ (see figure 3.1). In its initial configuration, the tube is subject to a dimensionless axial tension force $\tilde{F} = O(1)$ at both ends and is axially uniform with an elliptical cross-section. The elliptical cross-section has circumference 2π, and an ellipticity σ_0 defined so the major and minor axis ratio is $\coth \sigma_0$.

We consider deformations in the tube induced by a dimensionless transmural pressure $\tilde{P}$. We restrict attention to pressures that are even and π-periodic, and deformations that are odd and π-periodic. To describe the tube wall and its deformation, we adopt the elliptical co-ordinate system (τ, z) set out in Chapter 2, where τ is a dimensionless azimuthal co-ordinate, and z is an axial co-ordinate aligned with the tube's central axis. We introduce t as dimensionless time. From Chapter 2, the Cartesian position vector of the tube in its initial position is given by

$$\bar{\mathbf{r}}(\tau, z) = a \begin{pmatrix} c\cosh(\sigma_0)\cos(\tau) \\ c\sinh(\sigma_0)\sin(\tau) \\ \ell z \end{pmatrix}. \tag{3.7}$$

We also have the unit vectors $\hat{\boldsymbol{t}}, \hat{\boldsymbol{z}}$ and $\hat{\boldsymbol{n}}$ in the normal, azimuthal and axial directions respectively:

$$\hat{\boldsymbol{t}} = \frac{c}{h}\begin{pmatrix} -\cosh(\sigma_0)\sin(\tau) \\ \sinh(\sigma_0)\cos(\tau) \\ 0 \end{pmatrix}, \qquad \hat{\boldsymbol{z}} = \begin{pmatrix} 0 \\ 0 \\ 1 \end{pmatrix}, \qquad \hat{\boldsymbol{n}} = \frac{c}{h}\begin{pmatrix} \sinh(\sigma_0)\cos(\tau) \\ \cosh(\sigma_0)\sin(\tau) \\ 0 \end{pmatrix}. \tag{3.8}$$

j	$\sqrt{\bar{A}(s_j) - \bar{A}(s_0)}$	s_j
0	0	∞
1	γ	0.9540
2	2γ	0.6
3	3γ	0.3840
4	4γ	0.2194
5	5γ	0.0755

Table 3.1: The representative eccentricity parameter values s_j of σ_0. The values were chosen such that $\sqrt{\bar{A}(s_j) - \bar{A}(s_0)} = \gamma j$ is linear in j, where $\gamma = \frac{1}{2}\sqrt{\bar{A}(0.6) - \bar{A}(s_0)}$ is chosen such that $s_2 = 0.6$ for a comparison with the study of Whittaker et al. (2010b). The resulting elliptical cross-sections are shown in figure 3.2. The s_j values were deduced numerically using the built in `Matlab` function `fzero`.

Here the constant normalisation factor $c(\sigma_0)$ is given by

$$c = \frac{\pi \operatorname{sech}(\sigma_0)}{2E(\operatorname{sech}(\sigma_0))}, \tag{3.9}$$

and the scale factor $h(\tau)$ is given by

$$h(\tau) = c\left(\frac{1}{2}\cosh(2\sigma_0) - \frac{1}{2}\cos(2\tau)\right)^{\frac{1}{2}} > 0. \tag{3.10}$$

The cross-sectional area $\bar{A}$ and the base-state azimuthal curvature $\bar{B}(\tau)$ of the undeformed tube are given respectively by

$$\bar{A} = \pi a^2 \frac{c^2 \sinh(2\sigma_0)}{2}, \qquad \bar{B}(\tau) = -\frac{c^2 \sinh(2\sigma_0)}{2h^3}. \tag{3.11}$$

Throughout this Chapter we shall refer to a set of six representative values of σ_0, $(s_0, s_1, s_2, s_3, s_4, s_5)$, which are presented in table 3.1. Figure 3.2 shows the corresponding elliptical cross-sections.

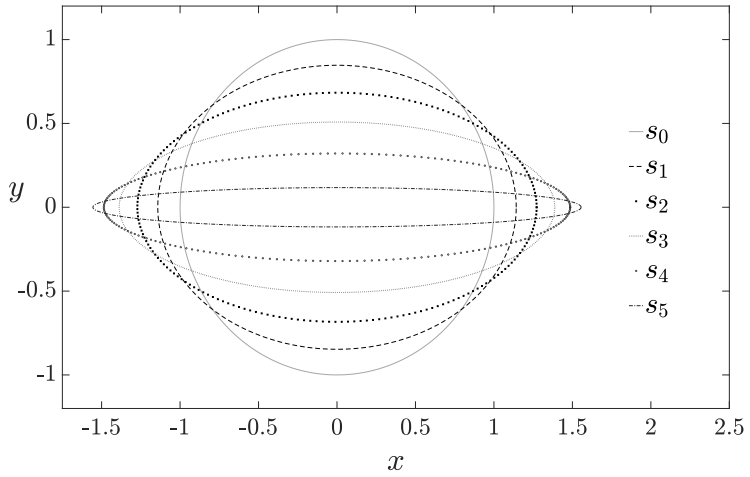

Figure 3.2: The elliptical cross-sections for $\sigma_0 \in \{s_0, s_1, s_2, \ldots, s_5\}$ as given in table 3.1. The curves are plotted using (3.9) and (3.7) with $a = 1$.

To describe the deformation of the tube, we adopt the four deformation functions: $\xi(\tau, z, t), \eta(\tau, z, t), \zeta(\tau, z, t)$ and $\zeta_a(z, t)$ that were introduced in Chapter 2. In terms of time t, the deformed position vector of the tube is given by

$$\begin{aligned} \boldsymbol{r}(\tau, z, t) = \bar{\boldsymbol{r}}(\tau, z) + \frac{\epsilon a}{h(\tau)} \left(\xi(\tau, z, t)\hat{\boldsymbol{n}} + \eta(\tau, z, t)\hat{\boldsymbol{t}} \right) \\ + \epsilon a \ell \left(\frac{1}{\ell^2} \zeta(\tau, z, t) + \delta^2 \zeta_a(z, t) \right) \hat{\boldsymbol{z}}. \end{aligned} \tag{3.12}$$

Finally, using the inextensibility constraints from Chapter 2 and substituting the expression (3.11) for $\bar{B}$, we have the revised inextensibility constraints

$$\xi \sinh(2\sigma_0) + \frac{2h^2}{c^2} \frac{\partial \eta}{\partial \tau} - \eta \sin(2\tau) = 0, \tag{3.13}$$

$$\frac{\partial \eta}{\partial z} + \frac{\partial \zeta}{\partial \tau} = \frac{h(\tau)}{2\pi} \frac{\mathrm{d}}{\mathrm{d}z} \int_0^{2\pi} \eta \, \mathrm{d}\tau. \tag{3.14}$$

3.2.2 Governing equations for the azimuthal displacement η

In Chapter 2 it was shown that the azimuthal displacement η is governed by the PDE

$$\hat{\mathscr{L}}(\hat{\mathscr{K}}(\eta)) - \tilde{F}\frac{\partial^2}{\partial z^2}\hat{\mathscr{J}}(\eta) + M\frac{\partial^2}{\partial t^2}\hat{\mathscr{J}}(\eta) = -\tanh^2 2\sigma_0 \frac{\partial}{\partial \tau}\left(\frac{\tilde{P}(\tau, z, t)}{\bar{B}(\tau)}\right), \tag{3.15}$$

where the linear differential operators $\hat{\mathscr{L}}, \hat{\mathscr{K}}$ and $\hat{\mathscr{J}}$, are given explicitly by

$$\hat{\mathscr{L}}(\eta) = \tanh(2\sigma_0)\left[-\bar{B}\frac{\partial}{\partial \tau}\left(\frac{\eta}{h}\right) - \frac{\partial}{\partial \tau}\left(\frac{1}{\bar{B}h}\frac{\partial}{\partial \tau}\left(\frac{1}{h}\frac{\partial}{\partial \tau}\left(\frac{\eta}{h}\right)\right)\right)\right], \tag{3.16}$$

$$\hat{\mathscr{J}}(\eta) = \tanh^2(2\sigma_0)\left[\eta - \frac{\partial}{\partial \tau}\left(\frac{1}{\bar{B}^2 h}\frac{\partial}{\partial \tau}\left(\frac{\eta}{h}\right)\right)\right], \tag{3.17}$$

$$\hat{\mathscr{K}}(\eta) = \tanh(2\sigma_0)\frac{\partial}{\partial \tau}\left[\frac{\bar{B}\eta}{h} + \frac{1}{h}\frac{\partial}{\partial \tau}\left(\frac{1}{\bar{B}h}\frac{\partial}{\partial \tau}\left(\frac{\eta}{h}\right)\right)\right]. \tag{3.18}$$

These operators differ slightly from when they were originally presented in Chapter 2 due to the inclusion of the linear scaling $\tanh^2 2\sigma_0$. This scaling is introduced to prevent unbounded behaviour in both $\hat{\mathscr{J}}(\eta)$ and the forcing of (3.15) as $\sigma_0 \to 0$, which arises due to the small σ_0 behaviour of the azimuthal curvature ($\bar{B} = O(\sigma_0)$ as $\sigma_0 \to 0$).

As explained in Chapter 2, the symmetries of the problem mean that we can restrict the azimuthal domain to $\tau \in (0, \pi/2)$.

The boundary conditions on η are given by

$$\eta = 0 \qquad \text{on} \qquad z = 0, 1, \tag{3.19}$$

$$\eta = \frac{\partial^2 \eta}{\partial \tau^2} = \frac{\partial^4 \eta}{\partial \tau^4} = 0 \qquad \text{on} \qquad \tau = 0, \frac{\pi}{2}. \tag{3.20}$$

In this Chapter we seek a solution of (3.15)–(3.20) using an eigenfunction expansion method. Once a solution for η has been found, the remaining displacement functions can be determined by using the inextensibility constraints (3.13)–(3.14).

3.3 A generalised eigenvalue problem

In this section we introduce a generalised eigenvalue problem whose eigenfunctions will be used to construct a solution to (3.15)–(3.20). We will show that the operators $\hat{\mathscr{L}}\hat{\mathscr{K}}$ and $\hat{\mathscr{J}}$ are self-adjoint, as well as present the fundamental result that the eigenfunctions form a complete set. We compute numerical solutions to the eigenvalue problem at each $\sigma_0 \in \{s_1, s_2, s_3, s_4, s_5\}$, and also obtain an analytical solution in the limit $\sigma_0 \to \infty$.

3.3.1 The eigenvalue problem

The generalised eigenvalue problem for $y(\tau)$ that we need to consider in order to construct solutions to (3.15)–(3.20) is:

$$\hat{\mathscr{L}}\hat{\mathscr{K}}(y) - \lambda\hat{\mathscr{J}}(y) = 0 \qquad \text{for} \qquad \tau \in (0, \pi/2), \tag{3.21}$$

subject to

$$y = \frac{\mathrm{d}^2 y}{\mathrm{d}\tau^2} = \frac{\mathrm{d}^4 y}{\mathrm{d}\tau^4} = 0 \qquad \text{on} \qquad \tau = 0, \frac{\pi}{2}. \tag{3.22}$$

We observe that (3.21) is a 6th-order ODE for $y(\tau)$, with one parameter λ (the eigenvalue) and six boundary conditions. Since the system is linear and homogeneous, the remaining degree of freedom is the normalisation (linear

scaling) of the solutions (see below). Let $y = Y_n(\tau)$ be the eigenfunctions of (3.21) with corresponding eigenvalues λ_n, ordered such that $\lambda_1 < \lambda_2 < ....$

3.3.2 Self-adjointness of the operators and eigenfunction orthogonality

We define the inner product

$$\langle u, v \rangle = \int_0^{\pi/2} \frac{1}{h} uv \mathrm{d}\tau. \tag{3.23}$$

In Appendix 3.A.2 we show that the operators $\hat{\mathscr{L}}\hat{\mathscr{K}}$ and $\hat{\mathscr{J}}$ are symmetric (with respect to the above inner product) on the space of functions that satisfy the boundary conditions (3.22).

In Appendix 3.B we use the self-adjointness of the operators to deduce the orthogonality relationship

$$\langle Y_n, \hat{\mathscr{J}}(Y_m) \rangle = 0 \qquad \text{for} \qquad n \neq m. \tag{3.24}$$

The individual eigenfunctions Y_n are not orthogonal to one another. Moreover, it was also shown that the bilinear form $\langle u, \hat{\mathscr{J}}(v) \rangle$ is positive definite on $(0, \pi/2)$. We therefore define the normalisation condition

$$\langle Y_n, \hat{\mathscr{J}}(Y_n) \rangle \equiv \int_0^{\pi/2} \frac{1}{h} Y_n \hat{\mathscr{J}}(Y_n) \mathrm{d}\tau = 1, \tag{3.25}$$

which sets the amplitude of the eigenfunctions. This condition, together with

the orthogonality result (3.24) yields the property

$$\langle Y_n, \hat{\mathscr{J}}(Y_m)\rangle = \delta_{nm}, \tag{3.26}$$

where δ_{nm} is the Kronecker delta.

In Appendix A we prove that the set of eigenfunctions Y_n form a *complete set*, in the sense that any smooth function satisfying the boundary conditions (3.22) can be represented as a linear combination of the eigenfunctions Y_n.

3.3.3 The circular limit $\sigma_0 \to \infty$

For general σ_0, the system (3.21), (3.22) and (3.25) can only be solved numerically. However, analytic results can be obtained in the limit $\sigma_0 \to \infty$, which corresponds to the tube's initial cross-section becoming circular. These results are then used to formulate an initial guess when solving the problem numerically for general σ_0 in §3.3.4. The analytical results can also be used as a check of the numerical solutions.

It is simple to show that in the limit as $\sigma_0 \to \infty$, we have $\bar{B} \to -1$ and $h \to 1$. It follows that in this circular limit, the eigenvalue problem (3.21) reduces to

$$\frac{\mathrm{d}^6 Y_n}{\mathrm{d}\tau^6} + 2\frac{\mathrm{d}^4 Y_n}{\mathrm{d}\tau^4} + (1-\lambda_n)\frac{\mathrm{d}^2 Y_n}{\mathrm{d}\tau^2} + \lambda_n Y_n = 0, \tag{3.27}$$

subject to

$$Y_n = \frac{\mathrm{d}^2 Y_n}{\mathrm{d}\tau^2} = \frac{\mathrm{d}^4 Y_n}{\mathrm{d}\tau^4} = 0 \qquad \text{on} \qquad \tau = 0, \frac{\pi}{2}. \tag{3.28}$$

The normalisation condition (3.25) becomes

$$\int_0^{\pi/2} Y_n^2 + \left(\frac{\mathrm{d}Y_n}{\mathrm{d}\tau}\right)^2 \mathrm{d}\tau = 1, \tag{3.29}$$

after applying integration by parts.

The ODE (3.27) has constant coefficients and contains only even derivatives of τ. This observation, together with the periodicity implied by the boundary conditions (3.22), suggests we should seek solutions of the form

$$Y_n = D_n \sin(2n\tau) \quad \text{for} \quad n \in \mathbb{N}, \tag{3.30}$$

where the constants D_n are set by the normalisation (3.29). By substituting (3.30) into (3.27) and arranging for λ_n we find that

$$\lambda_n = \frac{64n^6 - 32n^4 + 4n^2}{1 + 4n^2}. \tag{3.31}$$

Finally, the normalisation condition (3.29) yields D_n, and hence the solution

$$Y_n(\tau) = \frac{2}{\sqrt{\pi(1 + 4n^2)}} \sin(2n\tau). \tag{3.32}$$

Plots of the eigenfunctions (3.32) are shown in figure 3.3.

3.3.4 Numerical method for general σ_0

The eigenvalue problem (3.21)–(3.22) and (3.25) with $y = Y_n(\tau)$ was solved numerically by using the built in `Matlab` solver `bvp4c`. The solver requires that we write the governing equation as a first-order coupled system of ODEs.

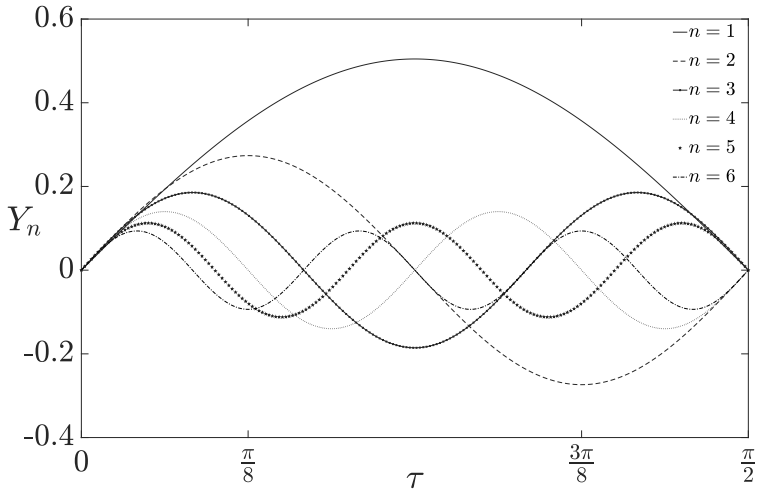

Figure 3.3: Plots of the eigenfunctions Y_n for modes $n = 1, 2, ..., 6$ in the limit as $\sigma_0 \to \infty$, corresponding to analytically obtained solutions (3.32) of the system (3.27)–(3.29).

We do this in the standard way by using Y_n and its first five derivatives as the variables.

For the normalisation, the eigenfunctions were initially normalised subject to $Y_n'(0) = 1$, since this was numerically more convenient than using the integral condition (3.25) when calling the solver. Once a numerical solution of (3.21)–(3.22) has been found, it is scaled to satisfy the required normalisation (3.25).

The solver `bvp4c` requires an initial guess for the solution and any parameters (the eigenvalue in this case). Initially, when considering an approximation for the eigenfunctions of (3.21)–(3.22), it seemed that the analytical results for $\sigma_0 \to \infty$ studied in §3.3.3 would provide a sufficient approximation for all σ_0. However, using one of these eigenfunctions as our initial guess, the solver would sometimes (and unpredictably) converge to a different solution (corresponding to a different mode number n), particularly at smaller σ_0.

Therefore, in order to obtain a reliable solution for the nth mode at each σ_0, we iterated through descending values of σ_0 and used each preceding solution as the initial approximation $\tilde{y}$ of the eigenfunction at the next value of σ_0. In order to provide an initial estimate $\tilde{\lambda}_n$ of the eigenvalue, we calculated the Rayleigh quotient for each σ_0 using our eigenfunction estimate:

$$\tilde{\lambda}_n = \frac{\langle \tilde{y}, \hat{\mathscr{L}}\hat{\mathscr{K}}(\tilde{y})\rangle}{\langle \tilde{y}, \hat{\mathscr{J}}(\tilde{y})\rangle}. \tag{3.33}$$

For each n and σ_0, once the approximations $\tilde{y}_n$ and $\tilde{\lambda}_n$ had been determined, we called `bvp4c` on an initial mesh of 500 points on the interval $\tau \in (0, \pi/2)$, which found a numerical approximation of the system. Each solution y_n from `bvp4c` then needed to be scaled to satisfy the normalisation condition (3.25). The inner product

$$\begin{aligned}\gamma_n &= \langle y_n, \hat{\mathscr{J}}(y_n)\rangle, \\ &= \int_0^{\pi/2} \frac{1}{h} y_n \hat{\mathscr{J}}(y_n)\,\mathrm{d}\tau,\end{aligned} \tag{3.34}$$

was evaluated numerically. Once γ_n had been found, the normalised eigenfunction was computed as

$$Y_n(\tau) = \frac{1}{\sqrt{\gamma_n}} y_n(\tau). \tag{3.35}$$

3.3.5 Numerical results for the eigenvalue problem

In figure 3.4 we plot the normalised eigenfunctions $Y_n(\tau)$ for modes $n = 1, 2, ..., 6$ that satisfy (3.21), (3.22) and (3.25) for ellipticity parameter $\sigma_0 \in$

σ_0	λ_1	λ_2	λ_3	λ_4	λ_5	λ_6
$s_0 = \infty$	7.20000	211.765	1191.89	3907.94	9703.96	20308.0
$s_1 = 0.9540$	6.97182	207.340	1180.73	3887.93	9672.74	20263.1
$s_2 = 0.6$	6.42638	194.436	1140.73	3811.43	9552.18	20090.5
$s_3 = 0.3840$	5.83285	176.578	1066.20	3636.83	9240.97	19614.3
$s_4 = 0.2194$	5.38682	160.336	979.575	3384.11	8695.61	18631.7
$s_5 = 0.0755$	5.16604	151.227	922.705	3191.48	8217.27	17647.5

Table 3.2: Numerical results for the eigenvalues λ_n of (3.21)–(3.22). The eigenvalues are shown for the first six modes and are calculated numerically at each $\sigma_0 \in \{s_0, s_1, s_2, s_3, s_4, s_5\}$. The row corresponding to $s_0 = \infty$ contains values for the eigenvalues in the limit $\sigma_0 \to \infty$ from (3.31).

$\{s_0, s_1, s_2, ..., s_5\}$ (see table 3.1). It can be seen that the number of half-oscillations of each eigenfunction present on the interval $(0, \pi/2)$ is equal to the mode number n. Moreover, we observe that for decreasing values of σ_0 relative to the $\sigma_0 = \infty$ case, the corresponding eigenfunctions are increasingly out of phase (to the right) with the analytic limits $Y_n \propto \sin(2n\tau)$. The amplitude of the eigenfunctions is found to be larger towards the $\tau = 0$ end of the azimuthal domain.

Figure 3.5 shows the eigenvalues λ_n (scaled by their circular limit behaviour (3.31)) plotted against σ_0 for modes $n = 1, 2, ..., 6$. We observe that, for each n, the plots maintain a similar-shaped profile. However, there are large differences in the magnitude of λ_n (see table 3.2) as we change the mode number, n. Figure 3.5 also shows that the numerically obtained eigenvalues λ_n converge to the analytically obtained limits (3.31) as $\sigma_0 \to \infty$.

3.4 Solution by series expansions

In this section we seek a full series solution to (3.15)–(3.20). We represent the solution as a sum over the eigenfunctions studied in §3.3.1, and show

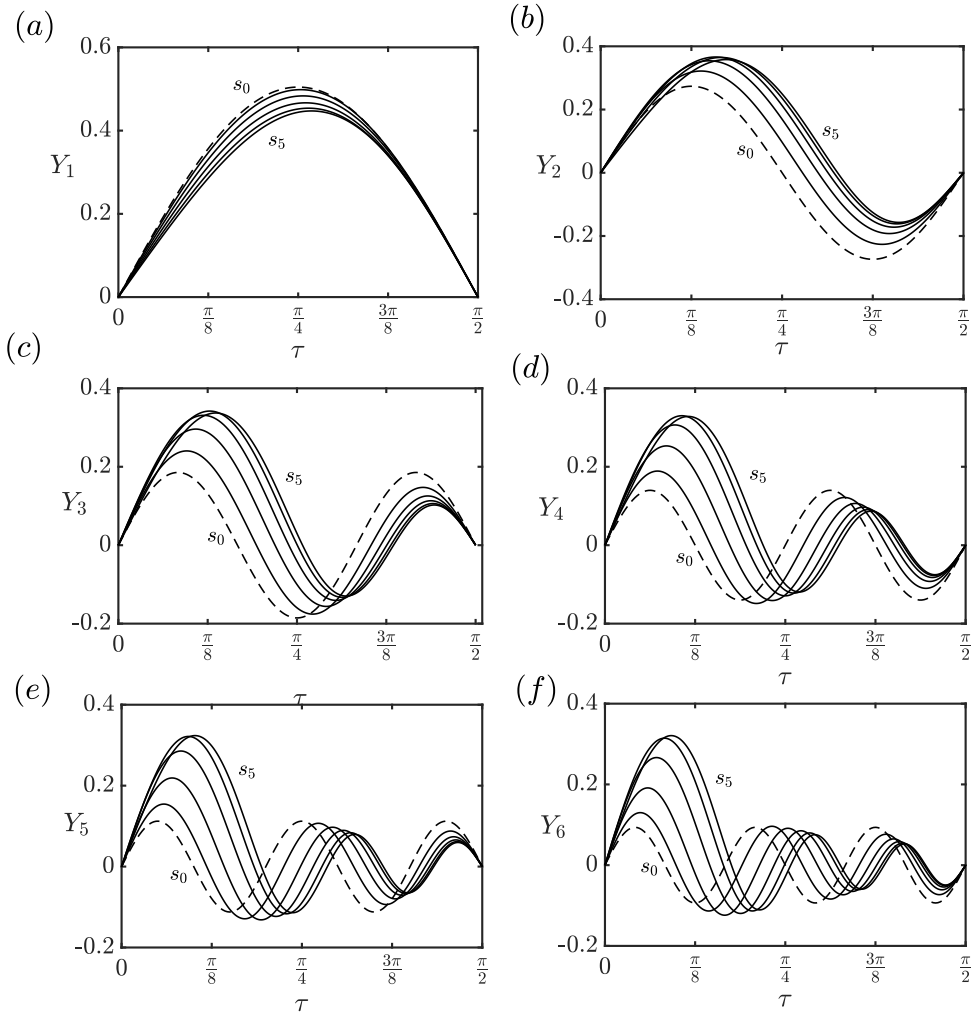

Figure 3.4: Numerical solutions to the system (3.21), (3.22) and (3.25) for $y = Y_n(\tau)$ (the eigenfunctions) for modes $n = 1, 2, \ldots, 6$ with $\sigma_0 \in \{s_0, s_1, s_2, s_3, s_4, s_5\}$. The dashed curves represent the analytic solution (3.32) obtained in the limit $\sigma_0 \to \infty$.

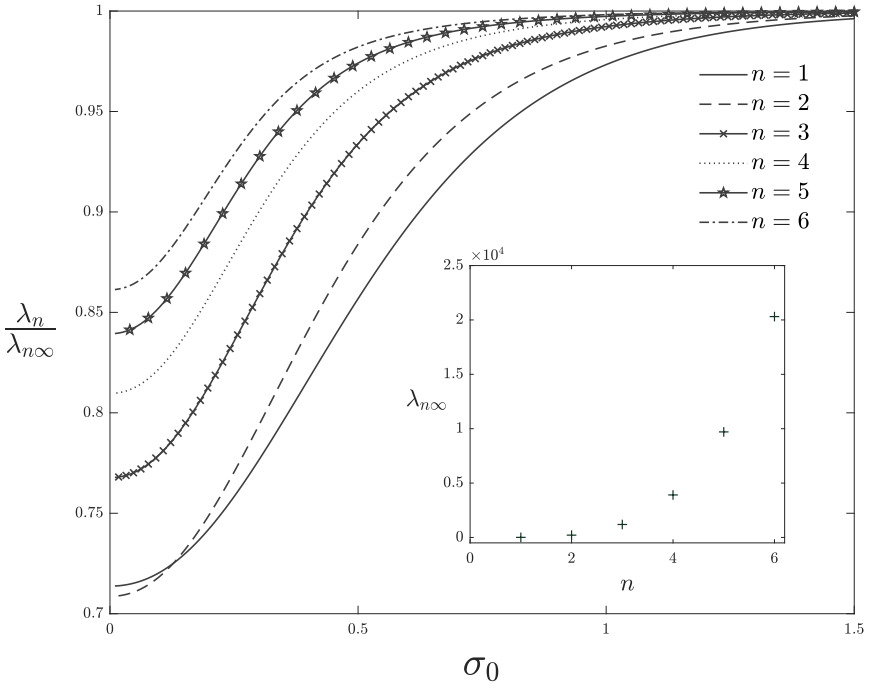

Figure 3.5: Numerical solutions for the eigenvalues λ_n, plotted against eccentricity parameter σ_0 for modes $n = 1, 2, ..., 6$. Each eigenvalue λ_n has been scaled by its value $\lambda_{n\infty}$ in the circular limit ($\sigma \to \infty$), as given analytically in (3.31). In the inset we plot the circular limit eigenvalues $\lambda_{n\infty}$ against n to give an indication of the relative sizes of the eigenvalues corresponding to different azimuthal modes.

that this allows us to fully decompose the governing equation (3.15) into a system of uncoupled linear PDEs with constant coefficients.

3.4.1 Decomposition of $\eta(\tau, z, t)$

Let $\eta(\tau, z, t)$ be the solution of (3.15)–(3.20). We assume on physical grounds that such a solution will exist. Recall the inner product (3.23) and define

$$a_n(z,t) = \langle \eta, \hat{\mathscr{J}}(Y_n) \rangle = \int_0^{\pi/2} \frac{1}{h} \eta \hat{\mathscr{J}}(Y_n(\tau)) \, \mathrm{d}\tau. \tag{3.36}$$

Owing to the completeness of the eigenfunctions Y_n (see §3.3.2) and the orthogonality relation (3.26), we can express $\eta(\tau, z, t)$ as

$$\eta(\tau, z, t) = \sum_{n=1}^{\infty} a_n(z, t) Y_n(\tau). \tag{3.37}$$

The boundary conditions on $a_n(z, t)$ can then be derived from the pinned-end conditions (3.19), we find that

$$a_n = 0 \qquad \text{on} \qquad z = 0, 1. \tag{3.38}$$

We now take the inner product of (3.15) with Y_n to obtain

$$\langle \hat{\mathscr{L}}\hat{\mathscr{K}}(\eta), Y_n \rangle - \tilde{F}\frac{\partial^2}{\partial z^2}\langle \hat{\mathscr{J}}(\eta), Y_n \rangle + M\frac{\partial^2}{\partial t^2}\langle \hat{\mathscr{J}}(\eta), Y_n \rangle = Q_n(z, t), \tag{3.39}$$

where

$$Q_n(z, t) = -\tanh^2(2\sigma_0) \int_0^{\pi/2} \frac{1}{h}\frac{\partial}{\partial \tau}\left(\frac{\tilde{P}(\tau, z, t)}{\bar{B}(\tau)}\right) Y_n(\tau)\, \mathrm{d}\tau. \tag{3.40}$$

For the case in which the pressure is azimuthally uniform[1], we can write

$$Q_n(z, t) = \tilde{P}(z, t) q_n, \tag{3.41}$$

where

$$q_n = \tanh^2(2\sigma_0) \int_0^{\pi/2} C_P(\tau) Y_n(\tau)\, \mathrm{d}\tau, \tag{3.42}$$

[1]This case is applicable for the models derived by Whittaker et al. (2010d), Whittaker et al. (2010a) and Whittaker et al. (2010c)

and

$$C_P(\tau) = \frac{3\sin(2\tau)}{\sinh(2\sigma_0)}. \tag{3.43}$$

Since $\hat{\mathscr{L}}\hat{\mathscr{K}}$ is self-adjoint with respect to (3.23) on the space of functions that satisfy (3.22), and because Y_n is an eigenfunction of (3.21), we have

$$\langle \hat{\mathscr{L}}\hat{\mathscr{K}}(\eta), Y_n\rangle = \langle \eta, \hat{\mathscr{L}}\hat{\mathscr{K}}(Y_n)\rangle = \lambda_n \langle \eta, \hat{\mathscr{J}}(Y_n)\rangle. \tag{3.44}$$

Since $\hat{\mathscr{J}}$ is also self-adjoint, (3.39) becomes

$$\lambda_n \langle \eta, \hat{\mathscr{J}}(Y_n)\rangle - \tilde{F}\frac{\partial^2}{\partial z^2}\langle \eta, \hat{\mathscr{J}}(Y_n)\rangle + M\frac{\partial^2}{\partial t^2}\langle \eta, \hat{\mathscr{J}}(Y_n)\rangle = Q_n(z,t) \tag{3.45}$$

Recalling the definition of $a_n(z,t)$ in (3.36), we obtain:

$$\lambda_n a_n - \tilde{F}\frac{\partial^2 a_n}{\partial z^2} + M\frac{\partial^2 a_n}{\partial t^2} = Q_n(z,t), \quad \text{for } n = 1, 2, 3, \cdots. \tag{3.46}$$

Equation (3.46) is an uncoupled system of PDEs for the axial modes $a_n(z,t)$, forced by $Q_n(z,t)$. We interpret Q_n as the contribution from the pressure to the nth eigenmode. For a given transmural pressure $\tilde{P}$, we can obtain Q_n (via (3.40)) using the numerical solutions for the eigenfunctions $Y_n(\tau)$. Equation (3.46) can then be solved for $a_n(z,t)$ for each n subject to the boundary conditions given by (3.38). Once the modes $a_n(z,t)$ are known, the solution for η is then given by (3.37).

3.4.2 Contribution to the area change

A tube law provides a relation between the transmural pressure and the tubes cross-sectional area. In place of a single such equation here, we instead

obtain a set of equations for the contribution to the area change from each of the azimuthal eigenmodes.

Whittaker et al. (2010b) showed that at leading order, the area change of the tube's cross-section is given by

$$A - \bar{A} = \epsilon a^2 \int_0^{2\pi} \xi(\tau, z, t) \mathrm{d}\tau + O(\epsilon^2). \tag{3.47}$$

By using (3.13) we can eliminate ξ from (3.47) to obtain

$$A - \bar{A} = \epsilon a^2 \int_0^{2\pi} \left(\frac{\sin(2\tau)}{\sinh(2\sigma_0)} \eta - \frac{2h^2}{c^2 \sinh(2\sigma_0)} \frac{\partial \eta}{\partial \tau} \right) \mathrm{d}\tau + O(\epsilon^2). \tag{3.48}$$

Using the symmetry of η, we can restrict the range of integration to $(0, \pi/2)$ and multiply the result by 4. Noting that $2h^2/c^2 = \cosh(2\sigma_0) - \cos(2\tau)$, and that $\eta = 0$ at $\tau = 0, \pi/2$, we can use integration by parts to simplify the second term in the integrand. We obtain:

$$A - \bar{A} = \frac{12\epsilon a^2}{\sinh(2\sigma_0)} \int_0^{\frac{\pi}{2}} \sin(2\tau)\, \eta(\tau, z, t)\, \mathrm{d}\tau + O(\epsilon^2). \tag{3.49}$$

Decomposing $\eta(\tau, z, t)$ as in (3.37) provides

$$A - \bar{A} = \frac{12\epsilon a^2}{\sinh(2\sigma_0)} \sum_{n=1}^{\infty} a_n(z, t) \int_0^{\frac{\pi}{2}} \sin(2\tau) Y_n(\tau) \mathrm{d}\tau + O(\epsilon^2). \tag{3.50}$$

We define the fractional area change $\epsilon\alpha(z, t)$, such that

$$\epsilon\alpha = \frac{A - \bar{A}}{\bar{A}}. \tag{3.51}$$

Substituting (3.50) into (3.51) and using the expression for $\bar{A}$ in (2.37), we obtain

$$\alpha = \frac{24}{\pi c^2 \sinh^2(2\sigma_0)} \sum_{n=1}^{\infty} a_n(z,t) \int_0^{\pi/2} \sin(2\tau) Y_n(\tau) \mathrm{d}\tau + O(\epsilon). \tag{3.52}$$

We define $\alpha_n(z,t) = a_n(z,t)t_n$, where t_n is given by

$$t_n = \frac{24}{\pi c^2 \sinh^2(2\sigma_0)} \int_0^{\pi/2} \sin(2\tau) Y_n(\tau) \mathrm{d}\tau. \tag{3.53}$$

Then it follows that

$$\alpha(z,t) = \sum_{n=1}^{\infty} \alpha_n(z,t), \tag{3.54}$$

and

$$\eta(\tau,z,t) = \sum_{n=1}^{\infty} \frac{1}{t_n} \alpha_n(z,t) Y_n(\tau). \tag{3.55}$$

We therefore interpret $\alpha_n(z,t)$ as the component of the relative area change corresponding to the nth azimuthal eigenmode. By (3.46) and (3.38), each α_n satisfies the PDE

$$\tilde{F} \frac{\partial^2 \alpha_n}{\partial z^2} - M \frac{\partial^2 \alpha_n}{\partial t^2} - \lambda_n \alpha_n = -Q_n t_n, \tag{3.56}$$

subject to

$$\alpha_n = 0 \qquad \text{on} \qquad z = 0, 1. \tag{3.57}$$

Equation (3.56) governs the components α_n, which when summed together, provide the change in cross-sectional area of an initially elliptical elastic-walled tube subject to a given transmural pressure $\tilde{P}(\tau,z,t)$. For simple analytic functions $\tilde{P}(\tau,z,t)$, the system (3.56)–(3.57) can be solved analyti-

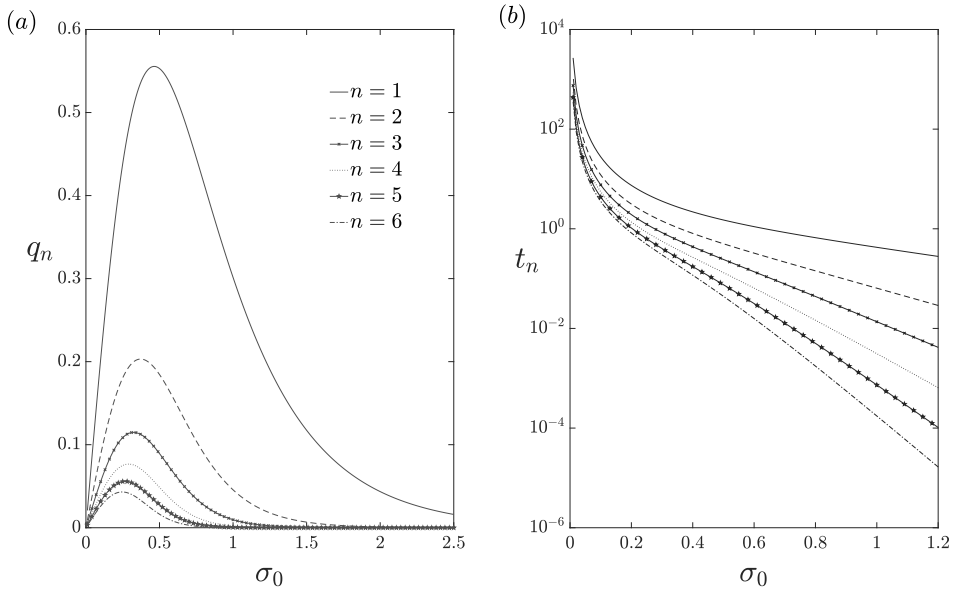

Figure 3.6: Numerical results for (a) q_n as defined in (3.42), and (b) t_n, as defined in (3.53), plotted as functions of σ_0 for $n = 1, 2, \ldots, 6$. Both plots demonstrate a dominant contribution from the fundamental mode $n = 1$.

cally for each n, though the evaluation of Q_n, t_n and λ_n will require numerical attention.

For $\tilde{P}$ uniform in τ, recall that $Q_n = \tilde{P} q_n$, where q_n is given by (3.42). In figure 3.6 we plot q_n and t_n numerically against σ_0 for $n = 1, 2, \ldots, 6$ and observe that in both cases there is a dominant contribution from the first ($n = 1$) mode. We shall term this the fundamental mode. The values for q_n and t_n are also tabulated for the representative ellipticity parameters in tables 3.3 and 3.4. The results demonstrate that a good approximation of the system could be obtained after truncating (3.54) after $n = 1$.

σ_0	q_1	q_2	q_3	q_4	q_5	q_6
$s_1 = 0.9540$	0.326229	0.053729	0.012425	0.003104	0.000797	0.000207
$s_2 = 0.6$	0.523926	0.153981	0.065155	0.030600	0.014980	0.007480
$s_3 = 0.3840$	0.540936	0.202923	0.111130	0.069308	0.045950	0.031499
$s_4 = 0.2194$	0.399920	0.167120	0.101920	0.071523	0.053940	0.042484
$s_5 = 0.0755$	0.154760	0.067428	0.042727	0.031198	0.024523	0.020169

Table 3.3: Results for the numerical constants q_n, as defined in (3.42), which measure the contribution from the (azimuthally uniform) pressure to the nth eigenmode. The values are given for the representative values $\sigma_0 \in \{s_1, s_2, s_3, s_4, s_5\}$. The circular limit case ($\sigma_0 = s_0$) has been omitted since $q_n \to 0$ when $\sigma_0 \to \infty$ for all n as is observed in figure 3.6.

σ_0	t_1	t_2	t_3	t_4	t_5	t_6
$s_1 = 0.9540$	0.468950	0.077235	0.017861	0.004462	0.001146	0.000299
$s_2 = 0.6$	1.104332	0.324563	0.137336	0.064500	0.031576	0.015767
$s_3 = 0.3840$	2.340500	0.878035	0.480852	0.299891	0.198821	0.136295
$s_4 = 0.2194$	6.272272	2.621097	1.598410	1.121761	0.845988	0.6663216
$s_5 = 0.0755$	48.12290	20.9690	13.2861	9.701156	7.62547	6.27148

Table 3.4: Results for the numerical constants t_n, as defined in (3.53), which measure the effect of the nth modes amplitude on the area change. The values are given for the representative values $\sigma_0 \in \{s_1, s_2, s_3, s_4, s_5\}$.

3.4.3 Comparison with Whittaker et al. (2010b)

In the present notation, the 'tube law' derived by Whittaker et al. (2010b) — which applies when the transmural pressure is steady and azimuthally uniform — is given by

$$k_0\alpha - k_2\tilde{F}\frac{\mathrm{d}^2\alpha}{\mathrm{d}z^2} = \tilde{P}(z), \tag{3.58}$$

where k_0 and k_2 are numerically determined constants. If we truncate expansion (3.54) after $n = 1$, and assume a steady deformation in response to a steady azimuthally uniform transmural pressure, then equation (3.56)

reduces to

$$\frac{\lambda_1}{q_1 t_1}\alpha_1 - \frac{\tilde{F}}{q_1 t_1}\frac{\mathrm{d}^2\alpha_1}{\mathrm{d}z^2} = \tilde{P}(z). \tag{3.59}$$

This is the same form as (3.58), but with differently computed coefficients.

In figure 3.7, we plot the results of Whittaker et al. (2010b) for k_0 and k_2 together with the expressions λ_1/q_1t_1 and $1/q_1t_1$ (scaled by their circular limit behaviour) appropriate for a comparison. We find that better agreement is found for the comparisons involving k_0, although in both cases, we observe that the two solutions converge towards agreement in the limit as $\sigma_0 \to \infty$. The reason for the agreement at large σ_0 is because the eigenfunction expansion (3.37) of η becomes exactly the Fourier expansion used by Whittaker et al. (2010b) in this circular limit (see §3.3.3). Moreover, for both models, the amplitude of the higher-order azimuthal modes become asymptotically smaller than the amplitude of the fundamental mode. This can be justified by considering the ratio

$$\frac{q_n t_n}{q_1 t_1} = \left(\frac{\int_0^{\pi/2}\sin(2\tau)Y_n(\tau)\,\mathrm{d}\tau}{\int_0^{\pi/2}\sin(2\tau)Y_1(\tau)\,\mathrm{d}\tau}\right)^2. \tag{3.60}$$

Hence, using the analytical solution (3.32) for Y_n as $\sigma_0 \to \infty$, it follows (by orthogonality) that

$$\lim_{\sigma_0\to\infty}\frac{q_n t_n}{q_1 t_1} = 0 \qquad \text{for} \qquad n \geq 2. \tag{3.61}$$

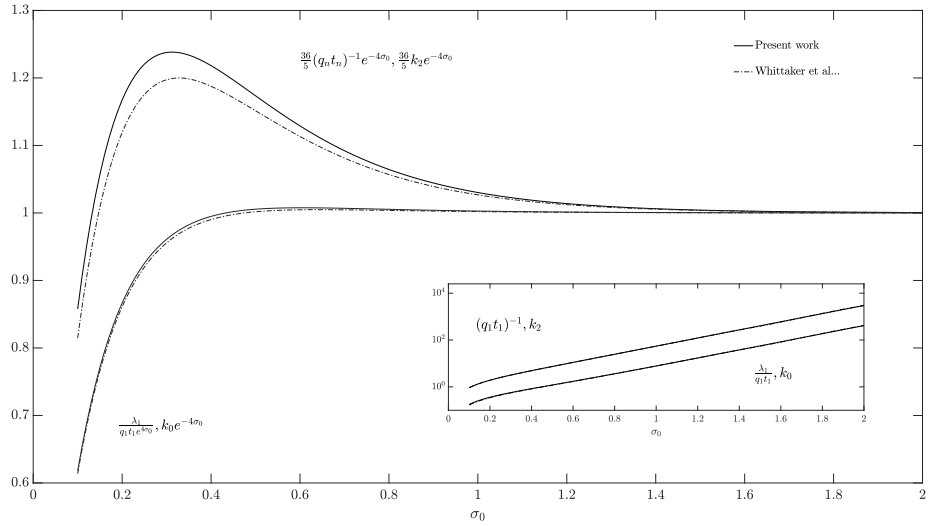

Figure 3.7: Comparison of the coefficients in the tube-law equations (3.58) and (3.59), as the ellipticity σ_0 is varied. The dot-dashed lines show the values of k_0 and k_2 from Whittaker et al. (2010b). The continuous lines show the values of λ_1/q_1t_1 and $1/q_1t_1$ from the present work. In the main figure the values have been scaled by their respective asymptotic forms $e^{4\sigma_0}$ and $5/36e^{4\sigma_0}$ as $\sigma_0 \to \infty$. The raw values are shown in the inset.

3.5 Application and truncation error estimates

In this section we shall consider the errors incurred by truncating the expansion (3.54); first by constructing general estimates for the magnitude of each α_n, and secondly by considering the specific case of a uniform transmural pressure (for which analytical solutions can be obtained).

3.5.1 Estimates of relative area change for steady problems

We can use (3.56) to obtain estimates for the magnitude of each α_n, which contributes to the relative area change through (3.54). We consider a steady problem in which $\tilde{P} = \tilde{P}(z)$ and $\alpha_n = \alpha_n(z)$. Equation (3.56) then reduces

to the ODE

$$\tilde{F}\frac{\mathrm{d}^2\alpha_n}{\mathrm{d}z^2} - \lambda_n\alpha_n = -q_n t_n \tilde{P}(z). \tag{3.62}$$

Recall that $z \in (0,1)$ and $\tilde{P}(z) = O(1)$.

When $\tilde{F} \gg \lambda_n$, the second term in (3.62) does not contribute at leading order. An estimate $\hat{\alpha}_n$ for the magnitude of the relative area change when $\tilde{F} \gg \lambda_n$ is then

$$|\alpha_n(z)| \sim \hat{\alpha}_n = \frac{q_n t_n}{\tilde{F}}. \tag{3.63}$$

Conversely, for $\tilde{F} \ll \lambda_n$, we neglect the first term in (3.62) at leading order. The estimate $\check{\alpha}_n$ for the relative area change is then

$$|\alpha_n(z)| \sim \check{\alpha}_n = \frac{q_n t_n}{\lambda_n}. \tag{3.64}$$

Figure 3.8 shows the ratios $\hat{\alpha}_n/\hat{\alpha}_1$ and $\check{\alpha}_n/\check{\alpha}_1$ between the higher mode estimates for α_n and the first mode estimate, plotted against σ_0. In both (a) and (b) we see that for smaller σ_0, the higher-order modes provide a more substantial contribution to the relative area change, and become less important as σ_0 becomes larger. Physically, the increase in σ_0 corresponds to the tubes initial cross-section becoming circular. This means that the accuracy in approximating the relative area change of the tube by truncating (3.54) at $n = 1$ depends on the ellipticity of the tubes initial cross-section. For tubes that initially have highly elliptical cross-sections (see figure 3.2), contributions from the higher-order terms in (3.54) may be required.

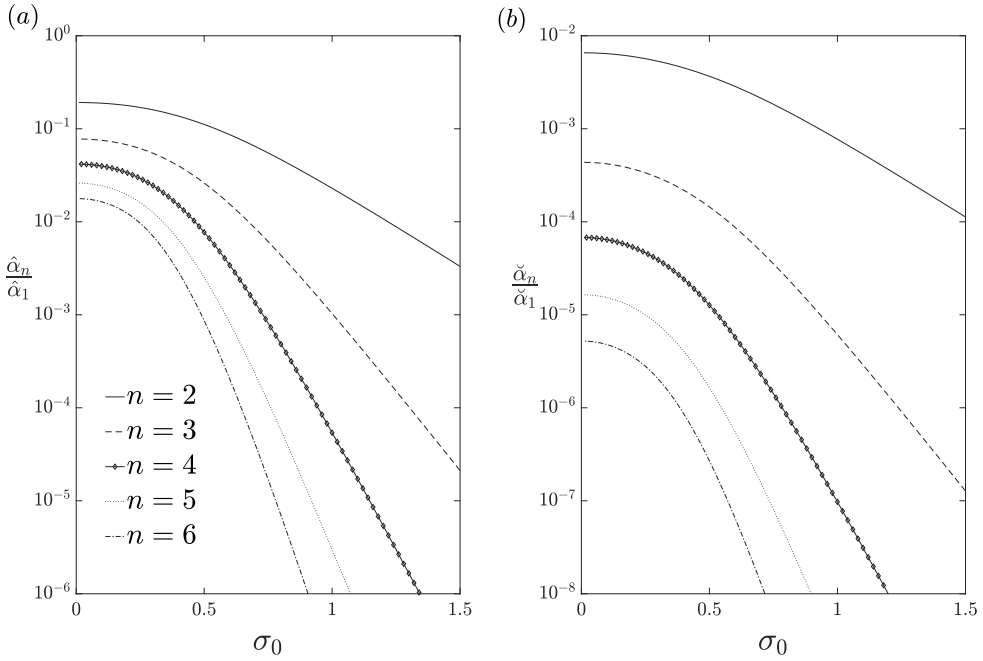

Figure 3.8: (a) Numerical results for the ratio between the estimates $\hat{\alpha}_n$ for $n = 2, 3, ..., 6$ and the estimate $\hat{\alpha}_1$ from (3.63). (b) Numerical results for the ratio between the estimates $\breve{\alpha}_n$ for $n = 2, 3, ..., 6$ and the estimate $\breve{\alpha}_1$ from (3.64).

3.5.2 Analytic solution for a steady uniform pressure

For a steady uniform transmural pressure say $\tilde{P} = -1$, we can solve (3.56)–(3.57) analytically. By using standard methods for solving linear ODEs with constant coefficients, we find the steady solution

$$\alpha_n(z) = -\frac{q_n t_n}{\lambda_n}\left[1 - \frac{\cosh[\mu_n(z - \frac{1}{2})]}{\cosh\left(\frac{\mu_n}{2}\right)}\right], \tag{3.65}$$

where $\mu_n^2 = \lambda_n/\tilde{F}$.

In figure 3.9 we plot the initial and deformed cross-sectional shapes of the tube located at $z = 0.5$, and in figure 3.10, we plot the solutions (3.65) with $\tilde{P} = -1$ for $\tilde{F} = 1$ and $\tilde{F} = 3$. Comparing with the work of Whittaker

et al. (2010b) (plotted in figure 3.10) we see that for $n = 1$ and $\sigma_0 = 0.6$ our results are in good agreement.

The solutions (3.65) for α_n have a maximum amplitude at $z = 1/2$, given by

$$\alpha_n\left(\tfrac{1}{2}\right) = -\frac{q_n t_n}{\lambda_n}\left[1 - \operatorname{sech}\left(\frac{\mu_n}{2}\right)\right]. \tag{3.66}$$

When μ_n is large (corresponding to $\tilde{F} \ll \lambda_n$), we see that

$$|\alpha_n(\tfrac{1}{2})| \sim \frac{q_n t_n}{\lambda_n} \qquad \text{for} \qquad \mu_n \gg 1, \tag{3.67}$$

in agreement with the estimate (3.64).

Conversely, for small μ_n ($\tilde{F} \gg \lambda_n$), by making use of the Taylor expansion of $\operatorname{sech}(\mu_n)$, we find that

$$|\alpha_n\left(\tfrac{1}{2}\right)| \sim \frac{q_n t_n}{8\lambda_n}\mu_n^2 \quad \text{for} \;\; \mu_n \ll 1. \tag{3.68}$$

Since $\mu_n^2 = \lambda_n/\tilde{F}$, this is consistent with the estimate (3.63).

Figures 3.11 and 3.12 show contour plots of the ratios α_2/α_1 and $\alpha_3/(\alpha_1 + \alpha_2)$ evaluated at $z = 0.5$ in $(\tilde{F}, \sigma_0)$ parameter space. The plots provide an understanding of the relative error induced by truncating (3.54) after the first and second modes respectively. Whilst the features of both Figs 3.11 and 3.12 are similar, we find that the retention of the second mode provides an improvement in the error by a factor of between 10^{-1} and $10^{-4.5}$.

The contour plots 3.11 and 3.12 show that the relative error induced by truncation decreases monotonically as the ellipticity parameter σ_0 is increased. This observation is in agreement with our analysis in §3.4.3, where it was shown that the higher order azimuthal modes vanish in the circular

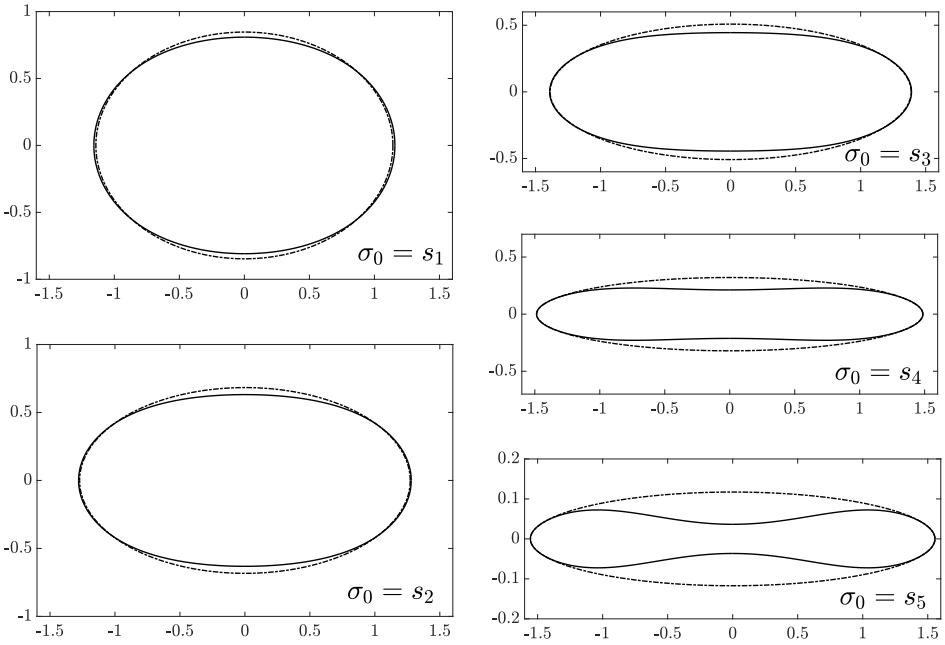

Figure 3.9: Cross-sectional deformations of an initially elliptical elastic-walled tube induced by a steady uniform transmural pressure for different initial ellipticities. The figure shows the midpoint $z = 1/2$, with the dashed line showing the undeformed and the solid lines showing the deformed wall. All the figures use the same transmural pressure $\tilde{P} \equiv -1$ with $\epsilon = 0.6$, $a = 1$ and have the same dimensionless tension $\tilde{F} = 1$. The area changes α_n were calculated using (3.65) and then η was computed from (3.55) and ξ from (3.13). The deformation is then found using (3.12). The expansion (3.54) was truncated after $n = 2$ since adding further modes produced indistinguishable results.

limit $\sigma_0 \to \infty$. In both plots we see that smaller values of the axial tension result in a smaller relative error, with the added feature that the error seems to tend towards being independent of $\tilde{F}$ when $\tilde{F}$ is either large or small. To explain these features we consider the dominant contribution α_{n+1}/α_1 to the relative error in truncating (3.54) after the nth mode. Using the estimates

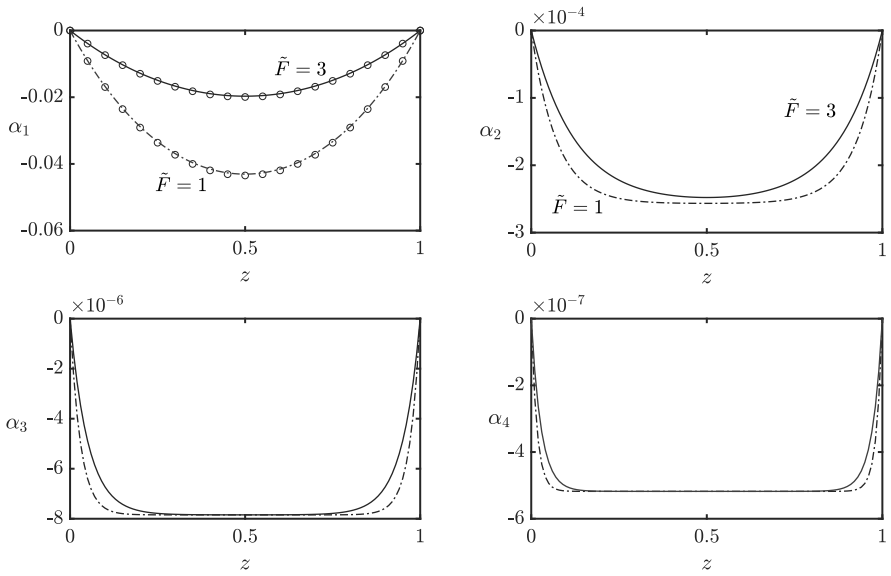

Figure 3.10: Plots of (3.65) corresponding to solutions of (3.56) for a given transmural pressure $\tilde{P} = -1$ where $\sigma_0 = 0.6$ and $\tilde{F} = 1, 3$. We also plot the results of Whittaker et al. (2010b) with the first mode solution using open circles.

(3.63) and (3.64) we find that

$$\frac{\alpha_{n+1}}{\alpha_1} \sim \frac{q_{n+1}t_{n+1}}{q_1 t_1} \qquad \text{for} \qquad \tilde{F} \gg \lambda_n, \tag{3.69}$$

$$\frac{\alpha_{n+1}}{\alpha_1} \sim \frac{\lambda_1}{\lambda_{n+1}} \frac{q_{n+1}t_{n+1}}{q_1 t_1} \qquad \text{for} \qquad \tilde{F} \ll \lambda_n. \tag{3.70}$$

Examining (3.69)–(3.70) we see that both are independent of $\tilde{F}$. Moreover, the presence of the factor λ_1/λ_{n+1} in (3.70) justifies mathematically why the error decreases with an increase in dimensionless axial tension, since $\lambda_{n+1} \ll \lambda_1$ for every n.

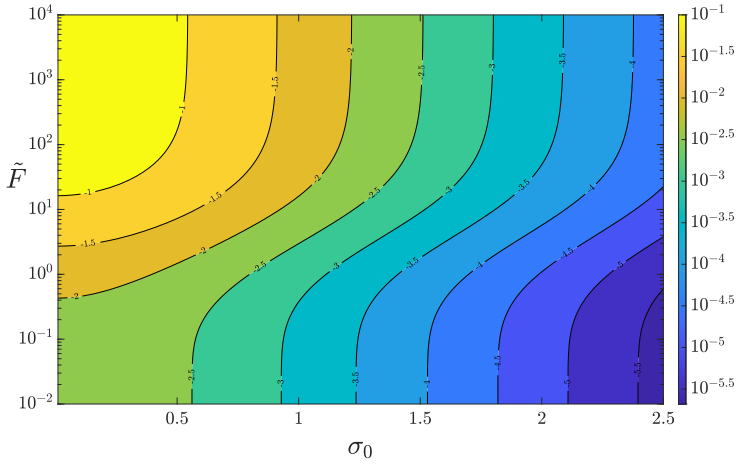

Figure 3.11: Contour plots of the ratio $\alpha_2(1/2)/\alpha_1(1/2)$ computed using (3.65) for a uniform transmural pressure. This illustrates how changes in $\tilde{F}$ and σ_0 affect the error when truncating the expansion (3.54) after the first mode.

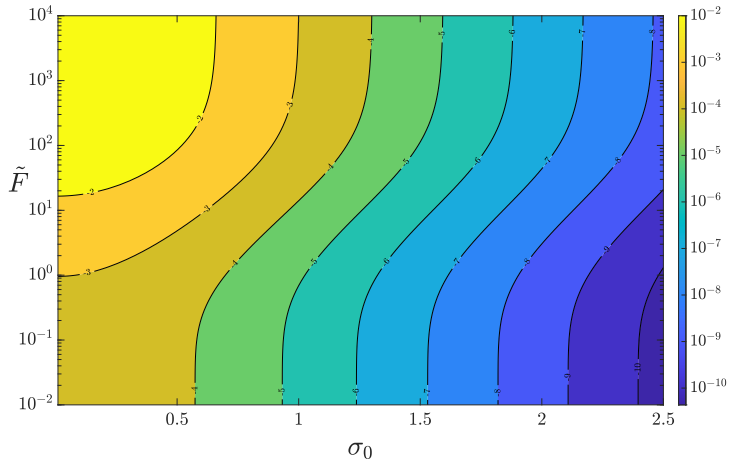

Figure 3.12: Contour plots of the ratio $\alpha_3(1/2)/(\alpha_1(1/2)+\alpha_2(1/2))$ computed using (3.65) for a uniform transmural pressure. This illustrates how changes in $\tilde{F}$ and σ_0 affect the error when truncating the expansion (3.54) after the second mode.

3.5.3 Solution for free oscillatory modes of the tube wall

In the absence of any transmural pressure ($\tilde{P} \equiv 0$), we can solve for the free oscillatory modes of the tube. Using (3.56)–(3.57), the unsteady contributions $\alpha_n(z,t)$ of α satisfy

$$\frac{\partial^2 \alpha_n}{\partial z^2} - \frac{M}{\tilde{F}} \frac{\partial^2 \alpha_n}{\partial t^2} - \frac{\lambda_n}{\tilde{F}} \alpha_n = 0, \tag{3.71}$$

subject to

$$\alpha_n = 0 \quad \text{on} \quad z = 0, 1. \tag{3.72}$$

Motivated by the form of the boundary conditions (3.72), we seek solutions for $\hat{\alpha}_n(z,t)$ of the form

$$\alpha_n(z,t) = Re\left(\sum_{m=1}^{\infty} A_n \sin(m\pi z) e^{i\omega_{mn} t} \right) \quad \text{for} \quad m = 1, 2, \cdots \tag{3.73}$$

Substituting (3.73) into (3.71), we obtain the dispersion relation for the free oscillatory modes

$$\omega_{mn}^2 = \frac{\tilde{F}\pi^2 m^2 + \lambda_n}{M}. \tag{3.74}$$

In figure 3.13 we plot the oscillation frequencies ω_{mn} corresponding to the first four axial modes ($m = 1, 2, 3, 4$) for $n = 1, 2, 3$. The plots demonstrate that an increase in azimuthal mode number n results in a higher frequency. This is because of the rate at which λ_n increases with n (see figure 3.5).

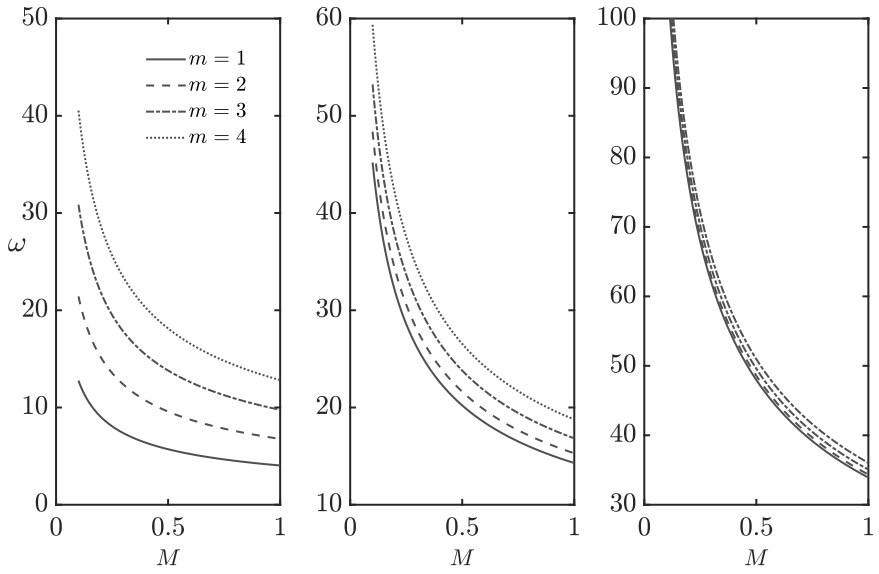

Figure 3.13: The oscillation frequencies ω_m corresponding to the first four axial modes ($m = 1, 2, 3, 4$) plotted against the inertia coefficient M for the first three azimuthal modes ($n = 1, 2, 3$).

3.6 Conclusions

In this Chapter we have produced the first formal solution of the problem initially formulated by Whittaker et al. (2010b) of the small-amplitude deformations of a long thin-walled elastic tube that has an initially axially uniform elliptical cross-section.

To obtain the solution, we used an eigenfunction expansion method, which involved writing the azimuthal displacement $\eta(\tau, z, t)$ as a sum over the azimuthal eigenfunctions $Y_n(\tau)$ of a generalised eigenvalue problem. This allowed us to derive a series expansion for the tube's dimensionless relative area change α in terms of the dimensionless functions $\alpha_n(z, t)$, which correspond to the area change associated with each azimuthal eigenmode. We showed that the equations for the α_n decouple completely, with each satisfying a

PDE

$$\tilde{F}\frac{\partial^2 \alpha_n}{\partial z^2} - M\frac{\partial^2 \alpha_n}{\partial t^2} - \lambda_n \alpha_n = -Q_n t_n, \tag{3.75}$$

where the forcing Q_n from the dimensionless transmural pressure $\tilde{P}$ is given by

$$Q_n(z,t) = -\tanh^2 2\sigma_0 \int_0^{\pi/2} \frac{1}{h}\frac{\partial}{\partial \tau}\left(\frac{\tilde{P}(\tau,z,t)}{\bar{B}(\tau)}\right) \mathrm{d}\tau. \tag{3.76}$$

The coefficients involve the following quantities. In (3.75), $\tilde{F}$ is the dimensionless axial tension, M is the dimensionless inertia coefficient of the tube, λ_n is the eigenvalue of the eigenfunction $Y_n(\tau)$, and t_n is an integral of $Y_n(\tau)$ defined in (3.53). In (3.76), σ_0 defines the initial ellipticity of the tube, $h(\tau)$ is the dimensionless scale factor for the elliptical co-ordinates system and $\bar{B}(\tau)$ is the base-state azimuthal curvature. We interpret the terms present on the left-hand side of (3.75) as contributions to the amplitude of the nth azimuthal pressure mode owing to different physical effects. The first term represents axial tension–curvature effects, the second is wall inertia, and the third term arises due to azimuthal bending. The sum of these three terms matches the overall amplitude of the nth mode pressure forcing Q_n.

This model represents a substantial improvement of previous studies. In the solution method of Whittaker et al. (2010b) and Walters et al. (2018), there are two significant limitations that we draw attention to. Firstly, the ad hoc truncation results in the corrections to the fundamental mode being difficult to calculate, which means that an understanding of the relative error induced by truncating the expansion cannot easily be obtained. Secondly, the pressure is assumed to be azimuthally uniform, which places limitations on future investigation. In the current work, we overcome both of these limi-

tations. The eigenfunction expansion method used here allows the azimuthal modes to completely decouple, meaning that a formal series solution can be obtained, and that an analysis of the error induced after *any* truncation can be constructed trivially. This significant result has allowed us to justify that the leading azimuthal mode provides a dominant contribution to the change in cross-sectional area of the tube. This observation was first made by Whittaker et al. (2010b); however, they were unable to comprehensively justify such an argument quantitatively due their invoked ad-hoc assumption.

The 'tube law' like equations (3.75) derived here can be used in a variety of contexts. In this Chapter we have shown that we can obtain an analytical solution for the case in which the deformations are induced by a steady uniform transmural pressure. We verified that the fundamental azimuthal mode yields the dominant contribution to the change in cross-sectional area, and produced contour plots demonstrating the accuracy of the respective solutions after truncating at the first and second modes throughout different regions of $(\sigma_0, \tilde{F})$ space. As we shall see in Chapter 4, it is often convenient to write (3.75) in terms of the tube's cross-sectional area. For the specific case of coupling the results here to the leading-order fluid mechanics (in which the hydrodynamic pressure is azimuthally uniform), we can write (3.75) in dimensional variables as follows

$$ma\frac{\partial^2}{\partial t^{*2}}\left(\frac{A_n^*}{A_0^*}\right) - \frac{F}{2\pi}\frac{\partial^2}{\partial z^{*2}}\left(\frac{A_n^*}{A_0^*}\right) + \frac{\lambda_n K}{a^3}\left(\frac{A_n^*}{A_0^*}\right) = Q_n^*(z,t)t_n, \qquad (3.77)$$

where starred variables represent dimensional quantities. Here, F is the dimensional axial tension, K is the bending stiffness, Q_n^* is the forcing from the transmural pressure which can be calculated via (3.76) with $\tilde{P} = p_{\text{tm}}^*$,

and we have defined A_n^* as the dimensional perturbation to the cross-sectional area associated with the nth azimuthal eigenmode. The total area change is then given by

$$A^*(z,t) - A_0^* = \sum_{n=1}^{\infty} A_n^*(z,t). \tag{3.78}$$

Equation (3.77) will be used to couple the fluid and solid mechanics via the transmural pressure p_{tm}^* in Chapter 4. However, at least for the oscillatory problem, the azimuthal modes no longer decouple. Area displacements that are associated with the first azimuthal eigenmode create a pressure distribution in the fluid that forces all of the azimuthal eigenmodes. We can address this limitation by calling on the analysis in the present work that justified a dominant fundamental azimuthal mode. This result means that the dominant contribution to the pressure in the fluid is forced by the $n = 1$ azimuthal mode, and that the response from this pressure is to excite predominantly the first azimuthal mode. Consequently, the coupling with higher-order azimuthal modes is weak. The result of this simplification is the ability to compute a series solution.

The ability to permit azimuthal variation into the transmural pressure is significant for future study. In Chapter 4 we consider a model (applicable for the parameter regimes considered here) that couples the wall motion to an internally conveyed viscous fluid. For a regime in which oscillations in the tube wall are of high-frequency and long-wavelength, the tube-law derived by Whittaker et al. (2010b) was adequate, since the hydrodynamic pressure was azimuthally uniform at leading order. To incorporate higher-order effects from the fluid mechanics, we would need to allow azimuthal variation in the transmural pressure, which the results in this Chapter permit.

Whilst the results presented in this chapter are developments on previous theoretical and rational descriptions of the Starling resistor, the model is not without its limitations. The action of retaining only leading-order contributions in (3.15) linearises the problem, and therefore non-linear affects (such as instability saturation) are not captured. There are two main drawbacks when considering the initial geometry of the tube. In various biomedical contexts we might expect to find axially non-uniform tubes, whose initial cross-sectional shapes are not necessarily elliptical.

The limitations discussed here provide the foundations for future study. In Chapter 5 we will consider the case of different initial cross-sectional shapes. When trying to introduce initially axially non-uniform features (which applies to blood vessels that are partially collapsed) in the tube, more work is required in deriving new governing equations that measure the deformations. One potential avenue might be to capture all of the axial dependence within the ellipticity parameter σ_0.

APPENDICES

3.A The differential operators $\hat{\mathscr{L}}, \hat{\mathscr{K}}, \hat{\mathscr{J}}$

3.A.1 Expressions for the operators

When considering the numerical solution of (3.21)–(3.22), it was convenient to use alternative definitions for the operators $\hat{\mathscr{L}}\hat{\mathscr{K}}$ and $\hat{\mathscr{J}}$. The definitions

we used are given by:

$$\hat{\mathscr{L}}(\eta) = \frac{2}{c^2\cosh(2\sigma_0)}\left(\frac{\partial^3}{\partial\tau^3} + L_2\frac{\partial^2}{\partial\tau^2} + L_1\frac{\partial}{\partial\tau} + L_0\right)\eta, \tag{3.79}$$

$$\hat{\mathscr{K}}(\eta) = \frac{-2}{c^2\cosh(2\sigma_0)}\frac{\partial}{\partial\tau}\left(1 + \frac{\partial^2}{\partial\tau^2}\right)\eta, \tag{3.80}$$

$$\begin{aligned}\hat{\mathscr{J}}(\eta) = \Bigg(&- \frac{(\cosh(2\sigma_0) - \cos(2\tau))^2}{\cosh^2(2\sigma_0)}\frac{\partial^2\eta}{\partial\tau^2} \\ &- \frac{3(\cosh(2\sigma_0) - \cos(2\tau))\sin(2\tau)}{\cosh^2(2\sigma_0)}\frac{\partial\eta}{\partial\tau} \\ &+ \frac{2\sinh^2(2\sigma_0) + 3\sin^2(2\tau) - (\cosh(2\sigma_0) - \cos(2\tau))^2}{\cosh^2(2\sigma_0)}\eta\Bigg).\end{aligned} \tag{3.81}$$

The azimuthally varying coefficients L_2, L_1 and L_0 present in (3.79) are given explicitly by:

$$L_2 = -\frac{3\sin(2\tau)}{\cosh(2\sigma_0) - \cos(2\tau)}, \tag{3.82}$$

$$L_1 = -\frac{(2\cos^2(2\tau) + 8\cosh(2\sigma_0)\cos(2\tau) - 9 - \cosh^2(2\sigma_0))}{(\cosh(2\sigma_0) - \cos(2\tau))^2}, \tag{3.83}$$

$$L_0 = \frac{3\sin(2\tau)(\cosh^2(2\sigma_0) - 5 + 4\cosh(2\sigma_0)\cos(2\tau))}{(\cosh(2\sigma_0) - \cos(2\tau))^3}. \tag{3.84}$$

The expressions for $\hat{\mathscr{L}}\hat{\mathscr{K}}$ and $\hat{\mathscr{J}}$ convenient for proving symmetry (see 3.A.2) are given by:

$$\hat{\mathscr{L}}(\eta) = \tanh(2\sigma_0)\left[-\bar{B}\frac{\partial}{\partial\tau}\left(\frac{\eta}{h}\right) - \frac{\partial}{\partial\tau}\left(\frac{1}{\bar{B}h}\frac{\partial}{\partial\tau}\left(\frac{1}{h}\frac{\partial}{\partial\tau}\left(\frac{\eta}{h}\right)\right)\right)\right]. \tag{3.85}$$

$$\hat{\mathscr{J}}(\eta) = \tanh^2(2\sigma_0)\left[\eta - \frac{\partial}{\partial\tau}\left(\frac{1}{\bar{B}h}\frac{1}{\bar{B}}\frac{\partial}{\partial\tau}\left(\frac{\eta}{h}\right)\right)\right]. \tag{3.86}$$

$$\hat{\mathscr{K}}(\eta) = \tanh(2\sigma_0)\frac{\partial}{\partial\tau}\left[\frac{\bar{B}\eta}{h} + \frac{1}{h}\frac{\partial}{\partial\tau}\left(\frac{1}{\bar{B}h}\frac{\partial}{\partial\tau}\left(\frac{\eta}{h}\right)\right)\right]. \tag{3.87}$$

3.A.2 Proof that the operators $\hat{\mathscr{L}}\hat{\mathscr{K}}$ and $\hat{\mathscr{J}}$ are self-adjoint

We present now the proof that the operators $\hat{\mathscr{L}}\hat{\mathscr{K}}$ and $\hat{\mathscr{J}}$ are both self-adjoint operators with respect to the inner product $\langle u, v\rangle$ (3.23), namely

$$\langle u, v\rangle = \int_0^{\frac{\pi}{2}} \frac{1}{h} uv \mathrm{d}\tau, \tag{3.88}$$

for u and v smooth functions which satisfy the boundary conditions

$$u = \frac{\mathrm{d}^2 u}{\mathrm{d}\tau^2} = \frac{\mathrm{d}^4 u}{\mathrm{d}\tau^4} = 0 \ \text{ on } \ \tau = 0, \frac{\pi}{2}. \tag{3.89}$$

The operator $\hat{\mathscr{J}}$

Consider the inner product $\langle u, \hat{\mathscr{J}}(v)\rangle$ using the definition of $\hat{\mathscr{J}}$ in (3.86). Integrating by parts twice, it can be shown that:

$$\begin{aligned}\langle u, \hat{\mathscr{J}}(v)\rangle = \langle \hat{\mathscr{J}}(u), v\rangle - \tanh^2 2\sigma_0 \Bigg(&\left[\frac{1}{B^2 h}\frac{\partial}{\partial\tau}\left(\frac{u}{h}\right)\frac{v}{h}\right]_0^{\pi/2} \\ &- \left[\frac{1}{B^2 h}\frac{\partial}{\partial\tau}\left(\frac{v}{h}\right)\frac{u}{h}\right]_0^{\pi/2}\Bigg).\end{aligned} \tag{3.90}$$

Hence the operator $\hat{\mathscr{J}}$ is self-adjoint.

Furthermore, our analysis also requires that $\langle u, \hat{\mathscr{J}}(v)\rangle$ is positive definite on $[0, \pi/2]$. Using integration by parts, with $\hat{\mathscr{J}}$ again in the form of (3.17), it can be shown that:

$$\langle u, \hat{\mathscr{J}}(u)\rangle = \tanh^2(2\sigma_0) \int_0^{\pi/2} \left(\frac{1}{h}|u|^2 + \frac{1}{(\bar{B})^2 h}\left|\frac{\partial}{\partial\tau}\left(\frac{u}{h}\right)\right|^2 \right) \mathrm{d}\tau. \tag{3.91}$$

Since $h > 0$ on $[0, \pi/2]$, the inner product $\langle \hat{\mathscr{J}}(u), v\rangle$ is positive definite.

The operator $\hat{\mathscr{L}}\hat{\mathscr{K}}$

Consider the inner product $\langle \hat{\mathscr{L}}\hat{\mathscr{K}}(u), v\rangle$, where $\hat{\mathscr{L}}$ and $\hat{\mathscr{K}}$ are as defined in (3.16)–(3.18). Integrating by parts recursively, it can be shown that:

$$\begin{aligned}\langle \hat{\mathscr{L}}\hat{\mathscr{K}}(u), v\rangle = \langle u, \hat{\mathscr{L}}\hat{\mathscr{K}}(v)\rangle - \frac{2}{c^2\cosh 2\sigma_0}\Bigg(&- \left[\frac{\bar{v}}{h}\hat{\mathscr{K}}(u)\right]_0^{\pi/2} \\ &- \left[\frac{\partial^2}{\partial\tau^2}\left(\frac{1}{h}\hat{\mathscr{K}}(u)\right)\bar{v}\right]_0^{\pi/2} + \left[\frac{\partial}{\partial\tau}\left(\frac{1}{h}\hat{\mathscr{K}}(u)\right)\frac{\partial\bar{v}}{\partial\tau}\right]_0^{\pi/2} - \\ &\left[\frac{1}{h}\hat{\mathscr{K}}(u)\frac{\partial^2\bar{v}}{\partial\tau^2}\right]_0^{\pi/2}\Bigg) + \frac{2}{c^2\cosh 2\sigma_0}\Bigg(- \left[\frac{u}{h}\hat{\mathscr{K}}(\bar{v})\right]_0^{\pi/2} \\ &- \left[\frac{\partial^2}{\partial\tau^2}\left(\frac{1}{h}\hat{\mathscr{K}}(\bar{v})\right)u\right]_0^{\pi/2} + \left[\frac{\partial}{\partial\tau}\left(\frac{1}{h}\hat{\mathscr{K}}(\bar{v})\right)\frac{\partial u}{\partial\tau}\right]_0^{\pi/2} \\ &- \left[\frac{\partial^2}{\partial\tau^2}\left(\frac{1}{h}\hat{\mathscr{K}}(\bar{v})\right)u\right]_0^{\pi/2}\Bigg). \end{aligned} \tag{3.92}$$

Hence, when u and v satisfy (3.89), the boundary terms vanish and the operator is shown to be self-adjoint.

3.B Orthogonality relation for the eigenfunctions $Y_n(\tau)$

Let Y_n and Y_m be the eigenfunctions of (3.21), with corresponding eigenvalues λ_n and λ_m, defined on $(0, \pi/2)$. Using the linearity of the inner product $\langle\cdot,\cdot\rangle$, and the symmetry of the operators $\hat{\mathscr{L}}\hat{\mathscr{K}}$ and $\hat{\mathscr{J}}$, we find that

$$\lambda_m\langle Y_n, \hat{\mathscr{J}}(Y_m)\rangle = \langle Y_n, \lambda_m\hat{\mathscr{J}}(Y_m)\rangle,$$

$$
\begin{aligned}
&= \langle Y_n, \hat{\mathscr{L}}\hat{\mathscr{K}}(Y_m)\rangle, \\
&= \langle \hat{\mathscr{L}}\hat{\mathscr{K}}(Y_n), Y_m\rangle, \\
&= \langle \lambda_n \hat{\mathscr{J}}(Y_n), Y_m\rangle, \\
&= \lambda_n \langle \hat{\mathscr{J}}(Y_n), Y_m\rangle, \\
&= \lambda_n \langle Y_n, \hat{\mathscr{J}}(Y_m)\rangle. \qquad (3.93)
\end{aligned}
$$

Hence

$$(\lambda_m - \lambda_n)\langle Y_n, \hat{\mathscr{J}}(Y_m)\rangle = 0. \qquad (3.94)$$

Thus, for $n \neq m$, assuming that there are no repeated eigenvalues, we have the orthogonality relationship

$$\langle Y_n, \hat{\mathscr{J}}(Y_m)\rangle = 0. \qquad (3.95)$$

Chapter 4

Modelling the fluid-structure interaction in a Starling resistor

Synopsis

We present a theoretical description of the fluid-structure interaction observed within the Starling resistor. The typical setup consists of a pre-stretched finite length thin-walled elastic tube mounted between two rigid tubes. The collapsible section is enclosed within a pressure chamber and a viscous fluid is driven through the system by imposing an axial volume flux. Valid within a long-wavelength thin-walled regime, we use our own results to model the wall motion. These results arise from the solution of a generalised eigenvalue problem, and avoid the need to invoke the ad-hoc assumptions made in previous studies. The wall mechanics are then coupled to the fluid mechanics using the Navier–Stokes equations, under the assumption that the oscillations in the tube wall are of small amplitude, long-wavelength and high-frequency. We derive the respective steady and oscillatory problems for this fluid-structure interaction. In both cases, we compute series solutions, which allow us to estimate the errors incurred after truncation.

4.1 Introduction

Whittaker et al. (2010c) were the first to construct a three-dimensional theoretical model of the high-frequency self-excited oscillations observed in a Starling resistor. They investigated the problem of an elastic-walled tube with an initially axially uniform elliptical cross-section conveying an incompressible viscous fluid. To derive the model, Whittaker et al. (2010c) combined their own asymptotic descriptions for the fluid mechanics (Whittaker et al., 2010d) and wall mechanics (Whittaker et al., 2010b).

We now summarise the methodology set out in Whittaker et al. (2010c). Whittaker et al. (2010d) considered the motion of the fluid in response to a rapidly oscillating elastic-walled tube. They showed that the conservation of mass and axial momentum provided a system of two differential equations relating the axial fluid velocity, w, the fluid pressure p, and the cross-sectional area of the tube A. As reviewed in detail in Chapter 3, Whittaker et al. (2010b) derived a tube law systematically from shell theory, which takes the form of a differential equation relating A with $p - p_{\text{ext}}$, where p_{ext} is the (known) steady external pressure. In total this means that their asymptotic model of the full coupled problem involves a system of three equations relating three dependent variables w, p and A. Whittaker et al. (2010c) manipulated this system to eliminate w and A in favour of the pressure, p. This problem was solved to find the normal modes of the system. After an assessment of the systems energy budget, they used these normal mode solutions to demonstrate that their model exhibits self-excited oscillations, induced by the sloshing instability (see §1.1.7 of Chapter 1). On computing the growth rates, frequencies and mode shapes of the oscillations, they compared their

work directly with numerical simulations and obtained good agreement. The model of Whittaker et al. (2010c) was then extended by Walters et al. (2018) to include effects due to the inertia of the tube wall. It was found that the addition of wall inertia has a stabilising effect on the system.

Whilst the work of both Whittaker et al. (2010c) and Walters et al. (2018) are significant improvements on previous attempts to accurately model the Starling resistor, the method used to derive the tube law — which couples the fluid and wall mechanics — has its limitations. By projecting the azimuthal displacement onto a basis of azimuthal Fourier modes, an adhoc approximation based on the relative sizes of each azimuthal mode was used to decouple the modes (essentially truncating at $n = 1$), allowing for the derivation of the tube law. The main problem with this approach is the difficulty in calculating the relative error after neglecting contributions to the series solution. In Chapter 3, we overcame these limitations by instead projecting the solution onto a basis of eigenfunctions, resulting from a generalised eigenvalue problem. This new method resulted in a formal series solution for the whole system, whilst significantly simplifying the calculations required to compute the relative error incurred by truncating the solution after any azimuthal mode.

In this chapter, we consider the fluid-structure interaction problem of a viscous fluid conveyed within a long thin-walled elastic tube which has an initially axially uniform elliptical cross-section. We model the wall mechanics using our own results from Chapter 3, and then adapt the methodology of Whittaker et al. (2010c) and Walters et al. (2018) to couple this to the fluid mechanics. We consider the steady and oscillatory problems in turn, deriving

series expansions in both cases.

We organise this chapter as follows. In §4.2 we provide a full description of the physical setup. The problem is decomposed into steady and oscillatory parts and then non-dimensionalised. The various parameter regimes in which our model is considered are then presented. In §4.3 we introduce the models used to describe the fluid and wall mechanics respectively. In §4.4 we consider the steady problem, and show that the component of the change in cross-sectional area corresponding to the nth azimuthal eigenmode is governed by a simple second-order linear ordinary differential equation, forced by the steady component of the transmural pressure. In §4.5 we consider the unsteady problem. We show that the governing equation is much more complicated than for the steady case, since the azimuthal modes no longer decouple at leading order. Area displacements that are associated with the first azimuthal eigenmode create a pressure distribution in the fluid that forces all of the azimuthal eigenmodes. We show that we can overcome this limitation by observing that the fundamental azimuthal mode dominates the area displacements. This means that the dominant contribution to the pressure in the fluid is forced by the $n = 1$ azimuthal mode, and that the response from this pressure is to excite predominantly the first azimuthal mode. This analysis results in weak coupling between the higher-order azimuthal modes. We show that this simplification enables us to adopt a series expansion for the normal modes and oscillation frequencies of the system. In §4.6, we use our normal mode solutions to compute a stability threshold for the onset of self-excited oscillations in the tube wall by determining the critical Reynolds number beyond which an instability will grow. Finally, in §4.7, we discuss

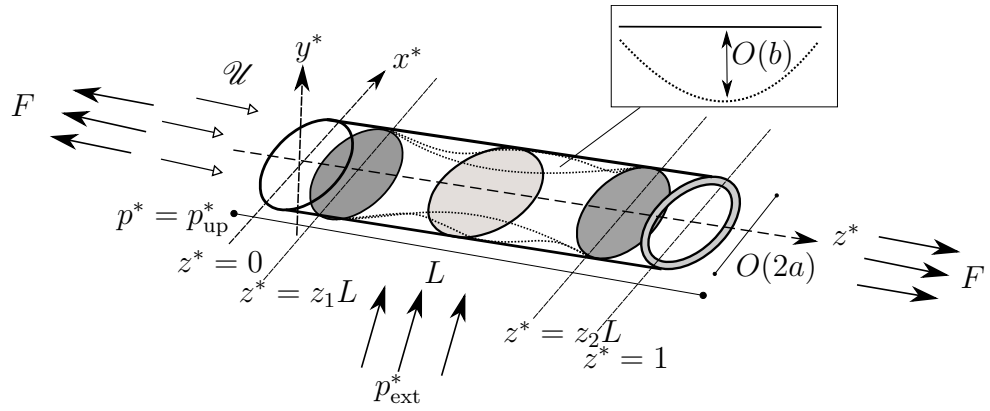

Figure 4.1: The setup of an idealised Starling resistor. An initially elliptical elastic-walled tube is pinned between two rigid extensions. Fluid is driven through the system by imposing a steady dimensional axial volume flux of size $A_0^* \mathscr{U}$ at the downstream end $z^* = 1$.

our results and comment on potential future work.

4.2 Setup

4.2.1 Problem description

We adopt the setup of Chapter 2 by considering a thin-walled tube of dimensional length L and circumference $2\pi a$ (see figure 4.1). The tube has an initially axially uniform elliptical cross-section, which is aligned with the dimensional Cartesian co-ordinates (x^*, y^*, z^*) such that the tube's centre line lies along the z^* axis. We also introduce t^* as dimensional time. The major and minor axes of the tube's cross-section are aligned with the x^* and y^* axis respectively. The ellipticity of the tube's cross-section is set by the parameter σ_0 such that the major and minor axis of the cross-section are

given explicitly by $ac\cosh\sigma_0$ and $ac\sinh\sigma_0$ respectively, where

$$c(\sigma_0) = \frac{\pi\,\mathrm{sech}(\sigma_0)}{2E(\mathrm{sech}(\sigma_0))} \tag{4.1}$$

is a normalisation factor, which is introduced to set the tube's initial circumference to be $2\pi a$. Here

$$E(k) = \int_0^{\pi/2} (1 - k^2\sin^2(\phi))^{1/2}\,\mathrm{d}\phi \tag{4.2}$$

is the complete elliptic integral of the second kind. The tube's initial dimensional cross-sectional area A_0^* can then be calculated as

$$A_0^* = \pi a^2 c^2 \sinh(\sigma_0)\cosh(\sigma_0) = \pi a^2 \frac{\pi^2\tanh(\sigma_0)}{4[E(\mathrm{sech}(\sigma_0))]^2}. \tag{4.3}$$

Throughout this chapter we shall refer to a set of six representative values of σ_0, $(s_0, s_1, s_2, s_3, s_4, s_5)$ which are presented in table 3.1 in Chapter 3. The corresponding elliptical cross-sections are given in figure 3.2.

In accordance with the experimental setup of the Starling resistor, the tube is made up of an elastic section of material having dimensional mass per unit area m and wall thickness d occupying $z_1 L < z^* < z_2 L$, which is pinned between two rigid sections occupying $0 < z^* < z_1 L$ and $z_2 L < z^* < L$ respectively. In the elastic section, the tube is able to deform in response to the combined effect of the steady dimensional external pressure p_{ext}^* as well as the fluid traction. Since the elastic section of the tube is pinned between two rigid sections, a dimensional axial tension force, F, can be imposed at the two ends of the tube, which results in a uniform axial pre-stress of magnitude

$F/(2\pi ad)$. The elliptical cross-section seen in figure 4.1 is in this pre-stressed state. We assume that the elastic section of the tube is linearly elastic and behaves isotropically with incremental Young's modulus E and Poisson ratio ν. The bending stiffness is defined as

$$K = \frac{Ed^3}{12(1-\nu^2)}. \tag{4.4}$$

In this chapter, we investigate the case in which the tube conveys an incompressible, viscous fluid of density ρ and dynamic viscosity μ. The fluid is driven through the system by imposing a steady dimensional axial volume flux of size $A_0^*\mathscr{U}$ at the downstream end. At the upstream end, we fix the dimensional pressure $p^* = p^*_{\text{up}}$. We note that these boundary conditions are chosen so that the amplitude of the resulting oscillatory axial sloshing flow at the downstream end is zero, which significantly increases the likelihood that an instability will occur. We denote the dimensional axial fluid velocity component as w^* and the dimensional transverse fluid velocity vector as $\boldsymbol{u}^*_\perp$.

4.2.2 Oscillatory time scale

We consider the case of periodic oscillations in the tube wall, with typical (normal) amplitude $b \ll a$, and time scale T. Hence, the scale for the normal velocity of the wall is b/T. It is then natural to take b/T as the scale for the transverse oscillatory velocity in the fluid. The scale for the axial oscillatory velocity of the fluid is then estimated as $bL/(aT)$ through continuity.

We can formulate an explicit expression for the expected time scale T of the oscillations by assuming that the oscillations arise due to a balance

between axial fluid inertia and restoring forces from azimuthal bending of the tube wall [1]. The pressure scale associated with the forces due to azimuthal bending is Kb/a^4. Equating this with the unsteady axial inertial pressure scale $\rho L^2 b/(aT^2)$, we find that

$$T = \left(\frac{\rho a^3 L^2}{K}\right)^{1/2}. \tag{4.5}$$

4.2.3 Dimensionless quantities and parameter regimes

The setup described above gives rise to seven dimensionless quantities. There are three quantities associated with the geometry of the tube, which correspond to wall thickness, tube length and oscillation amplitude:

$$\delta = \frac{d}{a} \qquad \ell = \frac{L}{a}, \qquad \Delta = \frac{b(t^*)}{a}. \tag{4.6}$$

There are two independent dimensionless groups associated with the fluid mechanics. We follow Whittaker et al. (2010c) and define the Womersley number α and the Strouhal number St as:

$$\alpha^2 \equiv \frac{\rho a^2}{\mu T} = \left(\frac{\rho K}{a\ell^2\mu^2}\right)^{1/2} \qquad \text{and} \qquad St \equiv \frac{a}{\mathscr{U} T} = \left(\frac{K}{\rho a^3 \mathscr{U}^2}\right)^{1/2}. \tag{4.7}$$

The Womersley number α measures the relative importance of unsteady inertia to viscous effects. The Strouhal number St measures the relative importance of unsteady to convective inertia. The steady Reynolds number,

[1] In the regime specified in §4.2, there are two principal restoring forces to deformations of the tube wall: azimuthal bending and axial tension-curvature. By the assumption $\tilde{F} = O(1)$ in (2.6), their magnitudes are comparable, so either could be used here to estimate the timescale.

with its usual definition, can be expressed in terms of α and St, thus

$$Re = \frac{\rho \mathscr{U} a}{\mu} = \frac{\alpha^2}{St}. \tag{4.8}$$

There are two dimensionless groups associated with the solid mechanics of the tube wall. We define the dimensionless axial tension $\tilde{F}$ and inertia coefficient (or dimensionless mass) M as follows:

$$\tilde{F} = \frac{aF}{2\pi K \ell^2}, \qquad M = \frac{ma^4}{KT^2} \equiv \frac{m}{\rho a \ell^2}. \tag{4.9}$$

The dimensionless axial tension measures the ratio of the restoring forces due to axial curvature/tension effects $Fb/(2\pi aL^2)$ and azimuthal bending (Kb/a^4) respectively. The inertia coefficient was introduced by Walters et al. (2018) and is defined as the ratio between forces due to wall inertia (mb/T^2) and azimuthal bending or equivalently, the forces due to axial fluid inertia $(\rho a \ell^2 b/T^2)$.

Following the formulation of Whittaker et al. (2010c), we work within a parameter regime in which the tube is long and thin, subject to a large axial tension such that the tube exhibits small-amplitude, high-frequency deformations of long wavelength. Mathematically, these assumptions correspond to:

$$\ell \gg 1, \qquad \delta \ll 1, \qquad \Delta \ll 1, \qquad \alpha \gg 1, \qquad \ell St \gg 1. \tag{4.10}$$

We also adopt a regime in which tension/curvature, inertial effects from the tube wall and azimuthal bending effects can be present at leading order. This

means

$$\tilde{F} = O(1), \qquad \text{and} \qquad M \lesssim 1. \tag{4.11}$$

We assume that the time scale for the growth/decay of the oscillations is large in comparison with the time scale of the oscillations T. This multiple scales analysis was verified by Whittaker et al. (2011).

4.2.4 Non-dimensionalisation and scaling

We follow the non-dimensionalisation of Whittaker et al. (2010c). Axial lengths are scaled with the tube length L, transverse lengths with the radial scale a, and time with T. We write

$$(x^*, y^*, z^*) = (ax, ay, Lz), \quad A_0^* = a^2 A_0, \quad A^* = a^2 A, \quad t^* = Tt, \tag{4.12}$$

where the unstarred variables are the non-dimensional counterparts of the starred variants.

The velocity and pressure of the fluid are decomposed into their respective steady and oscillatory components. For the steady component, the axial scale is the mean flow $\mathscr{U}$, and the transverse scale $\mathscr{U}a/L$ arises from continuity and the tube's aspect ratio. For the oscillatory component, the transverse scale is the normal velocity scale b/T of the wall motion, and the axial scale bL/aT arises from continuity. When non-dimensionalising the pressure, the viscous scale is used for the steady component, and the oscillatory component is scaled with unsteady axial inertia. We therefore write:

$$\boldsymbol{u}_\perp^* = \frac{\mathscr{U}a}{L}\bar{\boldsymbol{u}}_\perp + \frac{b}{T}\hat{\boldsymbol{u}}_\perp = \frac{\mathscr{U}}{\ell}\left(\bar{\boldsymbol{u}}_\perp + \ell St \Delta \hat{\boldsymbol{u}}_\perp\right), \tag{4.13}$$

$$w^* = \mathscr{U}\,\bar{w} + \frac{Lb}{aT}\hat{w} = \mathscr{U}\left(\bar{w} + \ell St \Delta \hat{w}\right), \tag{4.14}$$

$$p^* - p^*_{\text{up}} = \frac{\mu L \mathscr{U}}{a^2}\bar{p} + \frac{\rho L^2 b}{aT^2}\hat{p} = \frac{\mu L \mathscr{U}}{a^2}\left(\bar{p} + \alpha^2 \ell St \Delta \hat{p}\right), \tag{4.15}$$

where overbars denote the steady components and hats the unsteady components. The dimensional external pressure p^*_{ext} (assumed to be steady) is non-dimensionalised on the steady viscous scale as

$$p^*_{\text{ext}} - p^*_{\text{up}} = \frac{\mu L \mathscr{U}}{a^2}\bar{p}_{\text{ext}}. \tag{4.16}$$

Using this expression, together with (4.15), we find that the dimensional transmural pressure p^*_{tm} can be written as

$$\begin{aligned} p^*_{\text{tm}} = p^* - p^*_{\text{ext}} &= (p^* - p^*_{\text{up}}) - (p^*_{\text{ext}} - p^*_{\text{up}}), \\ &= \frac{\mu L \mathscr{U}}{a^2}(\bar{p} - \bar{p}_{\text{ext}}) + \frac{\rho L^2 b}{aT^2}\hat{p}, \qquad (4.17) \\ &= \frac{K}{a^3}\left(\frac{1}{\alpha^2 \ell St}\left(\bar{p} - \bar{p}_{\text{ext}}\right) + \Delta(t)\hat{p}\right), \qquad (4.18) \end{aligned}$$

where $\bar{p}$ and $\hat{p}$ are evaluated at the tube wall.

The tube wall deforms in response to the transmural pressure, which in turn leads to changes in the cross-sectional area. The area is non-dimensionalised as

$$A^*(z,t) = a^2\left(A_0 + \frac{1}{\alpha^2 \ell St}\bar{A}(z) + \Delta(t)\hat{A}(z,t)\right), \tag{4.19}$$

in terms of steady and oscillatory perturbations. The oscillatory perturbation has been scaled using the natural scale (ab) from wall motion, whilst the steady perturbation is set to ensure that the ratio between the scales for steady and unsteady perturbations is the same as for the transmural pressure

in (4.18).

4.3 Mathematical modelling

We now present a description of the models used to describe the fluid and solid mechanics present in the problem described above. For the fluid mechanics, the internal fluid is described by the Navier–Stokes equations, which are simplified due to the small-amplitude, high-frequency and long-wavelength nature of the oscillations. For the solid mechanics, we model the wall motion using our results from Chapter 3, where we derived an expression for the relative change of the tube's cross-sectional area $A^* - A_0^*$ in terms of the transmural pressure p_{tm}^*. The fluid and solid mechanics are then coupled via A^* and p_{tm}^*.

4.3.1 Fluid mechanics

The fluid inside of the tube is governed by the Navier–Stokes equations (Batchelor, 1967)

$$\nabla \cdot \boldsymbol{u}^* = 0, \tag{4.20}$$

$$\rho\left(\frac{\partial \boldsymbol{u}^*}{\partial t^*} + (\boldsymbol{u}^* \cdot \nabla)\boldsymbol{u}^*\right) = -\nabla p^* + \mu \nabla^2 \boldsymbol{u}^*, \tag{4.21}$$

subject to:

$$p^* = p_{\text{up}}^* \qquad \text{at} \qquad z^* = 0, \tag{4.22}$$

$$\iint_{\mathscr{A}^*(z^*,t^*)} w^* \,\mathrm{d}S^* = \mathscr{U} A_0^* \qquad \text{at} \qquad z^* = L. \tag{4.23}$$

and

$$\boldsymbol{u}^* = \boldsymbol{U}_W^* \qquad \text{on the wall,} \tag{4.24}$$

where $\boldsymbol{u}^*$ is the total dimensional fluid velocity and $\boldsymbol{U}_W$ is the velocity of the wall. In Appendix 4.A we also derive the dimensional cross-sectionally integrated mass conservation statement

$$\frac{\partial A^*}{\partial t^*} + \frac{\partial}{\partial z^*} \iint_{\mathscr{A}^*(z^*,t^*)} w^* \, \mathrm{d}S^* = 0, \tag{4.25}$$

where $\mathscr{A}^* \subset \mathbb{R}^2$ is the dimensional space enclosed by the tube cross-section.

Following Whittaker et al. (2010c), we substitute the representations (4.12)–(4.15) into (4.20)–(4.25) and apply standard long-wavelength approximations. The calculations are the same as those presented in Walters et al. (2018), so we omit the details for brevity. For the steady component, it is found that $\bar{p}$ is uniform within each cross-section at leading order. The axial component of the conservation of axial momentum equation (4.21) then yields the following leading-order balance between axial pressure gradient and viscosity:

$$\nabla^2 \bar{w} = \frac{\mathrm{d}\bar{p}}{\mathrm{d}z}. \tag{4.26}$$

(Nonlinear inertia and contributions from the oscillatory flow only enter at higher orders.)

We also have the leading-order steady component of the cross-sectionally integrated continuity equation (4.25)

$$\frac{\mathrm{d}}{\mathrm{d}z} \iint_{\bar{\mathscr{A}}(z)} \bar{w} \, \mathrm{d}S = 0, \tag{4.27}$$

where $\bar{\mathscr{A}}$ is the space enclosed by the dimensionless mean position of the wall.

For the oscillatory component, the long wavelength and high-frequency nature of the oscillations ($\alpha, \ell \gg 1$) result in both the axial velocity and pressure being cross-sectionally uniform (outside of viscous boundary layers) at leading order. The axial component of the conservation of momentum equation (4.21) reduces to an inertial balance between axial fluid velocity and axial pressure gradient:

$$\frac{\partial \hat{w}}{\partial t} = -\frac{\partial \hat{p}}{\partial \hat{z}}. \tag{4.28}$$

(Nonlinear inertia and viscous terms only enter at higher orders.)

The oscillatory component of the averaged continuity equation (4.25) yields

$$\frac{\partial \hat{A}}{\partial t} + A_0 \frac{\partial \hat{w}}{\partial z} = 0. \tag{4.29}$$

(Here we have neglected steady area contributions of $O(1/\alpha^2 \ell St) \ll 1$ in (4.19) and used the property that $\hat{w}$ is uniform within the cross-section.)

At the upstream end ($z = 0$), the fluid pressure is fixed as $p^* = p^*_{\mathrm{up}}$, which (by (4.15)) corresponds to the following boundary conditions on $\bar{p}$ and $\hat{p}$:

$$\bar{p} = \hat{p} = 0 \qquad \text{at} \qquad z = 0. \tag{4.30}$$

At the downstream end ($z = 1$), the axial volume flux is fixed. Using (4.28), and the fact that $\hat{w}$ is uniform in each cross-section, we have the boundary

conditions:

$$\iint_{\mathscr{A}(z)} \bar{w}\,\mathrm{d}S = A_0 \qquad \text{and} \qquad \frac{\partial \hat{p}}{\partial z} = 0 \qquad \text{at} \qquad z = 1. \tag{4.31}$$

We also have the boundary condition

$$\bar{w} = 0 \qquad \text{on the tube wall.} \tag{4.32}$$

Due to the presence of Stokes layers located adjacent to the tube wall (which have been neglected) there is no corresponding condition on $\hat{w}$.

Since the flexible section of the tube is pinned to two rigid sections, we have matching conditions located at the tube joins $z = z_1, z_2$. These conditions arise from the requirement that both axial volume flux and fluid pressure are continuous across the joins. For the steady component, we require:

$$[\bar{w}]^+_- = [\bar{p}]^+_- = 0, \qquad \text{at} \qquad z = z_1, z_2. \tag{4.33}$$

For the oscillatory component, we require

$$[\hat{w}]^+_- = [\hat{p}]^+_- = 0, \qquad \text{at} \qquad z = z_1, z_2. \tag{4.34}$$

On eliminating the oscillatory component of axial fluid velocity $\hat{w}$ between (4.28) and (4.29), we obtain the following oscillatory pressure-area relationship

$$\frac{\partial^2 \hat{p}}{\partial z^2} = \frac{1}{A_0}\frac{\partial^2 \hat{A}}{\partial t^2}. \tag{4.35}$$

Equation (4.35) provides a relationship between the oscillatory components of

the fluid pressure and the tube's cross-sectional area at leading order. In §4.5 we will use this result to couple the fluid and solid mechanics, formulating the problem in terms of only the pressure.

Using (4.28), the unsteady matching conditions (4.34) can be written as

$$\left[\frac{\partial \hat{p}}{\partial z}\right]_{-}^{+} = [\hat{p}]_{-}^{+} = 0 \qquad \text{at} \qquad z = z_1, z_2. \tag{4.36}$$

4.3.2 Wall mechanics

We model the elastic section of the tube described in §4.2 using our results from Chapter 3. The exterior pressure p^*_{ext} is assumed to be uniform and the fluid mechanics in §4.3.1 tells us that the internal pressure p_{int} is uniform in each cross-section at leading order. Hence, at leading order, the tube is forced by an azimuthally uniform transmural pressure p^*_{tm}. In response, it undergoes small-amplitude deformations about its initial elliptical configuration.

In Chapter 3, we decomposed the area perturbation $A^*(z,t) - A^*_0$ into a series of contributions indexed by the azimuthal mode number, n:

$$A^*(z,t) - A^*_0 = \sum_{n=1}^{\infty} A^*_n(z,t). \tag{4.37}$$

We showed that each component A^*_n is governed by the ordinary differential equation

$$ma\frac{\partial^2}{\partial t^{*2}}\left(\frac{A^*_n}{A^*_0}\right) - \frac{F}{2\pi}\frac{\partial^2}{\partial z^{*2}}\left(\frac{A^*_n}{A^*_0}\right) + \frac{\lambda_n K}{a^3}\left(\frac{A^*_n}{A^*_0}\right) = q_n t_n p^*_{\text{tm}} \tag{4.38}$$

subject to the pinned-end boundary conditions

$$A_n^* = 0 \qquad \text{at} \qquad z^* = z_1 L, z_2 L. \tag{4.39}$$

The positive constants λ_n and $q_n t_n$ depend only on the ellipticity of the tube. They are determined numerically through the solution of an eigenvalue problem and are tabulated for the representative σ_0 values as well as plotted as continuous curves in table 3.4 and figures 3.5–3.6 in Chapter 3.

We decompose each component A_n^* into its respective steady and oscillatory parts using the same scales present in (4.19) for A^*:

$$A_n^*(z,t) = a^2 \left(\frac{1}{\alpha^2 \ell St} \bar{A}_n(z) + \Delta(t) \hat{A}_n(z,t) \right). \tag{4.40}$$

Hence

$$\bar{A}(z) = \sum_{n=1}^{\infty} \bar{A}_n(z) \qquad \text{and} \qquad \hat{A}(z,t) = \sum_{n=1}^{\infty} \hat{A}_n(z,t). \tag{4.41}$$

Substituting expressions (4.18) and (4.40) for p_{tm}^* and A_n^* into (4.38)–(4.39) and making use of the other scalings in §4.2, we find that the non-dimensional governing equations for the steady and oscillatory wall deformations in the flexible part of the tube $z_1 < z < z_2$ are given respectively by:

$$\tilde{F} \frac{\mathrm{d}^2 \bar{A}_n}{\mathrm{d}z^2} - \lambda_n \bar{A}_n = -A_0 q_n t_n \left(\bar{p} - \bar{p}_{\text{ext}} \right), \tag{4.42}$$

subject to

$$\bar{A}_n = 0 \qquad \text{at} \qquad z = z_1, z_2, \tag{4.43}$$

and

$$\tilde{F}\frac{\partial^2 \hat{A}_n}{\partial z^2} - M\frac{\partial^2 \hat{A}_n}{\partial t^2} - \lambda_n \hat{A}_n = -A_0 q_n t_n \hat{p}(z,t), \tag{4.44}$$

subject to

$$\hat{A}_n = 0 \qquad \text{at} \qquad z = z_1, z_2. \tag{4.45}$$

In the rigid sections of the tube occupying $0 < z < z_1$ and $z_2 < z < 1$, we must ensure that the tube's cross-section remains fixed. We therefore impose

$$\bar{A} = \hat{A} = 0 \qquad \text{for} \qquad z \in (0, z_1) \qquad \text{and} \qquad z \in (z_2, 1). \tag{4.46}$$

4.4 The steady coupled problem

We now seek leading-order solutions of the steady component of the problem described in §4.2–§4.3. We find that, for the parameter regimes considered here, the fluid and solid mechanics decouple at leading order, resulting in explicit expressions being obtained for the steady component of the pressure $\bar{p}$ and the axial fluid velocity $\bar{w}$. We show that the perturbation to the tube's cross-sectional area obeys a simple second-order ordinary differential equation with constant coefficients and linear forcing, which can be solved analytically.

4.4.1 Steady governing equations and boundary conditions

For the fluid mechanics, the pressure $\bar{p}$ and axial fluid velocity $\bar{w}$ satisfy (4.26) and (4.27):

$$\nabla^2 \bar{w} = \frac{\mathrm{d}\bar{p}}{\mathrm{d}z}, \qquad \frac{\mathrm{d}}{\mathrm{d}z} \iint_{\mathscr{A}(z)} \bar{w} \, \mathrm{d}S = 0, \tag{4.47}$$

subject to the boundary conditions (4.30), (4.31) and (4.32):

$$\bar{p} = 0 \qquad \text{at} \qquad z = 0, \tag{4.48}$$

$$\iint_{\mathscr{A}(z)} \bar{w} \, \mathrm{d}S = A_0 \qquad \text{at} \qquad z = 1, \tag{4.49}$$

$$\bar{w} = 0 \qquad \text{on the tube wall.} \tag{4.50}$$

For the wall motion, the perturbation $\bar{A}$ to the tube's cross-section is given by

$$\bar{A}(z) = \sum_{n=1}^{\infty} \bar{A}_n(z) \qquad \text{for} \qquad z \in (z_1, z_2), \tag{4.51}$$

where each $\bar{A}_n$ is governed by (4.42)–(4.43):

$$\tilde{F} \frac{\mathrm{d}^2 \bar{A}_n}{\mathrm{d}z^2} - \lambda_n \bar{A}_n = -A_0 q_n t_n \left(\bar{p} - \bar{p}_{\text{ext}} \right), \tag{4.52}$$

subject to

$$\bar{A}_n = 0 \qquad \text{at} \qquad z = z_1, z_2. \tag{4.53}$$

For the rigid sections, we have from (4.46) that

$$A_n \equiv 0 \qquad \text{for} \qquad z \in (0, z_1) \qquad \text{and} \qquad z \in (z_2, 1). \tag{4.54}$$

Finally, we have the matching conditions (4.33)

$$[\bar{w}]^+_- = [\bar{p}]^+_- = 0, \qquad \text{at} \qquad z = z_1, z_2. \tag{4.55}$$

4.4.2 Solution for $\bar{w}$ and $\bar{p}$

From (4.40)–(4.41), the steady perturbation to the tube's cross-sectional area is $O(1/\alpha^2 \ell St)$, which is small when working within the parameter regime considered here. Hence, at leading order we seek a solution of the fluids problem (4.47)–(4.50) in the axially uniform undeformed tube.

Since the steady pressure $\bar{p}$ is uniform within each cross-section, and the tube is axially uniform, the base-state axial fluid velocity takes the form

$$\bar{w} = f(x, y)\frac{\mathrm{d}\bar{p}}{\mathrm{d}z}. \tag{4.56}$$

Using the steady mass conservation statement in (4.47), it follows that $\bar{p}$ is linear in z. Hence, the steady axial fluid velocity $\bar{w}$ and pressure $\bar{p}$ are solutions of a classical two-dimensional Poiseuille problem in the elliptical geometry. Following Batchelor (1967), we have

$$\bar{w}(x, y) = 2\left(1 - \frac{x^2}{c^2\cosh^2(\sigma_0)} - \frac{y^2}{c^2\sinh^2(\sigma_0)}\right), \tag{4.57}$$

$$\bar{p}(z) = -\bar{G}z, \tag{4.58}$$

where $\bar{G} = 16\cosh(2\sigma_0)/(c^2\sinh^2 2(\sigma_0))$.

4.4.3 Solution for $\bar{A}_n$

Using the expression (4.58) for $\bar{p}$, the governing equation for the components $\bar{A}_n$ for $z \in (z_1, z_2)$ is given by

$$\tilde{F}\frac{\mathrm{d}^2\bar{A}_n}{\mathrm{d}z^2} - \lambda_n \bar{A}_n = A_0 q_n t_n \left(\bar{G}z + \bar{p}_{\mathrm{ext}}\right), \tag{4.59}$$

subject to

$$\bar{A}_n = 0 \qquad \text{at} \qquad z = z_1, z = z_2. \tag{4.60}$$

We observe that (4.59) is a linear second-order ordinary differential equation with constant coefficients, which can be solved using standard methods.

We find that the solution for each component is given by

$$\bar{A}_n = -\left(\frac{A_0 q_n t_n}{\lambda_n}\right)\left\{\bar{p}_{\mathrm{ext}}\left(1 - \frac{\cosh\left[\mu_n(\xi - \frac{1}{2})\right]}{\cosh\left(\frac{1}{2}\mu_n\right)}\right) - \bar{G}\left(z_1 + (z_2 - z_1)\xi \right.\right.$$
$$\left.\left. - \frac{\sinh\left[\mu_n(\xi - \frac{1}{2})\right](z_2 - z_1)}{2\sinh\left(\frac{1}{2}\mu_n\right)} - \frac{\cosh\left[\mu_n(\xi - \frac{1}{2})\right](z_1 + z_2)}{2\cosh\left(\frac{1}{2}\mu_n\right)}\right)\right\}, \tag{4.61}$$

where

$$\xi = \frac{z - z_1}{z_2 - z_1}, \qquad \text{and} \qquad \mu_n^2 = \frac{\lambda_n}{\tilde{F}}\left(z_1 - z_2\right)^2. \tag{4.62}$$

In figure 4.2, we plot the solutions (4.61) for A_n corresponding to the first four azimuthal modes. We observe the presence of boundary layers of thickness $\tilde{F}^{1/2} \propto \mu_n^{-1}$ located adjacent to the joins at $z = z_1, z_2$. The deformations vary rapidly in space near the ends of the flexible section when $\tilde{F}$ is small. In the limit as $\tilde{F} \to 0$, we see that the solution in the interior becomes linear in z. From (4.61), the linear behaviour is given explicitly by

$$\frac{\bar{A}_n}{A_0} = -\frac{q_n t_n}{\lambda_n}\left(\bar{G}z + \bar{p}_{\mathrm{ext}}\right), \qquad \text{as} \qquad \tilde{F} \to 0. \tag{4.63}$$

As p_{ext} is increased, we find that the solution (4.61) becomes symmetric (see figure 4.64) about the midpoint of the tube $z = 0.5$. This result is as expected, since an increase in the external pressure would result in a less significant contribution from the viscous pressure drop in the fluid. The solution in this instance would become

$$\frac{\bar{A}_n}{A_0} \sim -\bar{p}_{\text{ext}} \left(\frac{q_n t_n}{\lambda_n} \right) \left(1 - \frac{\cosh\left[\mu_n(\xi - \frac{1}{2})\right]}{\cosh\left(\frac{1}{2}\mu_n\right)} \right) \qquad \text{for} \qquad p_{\text{ext}} \gg G, \quad (4.64)$$

which is symmetric about the midpoint of the tube. We note here that the presence of a large external pressure means that the solution (4.64) is of the same form as that derived in Chapter 3, where we solved the problem for the case of a uniform external pressure whilst neglecting contributions from the internal fluid.

Figure 4.4 demonstrates the effect of a large uniform external pressure on the deformation of the tube as a function of the axial co-ordinate, z. As predicted, the large external pressure means that contributions to wall displacement from the viscous pressure drop are small, and hence we see maximal displacement near the midpoint $z = 0.5$.

Figure 4.3 provides insight into how varying the ellipticity of the tube's initial cross-sectional area affects the fundamental contribution $\bar{A}_1$ to the change in cross-sectional area. As expected, we find that tubes with larger initial ellipticity are more compliant, and therefore are susceptible to larger changes in area.

In figure 4.5 we plot the ratio $\bar{A}_2/\bar{A}_1$, evaluated at $z = 0.7$, in order to gain an understanding of the errors incurred by truncating the expansion (4.51) after the first azimuthal mode. The results indicate that tubes with larger

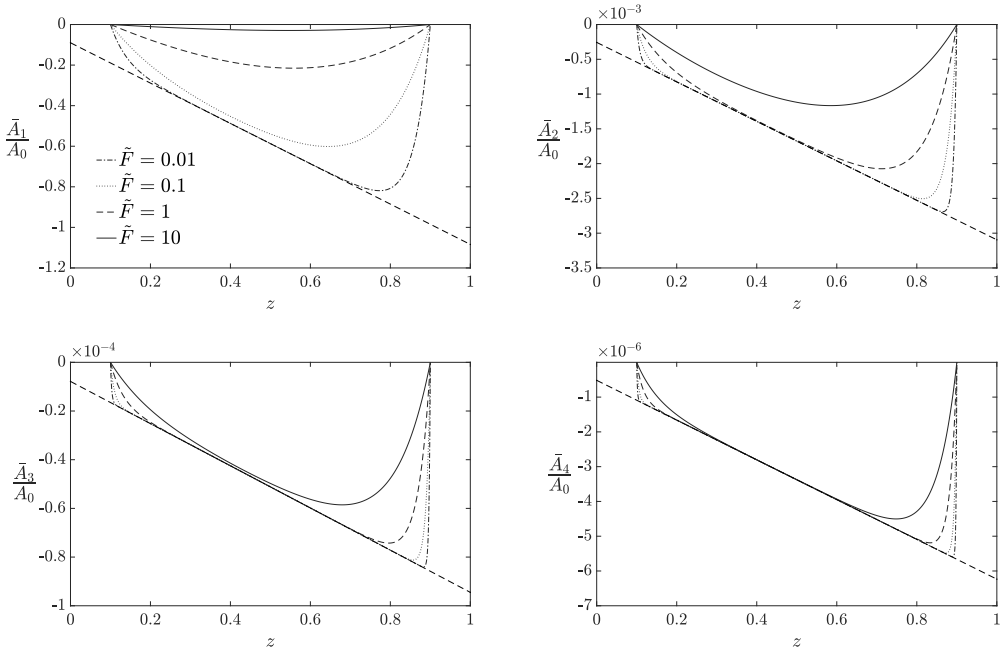

Figure 4.2: Solutions for the components $\bar{A}_n$, plotted for the first four azimuthal modes $n = 1, 2, 3, 4$. The curves were plotted using the analytical solution (4.61), with $p_{\text{ext}} = 1$, $\tilde{F} = 0.01, 0.1, 1, 10$ and $\sigma_0 = 0.6$. The data for $q_n t_n$ and λ_n can be found in Chapter 3. The dashed straight line is the limit (4.63) of the bulk solution as $\tilde{F} \to 0$.

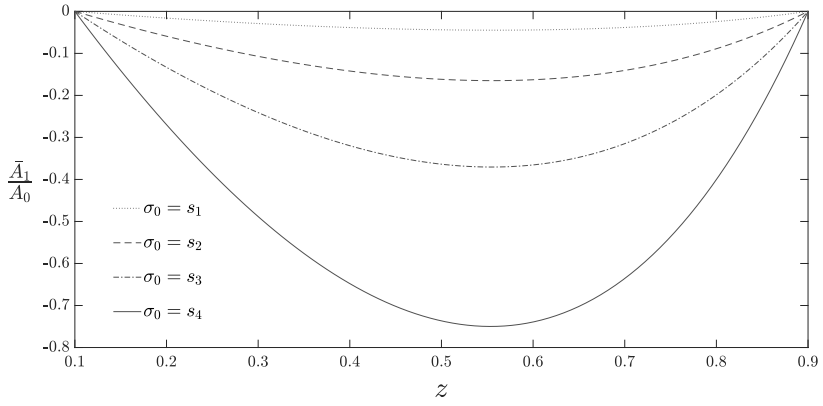

Figure 4.3: Solutions for the steady area change $\bar{A}_1$ associated with the first ($n = 1$) azimuthal mode, plotted against z for $\sigma_0 = s_1, s_2, s_3, s_4$, $p_{\text{ext}} = 1$ and $\tilde{F} = 1$. The solutions were obtained using the analytical solution (4.61).

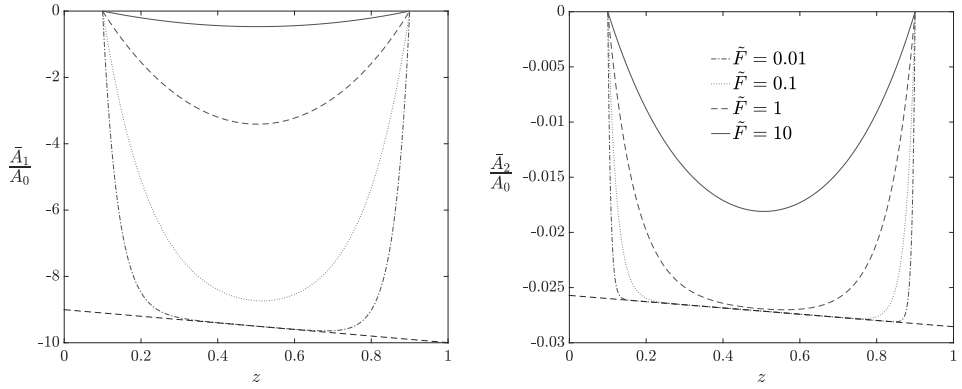

Figure 4.4: Solutions for the steady area change $\bar{A}_n$ from (4.61), plotted against z for the first two azimuthal modes with $\tilde{F} = 0.01, 0.1, 1, 10$. The tube is subject to a large uniform external pressure $p_{\text{ext}} = 100$

initial ellipticity result in a substantially larger relative contribution from the second azimuthal mode. In agreement with our results from Chapter 3, we find that an increase in the tension amounts to a larger error (up to $O(10^{-1})$ when $\tilde{F} = O(10^4)$).

4.5 The unsteady coupled problem

In this section we consider the unsteady component of the coupled problem described in §4.2–§4.3. We begin by first eliminating the oscillatory perturbation to the tube's area change $\hat{A}_n$ in favour of the pressure $\hat{p}$. After obtaining a solution within the rigid sections of the tube, we then derive the governing problem for motion within the flexible section. Unlike for the steady problem, the fluid and solid mechanics no longer decouple at leading order. To overcome this, we exploit a dominant contribution from the fundamental ($n = 1$) solid azimuthal mode, which means that the coupling is weak between the higher modes. Consequently, we derive a series solution of

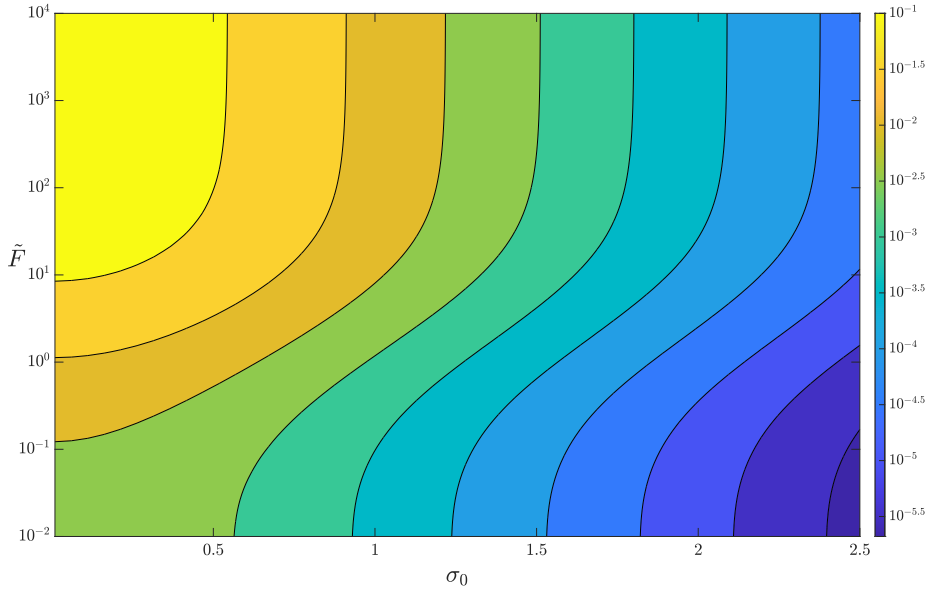

Figure 4.5: The values $\bar{A}_2/\bar{A}_1$, evaluated at $z = 0.7$, plotted throughout regions of $(\sigma_0, \tilde{F})$ parameter space with $p_{\text{ext}} = 1$. The values were computed using the analytical solution (4.61) for $\bar{A}_n$. The results give an indication of the errors incurred by approximating the steady system using the contribution to the chnage in area associated with the fundamental azimuthal mode.

the unsteady system.

4.5.1 Solution in the rigid sections

In the rigid sections, the tube's cross-section is fixed. Using (4.46) together with (4.35), we derive the governing equation

$$\frac{\partial^2 \hat{p}}{\partial z^2} = 0, \tag{4.65}$$

valid for $0 < z < z_1$ and $z_2 < z < 1$.

The boundary conditions on (4.65) are given by (4.30)–(4.31):

$$\hat{p} = 0 \qquad \text{at} \qquad z = 0 \qquad \text{and} \qquad \frac{\partial \hat{p}}{\partial z} = 0 \qquad \text{at} \qquad z = 1. \tag{4.66}$$

Solving (4.65) subject to (4.66), we find that

$$\hat{p}(z,t) = \begin{cases} G(t)z, & \text{for} \quad z \in (0, z_1), \\ H(t), & \text{for} \quad z \in (z_2, 1), \end{cases} \tag{4.67}$$

where $G(t)$ and $H(t)$ are arbitrary functions of time t, which will be determined later during the process of matching solutions between rigid and flexible sections.

We also have the matching conditions (4.36):

$$[\hat{p}]^+_- = \left[\frac{\partial \hat{p}}{\partial z}\right]^+_- = 0, \qquad \text{at} \qquad z = z_1, z_2. \tag{4.68}$$

Substituting the solution (4.67) into the matching conditions (4.68), we obtain the following explicit boundary conditions on $\hat{p}$ for $z_1 < z < z_2$:

$$z_1 \frac{\partial \hat{p}}{\partial z} - \hat{p} = 0, \qquad \text{at} \qquad z = z_1, \tag{4.69}$$

$$\frac{\partial \hat{p}}{\partial z} = 0, \qquad \text{at} \qquad z = z_2. \tag{4.70}$$

4.5.2 Governing equations in the flexible sections

We now derive equations that govern motion within the flexible section of the tube, $z_1 < z < z_2$. After eliminating the area variables $\hat{A}$ and $\hat{A}_n$, we present the governing equations for the coupled problem in terms of only the

pressure $\hat{p}$.

From §4.3.1–§4.3.2, the equations governing the fluid and wall motion $z_1 < z < z_2$ within the flexible section of the tube are given by (4.35),(4.41), (4.44)

$$\frac{\partial^2 \hat{p}}{\partial z^2} = \frac{1}{A_0}\frac{\partial^2 \hat{A}}{\partial t^2}, \tag{4.71}$$

$$\hat{A}(z,t) = \sum_{n=1}^{\infty} \hat{A}_n(z,t), \tag{4.72}$$

and

$$\tilde{F}\frac{\partial^2 \hat{A}_n}{\partial z^2} - M\frac{\partial^2 \hat{A}_n}{\partial t^2} - \lambda_n \hat{A}_n = -A_0 q_n t_n \hat{p}(z,t). \tag{4.73}$$

The conditions on $\hat{p}$ at the joins $z = z_1, z_2$ are given by (4.69)–(4.70). We also have the constraint (4.45) on the cross-sectional area at the joins

$$\hat{A}_n = 0 \qquad \text{at} \qquad z = z_1, z_2. \tag{4.74}$$

Motivated by (4.71) and the boundary conditions (4.69)–(4.70), we define $\hat{p}_n(z,t)$ as the solution of

$$\frac{\partial^2 \hat{p}_n}{\partial z^2} = \frac{1}{A_0}\frac{\partial \hat{A}_n}{\partial t^2}, \tag{4.75}$$

subject to:

$$z_1\frac{\partial \hat{p}_n}{\partial z} - \hat{p}_n = 0 \qquad \text{at} \qquad z = z_1, \tag{4.76}$$

$$\frac{\partial \hat{p}_n}{\partial z} = 0 \qquad \text{at} \qquad z = z_2. \tag{4.77}$$

With this definition, $\sum_{n=1}^{\infty} \hat{p}_n$ satisfies equation (4.71) for $\hat{p}$, and the boundary

conditions (4.69)–(4.70) for $\hat{p}$. Therefore, we can deduce that

$$\hat{p}(z,t) = \sum_{n=1}^{\infty} \hat{p}_n(z,t). \tag{4.78}$$

Hence, we interpret $\hat{p}_n$ as the component of the transmural pressure corresponding to the nth azimuthal mode.

Using (4.75), we can write condition (4.74) in terms of only $\hat{p}_n$

$$\frac{\partial^2 \hat{p}_n}{\partial z^2} = 0 \qquad \text{at} \qquad z = z_1, z_2. \tag{4.79}$$

Eliminating $\hat{A}_n$ between (4.73) and (4.75), the boundary-value problem for $\hat{p}_n$ in the flexible section of the tube is

$$\tilde{F}\frac{\partial^4 \hat{p}_n}{\partial z^4} - M\frac{\partial^4 \hat{p}_n}{\partial t^2 \partial z^2} - \lambda_n \frac{\partial^2 \hat{p}_n}{\partial z^2} = -q_n t_n \sum_{i=1}^{\infty} \frac{\partial^2 \hat{p}_i}{\partial t^2}, \tag{4.80}$$

subject to (4.76)–(4.77) and (4.79).

We can recognise that the governing equation (4.80) and its boundary conditions are linear and homogeneous. The pressure will therefore have arbitrary amplitude, which we shall set by imposing the normalisation

$$\int_0^1 \left(\frac{\partial}{\partial z} \sum_{n=1}^{\infty} \hat{p}_n \right)^2 \mathrm{d}z = 1. \tag{4.81}$$

The boundary-value problem for $\hat{p}_n$ consists of a coupled set of linear homogeneous fourth-order partial differential equations, together with two sets of boundary conditions at each join $z = z_1$ and $z = z_2$. There is also a global normalisation condition. We wish to find normal mode solutions.

Seeking a separable solution

We introduce the scaled axial co-ordinate

$$\zeta = \frac{z_2 - z}{z_2 - z_1}, \tag{4.82}$$

and seek solutions in which $\hat{p}_n$ varies harmonically in time with dimensionless frequency ω. We therefore write

$$\hat{p}_n(z,t) = Re\left(\tilde{p}_n(\zeta)e^{i\omega t}\right). \tag{4.83}$$

Substituting (4.83) into (4.76)–(4.81), the problem for $\tilde{p}_n$ is given by

$$\frac{\mathrm{d}^4\tilde{p}_n}{\mathrm{d}\zeta^4} + \frac{1}{\tilde{F}}\left(M\omega^2 - \lambda_n\right)(z_2 - z_1)^2\frac{\mathrm{d}^2\tilde{p}_n}{\mathrm{d}\zeta^2} = \frac{\omega^2 q_n t_n}{\tilde{F}}(z_2 - z_1)^4\sum_{i=1}^{\infty}\tilde{p}_i(\zeta), \tag{4.84}$$

subject to the boundary conditions:

$$\frac{\mathrm{d}\tilde{p}_n}{\mathrm{d}\zeta} = 0 \quad \text{at} \quad \zeta = 0, \tag{4.85}$$

$$\frac{z_1}{z_2 - z_1}\frac{\mathrm{d}\tilde{p}_n}{\mathrm{d}\zeta} + \tilde{p}_n = 0 \quad \text{at} \quad \zeta = 1, \tag{4.86}$$

$$\frac{\mathrm{d}^2\tilde{p}_n}{\mathrm{d}\zeta^2} = 0 \quad \text{at} \quad \zeta = 0, 1, \tag{4.87}$$

and the normalisation

$$\frac{z_1}{(z_2 - z_1)^2}\left(\sum_{n=1}^{\infty}\left.\frac{\mathrm{d}\tilde{p}_n}{\mathrm{d}\zeta}\right|_{\zeta=1}\right)^2 + \frac{1}{z_2 - z_1}\int_0^1\left(\sum_{n=1}^{\infty}\frac{\mathrm{d}\tilde{p}_n}{\mathrm{d}\zeta}\right)^2\mathrm{d}\zeta = 1. \tag{4.88}$$

	$\sigma_0 = s_1$	$\sigma_0 = s_2$	$\sigma_0 = s_3$	$\sigma_0 = s_4$
$\hat{Q}$	0.0298	0.0801	0.0873	0.0734
$\hat{\epsilon}$	0.0714	0.2652	0.5261	0.7581
$\tilde{Q}$	0.0245	0.0675	0.0726	0.0383
$\tilde{\epsilon}$	0.0722	0.2678	0.5321	0.7873

Table 4.1: Estimates of the numerical parameters Q and ϵ for the representative values of σ_0. The first pair $(\hat{Q}, \hat{\epsilon})$ are the estimates obtained by fitting the straight line (4.168) to the numerical data for $\log(q_n t_n)$. The second pair $(\tilde{Q}, \tilde{\epsilon})$ are improved estimates obtained by fitting the curve (4.170) to the numerical data for $\log(q_n t_n)$. Details of the fitting can be found in Appendix 4.B.

4.5.3 Behaviour of $q_n t_n$ for large n

In Chapter 3, we saw that $q_n t_n$ decays rapidly as n is increased. From (4.84), we see that the forcing for $\tilde{p}_1$ will be larger than $\tilde{p}_2$, and larger still than $\tilde{p}_3$, etc. Hence, we expect that $\tilde{p}_1$ will provide the dominant contribution to the global solution for the pressure, with each successive mode $\tilde{p}_i$ being smaller as the mode number i increases. In Appendix 4.B we study the numerical data obtained in Chapter 3 for $q_n t_n$.

4.5.4 Series solution for $\tilde{p}$ in the flexible section

Our analysis suggests the asymptotic behaviour

$$q_n t_n \sim Q\epsilon^{n-1} \qquad \text{as} \qquad n \to \infty \tag{4.89}$$

with $0 < \epsilon < 1$. Both Q and ϵ depend on the ellipticity parameter σ_0. They are estimated from the data for $n = 1, 2, \ldots 14$ (see Appendix 4.B), and the results are given in table (4.1).

Having found ϵ, we introduce Q_n such that

$$q_n t_n = Q_n \epsilon^{n-1}. \tag{4.90}$$

(Hence, $Q_n \to Q$ as $n \to \infty$). The Q_n are found to decrease monotonically with increasing n. We therefore consider a formal power series expansion in ϵ, assuming $q_n t_n = O(\epsilon^{n-1})$.

We expand ω and $\tilde{p}_n$ in powers of ϵ

$$\omega = \omega_0 + \epsilon\omega_1 + \epsilon^2\omega_2 + O(\epsilon^3), \tag{4.91}$$

$$\tilde{p}_n = \epsilon^{n-1}(p_{n0} + \epsilon p_{n1} + \epsilon^2 p_{n2} + O(\epsilon^3), \tag{4.92}$$

where the pre-factor ϵ^{n-1} present in (4.92) has been chosen after observing (4.84) together with (4.90). Substituting (4.91)–(4.92) into (4.84)–(4.87), we obtain

$$\begin{aligned}\frac{\mathrm{d}^4}{\mathrm{d}\zeta^4}(p_{n0} + \epsilon p_{n1}) + \frac{1}{\tilde{F}}(z_2 - z_1)^2 \left[M(\omega_0 + \epsilon\omega_1)^2 - \lambda_n\right] \frac{\mathrm{d}^2}{\mathrm{d}\zeta^2}(p_{n0} + \epsilon p_{n1}) \\ = \frac{1}{\tilde{F}}(\omega_0 + \epsilon\omega_1)^2 (z_2 - z_1)^4 Q_n(p_{10} + \epsilon p_{11} + \epsilon p_{20}) + O(\epsilon^2),\end{aligned} \tag{4.93}$$

subject to

$$\frac{\mathrm{d}}{\mathrm{d}\zeta}(p_{n0} + \epsilon p_{n1}) + O(\epsilon^2) = 0 \quad \text{at} \quad \zeta = 0, \tag{4.94}$$

$$\frac{z_1}{z_2 - z_1}\frac{\mathrm{d}}{\mathrm{d}\zeta}(p_{n0} + \epsilon p_{n1}) + p_{n0} + \epsilon p_{n1} + O(\epsilon^2) = 0 \quad \text{at} \quad \zeta = 1, \tag{4.95}$$

$$\frac{\mathrm{d}^2}{\mathrm{d}\zeta^2}(p_{n0} + \epsilon p_{n1}) + O(\epsilon^2) = 0 \quad \text{at} \quad \zeta = 0, 1. \tag{4.96}$$

Finally, the normalisation condition (4.88) becomes

$$\frac{z_1}{(z_2-z_1)^2}\left[\left(\frac{\mathrm{d}p_{10}}{\mathrm{d}\zeta}\right)^2+2\epsilon\frac{\mathrm{d}p_{10}}{\mathrm{d}\zeta}\left(\frac{\mathrm{d}p_{20}}{\mathrm{d}\zeta}+\frac{\mathrm{d}p_{11}}{\mathrm{d}\zeta}\right)\right]\Bigg|_{\zeta=1} + \frac{1}{z_2-z_1}\int_0^1\left(\frac{\mathrm{d}p_{10}}{\mathrm{d}\zeta}\right)^2+2\epsilon\frac{\mathrm{d}p_{10}}{\mathrm{d}\zeta}\left(\frac{\mathrm{d}p_{20}}{\mathrm{d}\zeta}+\frac{\mathrm{d}p_{11}}{\mathrm{d}\zeta}\right)\mathrm{d}\zeta+O(\epsilon^2)=1. \tag{4.97}$$

We now equate (4.93)–(4.97) at increasing powers of ϵ. Observing (4.93)–(4.96), the problem at $O(\epsilon^0)$ involves only the first azimuthal mode ($n=1$), and defines an eigenvalue problem for p_{10} and ω_0. At $O(\epsilon)$ only $n=1$ and $n=2$ will contribute towards the problem, which yields a problem for p_{20}, and a separate (coupled) problem for p_{11} and ω_1. The system for p_{20} is forced by p_{10} and ω_0, and the system for p_{11} is forced by p_{20}. A series solution can therefore be found by computing the relevant components iteratively, starting with the p_{10} problem. Writing $\hat{p}(z,t)=Re(\tilde{p}(z)\exp i\omega t)$ in (4.78) and using equations (4.83) and (4.92), the full axial mode for the pressure $\tilde{p}$ is then given by

$$\begin{aligned}\tilde{p}&=\sum_{n=1}^{\infty}\tilde{p}_n,\\ &=p_{10}+\epsilon(p_{11}+p_{20})+O(\epsilon^2).\end{aligned} \tag{4.98}$$

The series solution for the oscillation frequency is given by (4.91).

4.5.5 The $O(\epsilon^0)$ problem for ω_0 and p_{10}

Equating (4.93)–(4.97) at $O(\epsilon^0)$ with $n = 1$, we find that $p_{10}(\zeta)$ and ω_0 satisfy the following eigenvalue problem:

$$\frac{\mathrm{d}^4 p_{10}}{\mathrm{d}\zeta^4} + \frac{1}{\widetilde{F}}\left((M\omega_0^2 - \lambda_1)(z_2 - z_1)^2\right)\frac{\mathrm{d}^2 p_{10}}{\mathrm{d}\zeta^2} - \frac{1}{\widetilde{F}}Q_1\omega_0^2(z_2 - z_1)^4 p_{10} = 0, \quad (4.99)$$

subject to:

$$\frac{\mathrm{d}p_{10}}{\mathrm{d}\zeta} = 0 \quad \text{at} \quad \zeta = 0, \quad (4.100)$$

$$\frac{z_1}{z_2 - z_1}\frac{\mathrm{d}p_{10}}{\mathrm{d}\zeta} + p_{10} = 0 \quad \text{at} \quad \zeta = 1, \quad (4.101)$$

$$\frac{\mathrm{d}^2 p_{10}}{\mathrm{d}\zeta^2} = 0 \quad \text{at} \quad \zeta = 0, 1, \quad (4.102)$$

and the normalisation

$$\frac{z_1}{(z_2 - z_1)^2}\left(\frac{\mathrm{d}p_{10}}{\mathrm{d}\zeta}\right)^2\Big|_{\zeta=1} + \frac{1}{z_2 - z_1}\int_0^1 \left(\frac{\mathrm{d}p_{10}}{\mathrm{d}\zeta}\right)^2 \mathrm{d}\zeta = 1. \quad (4.103)$$

The eigenvalue problem (4.99)–(4.103) is of the same form as the problem derived by Walters et al. (2018) (and Whittaker et al. (2010c) for the case $M = 0$). However, it differs through the values of the numerical constants λ_1 and $Q_1 = q_1 t_1$. We proceed using the same solution method, although we omit some of the detailed calculations since they are covered comprehensively by Walters et al. (2018) and Whittaker et al. (2010c).

The general solution to (4.99) for p_{10} can be written as[2]

$$p_{10}(\zeta) = A\frac{\sinh(g\zeta)}{\sinh(g)} + B\frac{\sinh(g(1-\zeta))}{\sinh(g)} + C\cos(h\zeta) + D\sin(h\zeta), \quad (4.104)$$

where A, B, C and D are arbitrary constants, and g and h are real positive constants given by

$$g^2 = (z_2 - z_1)^2 \left[-\frac{(M\omega_0^2 - \lambda_1)}{2\tilde{F}} + \sqrt{\frac{(M\omega_0^2 - \lambda_1)^2}{4\tilde{F}^2} + \frac{1}{\tilde{F}} Q_1 \omega_0^2} \right], \quad (4.105)$$

and

$$h^2 = (z_2 - z_1)^2 \left[\frac{M\omega_0^2 - \lambda_1}{2\tilde{F}} + \sqrt{\frac{(M\omega_0^2 - \lambda_1)^2}{4\tilde{F}^2} + \frac{1}{\tilde{F}} Q_1 \omega_0^2} \right]. \quad (4.106)$$

Solution for ω_0

Substituting the general solution (4.104) into the boundary conditions (4.100)–(4.102) and seeking only non-trivial solutions, the following eigenvalue equation for ω_0 is obtained

$$\begin{aligned} z_1[2gh(1 - \cosh(g)\cos(h)) + (g^2 - h^2)\sinh(g)\sin(h)] \\ - (z_2 - z_1)\frac{g^2 + h^2}{gh}(g\sinh(g)\cos(h) + h\cosh(g)\sin(h)] = 0. \end{aligned} \quad (4.107)$$

In total there are three equations (4.105)–(4.107) relating g, h and ω_0. Following Walters et al. (2018), we take the difference and product of (4.105)–

[2]The factors of $1/\sinh(g)$ present in (4.104) have been introduced to overcome numerical difficulties that occur when finding solutions when $\tilde{F} \ll 1$.

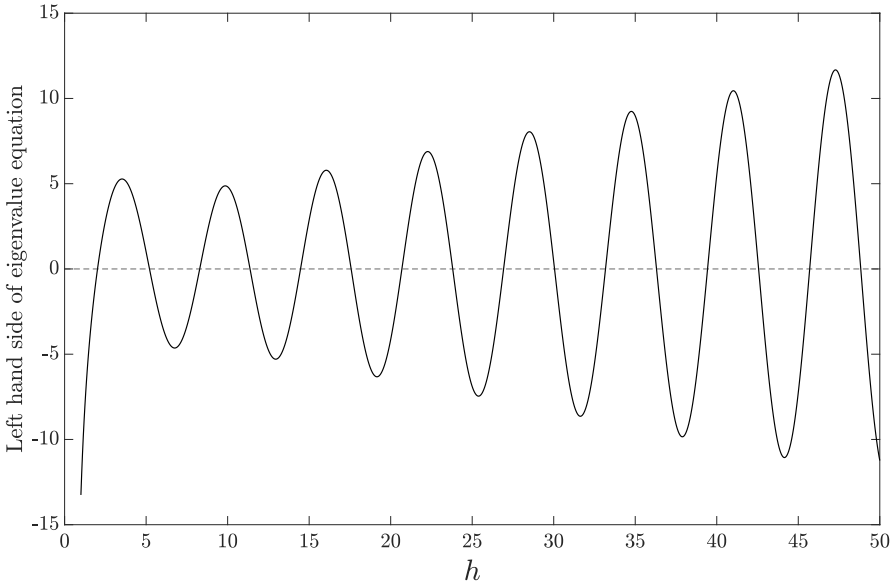

Figure 4.6: The left hand side of (4.107), plotted as a function of h after eliminating g using (4.109). The results indicate that there are countable many solutions for h, and hence g and ω.

(4.106) in turn, yielding

$$\omega_0^2 = \frac{\tilde{F} g^2 h^2}{Q_1 (z_2 - z_1)^4}, \tag{4.108}$$

and

$$g = \left[\frac{\frac{\lambda_1}{\tilde{F}} (z_2 - z_1)^2 + h^2}{1 + \frac{M h^2}{Q_1 (z_2 - z_1)^2}} \right]^{1/2}. \tag{4.109}$$

Observe that (4.109) allows for the elimination of g from (4.106). The resulting equation for h can then be solved numerically. Having obtained solutions for h, corresponding values of g and ω_0 can be recovered using (4.105) and (4.108) in turn.

Consistent with the results of Walters et al. (2018), we find countably many solutions (see figure 4.6) for h (and hence g and ω), which we shall

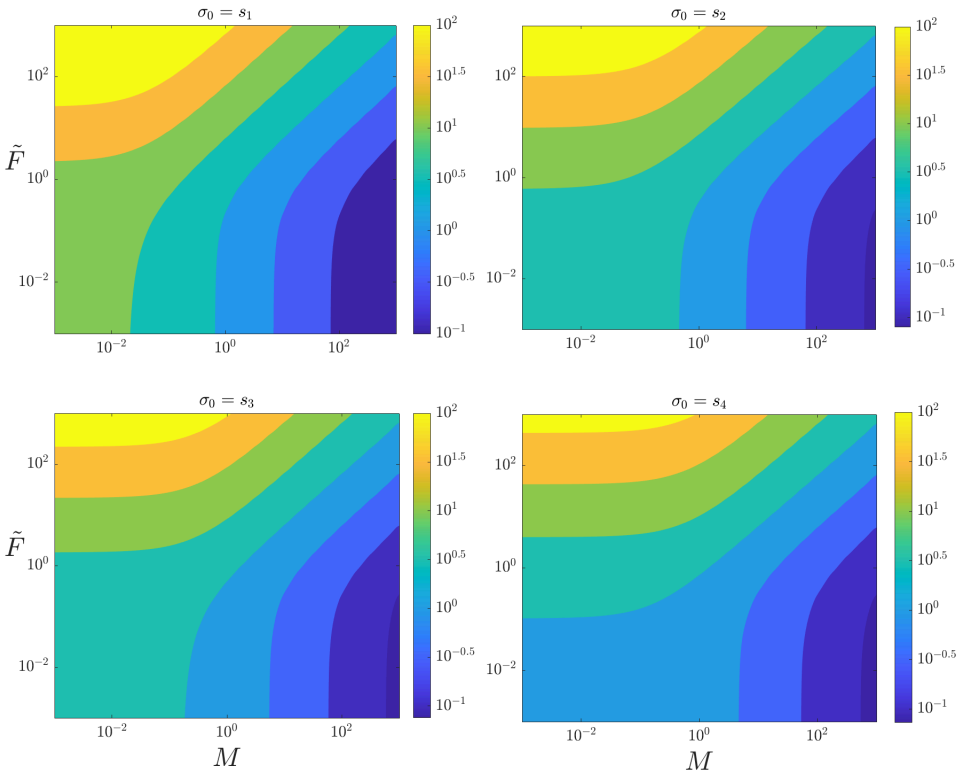

Figure 4.7: Values of $\omega_0^{(1)}$ plotted throughout $(M, \tilde{F})$ parameter space, for $\sigma_0 = s_1, s_2, s_3, s_4$. The values were calculated by substituting the numerical solutions for g and h into (4.108), with $z_1 = 0.1, z_2 = 0.9$. The values for $Q_1 = q_1 t_1$ were obtained from the numerical data for $q_n t_n$, which can be found in Chapter 3.

index with an oscillatory mode number j. We denote $\omega_0^{(1)}$ as the fundamental oscillation frequency.

In figure 4.7 we provide contour plots of the values for $\omega_0^{(1)}$. In general we find that the oscillation frequency increases with $\tilde{F}$, however decreases with the dimensionless mass M. As we vary σ_0, we find that tubes with an initially almost circular cross-section (larger σ_0) typically have larger natural eigenfrequencies than those with initially larger ellipticities, particularly for large $\tilde{F}$.

$\tilde{F}$	M	$\omega_0^{(1)}$	$\omega_0^{(2)}$	$\omega_0^{(3)}$	$\omega_0^{(4)}$	$\omega_0^{(5)}$
	0	6.119	19.104	33.881	51.012	70.921
	0.001	6.102	18.637	31.660	44.876	58.056
0.01	0.01	5.956	15.549	21.584	25.679	29.076
	0.1	4.908	7.697	8.528	9.239	9.999
	1	2.379	2.626	2.779	2.974	3.199
	0	7.010	25.73	54.591	94.925	147.457
	0.001	6.989	25.176	50.901	83.313	120.488
0.1	0.01	6.811	20.854	34.449	47.566	60.397
	0.1	5.545	10.224	13.620	17.220	20.852
	1	2.629	3.504	4.474	5.559	6.689
	0	11.865	59.792	145.235	269.936	434.357
	0.001	11.828	58.238	135.356	236.860	354.879
1	0.01	11.509	48.152	91.528	135.323	178.012
	0.1	9.284	23.641	36.295	49.092	61.520
	1	4.357	8.145	11.961	15.859	19.745

Table 4.2: Values for the oscillation frequencies $\omega_0^{(j)}$, tabulated for $j = 1, 2, \cdots, 5$ using $\sigma_0 = 0.6, z_1 = 0.1, z_2 = 0.9$, and a range of $(M, \tilde{F})$. To obtain the values we substituted the numerical solutions for g and h, as well the numerical data for Q_1 into the formula (4.108). he values for $Q_1 = q_1 t_1$ were obtained from the numerical data for $q_n t_n$, which can be found in Chapter 3.

For a comparison with Walters et al. (2018), in table 4.2 we tabulate the first five modes of the leading-order oscillation frequency $\omega_0^{(j)}$ for different values of M and $\tilde{F}$, with $\sigma_0 = 0.6$. We find that our results are in good agreement, with typical absolute errors of $O(10^{-2})$.

Solution for p_{10}

Substituting the general solution (4.104) into the boundary conditions (4.100) and (4.102), we can derive analytical expressions for the constants A, B and C in terms of g, h and the final constant, D. The final boundary condition (4.101) is satisfied automatically due to ω_0 being chosen to satisfy the

eigenvalue equation (4.107). We find that

$$A = \left[-\frac{h\left(\cos(h)\sinh(g)\,g + \sin(h)\,h\cosh(g)\right)}{g^2\left(\cos(h) - \cosh(g)\right)} \right] D, \tag{4.110}$$

$$B = \left[-\frac{h\left(\sin(h)\,h + \sinh(g)\,g\right)}{g^2\left(\cos(h) - \cosh(g)\right)} \right] D, \tag{4.111}$$

$$C = \left[\frac{\sin(h)\,h + \sinh(g)\,g}{h\left(\cos(h) - \cosh(g)\right)} \right] D, \tag{4.112}$$

where the parameters g and h are given by (4.105) and (4.106) respectively. The final constant, D, is set using the normalisation condition (4.103). In principle, an analytical expression can be obtained for D in terms of g, h and ω_0. However, this expression is prohibitively complex, so we choose not to present it here. We define $p_{10}^{(j)}$ as being the solution of (4.99)–(4.103) corresponding to the jth oscillatory mode.

We plot our solutions for $p_{10}^{(j)}$ in figure 4.8. In agreement with the results of Whittaker et al. (2010c) and Walters et al. (2018), for the parameters considered here we find that the number of extrema present in the solution for $p_{10}^{(j)}$ is equal to the mode number, j. For $j = 1$, increasing the inertia parameter M from 0 to 1 has only a small effect on $p_{10}^{(j)}$. However, for $j \geq 2$ there are noticeable changes in the curves with $p_{10}^{(j)}$ becoming more positive for odd j and more negative for even j.

4.5.6 The $O(\epsilon)$ problem for p_{20}

For every oscillatory mode j, there is an associated solution of the full coupled problem. Whittaker et al. (2010c) deduced that unsteady perturbations to the steady problem oscillating with a fundamental ($j = 1$) oscillation frequency were most unstable. Since our interests lie in predicting the onset of

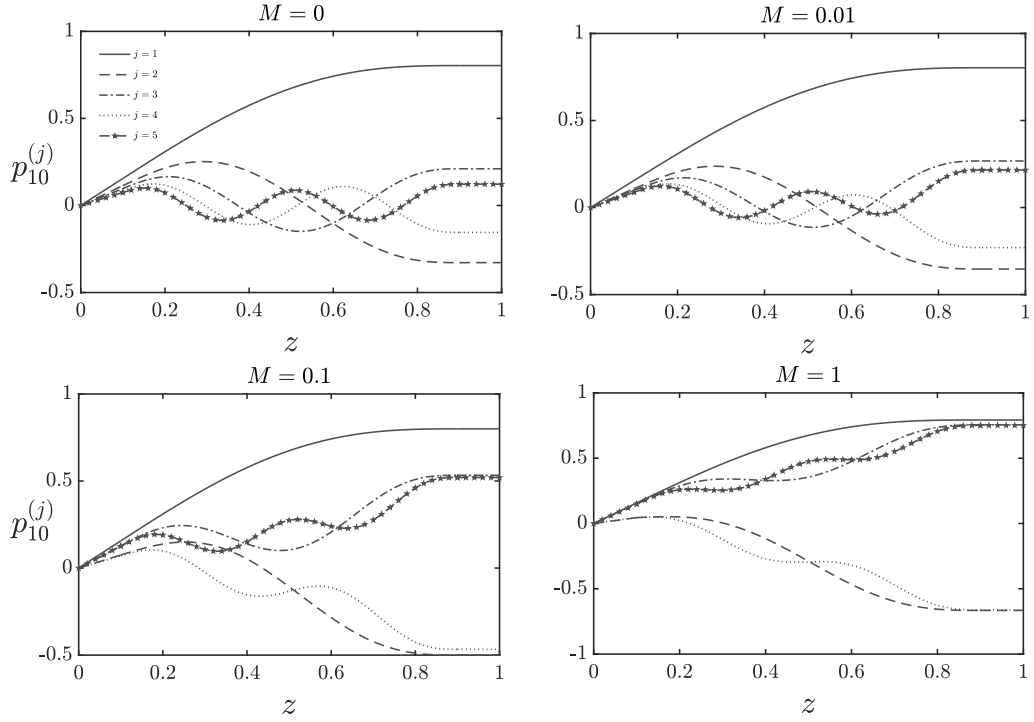

Figure 4.8: Solutions for $p_{10}^{(j)}(z)$ with $z_1 = 0.1, z_2 = 0.9, \sigma_0 = 0.6, \tilde{F} = 1$, and different values of the inertia parameter M and mode number j. The solutions were obtained by substituting the numerical data for g and h into the analytical solution (4.104) with (4.110)–(4.112) for $p_{10}^{(j)}$.

self-excited oscillations, for the remainder of this chapter we present normal-mode solutions corresponding to the fundamental ($j = 1$) mode. We proceed by dropping the superscript (j) notation with $j = 1$ assumed.

The $O(\epsilon)$ contributions to (4.93)–(4.96) with $n = 2$ yield the following system for p_{20}:

$$\frac{\mathrm{d}^4 p_{20}}{\mathrm{d}\zeta^4} - \psi^2 \frac{\mathrm{d}^2 p_{20}}{\mathrm{d}\zeta^2} = \frac{1}{\tilde{F}} \omega_0^2 Q_2 (z_2 - z_1)^4 p_{10}(\zeta), \tag{4.113}$$

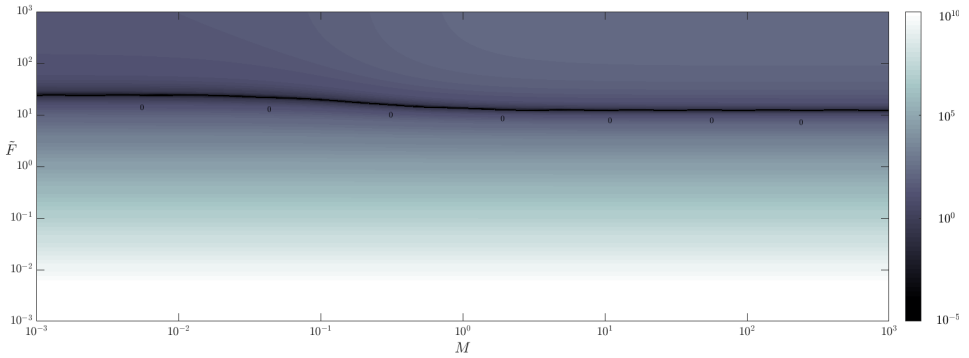

Figure 4.9: The values $\log|\psi^2 - g^2|$ plotted throughout $(M, \tilde{F})$ parameter space, for $\sigma_0 = s_2$. The values were calculated using the expression (4.117) for ψ^2 and the numerical solutions (4.105) and (4.108) for g and ω_0 respectively. We have chosen not to present results for varying σ_0 since this did not amount to an observable change in the plots.

subject to:

$$\frac{\mathrm{d}p_{20}}{\mathrm{d}\zeta} = 0 \quad \text{at} \quad \zeta = 0, \tag{4.114}$$

$$\frac{z_1}{z_2 - z_1}\frac{\mathrm{d}p_{20}}{\mathrm{d}\zeta} + p_{20} = 0 \quad \text{at} \quad \zeta = 1, \tag{4.115}$$

$$\frac{\mathrm{d}^2 p_{20}}{\mathrm{d}\zeta^2} = 0 \quad \text{at} \quad \zeta = 0, 1, \tag{4.116}$$

where

$$\psi^2 = \frac{1}{\tilde{F}}\left(\lambda_2 - M\omega_0^2\right)\left(z_2 - z_1\right)^2. \tag{4.117}$$

We observe that the governing equation (4.113) for p_{20} is a linear ordinary differential equation with constant coefficients. The forcing on the right hand side is known, since $p_{10}(\zeta)$ has already been found.

Solution for p_{20}

The system (4.113)–(4.116) can be solved for p_{20} using the standard approach of summing a complimentary function and particular integral.

In order to construct the particular intefgral for p_{20}, we must first determine whether the system is resonant, i.e whether the forcing from p_{10} coincides with the complementary function for the homogeneous problem. Given the form (4.8) of p_{10} and the sign of ψ^2, such resonance will occur precisely when $g^2 = \psi^2$. Figure 4.9 shows a contour plot of $\log|\psi^2 - g^2|$ in $(M, \tilde{F})$ parameter space. The plot demonstrates that there is a single line in the parameter space on which (4.113)–(4.116) becomes resonant. For this special case, a general solution can be obtained by assuming that the particular integral for p_{20}, takes the form

$$F_1\zeta\frac{\sinh(g\zeta)}{\sinh(g)} + F_2\zeta\frac{\sinh(g(1-\zeta))}{\sinh(g)} + F_3\cos(h\zeta) + F_4\sin(h\zeta), \tag{4.118}$$

where F_1, F_2, F_3 and F_4 are constants.

For convenience, we proceed under the assumption that $\psi^2 \neq g^2$. In this case, we find that the general solution of (4.113)–(4.116) is given by

$$\begin{aligned} p_{20}(\zeta) = \hat{A} + \hat{B}\zeta + \hat{C}\frac{\sinh(\psi\zeta)}{\sinh(\psi)} + \hat{D}\frac{\sinh(\psi(1-\zeta))}{\sinh(\psi)} \\ + C_1\frac{\sinh(g\zeta)}{\sinh(g)} + C_2\frac{\sinh(g(1-\zeta))}{\sinh(g)} + C_3\cos(h\zeta) + C_4\sin(h\zeta), \end{aligned} \tag{4.119}$$

where $\hat{A}, \hat{B}, \hat{C}, \hat{D}$ are arbitrary constants in the complementary function, and

the constants in the particular integral are given by:

$$C_1 = -\frac{(z_2 - z_1)^4 \, h \, (\sin(h)\, h + \sinh(g)\, g)\, D Q_2 \omega_0^2}{g^4 \, (\cos(h) - \cosh(g)) \, (g^2 - \psi^2) \, \tilde{F}}, \tag{4.120}$$

$$C_2 = -\frac{\omega_0^2 Q_2 \, (z_2 - z_1)^4 \, D h \, (2e^{2g} \cos(h) - e^{3g} - 2\cos(h) + e^{-g})}{2g^3 \tilde{F} \, (e^{2g} - 1) \, (\cos(h) - \cosh(g)) \, (g^2 - \psi^2)}, \tag{4.121}$$

$$C_3 = \frac{(z_2 - z_1)^4 \, C \omega_0^2 Q_2 D}{\tilde{F} h^2 \, (h^2 + \psi^2)}, \tag{4.122}$$

$$C_4 = \frac{\omega_0^2 Q_2 D \, (z_2 - z_1)^4}{\tilde{F} h^2 \, (h^2 + \psi^2)} \tag{4.123}$$

and D is the (known) normalisation constant in p_{10}.

To determine $\hat{A}, \hat{B}, \hat{C}$ and $\hat{D}$ we substitute (4.119)–(4.123) into the four boundary conditions (4.114)–(4.116) and solve the resulting linear system using `Maple`. Analytical expressions were obtained for $\hat{A}, \hat{B}, \hat{C}$ and $\hat{D}$ in terms of $z_1, z_2, M, \tilde{F}$ and the numerically determined constants h, g, ω_0, Q_1 and Q_2. However, due to the length of the symbolic expressions, we choose to omit the expressions here.

In figure 4.10 we plot solutions for ϵp_{20}, which is independent of ϵ, using (4.119). Unlike the solutions for p_{10}, we find that changes in the inertia coefficient result in an observable difference in the corresponding profiles for p_{20}. It can be observed that $M = 0$ results in a solution for p_{20} with maximal amplitude, with the amplitude of the solution then monotonically decreasing as M is increased. As we vary the ellipticity parameter, our results demonstrate that smaller σ_0 results in a larger amplitude of the solution.

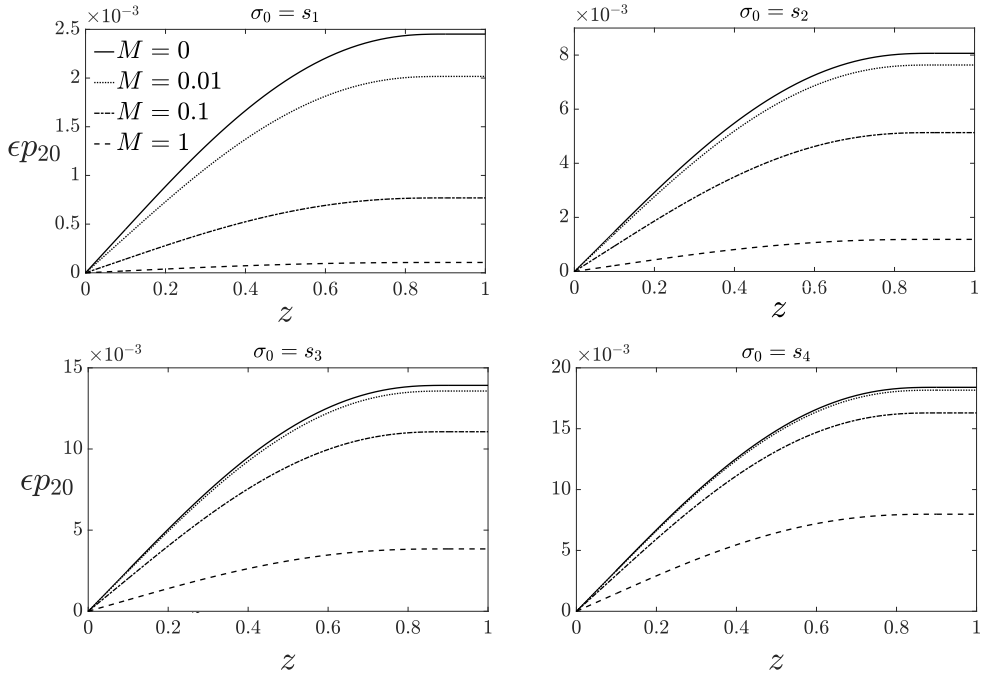

Figure 4.10: Solutions for ϵp_{20}, plotted for $M = 0, 0.01, 0.1, 1$ with $\tilde{F} = 1$, and $\sigma_0 = s_1, s_2, s_3, s_4$ with $z_1 = 0.1$ and $z_2 = 0.9$. The solutions were calculated using the expression (4.119). The coefficients present in the solutions were determined analytically in terms of the numerical constants h, g and ω within `Maple`. The second panel corresponds to $\sigma_0 = 0.6$ and allows for a comparison with Walters et al. (2018) and Whittaker et al. (2010c). The values for $\epsilon Q_2 = q_2 t_2$ were obtained from the numerical data for $q_n t_n$, which can be found in Chapter 3

4.5.7 The $O(\epsilon)$ problem for p_{11} and ω_1

Considering the $O(\epsilon)$ terms in (4.93)–(4.97) with $n = 1$, we derive the following problem for p_{11}:

$$\mathscr{L}(p_{11}) = S, \tag{4.124}$$

where

$$\mathscr{L}(y) = \frac{\mathrm{d}^4 y}{\mathrm{d}\zeta^4} + P\frac{\mathrm{d}^2 y}{\mathrm{d}\zeta^2} - Ry, \tag{4.125}$$

and

$$P \equiv \frac{1}{\tilde{F}}\left(M\omega_0^2 - \lambda_1\right)(z_2 - z_1)^2\,, \tag{4.126}$$

$$R \equiv \frac{1}{\tilde{F}}Q_1\omega_0^2(z_2 - z_1)^4 > 0, \tag{4.127}$$

$$S \equiv \frac{Q_1\omega_0}{\tilde{F}}(z_2 - z_1)^4(\omega_0 p_{20} + 2\omega_1 p_{10}) - \frac{1}{\tilde{F}}\left(2\omega_0\omega_1 M\right)(z_2 - z_1)^2\,\frac{\mathrm{d}^2 p_{10}}{\mathrm{d}\zeta^2}, \tag{4.128}$$

subject to:

$$\frac{\mathrm{d}p_{11}}{\mathrm{d}\zeta} = 0 \quad \text{at} \quad \zeta = 0, \tag{4.129}$$

$$\frac{z_1}{z_2 - z_1}\frac{\mathrm{d}p_{11}}{\mathrm{d}\zeta} + p_{11} = 0 \quad \text{at} \quad \zeta = 1, \tag{4.130}$$

$$\frac{\mathrm{d}^2 p_{11}}{\mathrm{d}\zeta^2} = 0 \quad \text{at} \quad \zeta = 0, 1. \tag{4.131}$$

At $O(\epsilon)$, the normalisation condition (4.97) becomes

$$\frac{z_1}{z_2 - z_1}p'_{10}(1)\left(p'_{20}(1) + p'_{11}(1)\right) + \int_0^1 \frac{\mathrm{d}p_{10}}{\mathrm{d}\zeta}\left(\frac{\mathrm{d}p_{20}}{\mathrm{d}\zeta} + \frac{\mathrm{d}p_{11}}{\mathrm{d}\zeta}\right)\mathrm{d}\zeta = 0. \tag{4.132}$$

The operator $\mathscr{L}$ here is the same as in equation (4.99), where ω_0 is set so that the associated homogeneous problem permits non-trivial solutions. By the *Fredholm Alternative* Kress et al. (1989), this means that a solution of (4.124)–(4.132) will exist only when the solutions of the adjoint of the associated homogeneous problem to (4.124)–(4.131) are orthogonal to the inhomogeneous part of (4.124). This condition is known as a secularity condition. In this case, it sets the oscillation frequency correction, ω_1.

The adjoint problem

The associated homogeneous problem of (4.124)–(4.132) is then given by

$$\mathscr{L}(p_{11}) = 0, \tag{4.133}$$

subject to the boundary conditions (4.129)–(4.132).

We define the inner product

$$\langle u, v \rangle = \int_0^1 uv \, \mathrm{d}\zeta. \tag{4.134}$$

Using integration by parts three times and applying the boundary conditions (4.129)–(4.131) on p_{11}, we can show that

$$\begin{aligned}\langle \mathscr{L} p_{11}, v \rangle = \langle p_{11}, \mathscr{L} v \rangle + \left[\frac{\mathrm{d}^3 p_{11}}{\mathrm{d}\zeta^3} v \right]_0^1 + \left(P \frac{\mathrm{d}^2 v}{\mathrm{d}\zeta^2} + \frac{\mathrm{d}^3 v}{\mathrm{d}\zeta^3} \right) p_{11} \Big|_{\zeta=0} \\ + \left[\frac{\mathrm{d}^2 v}{\mathrm{d}\zeta^2} + \frac{z_1}{z_2 - z_1} \left(P \frac{\mathrm{d}v}{\mathrm{d}\zeta} + \frac{\mathrm{d}^3 v}{\mathrm{d}\zeta^3} \right) \right] \frac{\mathrm{d}p_{11}}{\mathrm{d}\zeta} \Big|_{\zeta=1},\end{aligned} \tag{4.135}$$

for some sufficiently differentiable function v. In order to derive the adjoint problem, we require the boundary terms present in (4.135) to vanish. This requirement sets the adjoint boundary conditions.

We find that the adjoint problem for v is then given by

$$\mathscr{L}(v) = 0, \tag{4.136}$$

subject to:

$$v = 0 \quad \text{at} \quad \zeta = 0, 1, \tag{4.137}$$

$$P\frac{\mathrm{d}v}{\mathrm{d}\zeta} + \frac{\mathrm{d}^3 v}{\mathrm{d}\zeta^3} = 0 \quad \text{at} \quad \zeta = 0, \tag{4.138}$$

$$\frac{\mathrm{d}^2 v}{\mathrm{d}\zeta^2} + \frac{z_1}{z_2 - z_1}\left(P\frac{\mathrm{d}v}{\mathrm{d}\zeta} + \frac{\mathrm{d}^3 v}{\mathrm{d}\zeta^3}\right) = 0 \quad \text{at} \quad \zeta = 1. \tag{4.139}$$

The solution for v is sought in the same way as for p_{10} (see §4.5.5) and so we omit the detailed calculations here. We find that the solution is given by

$$v(\zeta) = A^\dagger \frac{\sinh(g\zeta)}{\sinh(g)} + B^\dagger \frac{\sinh(g(1-\zeta))}{\sinh(g)} + C^\dagger \cos(h\zeta) + D^\dagger \sin(h\zeta), \tag{4.140}$$

where:

$$A^\dagger = \left(\frac{g\cosh(g)\sin(h)\,(P+g^2) + h\sinh(g)\cos(h)\,(P-h^2)}{h\sinh(g)\,(P-h^2) + g^3\sin(h)}\right) B^\dagger, \tag{4.141}$$

$$C^\dagger = -B^\dagger, \tag{4.142}$$

$$D^\dagger = \left(\frac{h\sinh(g)\cot(h)\,(h^2-P) - g\cosh(g)\,(P+g^2)}{h\sinh(g)\,(P-h^2) + g^3\sin(h)} - \cot(h)\right) B^\dagger. \tag{4.143}$$

The final constant $B^\dagger$ sets the amplitude of the solution. This is arbitrary here, so we can simply choose $B^\dagger = 1$.

Expression for ω_1

Taking the inner product of the inhomogeneous part of (4.124) with v, equating the result with zero and arranging for ω_1, we find that

$$\omega_1 = \frac{(z_2 - z_1)^2 \omega_0 Q_1 \langle p_{20}, v \rangle}{2\left(M \left\langle \frac{\mathrm{d}^2 p_{10}}{\mathrm{d}\zeta^2}, v \right\rangle - Q_1 (z_2 - z_1)^2 \langle p_{10}, v \rangle\right)}. \tag{4.144}$$

Equation (4.144) is an expression for the oscillation frequency correction, ω_1, which ensures that a solution of (4.124)–(4.131) exists.

In figure 4.11 we plot the solutions (4.144) for $\epsilon\omega_1$. The plots maintain a similar profile to the leading-order component of the oscillation frequency, ω_0, but with significantly smaller magnitudes observed throughout parameter space. Much like in figure 4.7, an increase in M results in a lower frequency, however the solutions for the correction $|\epsilon\omega_1|$ decay much faster and to smaller values. Examining the effect of different initial ellipticities, we again retain the feature observed in figure 4.7, where we see an increase in the frequency with a decrease in σ_0. In table 4.3 we tabulate our results for a range of values of M, $\tilde{F}$ and σ_0.

Solution for p_{11}

Recall that p_{11} is the solution of $\mathscr{L}(p_{11}) = S$ as defined in (4.124)–(4.128) subject to the boundary conditions (4.129)–(4.131) and normalisation (4.132). Note that $\mathscr{L}$ with these conditions is singular (i.e., permits non-trivial solutions to the homogeneous problem) due to the choice of ω_0 and that S is in the image of $\mathscr{L}$ due to the choice of ω_1.

Since $\mathscr{L}(p_{10}) = 0$ and p_{10} satisfies the boundary conditions (4.129)–

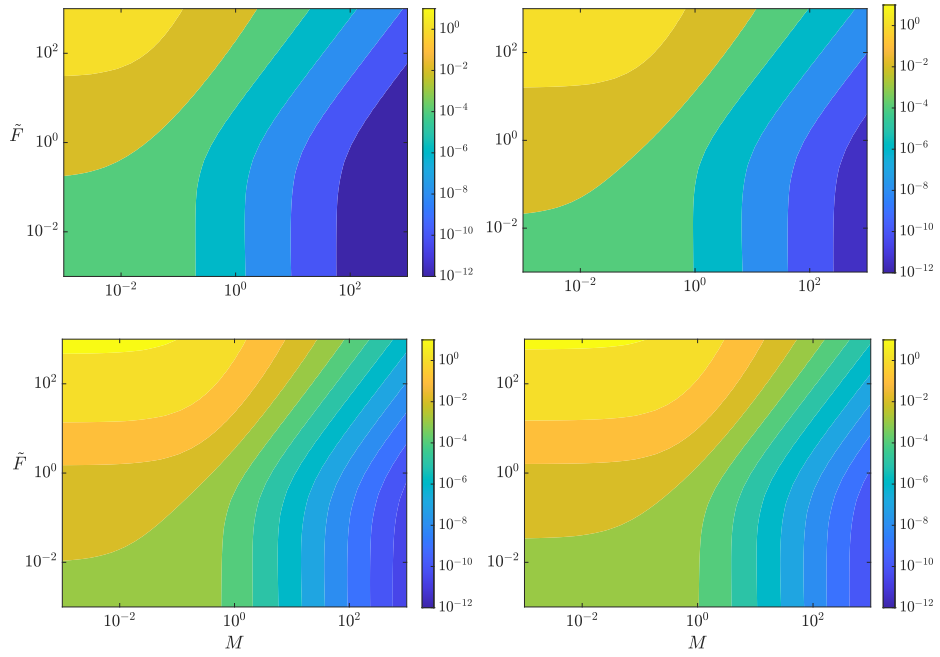

Figure 4.11: The values $\epsilon\omega_1$, plotted throughout $(M, \tilde{F})$ parameter space, for $\sigma_0 = s_1, s_2, s_3, s_4$. The values were calculated using the expression (4.144) with $z_1 = 0.1, z_2 = 0.9$ and the values for Q_1 were obtained from the numerical data for $q_n t_n$, which can be found in Chapter 3.

(4.131), we can write the solution for p_{11} as

$$p_{11}(\zeta) = \alpha p_{10}(\zeta) + p^\star(\zeta), \tag{4.145}$$

where $p^\star$ is a particular solution, of $\mathscr{L}(p_{11}) = S$ subject to (4.129)–(4.131), and α is chosen to ensure that the normalisation condition (4.132) is satisfied.

Obtaining a solution for $p^\star$ is complicated due to the singular nature of the system, and the fact that ω_0 and ω_1 have been determined numerically. The numerical error in ω_0 means that, in practice, the system is not quite singular. The numerical error in ω_1 means that the right hand side S is not quite in the true image of $\mathscr{L}$. These issues combine to give significant errors

	$\tilde{F}\backslash M$	0	0.1	1	10
$\sigma_0 = s_1$	0.1	-0.00863	-0.000441	-2.879×10^{-6}	-9.836×10^{-9}
	1	-0.0345	-0.00169	-1.139×10^{-5}	-3.934×10^{-8}
	10	-0.389	-0.0254	-0.000199	-7.021×10^{-7}
	100	-2.349	-0.283	-0.004584	-1.983×10^{-5}
$\sigma_0 = s_2$	0.1	-0.01367	-0.00427	-9.957×10^{-5}	-4.215×10^{-7}
	1	-0.0578	-0.0176	-0.000411	-1.786×10^{-6}
	10	-0.656	-0.231	-0.00694	-3.267×10^{-5}
	100	-3.872	-1.716	-0.108	-0.000861
$\sigma_0 = s_3$	0.1	-0.0148	-0.00814	-0.000530	-3.092×10^{-6}
	1	-0.0666	-0.0361	-0.00233	-1.403×10^{-5}
	10	-0.756	-0.447	-0.0374	-0.000263
	100	-4.306	-2.846	-0.417	-0.00617
$\sigma_0 = s_4$	0.1	-0.0131	-0.00951	-0.00148	-1.404×10^{-5}
	1	-0.0619	-0.0447	-0.00685	-6.721×10^{-5}
	10	-0.697	-0.529	-0.101	-0.00126
	100	-3.829	-3.075	-0.853	-0.025

Table 4.3: The values $\epsilon\omega_1$, tabulated for a variety of $M, \tilde{F}$ and σ_0. The values were obtained by substituting the solutions (4.108), (4.104) and (4.119) for ω_0, p_{10} and p_{20} into the analytical expression (4.144) for ω_1, with $z_1 = 0.1$ and $z_2 = 0.9$. The values for $Q_1 = q_1 t_1$ were obtained from the numerical data for $q_n t_n$, which can be found in Chapter 3.

in the solution for $p^\star$ obtained by solving this system.

In order to avoid these difficulties, we can instead consider an equivalent non-singular and well-posed problem for $p^\star$. First, the singular nature of the problem is removed by removing the mixed boundary condition (4.130). Since S is in the image of $\mathscr{L}$, the solution obtained for $p^\star$ will still satisfy this final boundary condition. Secondly, we ensure a well-posed problem for $p^\star$ by adding a new homogeneous boundary condition at $\zeta = 0$, which is not satisfied by p_{10}. The revised problem for $p^\star$ is thus:

$$\mathscr{L}(p^\star) = \frac{1}{\tilde{F}} Q_1 \omega_0 (z_2 - z_1)^4 (\omega_0 p_{20} + 2\omega_1 p_{10}) - \frac{1}{\tilde{F}} \left(2\omega_0 \omega_1 M\right) (z_2 - z_1)^2 \frac{\mathrm{d}^2 p_{10}}{\mathrm{d}\zeta^2}, \tag{4.146}$$

subject to:

$$p^\star = 0 \qquad \text{at} \qquad \zeta = 0, \tag{4.147}$$

$$\frac{\mathrm{d}p^\star}{\mathrm{d}\zeta} = 0 \qquad \text{at} \qquad \zeta = 0, \tag{4.148}$$

$$\frac{\mathrm{d}^2p^\star}{\mathrm{d}\zeta^2} = 0 \qquad \text{at} \qquad \zeta = 0, 1. \tag{4.149}$$

The formal solution to (4.146)–(4.149) still satisfies the original problem for $p^\star$, however, the practical solution is now much less sensitive to the small numerical errors in ω_0 and ω_1.

The system (4.146)–(4.149) is solved analytically by writing the general solution for $p^\star$ in the form

$$\begin{aligned} p^\star(\zeta) = A^\star\frac{\sinh(g\zeta)}{\sinh(g)} + B^\star\frac{\sinh(g(1-\zeta))}{\sinh(g)} + C^\star\cos(h\zeta) + D^\star\sin(h\zeta) \\ + C_1^\star + C_2^\star\zeta + C_3^\star\frac{\sinh(\psi\zeta)}{\sinh(\psi)} + C_4^\star\frac{\sinh(\psi(1-\zeta))}{\sinh(\psi)} + C_5^\star\frac{\zeta\sinh(g\zeta)}{\sinh(g)} \\ + C_6^\star\frac{\zeta\sinh(g(1-\zeta))}{\sinh(g)} + C_7^\star\zeta\cos(h\zeta) + C_8^\star\zeta\sin(h\zeta), \end{aligned} \tag{4.150}$$

where $A^\star, B^\star, C^\star, D^\star$ are arbitrary constants in the complimentary function and $C_1^\star, C_2^\star, \ldots C_8^\star$ are constants present in the particular integral. On substituting the particular integral into the governing equation (4.146) and using `Maple` to equate coefficients, we obtain analytical expressions for the constants $C_1^\star, C_2^\star, \ldots C_8^\star$ in terms of $z_1, z_2, M, \tilde{F}$ and the numerically determined constants h, g, ω_0, Q_1 and Q_2.

With the particular integral known, we can apply the boundary conditions (4.147)–(4.149) to the solution (4.150). Explicit expressions for the constants $A^\star, B^\star, C^\star$ and $D^\star$ can then be obtained using in terms of $z_1, z_2, M, \tilde{F}$ and

the numerically determined constants h, g, ω_0, Q_1 and Q_2 using `Maple`.

Having determined $p^\star$ uniquely, we use (4.150), together with the normalisation (4.97) at $O(\epsilon)$ to fix the constant, α. We find that α is given by

$$\alpha = \frac{1}{z_1 - z_2}\int_0^1 \frac{\mathrm{d}p_{10}}{\mathrm{d}\zeta}\left(\frac{\mathrm{d}p_{20}}{\mathrm{d}\zeta} + \frac{\mathrm{d}p^\star}{\mathrm{d}\zeta}\right)\mathrm{d}\zeta - \frac{z_1}{(z_2 - z_1)^2}\left[\frac{\mathrm{d}p_{10}}{\mathrm{d}\zeta}\left(\frac{\mathrm{d}p_{20}}{\mathrm{d}\zeta} + \frac{\mathrm{d}p_{11}}{\mathrm{d}\zeta}\right)\right]\Bigg|_{\zeta=1}. \tag{4.151}$$

We choose not to present the full analytical solution for p_{11} due to the expressions for the coefficients being prohibitively complex.

Solutions for ϵp_{11} are plotted in figure 4.12. The features of the plots are similar to those observed in figure 4.10. We find that changes in the inertia coefficient amount to an observable difference in the profiles for ϵp_{11}. The solution with maximal amplitude correspond to $M = 0$. In figure 4.13 we plot $\epsilon(p_{20} + p_{11})$ against z for $\sigma_0 = s_1, s_2, s_3, s_4$, which is the full $O(\epsilon)$ component of the expansion (4.98) for $\tilde{p}$. The plots demonstrate that varying both the inertia coefficient and ellipticity parameter has significant impact on the amplitude of the correction.

4.5.8 Truncation error estimates

With solutions for $p_{10}, p_{20}, p_{11}, \omega_0$ and ω_1 known for general σ_0, M and $\tilde{F}$, we can now investigate the error incurred by truncating the series expansions

$$\tilde{p}(z) = p_{10} + \epsilon\,(p_{11} + p_{20}) + O(\epsilon^2), \tag{4.152}$$

$$\omega = \omega_0 + \epsilon\omega_1 + O(\epsilon^2), \tag{4.153}$$

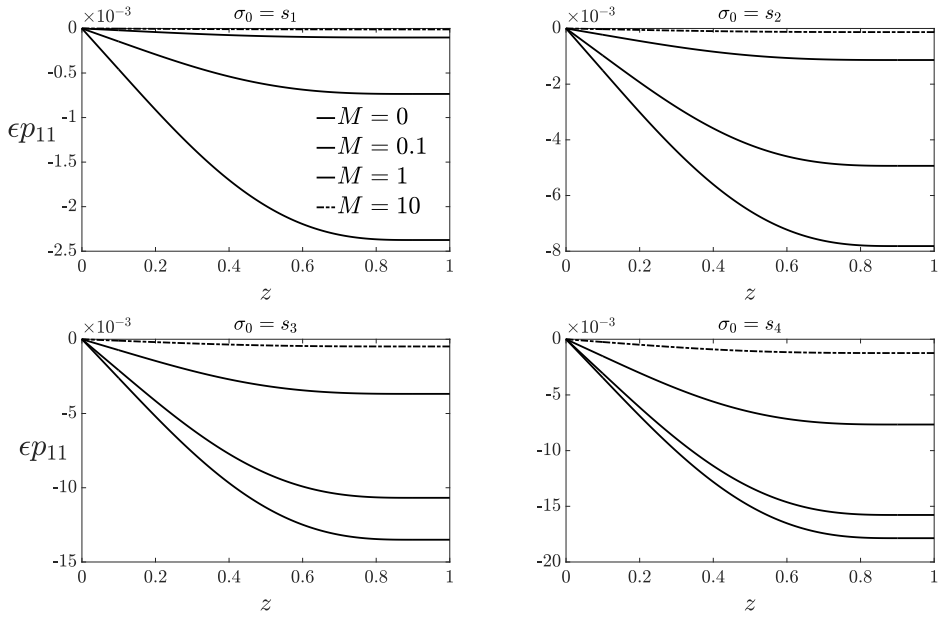

Figure 4.12: Solutions for ϵp_{11}, plotted for $M = 0, 0.1, 1, 10$, $\tilde{F} = 1$, $z_1 = 0.1, z_2 = 0.9$ and $\sigma_0 = s_1, s_2, s_3, s_4$. The plots were obtained using the analytical expressions (4.145) and (4.150), with analytical solutions for the coeffients determined using `Maple`. The amplitude of the solutions is set via the normalisation α, which is given explicitly by (4.151).

after $O(\epsilon^0)$. In figures 4.14 and 4.15 we plot the values $|\epsilon\omega_1/\omega_0|$ in $(M, \tilde{F})$ and $(\tilde{F}, \sigma_0)$ parameter space respectively, in order to gain an understanding of the errors incurred by truncating the expansion (4.153) for the oscillation frequency after $O(\epsilon^0)$. The results show that changes in $M, \tilde{F}$ and σ_0 have a significant impact on the magnitude of the relative error.

Figure 4.14 shows that an increase in M results in a decrease in the relative error, whilst increases in $\tilde{F}$ amount to an increase in the relative error. Examining variations in σ_0 in figure 4.15, we see that for fixed M, the error decreases monotonically with increasing σ_0 and/or decreasing $\tilde{F}$. As $\sigma_0 \to \infty$ (i.e., as the tube's initial cross-section becomes circular) the relative error approaches zero. In the large and small $\tilde{F}$ limits, we observe that the

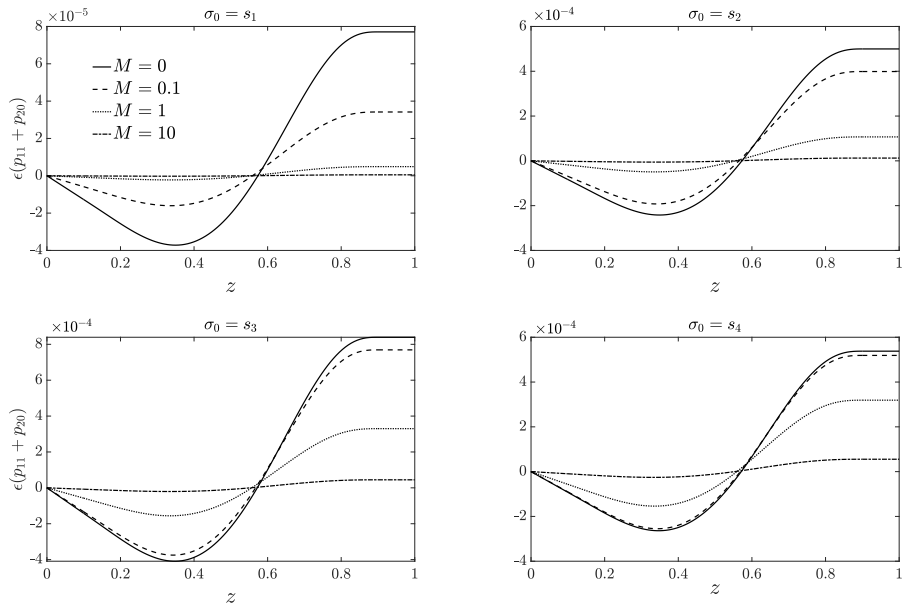

Figure 4.13: Solutions for $\epsilon(p_{20} + p_{11})$, plotted for $M = 0, 0.1, 1, 10$, $\tilde{F} = 1$, $z_1 = 0.1, z_2 = 0.9$ and $\sigma_0 = s_1, s_4$. The solution for p_{20} was obtained using (4.119)–(4.123), and for p_{11} we use (4.145) together with (4.150). Each of the constants involved are known in terms of $z_1, z_2, M, \tilde{F}$ and the numerically determined constants h, g, ω_0, Q_1 and Q_2.

relative error becomes independent of $\tilde{F}$.

In figure 4.16 we plot the values $\epsilon\left(p_{11} + p_{20}\right)/p_{10}$, evaluated at $z = 0.7$, throughout $(M, \tilde{F})$ parameter space. The results give an understanding of the error incurred by truncating the expansion (4.152) for $\tilde{p}$ after $O(\epsilon^0)$. Much like for the frequency, our results show that larger values of the inertia coefficient, M, result in a smaller relative error. We also observe that in this limit the error becomes independent of $\tilde{F}$, whilst for $M \lesssim O(1)$, we observe that the error becomes independent of M. In agreement with Chapter 3, we find that smaller values of σ_0, which correspond to more non-circular initial cross-sectional shapes, result in larger magnitudes of the relative error. Examining variations in the axial tension, we see that for fixed $M \lesssim O(1)$

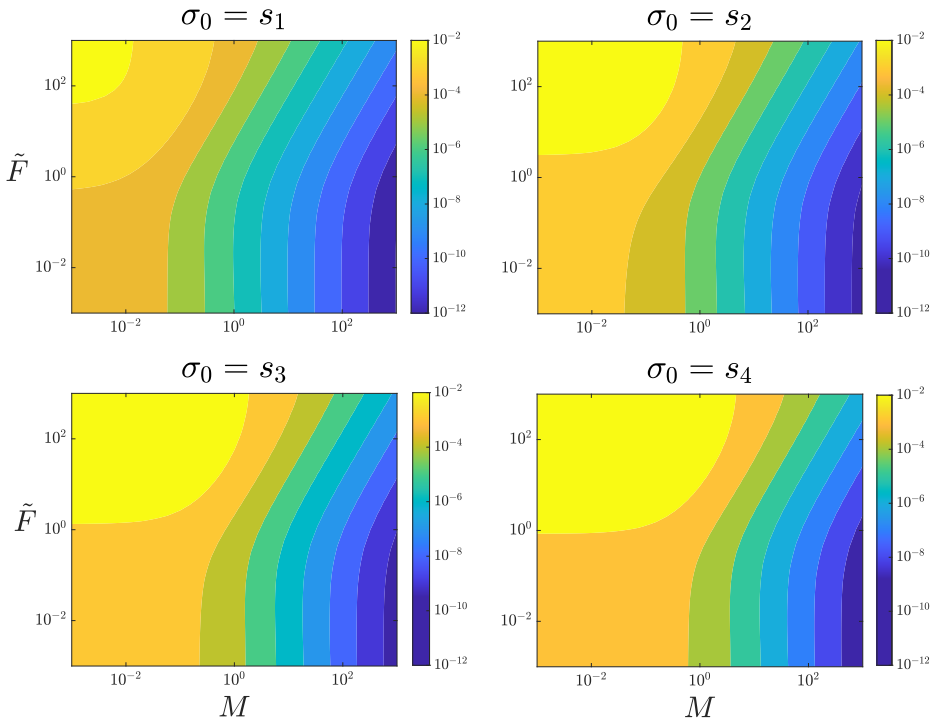

Figure 4.14: The values $|\epsilon\omega_1/\omega_0|$, plotted throughout regions of $(M, \tilde{F})$ parameter space. The values were computed using the analytical expressions (4.108) and (4.144). The results illustrate the error after truncating (4.153) after $O(\epsilon^0)$.

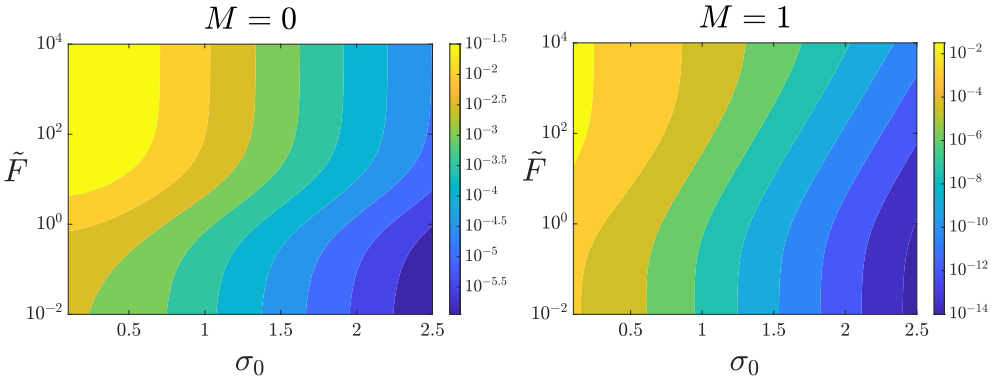

Figure 4.15: The values $|\epsilon\omega_1/\omega_0|$, plotted throughout regions of $(\tilde{F}, \sigma_0)$ parameter space, with $M = 0, 1$. The values were computed using the analytical expressions (4.108) and (4.144). The results illustrate the error after truncating (4.153) after $O(\epsilon^0)$.

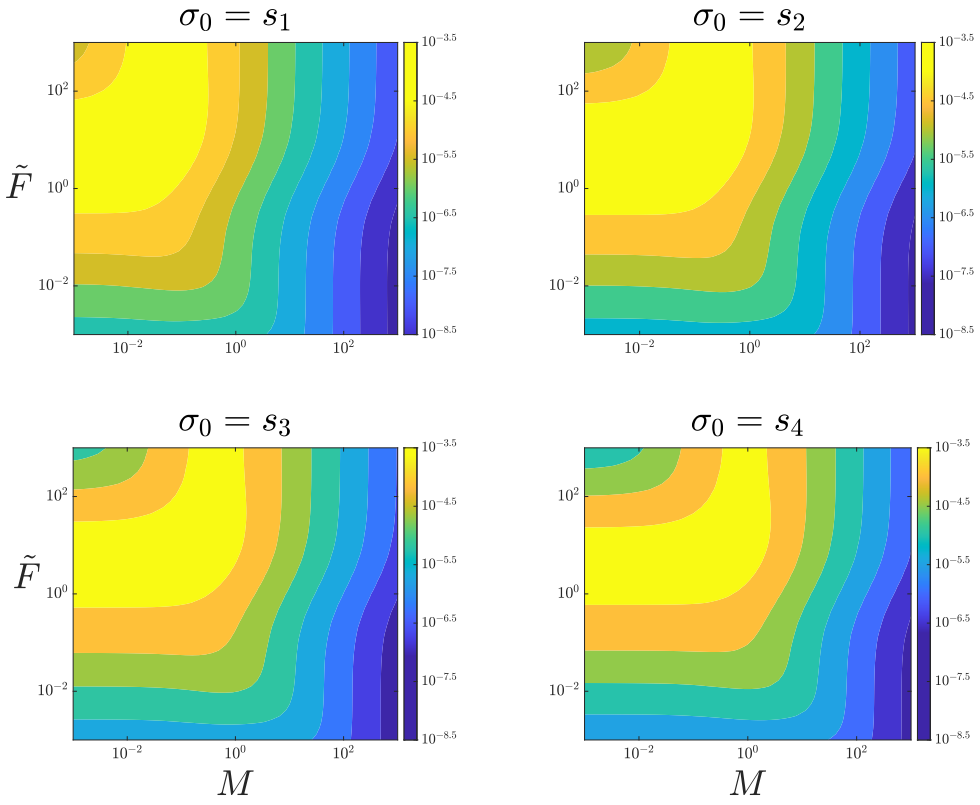

Figure 4.16: The values $|\epsilon\left(p_{11}+p_{20}\right)/p_{10}|$ evaluated at $z = 0.7$, plotted throughout regions of $(M, \tilde{F})$ parameter space. The values were computed using the analytical expressions (4.104), (4.119) and (4.145) for p_{10}, p_{11} and p_{20} respectively. The results give an indication of the error incurred by truncating (4.152) after $O(\epsilon^0)$.

the relative error is maximal at around $\tilde{F} = O(1)$ with $M = 0$, and decays in the large and small $\tilde{F}$ limits. Considering larger values of $\tilde{F}$, our results demonstrate that the behaviour of the error depends on the order of M.

In figure 4.17 we again plot values of $|\epsilon\left(p_{11}+p_{20}\right)/p_{10}|$, evaluated at $z = 0.7$, however this time we fix M whilst varying $\tilde{F}$ and σ_0. The results show very different behaviour of the error, depending on whether $M = 0$ or $M \neq 0$. When $M = 0$, we see that the error will decrease for both

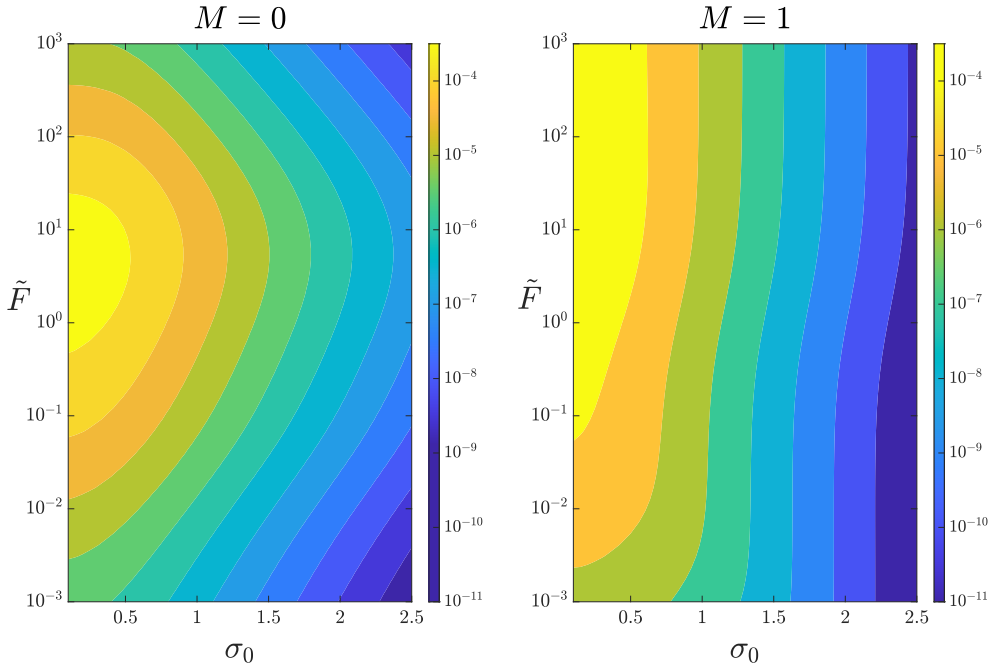

Figure 4.17: The values $|\epsilon\,(p_{11} + p_{20})\,/p_{10}|$ evaluated at $z = 0.7$, throughout regions of $(\tilde{F}, \sigma_0)$ parameter space, with $M = 0$ (top) and $M = 1$ (bottom). The values were computed using the analytical expressions (4.104), (4.119) and (4.145) for p_{10}, p_{11} and p_{20}. The results illustrate the error after truncating (4.152) after $O(\epsilon^0)$.

large and small $\tilde{F}$. However, when $M = 1$, the error only decreases as $\tilde{F} \to 0$, and tends towards being independent of $\tilde{F}$ as $\tilde{F} \to \infty$. In either case, we see that an increase in σ_0 result in a smaller relative error. This result is consistent our analysis in Chapter 3 when considering the case of a uniform transmural pressure, where it was argued that the corrections to the fundamental azimuthal mode vanish in the limit as $\sigma_0 \to \infty$.

4.6 Stability threshold for self-excited oscillations

In order for an instability to occur via the sloshing mechanism, there needs to be a sufficient influx of kinetic energy into the system to overcome losses due to the work done by the pressure at the tube ends as well as viscous dissipation. In this section, we compute the critical Reynolds number Re_c beyond which an instability will grow.

We adopt the results of Whittaker et al. (2010c) who obtained an expression for the tube's energy budget, which has been averaged over the length of the tube as well as one oscillation period. The energy budget of the oscillatory perturbation was found to be

$$\frac{\mathrm{d}E}{\mathrm{d}t} = \frac{1}{\ell St}\left(\mathscr{T} - \mathscr{P} - \mathscr{D}\right). \tag{4.154}$$

Here E is the mean dimensionless energy of the oscillatory perturbation, $\mathscr{T}$ is the mean flux of kinetic energy through the tube ends due to the oscillatory flow, $\mathscr{P}$ is the mean rate of working by the pressure at the tube ends due to the oscillatory flow, and $\mathscr{D}$ is the mean rate of dissipation by the oscillatory flow. Energy fluxes due to the mean flow were found to cancel out.

Whittaker et al. (2010c) obtained expressions for $\mathscr{T}$, $\mathscr{P}$, and $\mathscr{D}$, initially in terms of the axial fluid velocity, before re-arranging (using (4.28)) to obtain equivalent expressions in terms of the pressure. The explicit expressions are given by:

$$\mathscr{T} = \frac{3}{4\omega^2}\pi\ell^2 St^2\Delta^2|\tilde{p}'(0)|^2, \tag{4.155}$$

$$\mathscr{P} = \frac{1}{4}\pi\ell^2 St^2\Delta^2|\tilde{p}'(0)|^2, \tag{4.156}$$

$$\mathscr{D} = \frac{\pi\ell^3 St^3\Delta^2(2\omega)^{1/2}}{2\alpha\omega^2}\int_0^1 |\tilde{p}'(z)|^2\,\mathrm{d}z. \tag{4.157}$$

Observing (4.154), we can see that the growth or decay of the oscillations will depend on the sign of $\mathrm{d}E/\,\mathrm{d}t$, or equivalently $\mathscr{T} - \mathscr{P} - \mathscr{D}$. Setting $\mathscr{T} - \mathscr{P} - \mathscr{D} = 0$ and recalling $\alpha^2/St = Re$, the expression for the critical Reynolds number Re_c is given as

$$Re_c = \frac{\alpha\ell(2\omega)^{1/2}}{|\tilde{p}'(0)|^2}\int_0^1 |\tilde{p}'(z)|^2\,\mathrm{d}z. \tag{4.158}$$

For $Re < Re_c$, we have $\mathrm{d}E/\,\mathrm{d}t < 0$ and hence the flow is stable. For $Re > Re_c$ we have $\mathrm{d}E/\,\mathrm{d}t > 0$ and hence the flow is unstable.

In figure 4.18, we plot solutions for the critical Reynolds number (4.158) against the inertia coefficient M by substituting the expansions (4.152) and (4.153) for $\tilde{p}$ and ω into (4.158). We include both the leading order and $O(\epsilon)$ approximations for $\tilde{p}$ and ω to give an indication of the impact the correction to the fundamental azimuthal mode has on the solution. Our results are in good agreement with Walters et al. (2018) and Whittaker et al. (2010c) (for the case $M = 0$), which verifies the assertion that solutions corresponding to the fundamental azimuthal mode provide a good approximation for the critical Reynolds number. Our results demonstrate that for physically realistic parameter values, the contributions from the high-order azimuthal modes can be neglected.

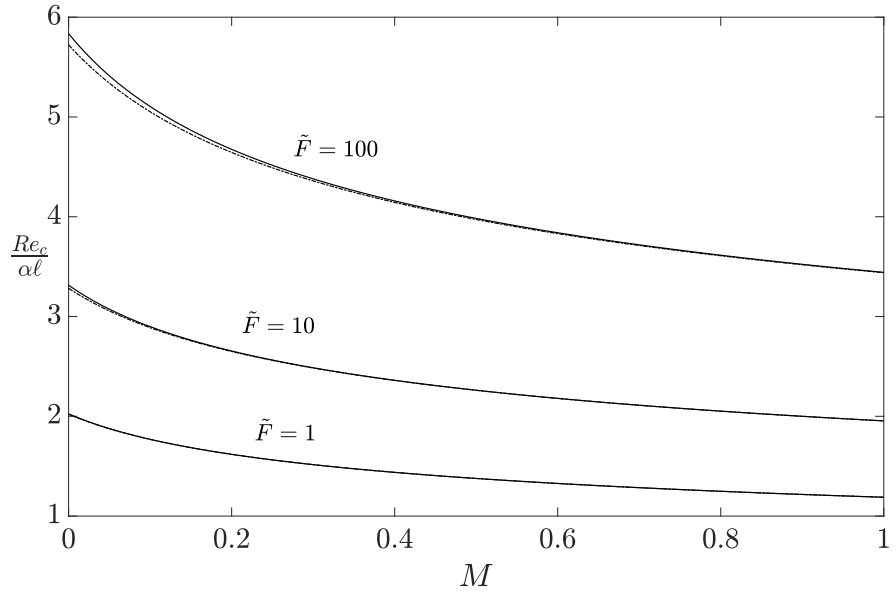

Figure 4.18: The critical Reynolds number $Re_c/(\alpha\ell)$ plotted against M with $z_1 = 0.1$, $z_2 = 0.9$, $\tilde{F} = 1, 10, 100$, and $\sigma_0 = 0.6$. These solutions were obtained by substituting the expansions (4.152) and (4.153) for the pressure and oscillation frequency truncated after $O(1)$ (dashed-dotted curves) and $O(\epsilon)$ (solid curves) into the expression (4.158) for the critical Reynolds number. All of the solutions correspond to the fundamental oscillatory mode, which is the most unstable.

4.7 Conclusions

In this chapter, we have derived series representations for the steady contributions and oscillatory normal modes for the problem formulated by Whittaker et al. (2010c) of the fluid–structure interaction of an initially elliptical thin-walled elastic tube conveying an incompressible viscous fluid. Valid when the oscillations in the tube wall are of small amplitude and high frequency, our solutions enable the first formal analysis of the errors incurred by writing the solution as a function of only the first azimuthal eigenmode.

In order to obtain the solutions, we coupled the fluid and solid mechanics

by combining the model from Chapter 3 measuring the wall deformations with the fluids model of Whittaker et al. (2010c), which uses the Navier–Stokes equations. The problem was then decomposed into steady and oscillatory parts.

For the steady component, the leading-order fluid and solid mechanics problems fully decouple, and the perturbation to the tube's cross-sectional area associated with the nth azimuthal solid eigenmode is shown to satisfy a simple second-order ordinary differential equation (4.59), with linear forcing. For every azimuthal mode number, n, an analytical solution is obtained for the corresponding component measuring the change in cross-sectional area.

For the unsteady case, we formulated the entire problem in terms of pressure modes $\hat{p}_n$, which give the pressure associated with the axial sloshing flow induced by the nth azimuthal solid deformation mode. The full internal pressure can then be obtained by summing each $\hat{p}_n$. Unlike for the steady problem, we found that the azimuthal modes do not decouple at leading order. The governing equation for the component of the pressure associated with each individual eigenmode was forced by a pressure distribution made up of the sum of each of the modes, and was shown to be of the form

$$\mathscr{L}(\hat{p}_n) = q_n t_n \sum_{n=1}^{\infty} \hat{p}_n. \tag{4.159}$$

To overcome difficulties induced by the coupling, we exploited the fact that the product $q_n t_n$, which multiplies the forcing in (4.159) decays rapidly with an increase in mode number, n. This enabled us to adopt a series expansion for the pressure and oscillation frequency.

With respect to a parameter, ϵ, which is the limiting decay rate of $q_n t_n$ as

$n \to \infty$, the series representations for the oscillation frequency and pressure take the forms

$$\tilde{p}(z) = p_{10} + \epsilon\,(p_{11} + p_{20}) + O(\epsilon^2), \tag{4.160}$$

$$\omega = \omega_0 + \epsilon\omega_1 + O(\epsilon^2). \tag{4.161}$$

Here ω_0 is the fundamental oscillation frequency, with first correction ω_1; p_{10} is the component of the pressure associated with the first azimuthal mode, with correction p_{11}; and p_{20} is the leading component of the pressure associated with the second azimuthal mode. Our results demonstrate that errors associated with truncating (4.152)–(4.161) after $O(\epsilon^0)$ are typically small, and hence throughout most of $(M, \tilde{F}, \sigma_0)$ parameter space, the system is well approximated by only p_{10} and ω_0. For certain limiting cases ($\tilde{F} \gg 1$ and $M \ll 1$), we found that errors associated with the oscillation frequency can grow to be as large as $O(1)$. However, this parameter regime is not particularly relevant for the modelling of self-excited oscillations based on physical grounds, since large $\tilde{F}$ corresponds to a stiff tube with negligible azimuthal bending, and small M represents negligible mass. We used our normal mode solutions to compute the critical Reynolds number Re_c such that $Re > Re_c$ will result in the onset of self-excited oscillations in the tube wall. Our results indicated that the higher-order azimuthal modes provide a negligible contribution to the critical Reynolds number, which formally justifies the adhoc assumption invoked by Whittaker et al. (2010b) and Walters et al. (2018).

The long-wavelength high-frequency oscillations assumed for this model result in the tube's transmural pressure (at leading–order) being cross-sectionally

uniform (i.e $\tilde{p} = \tilde{p}(z)$). A reasonable extension to the work presented in this chapter would be to include higher–order effects from the fluid mechanics, in which the pressure varies within the cross-section. It would be simple to include such dependence when modelling the wall motion, since our results from Chapter 3 permit azimuthal variation in the transmural pressure. Another way in which we could build upon the current work is by considering tubes with different initial cross-sectional shapes. One way of doing this would be to develop a model for the wall motion of a tube with arbitrary cross-section (see Chapter 5) and then follow a similar procedure to that outlined in this chapter. Other extensions and improvements include considering an initially axially non-uniform elliptical cross-section, which would apply in the context of a tube that has a partially collapsed initial configuration.

APPENDICES

4.A Cross-sectionally averaged continuity equation

In this Appendix we will derive the cross-sectionally integrated continuity equation that is used in §4.3.1. The result can either be derived using the Navier–Stokes equations together with boundary conditions, or from first principles. We have chosen to use the latter approach.

Consider the dimensional setup depicted in figure 4.19 involving a small section of collapsible tube of dimensional cross-sectional area $A^*(z,t)$ with a dimensional axial domain occupying $(z^*, z^* + \delta z^*)$, where $\delta z^* \ll 1$. Fluid is

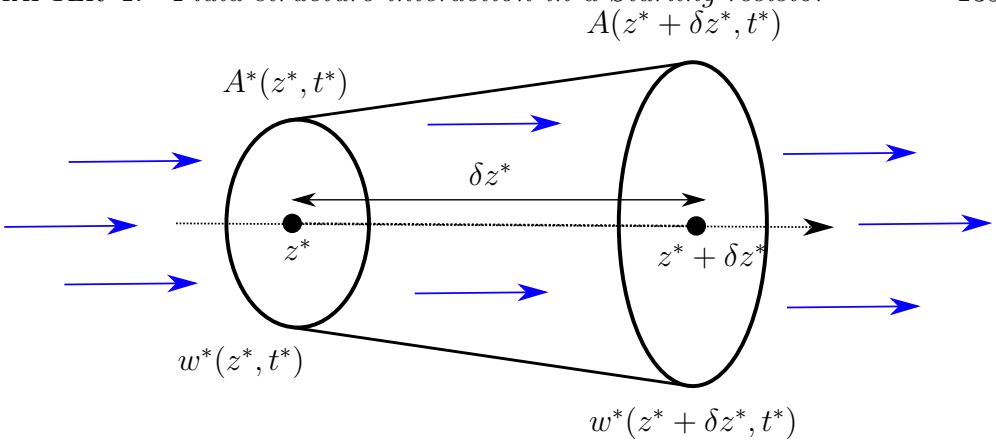

Figure 4.19: A small section of elastic-walled tube of dimensional length $\delta z^* \ll 1$ conveying an axial fluid flow. The cross-sectionally averaged dimensional axial fluid velocity is given by w^* and the varying dimensional cross-sectional area is denoted A^*.

driven through the tube. We denote the space enclosed by the cross-sectional area of the tube as $\mathscr{A}^*(z^*, t^*)$ and define

$$q^* = \iint_{\mathscr{A}^*(z^*,t^*)} w^* \, \mathrm{d}S^* \tag{4.162}$$

as the dimensional volume flux through each cross-section, where w^* is the dimensional axial component of fluid velocity. Since $\delta z^* \ll 1$, the tube remains approximately axially uniform over the small spatio-temporal scale in which changes in cross-sectional area occur. Physically we require that a difference in volume flux between the two ends of the tube over a given time period δt must be accommodated by an appropriate change in volume. Re-arranging (4.163) to give

$$[q^*(z^*, t^*) - q^*(z^* + \delta z^*, t^*)]\, \delta t^* = [A^*(z^*, t^* + \delta t^*) - A^*(z^*, t^*)]\, \delta z^* \tag{4.163}$$

Re-arranging (4.163),

$$\frac{q^*(z^*,t^*)-q^*(z^*+\delta z^*,t^*)}{\delta z}=\frac{[A^*(z^*,t^*+\delta t^*)-A^*(z^*,t^*)]}{\delta t^*} \tag{4.164}$$

and taking the dual limit as $\delta z^*, \delta t^* \to 0$, it follows that

$$\frac{\partial A^*}{\partial t^*}+\frac{\partial q^*}{\partial z^*}=0. \tag{4.165}$$

Finally, recalling (4.162), we arrive at the cross-sectionally averaged continuity equation

$$\frac{\partial A^*}{\partial t^*}+\frac{\partial}{\partial z^*}\iint_{\mathscr{A}^*(z^*,t^*)} w^*\,\mathrm{d}S^*=0. \tag{4.166}$$

4.B Fitting a curve to numerical data for $q_n t_n$

In §4.5.3 we assumed that the numerical data for $q_n t_n$, which was determined in Chapter 3 obeys the relationship

$$q_n t_n \sim Q\epsilon^{n-1} \qquad \text{as} \qquad n\to\infty. \tag{4.167}$$

In this Appendix we obtain estimates for the parameters Q and ϵ by fitting a curve to the numerical data obtained in Chapter 3 for $q_n t_n$. In figure 4.20, we plot $\log(q_n t_n)$ against n for $\sigma_0 \in \{s_1, s_2, s_3, s_4\}$. The plots strongly suggest that there is a linear relationship between $\log(q_n t_n)$ and mode number n, for large n. The obvious first candidate function to fit to the numerical data is therefore the straight line

$$\log(q_n t_n)=\log\hat{Q}+(n-1)\log\hat{\epsilon} \qquad \text{for} \qquad n\gg 1, \tag{4.168}$$

where $\hat{Q}$ and $\hat{\epsilon}$ are constants. Since we are investigating the decay of $q_n t_n$ for large n, the values for $\hat{Q}$ and $\hat{\epsilon}$ were chosen so that the straight line passes through the final two data points $q_{13}t_{13}$ and $q_{14}t_{14}$. For $\sigma_0 = 0.6$, which is the typical representative value used by Walters et al. (2018) and Whittaker et al. (2010c), the resulting straight line is then plotted together with the data for $\log(q_n t_n)$ against n in figure 4.21.

With first estimates $\hat{Q}$, $\hat{\epsilon}$ of Q and ϵ obtained, we plot the error in (4.168) against n and again observe an approximately linear profile in logarithmic space (see the inset of figure 4.21). We therefore improve our estimates of ϵ and Q by fitting the log of the error to a straight line. Hence, we want to fit

$$\log\left(\log(q_n t_n) - \left[\log\tilde{Q} + (n-1)\log\tilde{\epsilon}\right]\right) = \log c + (1-n)\log d, \quad (4.169)$$

for some constants $\tilde{Q}$, $\tilde{\epsilon}$, c and d. Re-arranging (4.169), we find that an improved fit for the numerical data $q_n t_n$ is given by

$$\log(q_n t_n) = \log\tilde{Q} + (n-1)\log\tilde{\epsilon} + cd^{1-n}. \quad (4.170)$$

The constants $\tilde{\epsilon}, \tilde{Q}, c$ and d are fixed by choosing the curve (4.170) to pass through the final four data points of $\log(q_n t_n)$. This defines a system of four non-linear algebraic equations, which was solved using the built in `Matlab` function `fsolve`. In figure 4.21 we plot the improved fit together with its associated linearised form against n. The results of this fitting procedure for the representative values of σ_0 can be found in table 4.1 in §4.5.3.

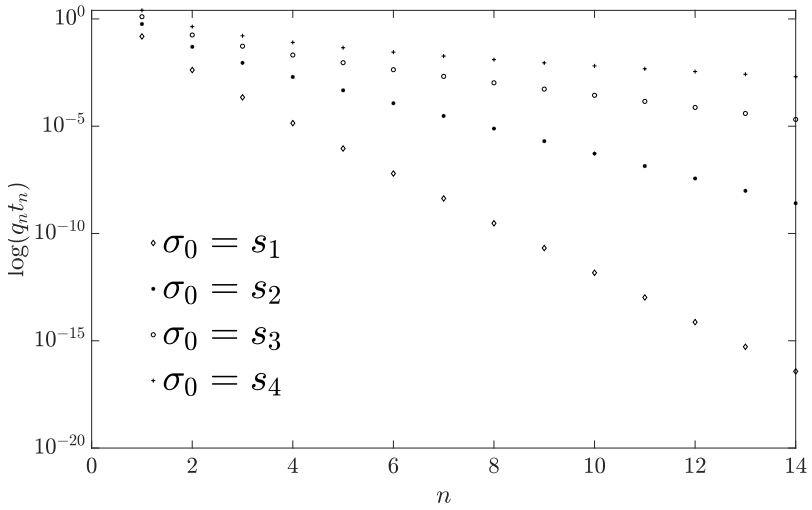

Figure 4.20: The points $\log(q_n t_n)$, plotted against azimuthal mode number $n = 1, 2, \ldots 12$, for ellipticity parameters $\sigma_0 = s_1, s_2, s_3, s_4$. Representative values for $q_n t_n$ and λ_n are given in Chapter 3.

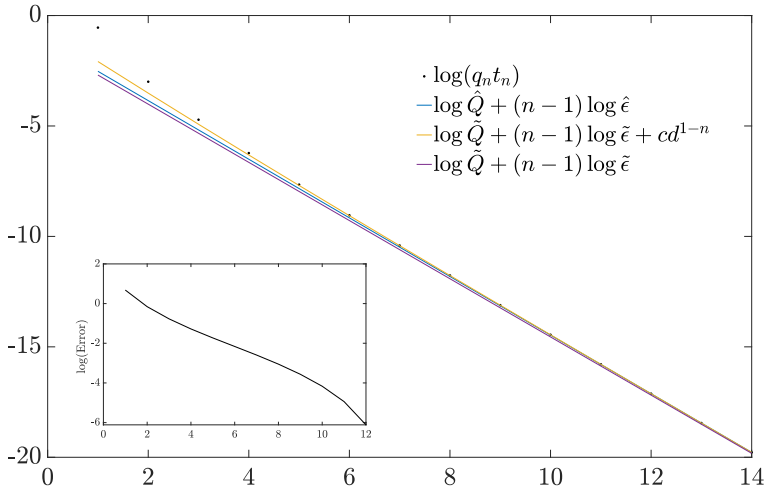

Figure 4.21: Approximations (4.168) and (4.170) of the numerical data for $\log(q_n t_n)$ with fitted coefficients. The inset shows the error in (4.168).

Chapter 5

Cross-sectional shapes exciting monomode deformations

Synopsis

In this chapter, we will derive a model for the wall deformation of an elastic-walled tube of arbitrary initial cross-sectional shape, and seek a family of initial shapes with the property that an azimuthally uniform transmural pressure will excite only a single azimuthal deformation mode.

5.1 Introduction

In Chapter 3, we saw, for the case of an initially elliptical tube, that an applied azimuthally uniform transmural pressure will excite an infinite number of azimuthal deformation modes. The azimuthal displacement η, which can be used to determine the remaining displacements in the tube wall, was then determined in the form of a series expansion

$$\eta(\tau, z, t) = \sum_{n=1}^{\infty} a_n(z, t) Y_n(\tau), \tag{5.1}$$

where (τ, z) is the elliptical-azimuthal co-ordinate system set out in Chapter 2. Here $Y_n(\tau)$ is the eigenfunction corresponding to the nth deformation eigenmode and $a_n(z,t)$ is its amplitude. Whilst this approach gave excellent results, in general truncating (5.1) after a given azimuthal mode will result in a small error from the higher-order azimuthal modes. In this chapter, we generalise our results from Chapter 3 to the case of an elastic tube of arbitrary cross-section. We then use this revised model to seek a family of initial cross-sectional shapes with the property that an azimuthally uniform transmural pressure will excite only a single azimuthal deformation mode, resulting in a finite semi-analytical solution of the solid mechanics problem.

To derive the model, we will first adopt the arclength version of the physical setup and governing equations introduced in Chapter 2. The eigenfunction expansion method used throughout Chapter 3 will then be replicated to obtain a system of generalised tube laws that collectively measure the relationship between the transmural pressure — which deforms the tube — and the corresponding changes in cross-sectional area.

To obtain the family of initial shapes, we treat the base-state azimuthal curvature — which defines the cross-sectional shape — as an additional unknown. We utilise this additional degree of freedom by imposing an extra condition on the system that ensures that contributions from only a single azimuthal mode are present in the expansion for η. The required condition is that a certain function of the base-state azimuthal curvature is orthogonal to all but one of the azimuthal eigenmodes, Y_n. This means that this function must be proportional to $\mathscr{J}(Y_n)$. The constant of proportionality, which we are free to specify, is denoted γ. It turns out that for a fixed mode, n, varying

γ allows us to find initial cross-sectional shapes with varying aspect ratios.

We find that numerical solutions of the revised eigenvalue problem exist on the domain $\gamma \in [-\gamma_{\text{crit}}, \gamma_{\text{crit}}]$, where γ_{crit} is the value of γ where the governing equations encounter a singularity, corresponding to the curvature becoming zero at a pair of isolated points in each cross section. We validate our solutions by computing asymptotic solutions of the eigenvalue problem, which are found to be in excellent agreement with the numerical results.

5.2 Problem description

We adopt the setup of Chapter 2 in dimensionless form and consider a long, thin-walled elastic tube of dimensionless length $\ell \gg 1$, dimensionless wall thickness $\delta \ll 1$ and dimensionless mass M (see figure 5.1). In its initial configuration, the tube is axially uniform with an arbitrary cross-sectional shape of circumference 2π and is subject to a dimensionless axial tension force $\tilde{F} = O(1)$ at both ends. The tube is aligned with dimensionless Cartesian co-ordinates (x, y, z), where z is aligned with the tubes central axis.

We adopt the arclength co-ordinate system (s, z) set out in Chapter 2, where $s \in (0, 2\pi)$ is a dimensionless arclength co-ordinate measured around the tube's midplane, and z is an axial co-ordinate aligned with the tube's central axis. We introduce t as dimensionless time.

The tube's initial cross-sectional shape is defined by the dimensionless base-state curvature $\bar{B}(s)$. As shown in Chapter 2, this is related to the angle θ of the wall in the x–y plane by

$$\frac{\mathrm{d}\theta}{\mathrm{d}s} = -\bar{B}(s). \tag{5.2}$$

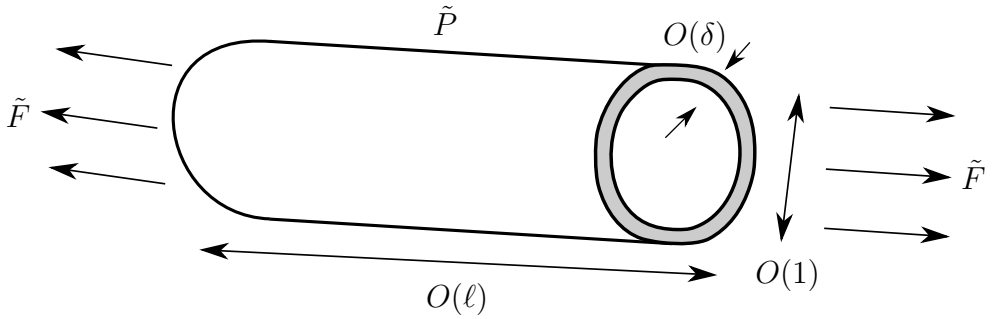

Figure 5.1: The typical setup showing the initial configuration of a long thin-walled tube of dimensionless length ℓ and wall thickness δ. The tube has an initially axially uniform arbitrary cross-sectional shape of $O(1)$ radial scale, and is subject to a dimensionless axial tension $\tilde{F}$. The tube will undergo deformations about this pre-stressed state in response to an applied dimensionless transmural pressure $\tilde{P}$.

We restrict our attention to shapes with symmetry in the x and y axes. Thus, given the total circumference 2π, we can restrict the arclength domain to $s \in (0, \pi/2)$. To ensure a smooth cross-section, θ must increase from 0 to $\pi/2$, while s increases from 0 to $\pi/2$. This requires

$$\int_0^{\pi/2} \bar{B}(s)\,\mathrm{d}s = -\frac{\pi}{2}. \tag{5.3}$$

We consider deformations in the tube induced by a dimensionless transmural pressure $\tilde{P}$, which is assumed to be both even and π-periodic. As explained in Chapter 2, this results in odd and π-periodic displacements in the tube wall, which from Chapter 2 are described using the displacement functions $\xi(s,z,t)$, $\eta(s,z,t)$, $\zeta(s,z,t)$ and $\zeta_a(z,t)$. The position vector of the tube in its deformed configuration is given by

$$\boldsymbol{r} = \bar{\boldsymbol{r}}(s,z) + a\epsilon\left(\xi(s,z,t)\hat{\boldsymbol{n}} + \eta(s,z,t)\hat{\boldsymbol{t}}\right) + a\epsilon\ell\left(\frac{1}{\ell^2}\zeta(s,z,t)\hat{\boldsymbol{z}} + \delta^2\zeta_a(z,t)\hat{\boldsymbol{z}}\right), \tag{5.4}$$

where the unit vectors $\hat{\boldsymbol{n}}$, $\hat{\boldsymbol{t}}$ and $\hat{\boldsymbol{z}}$ are measured in the normal, azimuthal and axial directions respectively and are given explicitly in Chapter 2.

5.2.1 Governing equations for the azimuthal displacement η

From Chapter 2, it was shown that with this setup the azimuthal displacement, η, is governed by the PDE

$$\mathscr{L}\mathscr{K}(\eta) - \tilde{F}\frac{\partial^2}{\partial z^2}\mathscr{J}(\eta) + M\frac{\partial^2}{\partial t^2}\mathscr{J}(\eta) = -\frac{\partial}{\partial s}\left(\frac{\tilde{P}(s,z,t)}{\bar{B}(s)}\right), \tag{5.5}$$

where operators $\mathscr{L}$, $\mathscr{K}$ and $\mathscr{J}$ are:

$$\mathscr{L}(\eta) = -\bar{B}\frac{\partial \eta}{\partial s} - \frac{\partial}{\partial s}\left(\frac{1}{\bar{B}}\frac{\partial^2 \eta}{\partial s^2}\right), \tag{5.6}$$

$$\mathscr{K}(\eta) = \frac{\partial}{\partial s}\left[\bar{B}\eta + \frac{\partial}{\partial s}\left(\frac{1}{\bar{B}}\frac{\partial \eta}{\partial s}\right)\right], \tag{5.7}$$

$$\mathscr{J}(\eta) = \eta - \frac{\partial}{\partial s}\left(\frac{1}{\bar{B}^2}\frac{\partial \eta}{\partial s}\right). \tag{5.8}$$

The boundary conditions on η are given by:

$$\eta = 0 \qquad \text{on} \qquad z = 0, 1, \tag{5.9}$$

$$\eta = \frac{\partial^2 \eta}{\partial s^2} = \frac{\partial^4 \eta}{\partial s^4} = 0 \qquad \text{on} \qquad s = 0, \pi/2. \tag{5.10}$$

If required, the other displacement functions can be recovered using the inextensibility constraints from Chapter 2, which relate the deformation func-

tions. In terms of arclength, they are given by:

$$-\xi\bar{B} + \frac{\partial \eta}{\partial s} = 0, \tag{5.11}$$

$$\frac{\partial \eta}{\partial z} + \frac{\partial \zeta}{\partial s} = 0. \tag{5.12}$$

(Note that the integral expression that occupied the right hand side of (5.12) when it was originally presented Chapter 2 has vanished by symmetry in η.)

5.2.2 Solution by eigenfunction expansion

As in Chapter 3, the problem (5.5)–(5.10) can be solved by seeking a solution of the form

$$\eta(s, z, t) = \sum_{n=1}^{\infty} a_n(z, t) Y_n(s), \tag{5.13}$$

where $Y_n(s)$ is the nth arclength eigenfunction with corresponding eigenvalue λ_n satisfying the following generalised eigenvalue problem

$$\mathscr{L}\mathscr{K}(Y_n) - \lambda_n \mathscr{J}(Y_n) = 0, \qquad \text{for} \qquad n = 1, 2, \ldots \tag{5.14}$$

subject to

$$Y_n = \frac{\mathrm{d}^2 Y_n}{\mathrm{d}s^2} = \frac{\mathrm{d}^4 Y_n}{\mathrm{d}s^4} = 0 \qquad \text{at} \qquad s = 0, \pi/2. \tag{5.15}$$

The properties of operator symmetry and eigenfunction orthogonality proven in Chapter 3 for the azimuthal co-ordinate system remain true for the arclength system. With respect to the standard inner product,

$$\langle u, v \rangle = \int_0^{\pi/2} uv \, \mathrm{d}s, \tag{5.16}$$

we have that the eigenfunctions satisfy

$$\langle Y_n, \mathscr{J}(Y_m)\rangle = 0 \qquad \text{for} \qquad n \neq m. \tag{5.17}$$

The amplitude of each eigenfunction is then set via the normalisation

$$\langle Y_n, \mathscr{J}(Y_n)\rangle = 1. \tag{5.18}$$

The eigenfunctions satisfying (5.14)–(5.15) form a complete set. This result can be proven by re-producing the calculations in Appendix A, with $h = 1$ and $\tau = s$.

Following the method outlined in Chapter 3, the solution of (5.5)–(5.10) for the azimuthal displacement η is given by (5.13), where each $a_n(z,t)$ satisfies the boundary value problem

$$\tilde{F}\frac{\partial^2 a_n}{\partial z^2} - M\frac{\partial^2 a_n}{\partial t^2} - \lambda_n a_n = -Q_n, \tag{5.19}$$

subject to

$$a_n = 0 \qquad \text{on} \qquad z = 0, 1. \tag{5.20}$$

Where

$$Q_n(z,t) = -\int_0^{\pi/2} \frac{\partial}{\partial s}\left(\frac{\tilde{P}(s,z,t)}{\bar{B}(s)}\right) Y_n(s)\,\mathrm{d}s. \tag{5.21}$$

The total fractional area change, α, is then given by

$$\alpha(z,t) = \sum_{n=1}^{\infty} \alpha_n(z,t)., \tag{5.22}$$

where $\alpha_n = a_n t_n$, and t_n is given by the integral

$$t_n = -\frac{4a^2}{\bar{A}} \int_0^{\pi/2} \frac{\mathrm{d}}{\mathrm{d}s}\left(\frac{1}{\bar{B}(s)}\right) Y_n(s)\,\mathrm{d}s. \tag{5.23}$$

Here $\bar{A}$ is the initial cross-sectional area of the tube, given explicitly by equation (2.12) in Chapter 2.

5.2.3 A family of cross-sectional shapes that excite monomode deformations

We now seek initial cross-sectional shapes, such that an azimuthally uniform transmural pressure excites only the nth azimuthal deformation mode in the expansion (5.13), for some fixed n. The initial cross-sectional shape is characterised by the base-state curvature $\bar{B}$. Henceforth, we treat $\bar{B}(s)$ as an additional unknown and seek solutions of the system with $a_m \equiv 0$ for all $m \neq n$.

From (5.19), we require $Q_m = 0$ for all $m \neq n$. The coefficients Q_n are defined in (5.21). Since the pressure is azimuthally uniform, we need

$$\int_0^{\pi/2} \frac{\mathrm{d}}{\mathrm{d}s}\left(\frac{1}{\bar{B}(s)}\right) Y_m(s)\,\mathrm{d}s = 0 \qquad \text{for all} \qquad m \neq n. \tag{5.24}$$

This means $\mathrm{d}(\bar{B}^{-1})/\,\mathrm{d}s$ must be orthogonal to all but one of the eigenfunctions $Y_n(s)$. Hence, by the orthogonality relation, (5.17), we require $\mathrm{d}(\bar{B}^{-1})/\,\mathrm{d}s$ to be proportional to $\mathscr{J}(Y_n)$, i.e.

$$\frac{\mathrm{d}}{\mathrm{d}s}\left(\frac{1}{\bar{B}(s)}\right) = \gamma\,\mathscr{J}(Y_n), \tag{5.25}$$

for some constant γ. Observing (5.25), we can see that $\gamma = 0$ represents the case of an initially circular cross-sectional shape (since the curvature $\bar{B}(s)$ must be uniform). It will turn out to be the case that as $|\gamma|$ is increased from zero the aspect ratio of the corresponding cross-sectional shape moves away from one. Thus, γ can be thought of as a parametrisation of the aspect ratio of the tube's initial cross section.

Therefore, the revised eigenvalue problem for $Y(s)$, $\bar{B}(s)$ and λ we need to consider is given by

$$\mathscr{L}\mathscr{K}(Y) - \lambda \mathscr{J}(Y) = 0, \tag{5.26}$$

$$\frac{\mathrm{d}}{\mathrm{d}s}\left(\frac{1}{\bar{B}}\right) = \gamma \mathscr{J}(Y), \tag{5.27}$$

where the differential operators $\mathscr{L}\mathscr{K}$ and $\mathscr{J}$ are as defined in (5.6)–(5.8).

The boundary conditions on Y are given by:

$$Y = \frac{\mathrm{d}^2 Y}{\mathrm{d}s^2} = \frac{\mathrm{d}^4 Y}{\mathrm{d}s^4} = 0 \qquad \text{at} \qquad s = 0, \pi/2. \tag{5.28}$$

We also have the integral condition (5.3) on $\bar{B}$

$$\int_0^{\pi/2} \bar{B}(s)\,\mathrm{d}s = -\frac{\pi}{2}. \tag{5.29}$$

The normalisation on Y is given by

$$\langle Y, \mathscr{J}(Y)\rangle = \int_0^{\pi/2} Y \mathscr{J}(Y)\,\mathrm{d}s = 1. \tag{5.30}$$

For each γ, the system (5.26)–(5.29) is sixth-order in Y (the eigenfunc-

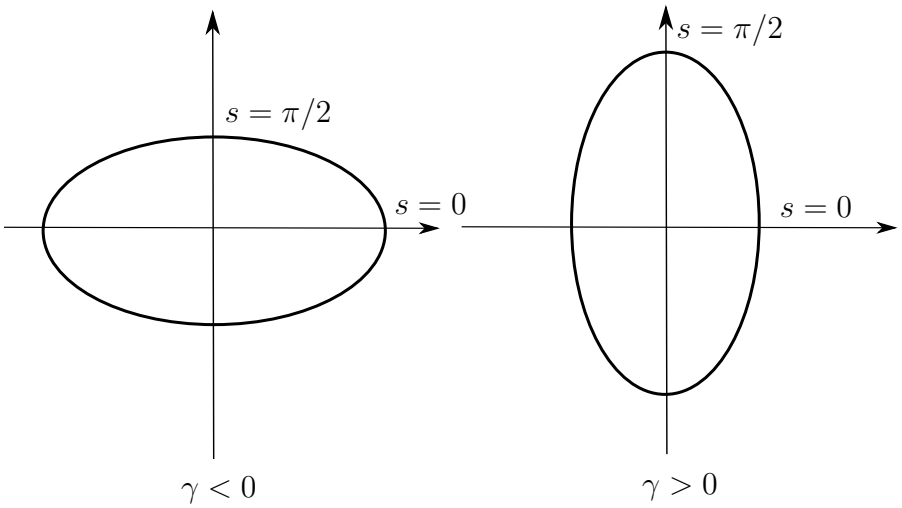

Figure 5.2: The two possible configurations of the ellipsoidal cross-sectional shapes arising from the solution of (5.26)–(5.30).

tion), first-order in $\bar{B}$ (the base-state curvature) and involves an unknown parameter λ (the eigenvalue). In total this means there are eight degrees of freedom, which when combined with the eight conditions (5.28)–(5.30) should result in a well-posed problem. We therefore proceed by seeking solutions of (5.26)–(5.30) with γ prescribed.

Observing the symmetry of the operators $\mathscr{L}\mathscr{K}$ and $\mathscr{J}$, we note that the system (5.26)–(5.29) is invariant under the transformation

$$\gamma \mapsto -\gamma, \qquad \text{and} \qquad s \mapsto \frac{\pi}{2} - s. \tag{5.31}$$

This invariance can be associated with the two possible configurations of the ellipsoidal cross-sectional shapes arising from the solution of (5.26)–(5.30). That is, by switching the major and minor axis between the x and y axis. We can therefore restrict our attention to $\gamma > 0$ without loss of generality.

Henceforth, we seek solutions in which only the first ($n = 1$) eigenmode is excited by an azimuthally uniform transmural pressure.

5.3 Analytical progress

For general γ, solutions of the full non-linear problem formulated in §5.2.3 have to be determined numerically. However, analytical progress can be made for $\gamma \ll 1$ by perturbing about a circular base-state.

5.3.1 Asymptotic expansions for $\gamma \ll 1$

Setting $\gamma = 0$ in (5.27) results in $\bar{B}$ being constant, and therefore corresponds to a circular base-state cross-sectional shape. Consequently, as shown in Chapter 3, the curvature $\bar{B}$ and eigenfunction Y decouple, and an analytical solution for the first eigenmode of (5.26)–(5.30) is given by:

$$Y = y_0(s) = \frac{2}{\sqrt{5\pi}} \sin(2s), \qquad \bar{B} \equiv -1, \qquad \text{and} \qquad \lambda = \lambda_0 = \frac{36}{5}. \quad (5.32)$$

Hence, for $\gamma \ll 1$ we seek an expansion of the form

$$Y(s) = \frac{2}{\sqrt{5\pi}} \sin(2s) + \gamma y_1(s) + \gamma^2 y_2(s) + \gamma^3 y_3(s) + O(\gamma^4), \quad (5.33)$$

$$\bar{B}(s) = -1 + \gamma b_1(s) + \gamma^2 b_2(s) + \gamma^3 b_3(s) + O(\gamma^4), \quad (5.34)$$

$$\lambda = \lambda_0 + \gamma \lambda_1 + \gamma^2 \lambda_2 + \gamma^3 \lambda_3 + O(\gamma^4), \quad (5.35)$$

where $\lambda_0 = 36/5$. Substituting (5.33)–(5.34) into (5.6)–(5.8) and using properties of the geometric series $(1 - x)^{-1}$, we obtain asymptotic expressions for

$\mathscr{J}(Y)$ and $\mathscr{LK}(Y)$. To $O(\gamma^3)$ we find that

$$\mathscr{J}(Y) = \frac{10}{\sqrt{5\pi}}\sin(2s) + \gamma \mathrm{J}_1(s) + \gamma^2 \mathrm{J}_2(s) + \gamma^3 \mathrm{J}_3(s) + O(\gamma^4), \tag{5.36}$$

and

$$\mathscr{LK}(Y) = \frac{72}{\sqrt{5\pi}}\sin(2s) + \gamma \mathrm{LK}_1(s) + \gamma^2 \mathrm{LK}_2(s) + \gamma^3 \mathrm{LK}_3(s) + O(\gamma^4), \tag{5.37}$$

where the components $\mathrm{J}_1(s), \mathrm{J}_2(s), \mathrm{J}_3(s), \mathrm{LK}_1(s), \mathrm{LK}_2(s)$ and $\mathrm{LK}_3(s)$ are given explicitly in Appendix 5.A.

Since the system is invariant under the transformation (5.31), for odd i, we expect $\lambda_i = 0$ and b_i and y_i to be odd about $s = \pi/4$, whilst for even i we expect b_i and y_i to be even about $s = \pi/4$.

5.3.2 The $O(\gamma)$ problem for b_1

Substituting the expansion (5.36) into (5.27) and (5.29) and equating at $O(\gamma)$, we find that b_1 satisfies

$$\frac{\mathrm{d}b_1}{\mathrm{d}s} = -\frac{10}{\sqrt{5\pi}}\sin(2s), \tag{5.38}$$

subject to

$$\int_0^{\pi/2} b_1(s)\,\mathrm{d}s = 0. \tag{5.39}$$

Solving (5.38)–(5.39) we obtain

$$b_1(s) = \frac{1}{\pi}\sqrt{5\pi}\cos(2s). \tag{5.40}$$

5.3.3 The $O(\gamma)$ problem for λ_1 and $y_1(s)$

Substituting the expansions (5.35)–(5.37) into (5.26)–(5.30) with b_1 known via (5.40) and then equating at $O(\gamma)$, we find that y_1 is governed by the following linear inhomogeneous ordinary differential equation with constant coefficients:

$$\frac{\mathrm{d}^6 y_1}{\mathrm{d}s^6} + 2\frac{\mathrm{d}^4 y_1}{\mathrm{d}s^4} + (1-\lambda_0)\frac{\mathrm{d}^2 y_1}{\mathrm{d}s^2} + \lambda_0 y_1 = \frac{10764}{5\pi}\sin(4s) - \frac{\sqrt{5\pi}}{\pi}\lambda_1 \sin(2s), \quad (5.41)$$

subject to:

$$y_1 = \frac{\mathrm{d}^2 y_1}{\mathrm{d}s^2} = \frac{\mathrm{d}^4 y_1}{\mathrm{d}s^4} = 0 \qquad \text{at} \qquad s = 0, \pi/2, \quad (5.42)$$

and the normalisation

$$\int_0^{\pi/2} \left(6y_1 - \frac{\mathrm{d}^2 y_1}{\mathrm{d}s^2}\right) \sin(2s)\,\mathrm{d}s = 0. \quad (5.43)$$

In Chapter 3, we showed (through the setting of λ_0) that the corresponding homogeneous problem associated with (5.41)–(5.42) permits the non-trivial solution

$$y(s) = \sin(2s). \quad (5.44)$$

Hence, by the Fredholm alternative, it follows that a solution of the inhomogeneous problem will exist only when the solutions of the adjoint of the associated homogeneous problem to (5.41)–(5.42) are orthogonal to the inhomogeneous part of (5.41). This solvability condition sets λ_1.

By taking the standard inner product of (5.41) with some sufficiently differentiable function, v (the adjoint eigenfunction), and integrating by parts recursively, it can be shown that the associated homogeneous problem of

(5.41)–(5.42) is formally self-adjoint. Hence, the adjoint eigenfunction is given by

$$v(s) = y(s) = \sin(2s). \tag{5.45}$$

Taking the inner product of the right hand side of (5.41) with $v(s)$ and equating the result with zero, we find that a solution of (5.41)–(5.43) will exist only when $\lambda_1 = 0$.

Setting $\lambda_1 = 0$ in (5.41) and using standard methods, the solution to (5.41)–(5.42) for y_1 is found to be

$$y_1(s) = -\frac{13}{21\pi}\sin(4s). \tag{5.46}$$

5.3.4 The $O(\gamma^2)$ problem for b_2

Substituting the expansion (5.36) into (5.27) and (5.29) using the expressions (5.40) and (5.46) for $b_1(s)$ and $y_1(s)$ and then equating at $O(\gamma^2)$, we find that b_2 satisfies

$$-\frac{\mathrm{d}}{\mathrm{d}s}\left(\frac{5}{\pi}\cos^2(2s) + b_2\right) = \frac{115}{21\pi}\sin(4s), \tag{5.47}$$

subject to

$$\int_0^{\pi/2} b_2(s)\,\mathrm{d}s = 0. \tag{5.48}$$

Solving (5.47)–(5.48), we obtain

$$b_2(s) = -\frac{95}{84\pi}\cos(4s). \tag{5.49}$$

5.3.5 The $O(\gamma^2)$ problem for λ_2 and y_2

Substituting the expansions (5.35)–(5.37) into (5.26)–(5.30) with b_1, b_2, λ_1 and y_1 all known, we equate at $O(\gamma^2)$ and find that y_2 satisfies

$$\frac{\mathrm{d}^6 y_2}{\mathrm{d}s^6} + 2\frac{\mathrm{d}^4 y_2}{\mathrm{d}s^4} + (1-\lambda_0)\frac{\mathrm{d}^2 y_2}{\mathrm{d}s^2} + \lambda_0 y_2 = -\frac{2\sqrt{5}}{35\pi^{3/2}}\Big[(35\pi\lambda_2 + 126)\sin(2s) + 103232\sin(6s)\Big]. \tag{5.50}$$

subject to

$$y_2 = \frac{\mathrm{d}^2 y_2}{\mathrm{d}s^2} = \frac{\mathrm{d}^4 y_2}{\mathrm{d}s^4} = 0 \qquad \text{at} \qquad s = 0, \pi/2, \tag{5.51}$$

and the normalisation

$$\int_0^{\pi/2} \left(6y_2 - \frac{\mathrm{d}^2 y_2}{\mathrm{d}s^2}\right)\sin(2s)\,\mathrm{d}s + \frac{8417}{3528}\sqrt{\frac{5}{\pi}} = 0. \tag{5.52}$$

We note that the homogeneous part of (5.50) is identical to that of (5.41). Imposing the same solvability condition as in §5.3.3, we find that a solution of (5.50)–(5.52) will exist only when

$$\lambda_2 = -\frac{18}{5\pi}. \tag{5.53}$$

With λ_2 determined, we again use standard methods to obtain

$$y_2(s) = \frac{\sqrt{5}}{\pi^{3/2}}\left(\frac{6452}{47943}\sin(6s) - \frac{8417}{8820}\sin(2s)\right). \tag{5.54}$$

5.3.6 The $O(\gamma^3)$ problem for b_3

Substituting the expansion (5.36) into (5.27) and (5.29) with b_1, b_2, y_1 and y_2 known and then equating at $O(\gamma^3)$, we find that b_3 satisfies

$$-\frac{\mathrm{d}}{\mathrm{d}s}\left[\frac{5\sqrt{5}}{42\pi^{3/2}}\left(\cos 6s + 22\cos 2s\right) + b_3\right] = \frac{\sqrt{5}(\sin(6s) + 8680727\,\sin(2s))}{1342404\pi^{3/2}}, \tag{5.55}$$

subject to

$$\int_0^{\pi/2} b_3(s)\,\mathrm{d}s = 0. \tag{5.56}$$

The solution of (5.55)–(5.56) is given by

$$b_3(s) = \frac{\sqrt{5}\,(4947261\cos(2s) + 2657060\cos(6s))}{8054424\pi^{3/2}}. \tag{5.57}$$

5.3.7 The $O(\gamma^3)$ problem for λ_3 and y_3

Substituting the expansions (5.36)–(5.37) as well as (5.35) into (5.26)–(5.30) using the previously determined expressions for $y_1, y_2, b_1, b_2, b_3, \lambda_1, \lambda_2$ and then equating at $O(\gamma^3)$, we find that the problem for y_3 is given by

$$\begin{aligned}\frac{\mathrm{d}^6 y_3}{\mathrm{d}s^6} + 2\frac{\mathrm{d}^4 y_3}{\mathrm{d}s^4} + (1-\lambda_0)\frac{\mathrm{d}^2 y_3}{\mathrm{d}s^2} + \lambda_0 y_3 \\ = \frac{29204572075}{671202\pi^2}\sin(8s) - \frac{1262156634}{671202\pi^2}\sin(4s) - \frac{1342404\sqrt{5}}{671202\sqrt{\pi}}\lambda_3\sin(2s),\end{aligned} \tag{5.58}$$

subject to

$$y_3 = \frac{\mathrm{d}^2 y_3}{\mathrm{d}s^2} = \frac{\mathrm{d}^4 y_3}{\mathrm{d}s^4} = 0 \qquad \text{at} \qquad s = 0, \pi/2, \tag{5.59}$$

and the normalisation

$$\int_0^{\pi/2} \left(6y_3 - \frac{\mathrm{d}^3 y_3}{\mathrm{d}s^3}\right) \sin(2s)\,\mathrm{d}s = 0. \tag{5.60}$$

Again the homogeneous part of (5.58) is the same as that of (5.41), so we have a solvability condition that the right hand side of (5.58) is orthogonal to $\sin(2s)$, which sets $\lambda_3 = 0$. The solution for y_3 is then found to be

$$y_3(s) = \frac{1}{\pi^2}\left(\frac{116866355}{216127044}\sin(4s) - \frac{596011675}{3473100504}\sin(8s)\right). \tag{5.61}$$

Substituting the expressions for $b_1, b_2, b_3, y_1, y_2, y_3, \lambda_1, \lambda_2$ and λ_3 into the expansions (5.33)–(5.35) yields asymptotic approximations for Y, $\bar{B}$ and λ accurate to $O(\gamma^3)$. These asymptotic solutions will later be compared with the full numerical solutions that will be computed in the following section.

5.4 Numerical solution of the full problem

In this section, we describe the numerical method used to obtain a numerical solution of (5.26)–(5.30). We find that distinct numerical solutions of (5.26)–(5.30) exist on the domain $\gamma \in [0, \gamma_{\mathrm{crit}}]$, where γ_{crit} is a limiting value of γ corresponding to a singularity appearing in the governing equations at $s = 0$. The limiting solution of (5.26)–(5.30) when $\gamma = \gamma_{\mathrm{crit}}$ is investigated in §5.5 below. In this section we concentrate on numerical solutions for $\gamma \in [0, \gamma_{\mathrm{crit}})$.

For numerical convenience, we chose to initially replace the integral normalisation (5.30) with an inhomogeneous boundary condition at $s = 0$. Once a solution has been found it can be re-normalised to satisfy (5.30). We also

want to avoid the other integral constraint (5.29). We therefore seek a solution for $\tilde{Y}, \bar{B}, \theta$ to a revised problem:

$$\mathscr{L}\mathscr{K}(\tilde{Y}) - \lambda \mathscr{J}(\tilde{Y}) = 0, \tag{5.62}$$

$$\frac{\mathrm{d}}{\mathrm{d}s}\left(\frac{1}{\bar{B}}\right) = \tilde{\gamma}\mathscr{J}(\tilde{Y}), \tag{5.63}$$

$$\frac{\mathrm{d}\theta}{\mathrm{d}s} = -\bar{B}, \tag{5.64}$$

where $\tilde{\gamma}$ is prescribed and we have introduced θ as a new independent variable. This avoids the need to impose the numerically inconvenient integral condition (5.29) on the curvature.

The boundary conditions on $\tilde{Y}$ are given by

$$\tilde{Y} = \frac{\mathrm{d}^2 Y}{\mathrm{d}s^2} = \frac{\mathrm{d}^4 Y}{\mathrm{d}s^4} = 0 \qquad \text{at} \qquad s = 0, \pi/2. \tag{5.65}$$

The conditions on θ are given by

$$\theta = 0 \qquad \text{at} \qquad s = 0 \qquad \text{and} \qquad \theta = \pi/2 \qquad \text{at} \qquad s = \pi/2. \tag{5.66}$$

The simplified normalisation is chosen as

$$\frac{\mathrm{d}\tilde{Y}}{\mathrm{d}s} = -\bar{B} \qquad \text{at} \qquad s = 0. \tag{5.67}$$

(The choice of normalisation (5.67) was found to be convenient when implementing the numerical method detailed in §5.4.1.)

For each $\tilde{\gamma}$, the solutions $\tilde{Y}, \bar{B}$ and λ of the revised system (5.62)–(5.67) satisfy the system (5.26)–(5.30) with the exception of the integral normal-

isation (5.30). Consequently, we note that the system (5.62)–(5.67) is not invariant under the transformation (5.31). The required solution that also satisfies (5.30) can then be obtained by scaling both $\tilde{Y}$ and $\tilde{\gamma}$ as follows

$$Y(s) = D\tilde{Y}(s), \qquad \text{and} \qquad \gamma = \frac{1}{D}\tilde{\gamma}, \tag{5.68}$$

where

$$D = \frac{1}{\sqrt{\int_0^{\pi/2} \tilde{Y}\,\mathscr{J}(\tilde{Y})\,\mathrm{d}s}}. \tag{5.69}$$

The first of these scalings ensures that Y satisfies the required normalisation (5.30), whilst the second is a consequence of the first, and is required so $Y(s)$ satisfies (5.27).

5.4.1 Numerical method

The eigenvalue problem (5.26)–(5.30) was solved numerically using the built in `Matlab` solver `bvp4c`. The solver requires that we write the governing equation as a first-order coupled system of ordinary differential equations. We do this by introducing variables $u_1, u_2, \ldots, u_8$, defined as

$$u_1 = \tilde{Y}, \tag{5.70}$$

$$u_2 = -\frac{1}{\bar{B}}\frac{\mathrm{d}\tilde{Y}}{\mathrm{d}s}, \tag{5.71}$$

$$u_3 = -\frac{\mathrm{d}}{\mathrm{d}s}\left(\frac{1}{\bar{B}}\frac{\mathrm{d}\tilde{Y}}{\mathrm{d}s},\right), \tag{5.72}$$

$$u_4 = -\mathscr{K}(\tilde{Y}), \tag{5.73}$$

$$u_5 = -\frac{\mathrm{d}}{\mathrm{d}s}\left[\mathscr{K}(\tilde{Y})\right], \tag{5.74}$$

$$u_6 = -\frac{\mathrm{d}^2}{\mathrm{d}s^2}\left[\mathscr{K}(\tilde{Y})\right], \tag{5.75}$$

$$u_7 = \theta, \tag{5.76}$$

$$u_8 = \bar{B}. \tag{5.77}$$

The precise form for the variables $u_1, u_2 \ldots, u_8$ were chosen to simplify the term in (5.26) involving the complicated operator $\mathscr{L}\mathscr{K}$, and overcomes having to use (5.27) to compute higher-order derivatives of $\bar{B}$. Overall, this results in a significantly simplified first-order system, which is given by

$$\frac{\mathrm{d}u_1}{\mathrm{d}s} = -u_2 u_8, \tag{5.78}$$

$$\frac{\mathrm{d}u_2}{\mathrm{d}s} = u_3, \tag{5.79}$$

$$\frac{\mathrm{d}u_3}{\mathrm{d}s} = u_4 + \frac{\tilde{\gamma} u_1 u_8 \left(u_1 u_8 + u_3\right)}{\tilde{\gamma} u_2 - 1} - u_2 u_8^2, \tag{5.80}$$

$$\frac{\mathrm{d}u_4}{\mathrm{d}s} = u_5, \tag{5.81}$$

$$\frac{\mathrm{d}u_5}{\mathrm{d}s} = u_6, \tag{5.82}$$

$$\frac{\mathrm{d}u_6}{\mathrm{d}s} = \lambda\left[u_1 u_8 + \frac{\tilde{\gamma} u_2 \left(u_1 u_8 + u_3\right)}{1 - \tilde{\gamma} u_2} + u_3\right] - \frac{\tilde{\gamma} u_6 \left(u_1 u_8 + u_3\right)}{1 - \tilde{\gamma} u_2} - u_5 u_8^2, \tag{5.83}$$

$$\frac{\mathrm{d}u_7}{\mathrm{d}s} = u_8, \tag{5.84}$$

$$\frac{\mathrm{d}u_8}{\mathrm{d}s} = \frac{\tilde{\gamma} u_8 \left(u_1 u_8 + u_3\right)}{\tilde{\gamma} u_2 - 1}. \tag{5.85}$$

From (5.65)–(5.67), the boundary conditions on $u_1, u_2 \ldots u_8$ that were passed through the solver are given by:

$$u_1 = u_3 = u_5 = 0, \qquad u_2 = 1, \qquad u_7 = 0 \qquad \text{on} \qquad s = 0, \tag{5.86}$$

and

$$u_2 = u_4 = u_6 = 0, \qquad u_8 = \pi/2 \qquad \text{on} \qquad s = \pi/2. \tag{5.87}$$

The solver `bvp4c` requires an initial guess for the solution and any parameters (the eigenvalue λ in this case). For general $\tilde{\gamma}$, a solution was obtained by starting from the analytical solution (5.32) for $\tilde{\gamma} = 0$ and using parameter continuation.

Once numerical solutions for $\tilde{Y}$,$\bar{B}$ and λ satisfying (5.62)–(5.67) were obtained for a given $\tilde{\gamma}$, we scaled $\tilde{Y}$ and $\tilde{\gamma}$ using (5.69) to yield a solution of (5.26)–(5.30). To compute solutions for a prescribed value of γ (rather than $\tilde{\gamma}$), we implemented an iterative numerical scheme that executes a binary search algorithm to determine the value of $\tilde{\gamma}$ required to achieve a prescribed value of γ accurate to 10^{-5}.

Using this numerical method, we were able to compute numerical solutions of (5.26)–(5.30) for prescribed values of $\gamma > 0$ up to around $\gamma \approx 0.78$. Beyond this value, the solver produced unreliable results, or failed completely. This numerical difficulty can be associated with a singularity in the governing equations (5.62)–(5.63), which arises due to the curvature becoming zero. We consider this case independently in §5.5.

5.4.2 Results for $\gamma \in [0, \gamma_{\text{crit}})$

In figure 5.3 we plot numerical and asymptotic solutions for the base-state curvature $\bar{B}$ as a function of arclength for fixed values of γ. For each γ, both functions have a global maximum at $s = 0$ and decrease monotonically

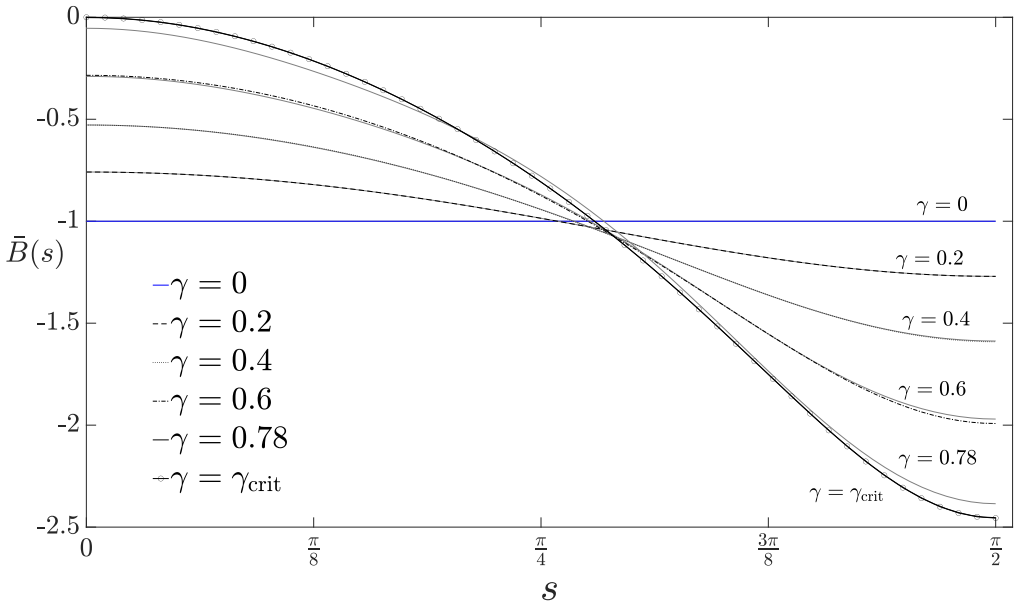

Figure 5.3: Numerical and asymptotic solutions for the base-state curvature $\bar{B}(s)$ with $\gamma = 0, 0.2, 0.4, 0.6, 0.78, \gamma_{\text{crit}}$, all plotted as a function of $s \in (0, \pi/2)$. Numerical solutions are plotted using a variety of line-styles, whereas asymptotic solutions are plotted as solid grey curves. Details of the solution corresponding to $\gamma = \gamma_{\text{crit}}$ can be found in §5.5.

until reaching a global minimum at $s = \pi/2$. Our results demonstrate that our asymptotic predictions are in excellent agreement with our numerical solutions, even for reasonably large values of γ.

In figure 5.4 we plot the corresponding cross-sectional shape that arises from the numerical solution of (5.26)–(5.30) for fixed values of γ. The plots were obtained by substituting the numerical solutions for $\theta(s)$ into the expressions (2.12) given in Chapter 2 for the Cartesian position vector of the tube's initial cross-section. The solutions indicate that the resulting cross-sectional shape is elliptical-like, and becomes more non-circular as γ is increased. We have included the circular ($\gamma = 0$) solution for reference.

In figure 5.5 we plot numerical and asymptotic solutions for the first mode

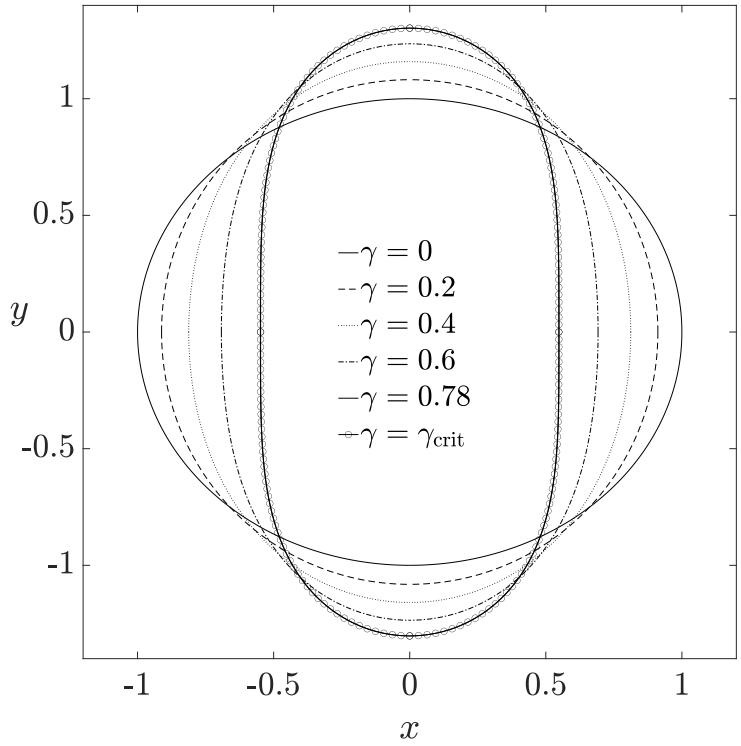

Figure 5.4: The cross-sectional shapes arising from the numerical solution of (5.26)–(5.30) when $\gamma = 0, 0.2, 0.4, 0.6, 0.78, \gamma_{\text{crit}}$. For $\gamma \neq \gamma_{\text{crit}}$, the plots were obtained by substituting the numerical solutions for $\bar{B}(s)$ into the expressions given in Chapter 2 for the Cartesian position vector of the tube's initial cross-section. Details of the solution corresponding to $\gamma = \gamma_{\text{crit}}$ can be found in §5.5.

eigenfunction $Y(s)$ of (5.26)–(5.30) as a function of arclength for fixed values of γ. The results indicate that increasing γ from zero results in a phase-shift (to the right) of the maximum value of Y as well as a reduction in its amplitude. The final value $\gamma = 0.78$ was included as a representative value indicating the behaviour of the solution close to where the solver fails to find a solution due to the reasons discussed in §5.5. The results show excellent agreement between the numerical and asymptotic predictions.

In figure 5.6 we plot numerical and asymptotic solutions for the eigen-

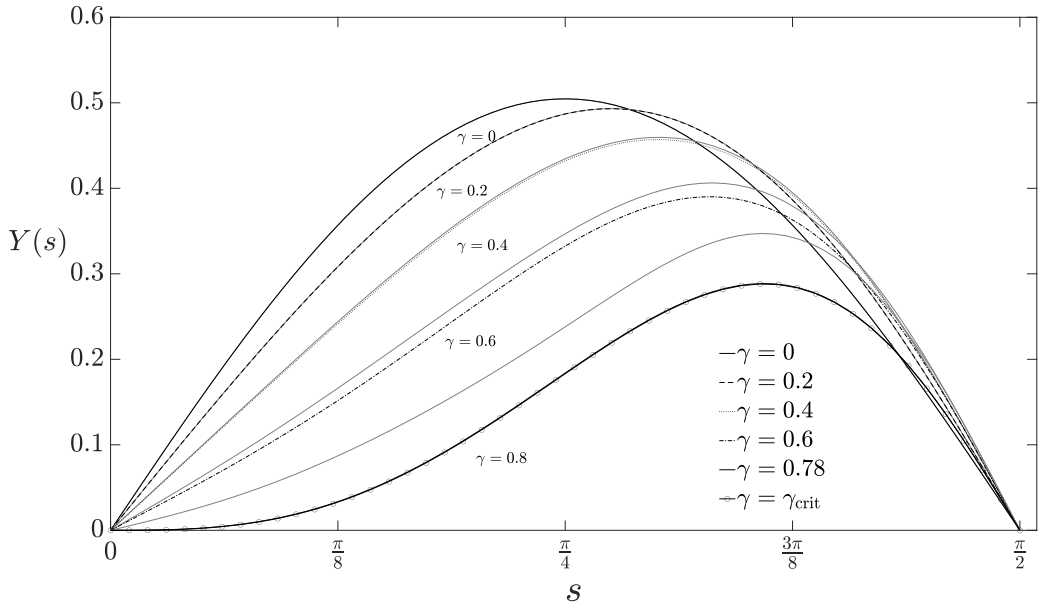

Figure 5.5: Numerical and asymptotic solutions of (5.26)–(5.30) for the eigenfunction Y at $\gamma = 0, 0.2, 0.4, 0.6, 0.78, \gamma_{\text{crit}}$, plotted as a function of $s \in (0, \pi/2)$. Numerical solutions are plotted using a variety of line-styles, whereas asymptotic solutions are plotted as solid grey curves. Details of the solution corresponding to $\gamma = \gamma_{\text{crit}}$ can be found in §5.5.

value λ, the base-state curvature $\bar{B}$ at $s = 0$ and the first derivative of the eigenfunction Y at $s = 0$ as functions of γ. For the eigenvalue, our results demonstrate that an increase in γ amounts to a reduction in λ. As before, we observe excellent agreement between the asymptotic and numerical solutions. For the curvature, we observe that the magnitude of $\bar{B}(0)$ reduces with an increase in γ and is approximately linear. For $Y'(0)$, we observe that an increase in γ amounts to a reduction in the magnitude of $Y'(0)$, and that the profile is approximately linear at smaller values of γ. We observe that these numerical results indicate that there exists some γ_{crit} such that $\bar{B}(0) \to 0$ and $Y'(0) \to 0$ as $\gamma \to \gamma_{\text{crit}} \approx 0.78$. In the following section, we argue that the dual limit $\bar{B}(0) \to 0$ and $Y'(0) \to 0$ as $\gamma \to \gamma_{\text{crit}}$ results in

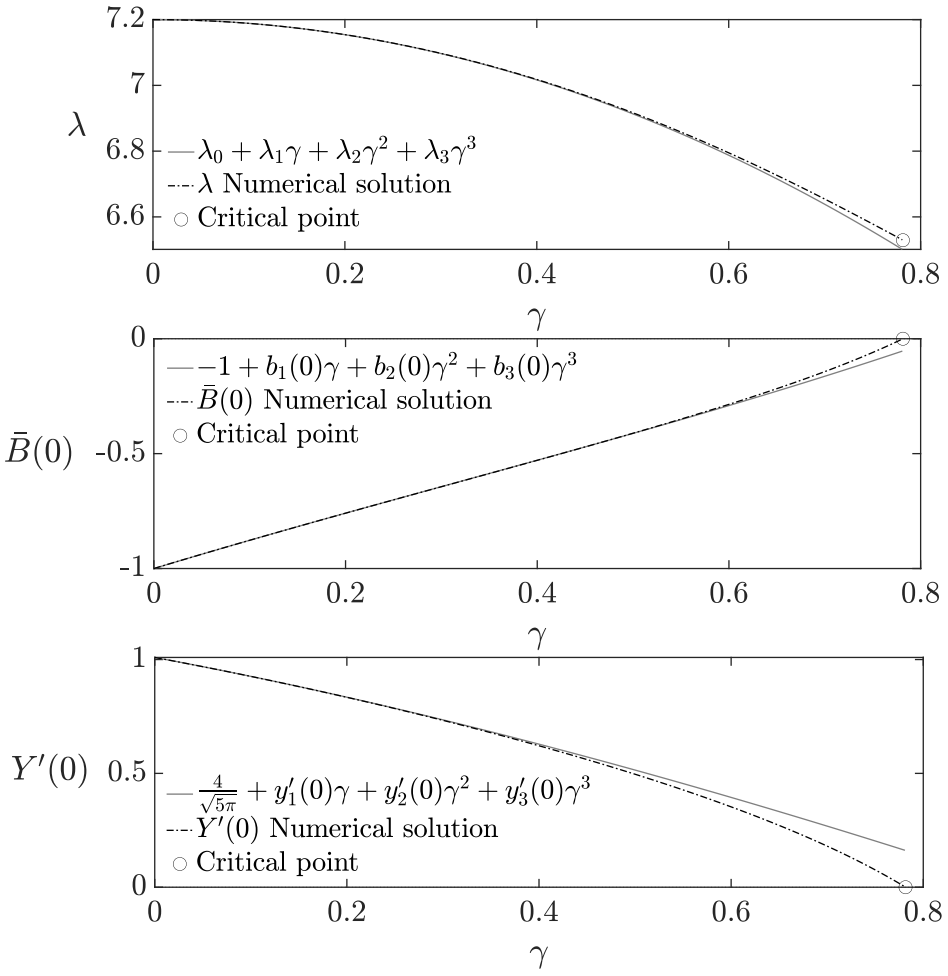

Figure 5.6: Numerical and asymptotic solutions for (top) the eigenvalue λ, (middle) the base-state curvature $\bar{B}$ evaluated at $s = 0$ and (bottom) the eigenfunction derivative Y' evaluated at zero, all plotted as functions of $\gamma \in [0, \gamma_{\text{crit}}]$. The solution at $\gamma = \gamma_{\text{crit}}$ is plotted using an open circle. Details of the solution corresponding to $\gamma = \gamma_{\text{crit}}$ can be found in §5.5.

the governing equations of (5.26)–(5.30) becoming singular, which explains the numerical issues encountered in this section. We investigate this further below, and also solve for the limiting form of the solution at $\gamma = \gamma_{\text{crit}}$.

5.5 The critical value $\gamma = \gamma_{\text{crit}}$

We now investigate the cause of the numerical solvers failure to find solutions for larger γ. Re-arranging equation (5.27), we find that an expression for $\bar{B}'(s)$ is given by

$$\frac{\mathrm{d}\bar{B}}{\mathrm{d}s} = -\frac{\gamma\bar{B}\left[Y\bar{B} - \frac{\mathrm{d}}{\mathrm{d}s}\left(\frac{1}{\bar{B}}\frac{\mathrm{d}Y}{\mathrm{d}s}\right)\right]}{1 + \frac{\gamma}{\bar{B}}\frac{\mathrm{d}Y}{\mathrm{d}s}}. \tag{5.88}$$

Hence, if the denominator of (5.88) ever becomes zero within the domain, then there is a singularity in the system (5.26)–(5.30). We hypothesise that the appearance of this singularity is the cause of the apparent termination of the branch of solutions ending at $\gamma = \gamma_{\text{crit}}$.

5.5.1 Numerical evidence for the singularity formation

In figure 5.7 we plot numerical solutions for the denominator $1+\gamma Y'(s)/\bar{B}(s)$ of (5.88) as a function of arclength as well as numerical and asymptotic predictions for the endpoint $1 + \gamma Y'(0)/\bar{B}(0)$ as a function of γ. The plots indicate that as γ is increased to some critical value, the denominator of (5.88) approaches zero at $s = 0$. We can associate this behaviour with the dual limit $\bar{B}, Y' \to 0$ as $\gamma \to \gamma_{\text{crit}}$, (see the numerical results presented in §5.4.2) resulting in a distinguished limit for $Y'/\bar{B}$. This analysis indicates the possibility of a limiting solution, valid as $\gamma \to \gamma_{\text{crit}}$. We explore this solution in §5.5.3.

Observing figure 5.3, we see that for every $\gamma > 0$, the base-state curvature $\bar{B}(s) < 0$ has a negative global maximum occurring at $s = 0$. The profile for $\bar{B}$ then decays monotonically until it reaches its global minimum, which occurs at $s = \pi/2$. The profile for $Y'(s)$ is similar to this, however differs in

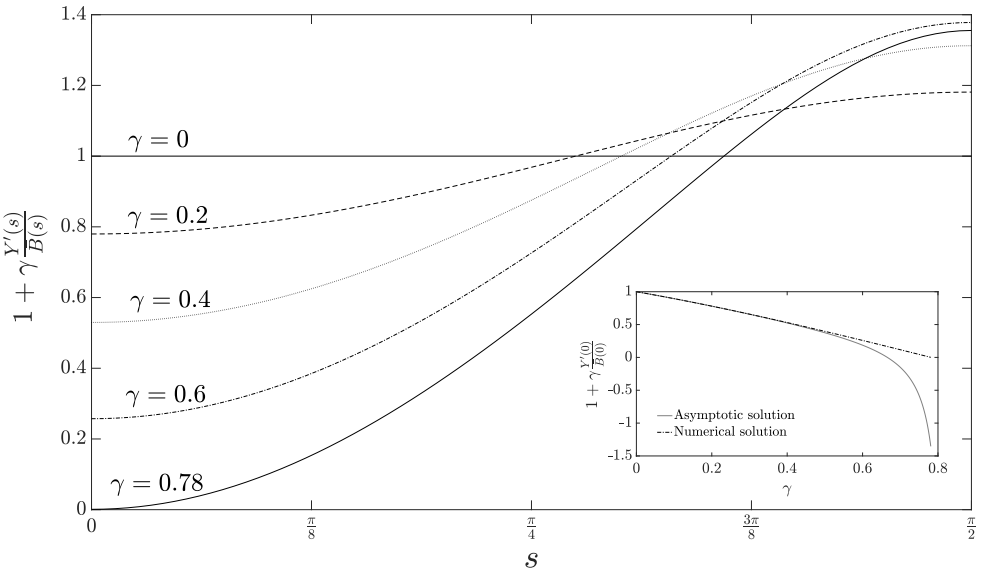

Figure 5.7: Numerical solutions for the denominator $\bar{B}(s) + \gamma Y'(s)$ of (5.88) as a function of arclength. The inset shows numerical and asymptotic predictions for the endpoint $\bar{B}(0) + \gamma Y'(0)$ as a function of γ.

that its global maximum is fixed by the normalisation at a positive value. The profile for Y' then decays monotonically until it reaches its global minimum, which is negative. Consequently, we expect that if $\gamma = \gamma_{\text{crit}}$ does indeed correspond to the first occasion in which (5.88) becomes singular, then this singularity will occur at $s = 0$.

5.5.2 Possibility of a singularity in the interior of the domain

If solutions were to exist with $\gamma > \gamma_{\text{crit}}$, it seems likely that a zero of $1+\gamma Y'/\bar{B}$ would lie inside the domain $s \in (0, \pi/2)$. We now consider the possibility of this singularity in (5.88) occurring at a point $s = s_0 \in (0, \pi/2)$. Unless the numerator of (5.88) also vanishes at this point, there will be singularity in

$\bar{B}'$ at $s = s_0$. After observing the governing equation (5.5) for the case in which the pressure is azimuthally uniform, we can see that the forcing term $f^{(\eta)}$ on the right hand side can be written as

$$f^{(\eta)} = \tilde{P}(z,t)\frac{1}{B(s)^2}\frac{\mathrm{d}\bar{B}}{\mathrm{d}s}. \tag{5.89}$$

Hence, for an imposed non-zero transmural pressure $\tilde{P}$, if $\bar{B}'$ is to contain a singularity at some point in the domain, then either the curvature must become infinite at that point, or $f^{(\eta)}$ will also contain a singularity there. For the former, it could be possible to construct a solution of (5.26)–(5.30) where the curvature becomes infinite at a point. This would result in a cross-sectional shape with sharp corners. However, this is physically unrealistic in the biological contexts considered here, so we proceed under the assumption that the global solution for the curvature remains finite. For the latter, since $f^{(\eta)}$ balances a combination of three forces, it should not contain a singularity. Hence, we arrive at the conclusion that if the problem (5.26)–(5.30) contains a non-removable singularity in $\bar{B}'$, then the resulting solution will be unphysical.

In order for the singularity to be removable in (5.88), we require either $\bar{B} = 0$ or $\bar{B}Y - \left(Y'/\bar{B}\right)' = 0$ at $s = s_0$. Both of these situations are possible, however, we note that if $\bar{B}(s_0) = 0$, then in order to avoid $f^{(\eta)}$ becoming singular, we require an additional condition, namely that $\bar{B}'(s_0) = 0$.

At an interior point in the domain, neither of the conditions $\bar{B}Y - \left(Y'/\bar{B}\right)' = 0$ or $\bar{B} = 0$ at $s = s_0$ are satisfied (in general) automatically, so to have a removable singularity in (5.88) we are required to impose one of them as an extra condition on the system. In figure 5.8 we provide a visual

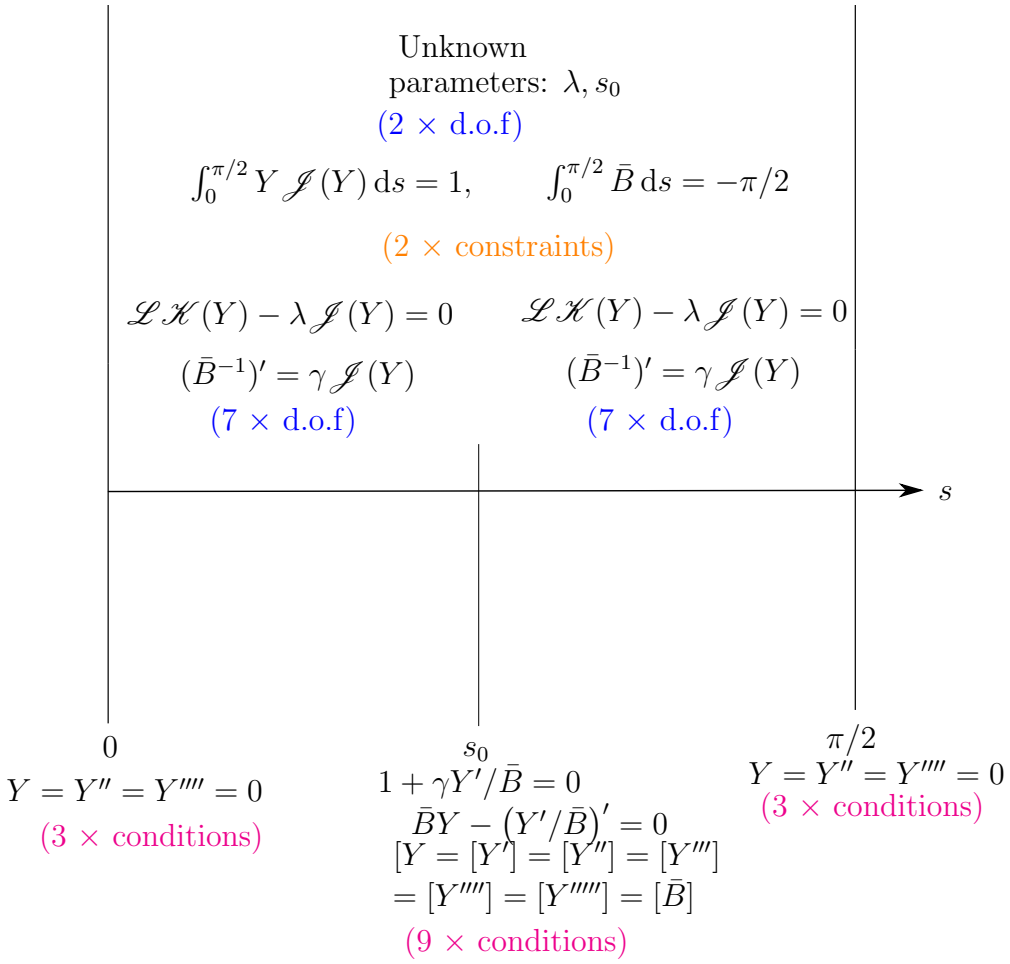

Figure 5.8: Visual description of the system (5.26)–(5.30) together with the additional conditions $1 + \gamma Y'/\bar{B} = 0$ and $\bar{B}Y - \left(Y'/\bar{B}\right)' = 0$ at $s = s_0$. The degrees of freedom (d.o.f) are labelled in blue, the integral constraints are labelled in orange, and the conditions at the boundaries and $s = s_0$ interface are labelled in magenta. In total the system comprises of 16 degrees of freedom, 15 boundary/interface conditions and 2 integral constraints.

description of the system (5.26)–(5.30) together with the extra conditions $1 + \gamma Y'/\bar{B} = 0$ and $\bar{B}Y - \left(Y'/\bar{B}\right)' = 0$ at $s = s_0$. (The same argument can be made by choosing to impose $\bar{B} = 0$ rather than $\bar{B}Y - \left(Y'/\bar{B}\right)' = 0$ at $s = s_0$.) The figure shows that in total the system involves 16 degrees of freedom, and 17 conditions/constraints (15 boundary conditions + 2 integral

constraints). Hence, imposing either $\bar{B}Y - \left(Y'/\bar{B}\right)' = 0$ or $\bar{B} = 0$ at $s = s_0$ results in the system becoming over-determined. We therefore conclude that a physical solution of (5.26)–(5.30) for $\gamma > \gamma_{\text{crit}}$ can exist (at most) discrete values of γ.

5.5.3 Computing γ_{crit} and the limiting solution at $\gamma = \gamma_{\text{crit}}$

On the assumption that $1 + \gamma Y'/\bar{B} = 0$, and $\bar{B} = Y' = 0$ at $s = 0$ when $\gamma = \gamma_{\text{crit}}$, we now seek a limiting solution of the system (5.26)–(5.30) and at the same time obtain a precise numerical value for γ_{crit}. As before, we will initially seek a numerical solution of the revised system (5.62)–(5.67) (written as the first-order system specified in §5.4.1) and then rescale the solutions to satisfy the required integral normalisations.

Examining (5.88), we see that the denominator in the expression for $\mathrm{d}\bar{B}(s)/\,\mathrm{d}s$ will vanish at $s = 0$. However, owing to the boundary conditions $Y = Y'' = 0$ at $s = 0$ the numerator will vanish there also. Hence, the singularity should be removable, although it may still cause numerical difficulties.

We therefore propose to solve the system (5.62)–(5.67) for $\tilde{Y}(s), \bar{B}(s)$ and λ, with the additional condition

$$1 + \frac{\tilde{\gamma}}{\bar{B}} \frac{\mathrm{d}\tilde{Y}}{\mathrm{d}s} = 0, \qquad \text{at} \qquad s = 0, \tag{5.90}$$

while treating $\tilde{\gamma}$ as an additional unknown. By the revised normalisation condition (5.67), we can immediately use (5.90) to deduce that $\tilde{\gamma} = 1$.

Due to the singularity at $s = 0$, we restrict the numerical domain to $(\epsilon, \pi/2)$ for some small ϵ, and instead determine a series solution on the domain $(0, \epsilon)$ in order to determine the correct boundary conditions to apply in the numerical scheme at $s = \epsilon$.

To obtain the series solutions, we wrote down general expansions for each of the variables $u_1, u_2, \ldots, u_8$, in powers of s. The coefficients in the expansions of the different variables are related by the need for the expansions to satisfy the differential equations (5.78)–(5.85). Some of the coefficients will be set by the boundary conditions at $s = 0$, but some will be functions of unknown constants to be determined as part of the global solution. Since we require four boundary conditions to be satisfied at $s = \pi/2$, our expansions need to involve precisely four unknown constants, which we shall denote $\{a, b, c, d\}$.

The boundary conditions (5.87) together with the assumptions $\bar{B} = Y' = 0$ at $s = 0$ specify seven of the coefficients. We also assume that the leading-order component of u_8 is $O(s^2)$ based on the numerical results obtained in §5.4 (see figure 5.3).

The values of the two variables with no conditions imposed at $s = 0$ are natural to set as two of the four unknown constants. Thus, we set $u_4(0) = b$ and $u_6(0) = c$. We also set the leading-order component of the curvature as another unknown constant: $u_8''(0) = -a$. The expansions are then substituted into equations (5.78)–(5.85) to obtain expressions coupling the remaining coefficients. We found that in order to avoid a singularity in (5.83), we were required to set $\lambda = c$. The remaining coefficients were found to be coupled, and could all be written in terms of $u_6''(0)$ and the unknown constants

$\{a, b, c\}$. We therefore set $u_6''(0) = d$, our final unknown constant. The final expressions take the form:

$$u_1(s) = \frac{a}{6}s^3 + O(s^4), \tag{5.91}$$

$$u_2(s) = 1 + \frac{b}{2}s^2 + O(s^4), \tag{5.92}$$

$$u_3(s) = bs + \frac{c}{6}s^3 + O(s^4), \tag{5.93}$$

$$u_4(s) = b + \frac{c}{2}s^2 + O(s^4), \tag{5.94}$$

$$u_5(s) = cs + \frac{d}{6}s^3 + O(s^4), \tag{5.95}$$

$$u_6(s) = c + \frac{d}{2}s^2 + O(s^4), \tag{5.96}$$

$$u_7(s) = \frac{a}{6}s^3 + O(s^4), \tag{5.97}$$

$$u_8(s) = -\frac{a}{2}s^2 + O(s^4). \tag{5.98}$$

Using the expansions (5.91)–(5.98), we can determine the boundary conditions to be applied at $s = \epsilon$. The numerical scheme implemented in §5.4.1 was then replicated, where the chosen initial guess was the solution at $\gamma = 0.78$ ($\tilde{\gamma} = 0.990$), which was interpolated on the domain $(\epsilon, \pi/2)$. The solution of (5.26)–(5.30) at $\gamma = \gamma_{\text{crit}}$ has been included in all of the figures shown in §5.4.2. Notably, we observe that in all cases as γ increases through the interval $\gamma \in [0, \gamma_{\text{crit}})$, the corresponding numerical solutions appear to converge to the solution at the critical $\gamma = \gamma_{\text{crit}} = 0.7815$.

5.6 Conclusions

In this chapter, we have derived a model for the wall deformation of an elastic-walled tube of arbitrary initial cross-sectional shape, and sought a family of initial shapes with the property that an azimuthally uniform transmural pressure will excite only a single azimuthal deformation mode.

To generalise the model set out in Chapter 3, we first adopted the setup and governing equations of Chapter 2 in terms of an arclength co-ordinate, s. The eigenfunction expansion method used throughout Chapter 3 was then replicated to obtain a system of generalised tube-laws that measure the change in cross-sectional area of the tube.

Once a generalised model for an arbitrary initial cross-section had been established, we sought a family of initial cross-sectional shapes with the property that an azimuthally uniform transmural pressure would excite only the first azimuthal deformation mode. In order to achieve this, we sought a solution to a revised eigenvalue problem, in which we treated the base-state curvature $\bar{B}$ — which defines the cross-sectional shape — as an unknown dependent variable. To ensure that only the first azimuthal mode was excited by the pressure, we found that the curvature $\bar{B}$ needed to satisfy the additional equation

$$\frac{\mathrm{d}}{\mathrm{d}s}\left(\frac{1}{\bar{B}(s)}\right) = \gamma Y_1, \tag{5.99}$$

for some constant γ. (Given the orthogonality relation (5.17) and the expression (5.21), this ensures the modes with $n \geq 2$ have zero forcing.)

The constant γ is a measure of the non-circularity of the initial cross-sectional shape. For different prescribed values of γ, the revised eigenvalue

problem was solved numerically for the eigenfunction Y, with corresponding eigenvalue λ and the base-state curvature $\bar{B}$. We found that we were able to obtain distinct solution on the domain $\gamma \in [0, \gamma_{\text{crit}})$, where γ_{crit} corresponds to the first value of γ in which the first derivative of the base-state curvature encounters a singularity. After investigating the appearance of this singularity, we argued that in order for the corresponding solution to be physical, then the singularity must be removable. In general, we found that the action of removing the singularity places an additional condition on the system, which results in it becoming overdetermined. This led us to the conclusion that physical solutions of the revised eigenvalue problem with $\gamma > \gamma_{\text{crit}}$ can only exist at discrete values of γ.

We obtained a solution of the revised eigenvalue problem when $\gamma = \gamma_{\text{crit}}$, in which the boundary conditions on the eigenfunction result in the singularity being removable automatically. An extension to this work is to investigate the possibility that there are other locations at interior points in the domain such that the singularity is removable automatically, and whether a corresponding solution exists there.

An application of the work considered in this chapter is to re-visit the fluid-structure interaction problem considered in Chapter 4, but instead consider a tube with one of the unique cross-sectional shapes obtained above. Since the fluid pressure is azimuthally uniform at leading order for the parameter regimes considered here, we anticipate that using the cross-sectional shapes obtained above as a base-state configuration will provide simplification in the coupling between the modes at leading order.

Additional future work stemming from this chapter is to seek a family of

initial cross-sectional shapes with the property that a single $n \geq 2$ azimuthal mode is excited by an azimuthally uniform transmural pressure. This should be a relatively straight forward extension, since it would only require modifying the numerical method in §5.4 to use the analytical solutions from Chapter 3 for $n \geq 2$ as an initial guess when $\gamma = 0$. Solutions for $\gamma \neq 0$ can then be obtained using parameter continuation in γ.

APPENDICES

5.A Asymptotic expressions for the differential operators $\mathscr{J}(Y)$ and $\mathscr{LK}(Y)$ when $\gamma \ll 1$

Substituting (5.33)–(5.34) into (5.8) and using properties of the geometric series $(1-x)^{-1}$, we obtain asymptotic expressions for $\mathscr{J}(Y)$ and $\mathscr{LK}(Y)$. To $O(\gamma^3)$ we find that

$$\mathscr{J}(Y) = \frac{10}{\sqrt{5\pi}}\sin(2s) + \gamma \mathrm{J}_1(s) + \gamma^2 \mathrm{J}_2(s) + \gamma^3 \mathrm{J}_3(s) + O(\gamma^4), \tag{5.100}$$

where $\mathrm{J}_1, \mathrm{J}_2$ and J_3 are given explicitly by:

$$\mathrm{J}_1(s) = \frac{16}{\sqrt{5\pi}} b_1 \sin(2s) - \frac{8}{\sqrt{5\pi}} b_1' \cos(2s) + y_1 - y_1'', \tag{5.101}$$

$$\mathrm{J}_2(s) = \frac{16}{\sqrt{5\pi}}\left(\frac{3}{2}b_1^2 + b_2\right)\sin(2s) - \frac{8}{\sqrt{5\pi}}\left(3b_1 b_1' + b_2'\right)\cos(2s) - 2y_1' b_1' - 2b_1 y_1'' + y_2 - y_2'', \tag{5.102}$$

$$\begin{aligned}\mathrm{J}_3(s) = {} & \frac{16}{\sqrt{5\pi}}\left(2b_1^3 + 3b_1b_2 + b_3\right)\sin(2s) - \frac{8}{\sqrt{5\pi}}\left(3b_1'b_2 + 3b_1b_2' + b_3'\right)\cos(2s) \\ & - \frac{48}{\sqrt{5\pi}}b_1^2b_1' - 6y_1'b_1b_1' - 3y_1''b_1^2 - 2y_2'b_1' - 2b_2y_1'' - 2y_1'b_2' - 2b_1y_2'' \\ & + y_3 - y_3''. \end{aligned} \tag{5.103}$$

Similarly, we find that $\mathscr{LK}(Y)$ is given by

$$\mathscr{LK}(Y) = \frac{72}{\sqrt{5\pi}}\sin(2s) + \gamma\mathrm{LK}_1 + \gamma^2\mathrm{LK}_2 + \gamma^3\mathrm{LK}_3 + O(\gamma^4), \tag{5.104}$$

where:

$$\begin{aligned}\mathrm{LK}_1(s) = {} & -2y_1'''' - y_1^{(6)} - y_1'' - 171Ab_1''\sin(2s) + 86Ab_1'''\cos(2s) + 21Ab_1''''\sin(2s) \\ & - 2Ab_1^{(5)}\cos(2s) - 188Ab_1'\cos(2s) + 120Ab_1\sin(2s), \\ \mathrm{LK}_2(s) = {} & -2b_1y_1^{(6)} - y_2^{(6)} - (6Ab_1\cos(2s) + y_1')b_1^{(5)} - 2Ab_2^{(5)}\cos(2s) - 6b_1'y_1^{(5)} \\ & + (61Ab_1\sin(2s) - 22A\cos(2s)b_1' - 5y_1'' + y_1)b_1'''' + 21Ab_2''''\sin(2s) \\ & - 10b_1''y_1'''' - 2y_2'''' - 2y_2'''' + (177Ab_1'\sin(2s) - 40Ab_1''\cos(2s) \\ & + 246Ab_1\cos(2s) + 3y_1' - 10y_1''')b_1''' + 86Ab_2'''\cos(2s) \\ & + 120A(b_1'')^2\sin(2s) + (522Ab_1'\cos(2s) - 493Ab_1\sin(2s) + 3y_1'' \\ & + y_1)b_1'' + 2b_1y_1'' - 171Ab_2''\sin(2s) - y_2'' - (580Ab_1b_1' \\ & + 188Ab_2')\cos(2s) + (196Ab_1^2 - 372A(B_1')^2 + 120Ab_2)\sin(2s) \\ & + 2b_1'y_1', \end{aligned} \tag{5.105}$$

$$\begin{aligned}\mathrm{LK}_3(s) = {} & -66y_1'''b_1'b_1'' - y_3'' + 2y_2''b_1 + 2y_1'b_2' - ((12b_1^2A + 6Ab_2)\cos(2s) + 3y_1'b_1 \\ & + y_2')b_1^{(5)} - (6Ab_1\cos(2s) + y_1')b_2^{(5)} + (564A(b_1')^3 - (1152Ab_1^2 \\ & + 580Ab_2)b_1' - 580Ab_1b_2' - 188Ab_3')\cos(2s) + (256Ab_1^3 \end{aligned}$$

$$
\begin{aligned}
&- 1512Ab_1(b_1')^2 - 744Ab_2'b_1' + 392Ab_1b_2 + 120b_3A)\sin(2s) + 2(y_2'\\
&- y_1'b_1)b_1' - y_3^{(6)} - 10y_2''''b_1'' - 2y_2^{(6)}b_1 - 6y_2^{(5)}b_1' - 2y_3'''' - 6(3b_1b_1'\\
&+ b_2')y_1^{(5)} - (3b_1^2 + 2b_2)y_1^{(6)} + (177Ab_1'\sin(2s) - 40Ab_1''\cos(2s)\\
&+ 246Ab_1\cos(2s) + 3y_1' - 10y_1'''')b_2''' + (480Ab_1\sin(2s)\\
&- 192Ab_1'\cos(2s) - 30y_1'')(b_1'')^2 + (3b_1y_1'' + 240Ab_2''\sin(2s)\\
&+ 3y_2'' + (2100Ab_1b_1' + 522Ab_2')\cos(2s) + (816A(b_1')^2\\
&- 972Ab_1^2 - 493Ab_2)\sin(2s) - 3y_1'b_1' - y_1b_1 + y_2)b_1'' + (3b_2'' - 3(b_1')^2\\
&- b_1^2 + 2b_2)y_1'' + (522A\cos(2s)b_1' - 493Ab_1\sin(2s) + y_1)b_2''\\
&- (30b_1y_1''' + 10y_2''' + (160Ab_1\cos(2s) + 20y_1')b_1'' + 44b_1'y_1''\\
&+ 40Ab_2''\cos(2s) - (486Ab_1^2 - 136A(b_1')^2 + 246Ab_2)\cos(2s)\\
&- (706Ab_1b_1' + 177Ab_2')\sin(2s) - y_1b_1' - 3b_1y_1' - 3y_2')b_1''' + (y_2\\
&- 15b_1y_1'' - 5y_2'' - (88Ab_1b_1' + 22Ab_2')\cos(2s) + (121Ab_1^2\\
&+ 61Ab_2)\sin(2s) - 11y_1'b_1' + y_1b_1)b_1'''' + (61Ab_1\sin(2s)\\
&- 22Ab_1'\cos(2s) - 5y_1'' + y_1)b_2'''' - (24(b_1')^2 + 30b_1b_1'' + 10b_2'')y_1''''\\
&+ 21Ab_3''''\sin(2s) - 2Ab_3^{(5)}\cos(2s) - 171Ab_3''\sin(2s)\\
&+ 86Ab_3'''\cos(2s), \qquad (5.106)
\end{aligned}
$$

where $A = 2/(\sqrt{5\pi})$.

Chapter 6

Summary and conclusions

In this thesis, we have generalised the models of Whittaker et al. (2010b) and Walters et al. (2018) for the deformations of a long thin-walled initially elliptical elastic-walled tube to allow for arbitrary initial cross-sectional shapes and azimuthally varying transmural pressures. The first formal solution for the wall deformation of an initially elliptical tube was derived using an eigenfunction expansion method. This result was later generalised to produce a model for the wall mechanics of an elastic tube of arbitrary cross-sectional shape. This mechanistic model for the tube-wall deformation of an initially elliptical tube was then combined with the fluid mechanics model of Whittaker et al. (2010d) to produce an asymptotic description of the fluid-structure interaction arising from flow through a collapsible tube.

The physical problem that has been considered throughout this thesis was presented in Chapter 2. The set-up involved providing a description of the tube wall in its initial configuration, as well as the notation used to describe the displacements in the tube wall induced by an applied transmural pressure. The long thin-walled asymptotic regime used throughout this thesis was then introduced. The resulting physical set-up was similar to the set-up in Whittaker et al. (2010b), but differed due to modifications being required to accommodate the fact that the tube's base-state cross-sectional shape is arbitrary. By following the methodology set out by Whittaker et al. (2010b),

the governing problem for the tube-wall deformation was formulated in terms of the following PDE

$$\mathscr{L}(\mathscr{K}(\eta)) - \tilde{F}\frac{\partial^2}{\partial z^2}\mathscr{J}(\eta) + M\frac{\partial^2}{\partial t^2}\mathscr{J}(\eta) = -\frac{\partial}{\partial \tau}\left(\frac{\tilde{P}(\tau, z, t)}{\bar{B}(\tau)}\right), \qquad (6.1)$$

for the dimensionless azimuthal displacement function η, with respect to an arbitrary dimensionless azimuthal co-ordinate τ, a dimensionless axial co-ordinate z, and dimensionless time, t. Here $\mathscr{L}$, $\mathscr{K}$ and $\mathscr{J}$ are differential operators in τ, $\tilde{F}$ and M are the dimensionless axial tension and mass respectively, and $\bar{B}$ is the base-state azimuthal curvature. After providing a general framework, we defined two specific co-ordinates system in preparation for the analysis of future chapters. To facilitate the analysis of chapters 3 and 4, in which the wall deformation and subsequent fluid-structure interaction of flow through an initially elliptical tube is considered, we introduced the elliptical azimuthal co-ordinate system used by Whittaker et al. (2010b). To facilitate the analysis of Chapter 5, we introduced an intrinsic arclength co-ordinate system, which is a convenient co-ordinate system to use when the initial cross-sectional shape is unknown in advance.

In Chapter 3 we adopted the physical set-up from Chapter 2 for the case of an initially elliptical tube, and derived a formal series solution for the small-amplitude deformations of the tube that are induced by an applied transmural pressure. To obtain the solution, an eigenfunction expansion method was employed that resulted in the governing problem for η simplifying to a remarkably simple system (3.46) of uncoupled partial differential equations for the amplitude $a_n(z, t)$ of each azimuthal mode as a function of the axial co-ordinate z and time t. The main benefit of this approach is

that it alleviates the need to invoke ad hoc assumptions made by Whittaker et al. (2010b) and Walters et al. (2018) in order to decouple the modes. By relating each axial mode to an associated contribution to the change in area α_n, the following system of tube law like equations were derived

$$\tilde{F}\frac{\partial^2 \alpha_n}{\partial z^2} - M\frac{\partial^2 \alpha_n}{\partial t^2} - \lambda_n \alpha_n = -Q_n(z,t)t_n, \tag{6.2}$$

which collectively describe the relationship between the tube's cross-sectional area and the transmural pressure via the sum $\alpha(z,t) = \sum_{n=1}^{\infty} \alpha_n(z,t)$. Here λ_n is the eigenvalue of the eigenfunction $Y_n(\tau)$ of a generalised eigenvalue problem, Q_n measures the contribution from the pressure to the nth azimuthal eigenmode, and t_n is the component of the area change associated with the nth azimuthal eigenmode. The simplicity of the system of equations (6.2) is striking, and results in contributions from the higher-order azimuthal modes — which previous models were unable to obtain without major effort — being very easy to compute. We demonstrated a simple application of our new model for the wall deformation by considering the case of an imposed uniform transmural pressure. We showed than a solution for each area change contribution α_n could be determined analytically, and formally verified the hypothesis of Whittaker et al. (2010b) that the fundamental azimuthal mode provides the dominant contribution to the solution.

In Chapter 4, we produced an asymptotic description of the high-frequency fluid-structure interaction arising from the flow through an initially elliptical long thin-walled elastic-walled tube. To produce the model, we combined our own results for the wall deformation set out in Chapter 3 with the fluids model of Whittaker et al. (2010d). By decomposing the problem into

steady and oscillatory parts, we obtained series solutions for the steady contributions and oscillatory normal modes of the resulting system. The main advantage of using our results from Chapter 3 to model the wall deformation is the ability to include contributions from the higher-order azimuthal modes. Whilst for the oscillatory problem this did induce additional mathematical complexity (the azimuthal modes did not decouple at leading order), we leveraged the fact that contributions to the solution from each azimuthal mode decay rapidly with increasing mode number. This enabled us to obtain series expansions for the pressure and wall/fluid oscillation frequency, which resulted in the relatively simple computation of the errors incurred by truncating the expansions after a given azimuthal mode.

In Chapter 5, we derived a model for the wall deformation of an elastic tube with an arbitrary initial cross-sectional shape, and then used this model to compute a family of initial cross-sections such that an azimuthally uniform transmural pressure will excite only a single azimuthal deformation mode. This generalised model was derived by adopting the set-up of Chapter 2 in terms of the intrinsic arclength co-ordinate system, and replicating the eigenfunction expansion method set out in Chapter 3. The resulting model is the first three-dimensional model for the wall deformation of an elastic tube having an arbitrary cross-sectional shape. Having established a model for the deformations of a tube with arbitrary cross-section, as an application we treated the base-state curvature $\bar{B}$ — which defines the initial cross-section — as an additional unknown. The new dependent variable $\bar{B}$ was then required to satisfy an additional equation that ensures only a single azimuthal mode is excited by an azimuthally uniform transmural pressure. The system was

solved numerically. A one-parameter family of cross-sectional shapes was found where an azimuthally uniform transmural pressure only excites the first azimuthal mode. An asymptotic solution of the system was also found, and were in excellent agreement with the numerical results along the entire solution branch. The solution branch terminated unexpectedly at a moderate aspect ratio. Further investigation is needed in order to fully understand this.

The results obtained in this thesis have provided valuable insight into some of the unanswered questions that have arisen from the initial analysis of Whittaker et al. (2010c). In their work, an error of up to eight percent in the asymptotic prediction for the critical Reynolds number was found after comparing with direct numerical simulations. Possible primary sources of this error included azimuthal truncation in the solid mechanics, the neglect of Womersley layers in the fluid mechanics, and also the neglect of azimuthally non-uniform corrections in the fluid pressure. In this thesis, we have formally ruled out the possibility of azimuthal truncation as being a primary source of this error. Unlike in previous studies, the mathematical models produced here are also capable of including corrections from the fluid pressure. Since these corrections are azimuthally varying, the models for the wall mechanics derived in Chapter 3 and Chapter 5 that permit azimuthal variation in the transmural pressure are adequate for the analysis.

Appendix A

Completeness of the azimuthal eigenfunctions $Y_n(\tau)$

A.1 Introduction

In this Appendix we prove that the eigenfunctions of the generalised eigenvalue problem introduced in Chapter 3

$$\hat{\mathscr{L}}\hat{\mathscr{K}}(u) - \lambda\hat{\mathscr{J}}(u) = 0, \tag{A.1}$$

subject to the boundary conditions,

$$u = \frac{\mathrm{d}^2 u}{\mathrm{d}\tau^2} = 0 \qquad \text{on} \qquad \tau = 0, \pi/2 \tag{A.2}$$

and

$$\frac{\mathrm{d}^4 u}{\mathrm{d}\tau^4} = 0 \qquad \text{on} \qquad \tau = 0, \pi/2, \tag{A.3}$$

form a basis for the underlying Hilbert space. This result will enable us to expand a general function as a sum over the eigenfunctions of this system.

To prove the result, we make use of theorem 6.3.1 of Blanchard and Brüning (2012):

Theorem A.1.1 (The Discrete Spectral Theorem) *Let H and K be two*

real Hilbert spaces with scalar products $\langle\cdot,\cdot\rangle_H$ *and* $\langle\cdot,\cdot\rangle_K$, $\dim(K)=\infty$, *and assume the following:*

(i) K *is dense in* H*;*

(ii) the identical embedding $i : K \hookrightarrow H$ *is (continuous and) compact.*

Then for every symmetric bilinear form a *on* K *which satisfies*

(iii) a *is continuous,*

(iv) a *is coercive, i.e*

$$a(u,u) \geq c\,\|u\|^2, \quad c>0,\ \forall u \in K, \tag{A.4}$$

there is a monotone increasing sequence (λ_m) *of eigenvalues,*

$$0 \leq \lambda_1 \leq \lambda_2 \leq \cdots \leq \lambda_m \to +\infty \tag{A.5}$$

and an orthonormal basis $\{e_m\}_{m\in\mathbb{N}} \subset K$ *of* H *such that*

$$a(e_m, v) = \lambda_m \langle e_m, v\rangle_H,\ \forall v \in K, \forall m \in \mathbb{N}. \tag{A.6}$$

$\{v_m\} = \{\lambda_m^{-1/2} e_m\}$ *is an orthonormal basis of* K *with respect to the scalar product* $\langle\cdot,\cdot\rangle = a(\cdot,\cdot)$ *on* K*.*

The proof is organised as follows: in §A.2 we introduce the Sobolev spaces H^1 and H^3, and define the corresponding inner products for which they form Hilbert spaces. The spaces H^1 and H^3 are not directly applicable to Theorem A.1.1, since their elements are not required to satisfy the boundary conditions (A.2)–(A.3). Instead, we define the spaces H and K, which are

subspaces of H^1 and H^3 respectively, and allow the appropriate boundary conditions on the zeroth and second derivatives to be included within the definition. The conditions on the fourth derivative are shown to be satisfied later. The function spaces H and K are then equipped with carefully chosen inner products $\langle\cdot,\cdot\rangle_H$ and $\langle\cdot,\cdot\rangle_K$. In §A.3, we prove that the spaces H and K form Hilbert spaces with respect to $\langle\cdot,\cdot\rangle_H$ and $\langle\cdot,\cdot\rangle_K$ — as required in the hypothesis of theorem A.1.1 — by exploiting the fact that they are closed subspaces of the Sobolev spaces H^1 and H^3. In §A.4, we define the coercive, continuous, and symmetric bilinear form $a = \langle\cdot,\cdot\rangle_K$, such that Theorem A.1.1 yields a basis of eigenfunctions, u_j of a, satisfying:

$$\langle u_j, v\rangle_K = \gamma_j \langle u_j, v\rangle_H \qquad \forall v \in K. \tag{A.7}$$

Equation (A.7) highlights the delicacy in defining the inner products $\langle\cdot,\cdot\rangle_H$ and $\langle\cdot,\cdot\rangle_K$, since they must be chosen such that (A.7) can be re-written as the weak form (see §A.2.3) of (A.1). Finally, in §A.5 we call on results from one-dimensional regularity theory to show that the weak eigenfunctions u_j of (A.1)–(A.2) are in fact classical eigenfunctions. We then use this result to deduce that the condition on the fourth derivative of (A.1)–(A.2) is satisfied automatically. Hence, the u_j are a basis of eigenfunctions of the system (A.1)–(A.3).

A.2 Setup

In this section we define the various function spaces and inner products we shall need in the later sections.

A.2.1 The eigenvalue problem

In the eigenvalue problem (A.1)–(A.3), the linear differential operators $\hat{\mathscr{L}}, \hat{\mathscr{K}}$ and $\hat{\mathscr{J}}$ are given by:

$$\hat{\mathscr{L}}(y) = \frac{2h}{c^2 \cosh 2\sigma_0} \frac{\mathrm{d}}{\mathrm{d}\tau}\left(1 + \frac{\mathrm{d}^2}{\mathrm{d}\tau^2}\right)\left(\frac{y}{h}\right), \tag{A.8}$$

$$\hat{\mathscr{K}}(y) = \frac{-2}{c^2 \cosh 2\sigma_0} \frac{\mathrm{d}}{\mathrm{d}\tau}\left(1 + \frac{\mathrm{d}^2}{\mathrm{d}\tau^2}\right) y, \tag{A.9}$$

$$\hat{\mathscr{J}}(y) = \tanh^2(2\sigma_0)\left(1 - \frac{\mathrm{d}}{\mathrm{d}\tau}\left(\frac{1}{\bar{B}^2 h}\frac{\mathrm{d}}{\mathrm{d}\tau}\right)\right)\left(\frac{y}{h}\right). \tag{A.10}$$

and the functions $h(\tau)$ and $\bar{B}(\tau)$ are:

$$h(\tau) = c\left(\frac{1}{2}\cosh 2\sigma_0 - \frac{1}{2}\cos 2\tau\right)^{1/2} > 0, \quad \bar{B}(\tau) = \frac{c^2}{2h^3}\sinh 2\sigma_0, \tag{A.11}$$

where $c > 0$ is a constant. We note that the operators (A.8)–(A.10) have been manipulated into a different form to what was initially presented in chapter 3. This new form was found to be more convenient for the work in this Appendix.

A.2.2 Function spaces H and K

In order to make sense of the derivatives present in (A.1), we introduce the Sobolev spaces $H^1([0, \pi/2])$ and $H^3([0, \pi/2])$, which are defined in the usual way as:

$$H^1 = \{u(\tau) \in W^{1,2} \mid \tau \in (0, \pi/2)\}, \tag{A.12}$$

$$H^3 = \{u(\tau) \in W^{3,2} \mid \tau \in (0, \pi/2)\}, \tag{A.13}$$

where $W^{k,2}$ represents the Sobolev space of functions in $L^2([a,b])$ that permits weak derivatives up to order k (Gilbarg et al., 1977).

The function spaces H^1 and H^3 are important because they form Hilbert spaces when equipped with an appropriate inner product (see §A.2.4). However, with respect to (A.1)–(A.3) they do not capture the desired behaviour at the end-points of $(0, \pi/2)$. We therefore define the spaces H and K:

$$H = \{u(\tau) \in H^1 \mid u = 0 \text{ on } \tau = 0, \pi/2\}, \tag{A.14}$$

$$K = \{u(\tau) \in H^3 \mid u = u'' = 0 \text{ on } \tau = 0, \pi/2\}. \tag{A.15}$$

If the spaces H and K are equipped with equivalent inner products to those placed on H^1 and H^3 respectively, then they become closed subspaces of H^1 and H^3. This is important when proving that both H and K form Hilbert spaces when equipped with an appropriate inner product (see §A.3).

The spaces H and K do not directly capture the the necessary behaviour that the fourth derivative of u vanishes at the end-points $\tau = 0, \pi/2$. This is due to the fact that we were unable to include the extra condition into the definition of K above, since functions in $W^{3,2}$ and hence H^3 are not guaranteed to have a fourth derivative. We will show later (see §A.5) that the condition (A.3) on the fourth derivative is satisfied naturally by the eigenfunction solutions.

A.2.3 Weak formulation

On multiplying both sides of (A.1) by v/h, where $v \in K$, and integrating by parts, we obtain

$$\frac{4}{(c^2 \cosh 2\sigma_0)^2} \int_0^{\pi/2} \frac{1}{h}(u' + u''')(v + v''') \, \mathrm{d}\tau \\ = \lambda \tanh^2 2\sigma_0 \int_0^{\pi/2} \frac{1}{h} uv + \frac{1}{h\bar{B}^2} \left(\frac{u}{h}\right)' \left(\frac{v}{h}\right)' \mathrm{d}\tau. \tag{A.16}$$

This is known as the weak formulation of (A.1). Weak eigenfunctions $u = u_j$ of (A.1)–(A.3) are defined as functions $u \in K$ that satisfy (A.16) for all $v \in K$. We note that by this definition weak eigenfunctions are not guaranteed to satisfy boundary condition (A.3) on the fourth derivative. These conditions will turn out to be satisfied naturally in §A.5.

A.2.4 Inner products on H and K

We now equip the function spaces H and K with inner products that will be convenient when we call on the Discrete Spectral Theorem. First, we consider the canonical inner products for which H^1 and H^3 form Hilbert spaces (Adams and Fournier, 2003):

$$\langle u, v \rangle_{H^1} = \int_0^{\pi/2} uv + u'v' \, \mathrm{d}\tau, \tag{A.17}$$

$$\langle u, v \rangle_{H^3} = \int_0^{\pi/2} uv + u'v' + u''v'' + u'''v''' \, \mathrm{d}\tau. \tag{A.18}$$

The induced norms $\|u\|_{H^1}$ and $\|u\|_{H^3}$ are then defined in the usual way:

$$\|u\|_{H^1}^2 = \langle u, u\rangle_{H^1} = \int_0^{\pi/2} u^2 + (u')^2 \,\mathrm{d}\tau, \tag{A.19}$$

$$\|u\|_{H^3}^2 = \langle u, u\rangle_{H^3} = \int_0^{\pi/2} u^2 + (u')^2 + (u'')^2 + (u''')^2 \,\mathrm{d}\tau. \tag{A.20}$$

To allow the basis provided by Theorem A.1.1 to comprise the eigenfunctions of (A.1)–(A.3), we define functions $\langle\cdot,\cdot\rangle_H$ and $\langle\cdot,\cdot\rangle_K$, motivated by the weak formulation (A.16) of the eigenvalue problem. Specifically, we define:

$$\langle u, v\rangle_H = \tanh^2 2\sigma_0 \int_0^{\pi/2} \frac{1}{h}uv + \frac{1}{\bar{B}^2 h}\left(\frac{u}{h}\right)'\left(\frac{v}{h}\right)' \mathrm{d}\tau, \tag{A.21}$$

$$\begin{aligned}\langle u, v\rangle_K = {} & \frac{4}{(c^2\cosh 2\sigma_0)^2}\int_0^{\pi/2} \frac{1}{h}(u' + u''')(v' + v''')\,\mathrm{d}\tau \\ & + \frac{4\tanh^2 2\sigma_0}{(c^2\cosh 2\sigma_0)^2}\int_0^{\pi/2} \frac{1}{h}uv + \frac{1}{\bar{B}^2 h}\left(\frac{u}{h}\right)'\left(\frac{v}{h}\right)' \mathrm{d}\tau.\end{aligned} \tag{A.22}$$

Then the weak formulation (A.16) can then be written as

$$\langle u, v\rangle_K = \gamma\langle u, v\rangle_H, \tag{A.23}$$

where

$$\gamma = \lambda - \frac{4\tanh^2 2\sigma_0}{(c^2\cosh 2\sigma_0)^2}. \tag{A.24}$$

In our definition of $\langle u, v\rangle_K$, we had the freedom to add any constant multiple of $\langle u, v\rangle_H$ because this is just a translation of the eigenvalue. The constant multiple we chose simplifies the algebra in §A.3.

The associated induced norms for H and K are then defined in the usual

way:

$$\|u\|_H^2 = \tanh^2 2\sigma_0 \int_0^{\pi/2} \frac{1}{h}u^2 + \frac{1}{\bar{B}^2 h}\left[\left(\frac{u}{h}\right)'\right]^2 \mathrm{d}\tau, \tag{A.25}$$

$$\|u\|_K^2 = \frac{4}{(c^2\cosh 2\sigma_0)^2}\int_0^{\pi/2}(u' + u''')^2\,\mathrm{d}\tau + \frac{4\tanh^2 2\sigma_0}{(c^2\cosh 2\sigma_0)^2}\int_0^{\pi/2}\frac{1}{h}u^2 + \frac{1}{\bar{B}^2 h}\left[\left(\frac{u}{h}\right)'\right]^2 \mathrm{d}\tau. \tag{A.26}$$

It is important that the relationships (A.21)–(A.22) do indeed define inner products on the spaces H and K. That is, they are real-valued, positive-definite symmetric bilinear forms on each space (Axler, 1997).

Clearly (A.21)–(A.22) show that both $\langle u, v\rangle_H$ and $\langle u, v\rangle_K$ define symmetric bilinear forms, that is, they are linear in u and v, and satisfy the symmetry property:

$$\langle u, v\rangle_H = \langle v, u\rangle_H, \quad \langle u, v\rangle_K = \langle u, v\rangle_K. \tag{A.27}$$

To show that $\langle u, v\rangle_H$ and $\langle u, v\rangle_K$ are positive-definite we consider the corresponding norms as defined in (A.25)–(A.26). Equation (A.25) shows that if $\|u\|_H = 0$ then $|u|^2 \equiv 0$. Similarly, equation (A.26) also shows that when $\|u\|_K = 0$ then $|u|^2 \equiv 0$. Hence, both (A.21)–(A.22) define positive definite symmetric bilinear forms, that is, they are inner products on the spaces H and K respectively.

A.3 H and K as Hilbert spaces

We now argue that the spaces H and K form Hilbert spaces when equipped with the inner products (A.21)–(A.22).

The function spaces H^1 and H^3 equipped respectively with the inner products $\langle\cdot,\cdot\rangle_{H_1}$ and $\langle\cdot,\cdot\rangle_{H_3}$ given in (A.17)–(A.18) are Hilbert spaces. The spaces H and K equipped respectively with the inner products $\langle\cdot,\cdot\rangle_H$ and $\langle\cdot,\cdot\rangle_K$ given in (A.21)–(A.22) are closed subspaces of H^1 and H^3 respectively. Since every closed subspace of a Hilbert space is itself a Hilbert space (Hislop and Sigal, 2012), the spaces H and K equipped respectively with $\langle\cdot,\cdot\rangle_H$ and $\langle\cdot,\cdot\rangle_K$ are also Hilbert spaces. A Hilbert space is a complete inner product space. Hence, H and K are complete with respect to the inner products (A.17)–(A.18). This means that every Cauchy sequence in the space H will converge, with respect to the norm $\|\cdot\|_{H^1}$ (given by (A.19)) induced by $\langle\cdot,\cdot\rangle_{H^1}$ to a limit inside of H. The same argument can be made about the space K with the inner product $\langle\cdot,\cdot\rangle_H$ and the associated induced norm $\|\cdot\|_{H^3}$.

Provided that H and K are equipped with inner products that respectively induce equivalent norms to $\|\cdot\|_{H^1}$ and $\|\cdot\|_{H^3}$, then they will have equivalent convergence properties, and hence will be Hilbert spaces also. In other words, if we can show that the norms $\|\cdot\|_H$ and $\|\cdot\|_K$ are equivalent to $\|\cdot\|_{H^1}$ and $\|\cdot\|_{H^3}$, then it follows that H and K form Hilbert spaces when equipped with the inner products (A.21)–(A.22). We dedicate the remainder of this section to proving these results.

A.3.1 Equivalence of the norms $\|u\|_H$ and $\|u\|_{H^1}$

The norms $\|u\|_H$ and $\|u\|_{H^1}$ are equivalent if and only if there exist positive constants C_1, C_2 such that

$$C_1 \|u\|_{H^1} \leq \|u\|_H \leq C_2 \|u\|_{H^1}, \qquad \forall u \in H. \tag{A.28}$$

Recall the norms for H and H^1:

$$\|u\|_H^2 = \tanh^2 2\sigma_0 \int_0^{\pi/2} \frac{1}{h} u^2 + \frac{1}{\bar{B}^2 h} \left[\left(\frac{u}{h} \right)' \right]^2 \mathrm{d}\tau, \tag{A.29}$$

$$\|u\|_{H^1}^2 = \int_0^{\pi/2} u^2 + (u')^2 \, \mathrm{d}\tau. \tag{A.30}$$

We will prove the two inequalities in (A.28) separately.

Lower bound: $C_1 \|u\|_{H^1} \leq \|u\|_H \ \forall u \in H$

We shall start with the norm $\|u\|_{H^1}$ and show that it is bounded above by a multiple of $\|u\|_H$. We let $u \in H$, and define $v(\tau) = u/h$. Substituting $u = vh$ in (A.30) and expanding the second term using the product rule, we obtain

$$\|u\|_{H^1}^2 = \int_0^{\pi/2} h^2 v^2 + \left[(h')^2 v^2 + \frac{1}{2} \left(h^2\right)' \left(v^2\right)' + h^2 \left(v'\right)^2 \right] \mathrm{d}\tau \tag{A.31}$$

Integrating the second term by parts, noting that v vanishes at the end-points of $(0, \pi/2)$ since $u \in H$, we obtain:

$$\|u\|_{H^1}^2 = \int_0^{\pi/2} \left[h^2 + (h')^2 - \frac{1}{2}(h^2)'' \right] v^2 + h^2 (v')^2 \, \mathrm{d}\tau, \tag{A.32}$$

$$= \int_0^{\pi/2} (h - h'') \frac{1}{h} u^2 + h^2 \left[\left(\frac{u}{h} \right)' \right]^2 \mathrm{d}\tau, \tag{A.33}$$

$$= \tanh^2 2\sigma_0 \int_0^{\pi/2} f_1(\tau)\frac{1}{h}u^2 + g_1(\tau)\frac{1}{h\bar{B}^2}\left[\left(\frac{u}{h}\right)'\right]^2 \mathrm{d}\tau, \tag{A.34}$$

where:

$$f_1(\tau) = \frac{h}{\tanh^2 2\sigma_0}\left(1 - \frac{1}{h}h''\right), \quad g_1(\tau) = \frac{h^3\bar{B}^2}{\tanh^2 2\sigma_0}. \tag{A.35}$$

Now f_1 and g_1 are clearly bounded above on $(0, \pi/2]$. Let M_1 be a positive upper bound, given by

$$M_1 = \max_{\tau\in[0,\pi/2]}(f_1(\tau), g_1(\tau), 1). \tag{A.36}$$

We then have

$$\|u\|_{H^1}^2 \leq M_1 \tanh^2 2\sigma_0 \int_0^{\pi/2} \frac{1}{h}|u|^2 + \frac{1}{\bar{B}^2 h}\left[\left(\frac{u}{h}\right)'\right]^2 \mathrm{d}\tau = M_1 \|u\|_H^2 . \tag{A.37}$$

Hence, by setting $C_1 \equiv M_1^{-1/2}$, it follows that $C_1 \|u\|_{H^1} \leq \|u\|_{H^1}$.

Upper bound: $\|u\|_H \leq C_2 \|u\|_{H^1} \ \forall u \in H$

Let $u \in H$. By expanding the derivative of u/h present in (A.29) using the product rule, we find that

$$\left[\left(\frac{u}{h}\right)'\right]^2 = \frac{h'}{h^2}u^2 + \left(\frac{1}{h}\right)^2 (u')^2 - \frac{2h'}{h^3}uu' \tag{A.38}$$

Substituting (A.38) into (A.29), we obtain

$$\|u\|_H^2 = \tanh^2 2\sigma_0 \int_0^{\pi/2} \frac{1}{h}\left(1 + \frac{(h')^2}{h^4\bar{B}^2}\right)u^2 + \frac{1}{h^3\bar{B}^2}(u')^2 - \frac{h'}{h^4\bar{B}^2}(u^2)' \,\mathrm{d}\tau. \tag{A.39}$$

Using integration by parts on the final term of (A.39), noting that u vanishes at the end-points of $(0, \pi/2)$, we find that

$$\|u\|_H^2 = \tanh^2 2\sigma_0 \int_0^{\pi/2} \frac{1}{h}\left[1 + \frac{(h')^2}{h^4\bar{B}^2} + h\left(\frac{h'}{h^4\bar{B}^2}\right)'\right]u^2 + \frac{1}{h^3\bar{B}^2}(u')^2 \,\mathrm{d}\tau, \tag{A.40}$$

$$= \int_0^{\pi/2} f_2(\tau)u^2 + g_2(\tau)(u')^2 \,\mathrm{d}\tau, \tag{A.41}$$

where

$$f_2(\tau) = \frac{\tanh^2 2\sigma_0}{h}\left[1 + \frac{(h')^2}{h^4\bar{B}^2} + h\left(\frac{h'}{h^4\bar{B}^2}\right)'\right], \tag{A.42}$$

$$g_2(\tau) = \frac{\tanh^2 2\sigma_0}{h^3\bar{B}^2}. \tag{A.43}$$

Clearly we can construct (positive) upper bounds for $f_1(\tau)$ and $g_1(\tau)$. Let $M_1 > 0$ such an upper bound, e.g. we might take

$$M_2 = \max_{\tau\in[0,\pi/2]}(f_2(\tau), g_2(\tau), 1). \tag{A.44}$$

Hence we have

$$\|u\|_H^2 \leq M_2 \int_0^{\pi/2} u^2 + (u')^2 \,\mathrm{d}\tau = M_2 \|u\|_{H^1}^2 . \tag{A.45}$$

Hence by setting $C_2 \equiv M_2^{1/2}$, it follows that $\|u\|_H \leq C_2 \|u\|_{H^1}$.

A.3.2 Equivalence of the norms $\|u\|_K$ and $\|u\|_{H^3}$

The norms $\|u\|_K$ and $\|u\|_{H^3}$ are equivalent if and only if there exist positive constants C_3, C_4 such that

$$C_3 \|u\|_{H^3} \leq \|u\|_K \leq C_4 \|u\|_{H^3}, \quad \forall u \in K. \tag{A.46}$$

Recall the norms for K and H^3:

$$\begin{aligned} \|u\|_K^2 = {} & \frac{4}{(c^2 \cosh 2\sigma_0)^2} \int_0^{\pi/2} \frac{1}{h}(u' + u''')^2 \, \mathrm{d}\tau \\ & + \frac{4 \tanh^2 2\sigma_0}{(c^2 \cosh 2\sigma_0)^2} \int_0^{\pi/2} \frac{1}{h} u^2 + \frac{1}{\bar{B}^2 h} \left[\left(\frac{u}{h} \right)' \right]^2 \mathrm{d}\tau, \end{aligned} \tag{A.47}$$

$$\|u\|_{H^3}^2 = \int_0^{\pi/2} u^2 + (u')^2 + (u'')^2 + (u''')^2 \, \mathrm{d}\tau. \tag{A.48}$$

To prove (A.46) we adopt a similar approach to that of §A.3.1, and consider each inequality in turn.

Lower bound: $C_3 \|u\|_{H^3} \leq \|u\|_K \ \forall u \in K$

It is convenient to start with the norm $\|u\|_{H^3}$ and show that it is bounded above by a multiple of $\|u\|_K$. Due to the presence of $(u''' + u')^2$ in $\|u\|_K$, we introduce $w = u'' + u$, with the aim of writing $\|u\|_K^2$ in terms of $w^2, (w')^2, u^2$ and $(u')^2$. To this end, we find that

$$\|u\|_{H^3}^2 = \int_0^{\pi/2} u^2 + (u')^2 + (u'')^2 + (u''')^2 \, \mathrm{d}\tau,$$

$$= \int_0^{\pi/2} \Big[(u''')^2 + 2(u'''u') + (u')^2\Big] + 3\Big[(u'')^2 + 2(u''u) + u^2\Big] + 6(u')^2 - 2(u)^2 - 2\Big[(u'''u') + (u'')^2\Big] - 6\Big[(u''u) + (u')^2\Big]\,\mathrm{d}\tau,$$

$$= \int_0^{\pi/2} (w')^2 + 3w^2 + 6(u')^2 - 2u^2 - 2\Big[(u''u')' - 6(u'u)'\Big]\,\mathrm{d}\tau, \quad \text{(A.49)}$$

The boundary conditions on the space K mean that terms in square brackets in the final line vanish. Thus, we obtain

$$\|u\|_{H^3}^2 = \int_0^{\pi/2} (w')^2 + 3w^2 + 6(u')^2 - 2u^2\,\mathrm{d}\tau. \quad \text{(A.50)}$$

To deal with the w^2 term, we require an additional lemma.

Lemma A.3.1 *Let $w \in H$, then there exists positive constant C such that*

$$\int_0^{\pi/2} w^2\,\mathrm{d}\tau \leq C \int_0^{\pi/2} (w')^2\,\mathrm{d}\tau. \quad \text{(A.51)}$$

Proof A.3.1 *Let $w \in H$ and consider the following:*

$$\int_0^{\pi/2} 1 \times w^2\,\mathrm{d}\tau = \Big[\tau w^2\Big]_0^{\pi/2} - \int_0^{\pi/2} \tau (w^2)'\,\mathrm{d}\tau, \quad \text{(A.52)}$$

$$= 0 - 2\int_0^{\pi/2} \tau w w'\,\mathrm{d}\tau, \quad \text{(A.53)}$$

$$\leq 2\left|\int_0^{\pi/2} \tau w w'\,\mathrm{d}\tau\right|, \quad \text{(A.54)}$$

$$\leq \max_{\tau\in[0,\pi/2]}(|2\tau|)\int_0^{\pi/2} |ww'|\,\mathrm{d}\tau, \quad \text{(A.55)}$$

$$\leq \pi\int_0^{\pi/2} |ww'|\,\mathrm{d}\tau. \quad \text{(A.56)}$$

The Cauchy-Schwartz inequality gives the following:

$$\int_0^{\pi/2} |ww'| \, \mathrm{d}\tau \leq \left(\int_0^{\pi/2} w^2 \, \mathrm{d}\tau \right)^{1/2} \left(\int_0^{\pi/2} (w')^2 \, \mathrm{d}\tau \right)^{1/2}, \tag{A.57}$$

Hence, we find that

$$\int_0^{\pi/2} w^2 \, \mathrm{d}\tau \leq \pi \left(\int_0^{\pi/2} w^2 \, \mathrm{d}\tau \right)^{1/2} \left(\int_0^{\pi/2} (w')^2 \, \mathrm{d}\tau \right)^{1/2}, \tag{A.58}$$

which yields the result

$$\int_0^{\pi/2} w^2 \, \mathrm{d}\tau \leq \pi^2 \int_0^{\pi/2} (w')^2 \, \mathrm{d}\tau. \tag{A.59}$$

Hence, the lemma is proved.

Using lemma (A.3.1) and recalling the definition of the operator $\hat{\mathscr{K}}(u)$ in (A.9), we find that:

$$\|u\|_{H^3}^2 \leq \int_0^{\pi/2} (C+3)(w')^2 + 6(u')^2 - 2u^2 \, \mathrm{d}\tau, \tag{A.60}$$

$$\leq \int_0^{\pi/2} \hat{C} \frac{1}{h} (u''' + u')^2 + 6(u')^2 - 2u^2 \, \mathrm{d}\tau, \tag{A.61}$$

where we have defined $\hat{C} > 0$, given explicitly by

$$\hat{C} = (C+3) \max_{\tau \in [0, \pi/2]} (h). \tag{A.62}$$

We now define $v(\tau) = u/h$ as before. Substituting $u = vh$ in the second term of (A.61) and expanding the derivative using the product rule; we find

that

$$\|u\|_{H^3}^2 \leq \int_0^{\pi/2} \hat{C}\frac{1}{h}(u''' + u')^2 + 6h'v^2 + 6h^2(v')^2 + 6hh'(v^2)' - 2u^2 \,\mathrm{d}\tau. \tag{A.63}$$

Integrating the fourth term of (A.63) directly and writing the result in terms of u; we find that:

$$\|u\|_{H^3}^2 \leq \int_0^{\pi/2} \hat{C}\frac{1}{h}(u''' + u')^2 - 2\left(\frac{3h''}{h} + 1\right)u^2 + 6h^2\left[\left(\frac{u}{h}\right)'\right]^2 \mathrm{d}\tau, \tag{A.64}$$

$$= \int_0^{\pi/2} \hat{C}\frac{1}{h}(u''' + u')^2 + \frac{f_3(\tau)\tanh^2 2\sigma_0}{h}u^2 + \frac{g_3(\tau)\tanh^2 2\sigma_0}{\bar{B}^2 h}\left[\left(\frac{u}{h}\right)'\right]^2 \mathrm{d}\tau, \tag{A.65}$$

where we have defined $f_3(\tau)$ and $g_3(\tau)$, given explicitly by:

$$f_3(\tau) = -\frac{2h}{\tanh^2 2\sigma_0}\left(\frac{3h''}{h} + 1\right), \tag{A.66}$$

$$g_3(\tau) = \frac{\bar{B}^2 h^3}{\tanh^2 2\sigma_0}. \tag{A.67}$$

Clearly $\hat{C}$, $f_3(\tau)$ and $g_3(\tau)$ are bounded above by positive constants. Let $M_3 > 0$ be such an upper bound. We might take

$$M_3 = \max_{\tau\in[0,\pi/2]}\left(\hat{C}, f_4(\tau), g_4(\tau), 1\right). \tag{A.68}$$

Hence we have

$$\|u\|_{H^3}^2 \leq M_3 \int_0^{\pi/2} \frac{1}{h}(u''' + u')^2 + \tanh^2 2\sigma_0 \left(\frac{1}{h}u^2 + \frac{1}{\bar{B}^2 h}\left[\left(\frac{u}{h}\right)'\right]^2\right) \mathrm{d}\tau, \tag{A.69}$$

$$= M_3 \frac{(c^2 \cosh 2\sigma_0)^2}{4} \|u\|_K^2 . \tag{A.70}$$

Hence setting $C_3 \equiv M_3^{-1/2} \frac{2}{(c^2 \cosh 2\sigma_0)}$, it follows that $C_3 \|u\|_{H^3} \leq \|u\|_K$.

Upper bound: $\|u\|_K \leq C_4 \|u\|_{H^3} \ \forall u \in K$

Expanding the first term in (A.47), we find that

$$\|u\|_K^2 = \frac{4}{(c^2 \cosh 2\sigma_0)^2} \int_0^{\pi/2} \frac{1}{h} \left[(u')^2 + 2(uu''') + (u''')^2 \right] \mathrm{d}\tau + \frac{4 \tanh^2 2\sigma_0}{(c^2 \cosh 2\sigma_0)^2} \int_0^{\pi/2} \frac{1}{h} u^2 + \frac{1}{\bar{B}^2 h} \left[\left(\frac{u}{h} \right)' \right]^2 \mathrm{d}\tau. \tag{A.71}$$

Integrating the second term of (A.71) by parts and noting that the second derivatives of functions in K vanish at the end-points of $(0, \pi/2)$; we obtain

$$\|u\|_K^2 = \frac{4}{(c^2 \cosh 2\sigma_0)^2} \int_0^{\pi/2} \frac{1}{h} (u')^2 - 2u'' \left(\frac{1}{h} u' \right)' + \frac{1}{h} (u''')^2 \, \mathrm{d}\tau + \frac{4 \tanh^2 2\sigma_0}{(c^2 \cosh 2\sigma_0)^2} \int_0^{\pi/2} \frac{1}{h} u^2 + \frac{1}{\bar{B}^2 h} \left[\left(\frac{u}{h} \right)' \right]^2 \mathrm{d}\tau. \tag{A.72}$$

Expanding the second term of (A.72) using the product rule, noting that

$$\bar{u}'' \left(\frac{1}{h} u' \right)' = \frac{1}{h} (u'')^2 - \frac{h'}{h^2} u'' u', \tag{A.73}$$

we then obtain the following:

$$\|u\|_K^2 = \frac{4}{(c^2 \cosh 2\sigma_0)^2} \int_0^{\pi/2} \frac{1}{h} (u')^2 - \frac{2}{h} (u'')^2 + \frac{2h'}{h^2} u'' u' + \frac{1}{h} (u''')^2 \, \mathrm{d}\tau + \frac{4 \tanh^2 2\sigma_0}{(c^2 \cosh 2\sigma_0)^2} \int_0^{\pi/2} \frac{1}{h} u^2 + \frac{1}{\bar{B}^2 h} \left[\left(\frac{u}{h} \right)' \right]^2 \mathrm{d}\tau. \tag{A.74}$$

Integrating the third term of (A.74) by parts noting that h' vanishes at the end-points of the interval $(0, \pi/2)$, we arrive at a convenient form for $\|u\|_K^2$, for which we can construct an upper bound.

$$\|u\|_K^2 = \frac{4}{(c^2\cosh 2\sigma_0)^2}\int_0^{\pi/2}\left[\frac{1}{h} - \left(\frac{h'}{h^2}\right)'\right](u')^2 - \frac{2}{h}(u'')^2 + \frac{1}{h}(u''')^2\,\mathrm{d}\tau + \frac{4\tanh^2 2\sigma_0}{(c^2\cosh 2\sigma_0)^2}\int_0^{\pi/2}\frac{1}{h}u^2 + \frac{1}{\bar{B}^2 h}\left[\left(\frac{u}{h}\right)'\right]^2\mathrm{d}\tau. \tag{A.75}$$

Since the second integral in (A.75) is just a constant multiple of $\|u\|_H^2$, we recall equation (A.45):

$$\|u\|_H^2 \leq M_1\int_0^{\pi/2}(u)^2 + (u')^2\,\mathrm{d}\tau, \quad M_1 > 0. \tag{A.76}$$

Using (A.76) we obtain:

$$\|u\|_K^2 \leq \frac{4}{(c^2\cosh 2\sigma_0)^2}\int_0^{\pi/2}\left[\frac{1}{h} - \left(\frac{h'}{h^2}\right)'\right](u')^2 - \frac{2}{h}(u'')^2 + \frac{1}{h}(u''')^2\,\mathrm{d}\tau + \frac{4M_1}{(c^2\cosh 2\sigma_0)^2}\int_0^{\pi/2}u^2 + (u')^2\,\mathrm{d}\tau, \tag{A.77}$$

$$= \frac{4}{(c^2\cosh 2\sigma_0)^2}\int_0^{\pi/2}M_1u^2 + \left[\frac{1}{h} - \left(\frac{h'}{h^2}\right)' + M_1\right](u')^2 - \frac{2}{h}(u'')^2 + \frac{1}{h}(u''')^2\,\mathrm{d}\tau, \tag{A.78}$$

$$= \int_0^{\pi/2}M_1u^2 + f_4(\tau)(u')^2 - 2g_4(\tau)(u'')^2 + g_4(\tau)(u''')^2\,\mathrm{d}\tau, \tag{A.79}$$

where we have defined

$$f_4(\tau) = \frac{4}{(c^2\cosh 2\sigma_0)^2}\left(\frac{1}{h} - \left(\frac{h'}{h^2}\right)' + M_1\right), \tag{A.80}$$

$$g_4(\tau) = \frac{4}{(c^2\cosh 2\sigma_0)^2}\frac{1}{h}. \tag{A.81}$$

Now defining

$$M_4 = \max_{\tau\in[0,\pi/2]}(m_1, f_4(\tau), g_4(\tau), 1) > 0, \tag{A.82}$$

we obtain

$$\|u\|_K^2 \leq M_4 \int_0^{\pi/2} u^2 + (u')^2 + (u'')^2 + (u''')^2 \,\mathrm{d}\tau = M_4 \|u\|_{H^3}^2 . \tag{A.83}$$

Hence setting $C_4 \equiv M_4^{1/2}$, it follows that $\|u\|_K \leq C_4 \|u\|_{H^3}$.

A.4 Application of the discrete spectral theorem

We now use Theorem A.1.1 to show that there exists a basis for the Hilbert spaces H and K consisting only of the eigenfunctions of (A.1)–(A.2).

Let H and K be the spaces as defined in §A.2.2. In section §A.3 we showed that H and K are Hilbert spaces with respect to the inner products (A.21)–(A.22).

The space K is dense in H since C_0^∞ (the set of infinitely differentiable coefficients with compact support in $\mathbb{R}^2$) is dense in H, and $C_0^\infty \subset K \subset H$. The embedding

$$K \hookrightarrow H \tag{A.84}$$

is continuous if and only if there exists $C_5 > 0$ such that

$$\|u\|_H \leq C_5 \|u\|_K . \tag{A.85}$$

Recall the norms for H and K and consider the following:

$$\|u\|_H = \frac{c^2\cosh 2\sigma_0}{2}\left(\frac{4\tanh^2 2\sigma_0}{(c^2\cosh 2\sigma_0)^2}\int_0^{\pi/2}\frac{1}{h}|u|^2+\frac{1}{\bar{B}^2 h}\left|\left(\frac{u}{h}\right)'\right|^2 \mathrm{d}\tau\right)^{1/2}, \tag{A.86}$$

$$\leq \frac{c^2\cosh 2\sigma_0}{2}\left(\frac{4}{(c^2\cosh 2\sigma_0)^2}\int_0^{\pi/2}\frac{1}{h}|u'+u'''|^2\,\mathrm{d}\tau + \frac{4\tanh^2 2\sigma_0}{(c^2\cosh 2\sigma_0)^2}\int_0^{\pi/2}\frac{1}{h}|u|^2+\frac{1}{\bar{B}^2 h}\left|\left(\frac{u}{h}\right)'\right|^2 \mathrm{d}\tau\right)^{1/2}, \tag{A.87}$$

$$= C_5\,\|u\|_K\,, \tag{A.88}$$

where

$$C_5 = \frac{c^2\cosh 2\sigma_0}{2} > 0. \tag{A.89}$$

Hence the embedding $K \hookrightarrow H$ is continuous. By the Kondrachov embedding theorem (Adams and Fournier, 2003), the embedding is compact.

Thus, defining the bilinear form

$$a = \langle\cdot,\cdot\rangle_K, \tag{A.90}$$

the discrete spectral theorem gives two orthonormal bases, $\{u_j\}$ and $\{u_j/\sqrt{\gamma_j}\}$ for the function spaces H and K respectively, such that the vectors $u_j \in K$ are the eigenfunctions satisfying

$$\langle u_j, v\rangle_K = \gamma_j\langle u_j, v\rangle_H, \quad \forall v \in K. \tag{A.91}$$

Substituting the inner products $\langle\cdot,\cdot\rangle_K$ and $\langle\cdot,\cdot\rangle_H$ into (A.91) and writing

$$\gamma_j = \lambda_j + \frac{4}{(c^2\cosh 2\sigma_0)^2}, \tag{A.92}$$

we find that

$$\int_0^{\pi/2} \frac{1}{h}\hat{\mathscr{K}}(u_j)\hat{\mathscr{K}}(v)\,\mathrm{d}\tau = \lambda_j \tanh^2\sigma_0 \int_0^{\pi/2} \frac{1}{h}u_j v + \frac{1}{\bar{B}^2 h}\left(\frac{u_j}{h}\right)'\left(\frac{v}{h}\right)'\mathrm{d}\tau, \quad \forall v \in K. \tag{A.93}$$

This is the weak formulation from §A.2.3. Hence, u_j is an eigenfunction of (A.1)–(A.3) in the weak sense. That is, it satisfies (A.93) and (A.2), but is not guaranteed (at this point) to satisfy (A.3).

A.5 Regularity theory and natural boundary conditions

In this section we use results from one-dimensional regularity theory to show that the weak eigenfunctions of (A.1)–(A.2) (i.e functions $u_j \in K$ such that (A.93) holds) are in fact classical eigenfunctions. We will then use this result to prove that the final boundary condition on the fourth derivative in (A.3) is satisfied naturally.

A.5.1 Regularity of the eigenfunctions

We begin by referring the reader to chapter 8 of Halperin and Schwartz (2019), where it is proven that every distributional solution for a linear ODE

with smooth coefficients is automatically a classical, smooth solution. This result can also be found in Donoghue (2014).

We now define what it means for a distribution to be identifiable with a point (classical) function, and prove that for every weak solution of an nth order linear ODE, there is a corresponding distributional solution. This means that the weak solutions u_j of (A.1)–(A.3) are classical solutions of (A.1)–(A.2).

Results for distributions

Definition A.5.1 *A distribution $F(\phi)$ on an interval I is said to be identified with a point function $f(\tau)$ if for every closed finite interval $(a,b) \in I$, $f(\tau)$ is summable on (a,b) and*

$$F(\phi) = \int_a^b f(\tau)\phi(\tau)\,\mathrm{d}\tau \quad \forall \phi(\tau) \in S_{(a,b)}. \tag{A.94}$$

Here $S_{(a,b)}$ is the set of continuous functions possessing derivatives $\phi^{(n)}(\tau)$ for any n, which, along with its self, vanish at $\tau = a, b$.

Definition A.5.2 *For any interval I, the derivative distribution, $F'(\phi)$, is defined by*

$$F'(\phi) = -F(\phi') \qquad \forall \phi(\tau) \in S_{(a,b)}. \tag{A.95}$$

Definition A.5.3 *Let $a(\tau)$ be a point function possessing continuous point function derivatives of all orders. Let $F(\phi)$ be the distribution restricted to test functions $\phi \in S_{(a,b)}$. Then the product $a(\tau)F(\phi)$ is defined as*

$$a(\tau)F(\phi(\tau)) = F(a(\tau)\phi(\tau)) \qquad \forall \phi(\tau) \in S_{(a,b)}. \tag{A.96}$$

Lemma A.5.1 *For each weak (point) solution,* $f(\tau)$*, of the ODE*

$$\sum_{k=0}^{n} a_k(\tau) f^{(k)}(\tau) = 0, \tag{A.97}$$

we can identify an associated distributional solution.

Proof A.5.1 *To prove this result, we firstly multiply (A.97) by the test function* $\phi \in S_{(a,b)}$ *and integrate over* (a, b)

$$\sum_{k=0}^{n} \int_a^b f^{(k)}(\tau) a_k(\tau) \phi(\tau)\, \mathrm{d}\tau = 0. \tag{A.98}$$

Integrating the k*th term by parts* α_k *times, noting that* $\phi \in S_{(a,b)}$*, we obtain the weak form for the ODE*

$$\sum_{k=0}^{n} \int_a^b (-1)^{\alpha}_k f^{(k-\alpha_k)}(\tau) (a_k(\tau)\phi(\tau))^{(\alpha_k)}\, \mathrm{d}\tau = 0. \tag{A.99}$$

We say that functions ϕ *that satisfy (A.99) are weak solutions of (A.97). Using definition A.5.1, we identify the weak solution* f *with the distribution* F *defined by*

$$F(\phi) = \int_a^b f(\tau)\phi(\tau)\, \mathrm{d}\tau. \tag{A.100}$$

Integrating each term a further $k - \alpha_k$ *times, we find that*

$$\sum_{k=0}^{n} \int_a^b (-1)^{\alpha}_k f(\tau) (a_k(\tau)\phi(\tau))^{(k)}\, \mathrm{d}\tau = 0. \tag{A.101}$$

Applying definition A.5.2 k *times, it follows that*

$$F^{(k)}(\phi(\tau)) = (-1)^k F(\phi^{(k)}(\tau)), \tag{A.102}$$

hence, equation (A.101) can be written as follows

$$\sum_{k=0}^{n} F^{(k)}(a_k(\tau)\phi(\tau))\,\mathrm{d}\tau = 0. \tag{A.103}$$

Finally, using the multiplication law for distributions (definition A.5.3), we obtain

$$\sum_{k=0}^{n} a_k(\tau)F^{(k)}(\phi(\tau))\,\mathrm{d}\tau = 0 \quad \forall\phi(\tau) \in S_{(a.b)}. \tag{A.104}$$

Therefore F is a distributional solution of the ODE (A.97), and hence the lemma is proved.

Equation (A.104) verifies the assertion that every weak solution to (A.97) (i.e. any point function f that satisfies (A.99)) can be identified with a corresponding distributional solution. Hence, by Halperin and Schwartz (2019), the weak eigenfunctions (i.e functions u_j that satisfy (A.93)) of (A.1)–(A.2) are in fact classical eigenfunctions.

A.5.2 Boundary condition on the fourth derivative

We now wish to show that the eigenfunctions u_j obtained above satisfy

$$u_j'''' = 0 \qquad \text{on} \qquad \tau = 0, \pi/2. \tag{A.105}$$

Suppose that $v \in K$ and u_j is a weak solution to (A.1)–(A.3). Then from above, u_j is also a classical solution of (A.1)–(A.2) and hence

$$u_j \in \{C^\infty \mid u_j = u_j'' = 0 \text{ on } \tau = 0, \pi/2\}, \tag{A.106}$$

where C^∞ is the set of infinitely differentiable (smooth) functions. We can now use integration by parts and the definitions of the operators $\hat{\mathscr{L}}, \hat{\mathscr{K}}$ and $\hat{\mathscr{J}}$ to show that equation (A.93) can be written as

$$\int_0^{\pi/2} \frac{1}{h}\left(\hat{\mathscr{L}}\hat{\mathscr{K}}(u_j) - \hat{\mathscr{J}}(u_j)\right) v \,\mathrm{d}\tau - \left[\frac{2}{hc^2\cosh^2 2\sigma_0} u_j'''' v'\right]_0^{\pi/2} = 0. \quad \text{(A.107)}$$

Since, u_j is a classical eigenfunction of (A.1) it follows that the boundary condition on the fourth derivative is satisfied naturally.

A.6 Summary

It has been shown that the eigenfunctions of the generalised eigenvalue problem (A.1)–(A.3) form a basis for the space of smooth differentiable functions whose even derivatives (up to order four) vanish at the end points of $\tau \in (0, \pi/2)$. The result was derived by defining function spaces H and K (see §A.2.2) in such a way that they form Hilbert spaces when equipped with inner products found in §A.2.4. The result that these spaces are indeed Hilbert spaces is proven in §A.3. The fact that H and K form Hilbert spaces allows for the application of the Discrete Spectral Theorem A.1.1, which proves the existence of a basis of functions u_j to the weak formulation. The problem was then to show that these eigenfunctions are in fact the eigenfunctions of the original problem. To show this, we showed that the eigenfunctions were in fact sufficiently more differentiable than when first defined and that the eigenfunctions have a fourth derivative that vanishes at the end-points of $(0, \pi/2)$. The details of these two results can be found in §A.5. With these final results proven, the main result follows.

Since the eigenfunctions of (A.1)–(A.3) form a basis for the Hilbert space H, for every $u \in H$, there exists a sequence of constants $a_j \in \mathbb{R}$ such that

$$u = \sum_{j=0}^{\infty} a_j u_j(\tau). \tag{A.108}$$

Using orthogonality with respect to the inner product $\langle \cdot, \cdot \rangle_H$, let u_j and u_k be eigenfunctions of (A.1)–(A.3) and define the following normalisation

$$\langle u_j, u_k \rangle = \delta_{jk}. \tag{A.109}$$

Taking the H inner product of (A.108) with u_k and using the normalisation (A.109) it follows that

$$a_j = \langle u, u_j \rangle_H, \tag{A.110}$$

$$= \langle u, \hat{\mathscr{J}}(u_j) \rangle_{L^2}. \tag{A.111}$$

Bibliography

Adams, R. A. and Fournier, J. J. (2003). *Sobolev spaces*. Elsevier.

Axler, S. (1997). *Linear algebra done right*. Springer Science & Business Media.

Baroud, C. N., Tsikata, S., and Heil, M. (2006). The propagation of low-viscosity fingers into fluid-filled branching networks. *J. Fluid Mech.*, 546:285–294.

Batchelor, G. K. (1967). *An Introduction to Fluid Dynamics*. Cambridge University Press.

Bertram, C. (1986). Unstable equilibrium behaviour in collapsible tubes. *J. Biomech. Engr*, 19(1):61–69.

Bertram, C. (2003). Experimental studies of collapsible tubes. In *Flow Past Highly Compliant Boundaries and in Collapsible Tubes: Proceedings of the IUTAM Symposium held at the University of Warwick, United Kingdom, 26–30 March 2001*, pages 51–65. Springer.

Bertram, C. and Pedley, T. (1982). A mathematical model of unsteady collapsible tube behaviour. *J. Biomech.*, 15(1):39–50.

Bertram, C., Raymond, C., and Butcher, K. (1989). Oscillations in a collapsed-tube analog of the brachial artery under a sphygmomanometer cuff. *J. Biomech. Engr*, 157:185—-191.

Bertram, C., Raymond, C., and Pedley, T. (1990). Mapping of instabilities for flow through collapsed tubes of differing length. *J. Fluids Struct.*, 4(2):125–153.

Binns, R. L. and Ku, D. N. (1989). Effect of stenosis on wall motion. a possible mechanism of stroke and transient ischemic attack. *Arteriosclerosis: Am. Heart J.*, 9(6):842–847.

Blanchard, P. and Brüning, E. (2012). *Variational methods in mathematical physics: a unified approach*. Springer Science & Business Media.

Cancelli, C. and Pedley, T. (1985). A separated-flow model for collapsible-tube oscillations. *J. Fluid Mech.*, 157:375–404.

Conrad, W. A. (1969). Pressure-flow relationships in collapsible tubes. *IEEE Trans. Bio. Eng*, 16(4):284–295.

Danahy, D. T. and Ronan Jr, J. A. (1974). Cervical venous hums in patients on chronic hemodialysis. *N. Engl. J. Med.*, 291(5):237–239.

Donoghue, W. F. (2014). *Distributions and Fourier transforms*. Academic Press.

Flaherty, J. E., Keller, J. B., and Rubinow, S. (1972). Post buckling behavior of elastic tubes and rings with opposite sides in contact. *Soc. Ind. Appl. Math.*, 23(4):446–455.

Flügge, W. (1972). *Tensor Analysis and Continuum Mechanics*. Springer.

Gilbarg, D., Trudinger, N. S., Gilbarg, D., and Trudinger, N. (1977). *Elliptic partial differential equations of second order*, volume 224. Springer.

Grotberg, J. B. and Gavriely, N. (1989). Flutter in collapsible tubes: a theoretical model of wheezes. *J. Appl. Physiol.*, 66(5):2262–2273.

Grotberg, J. B. and Jensen, O. E. (2004). Biofluid mechanics in flexible tubes. *Annu. Rev. Fluid Mech.*, 36(1):121–147.

Halperin, I. and Schwartz, L. (2019). *Introduction to the Theory of Distributions*. University of Toronto Press.

Hayashi, S., Hayase, T., and Kawamura, H. (1998). Numerical analysis for stability and self-excited oscillation in collapsible tube flow. *J. Biomech. Engr*, 120(4):468–475.

Hazel, A. L. and Heil, M. (2003). Steady finite-reynolds-number flows in three-dimensional collapsible tubes. *J. Fluid Mech.*, 486:79–103.

Heil, M. (2000). Finite reynolds number effects in the propagation of an air finger into a liquid-filled flexible-walled channel. *J. Fluid Mech.*, 424:21–44.

Heil, M. and Boyle, J. (2010). Self-excited oscillations in three-dimensional collapsible tubes: simulating their onset and large-amplitude oscillations. *J. Fluid Mech.*, 652:405–426.

Heil, M. and Hazel, A. L. (2011). Fluid–structure interaction in internal physiological flows. *Annu. Rev. Fluid Mech.*, 43:141–162.

Heil, M. and Jensen, O. E. (2003). Flows in deformable tubes and channels. In *Flow Past Highly Compliant Boundaries and in Collapsible Tubes*, pages 15–49. Springer.

Heil, M. and Pedley, T. J. (1996). Large post-buckling deformations of cylindrical shells conveying viscous flow. *J. Fluids Struct.*, 10(6):565–599.

Heil, M. and Waters, S. L. (2008). How rapidly oscillating collapsible tubes extract energy from a viscous mean flow. *J. Fluid Mech.*, 601:199–227.

Hislop, P. D. and Sigal, I. M. (2012). *Introduction to spectral theory: With applications to Schrödinger operators*, volume 113. Springer Science & Business Media.

Jensen, O. and Pedley, T. (1989). The existence of steady flow in a collapsed tube. *J. Fluid Mech.*, 206:339–374.

Jensen, O. E. and Heil, M. (2003). High-frequency self-excited oscillations in a collapsible-channel flow. *J. Fluid Mech.*, 481:235–268.

Katz, A. I., Chen, Y., and Moreno, A. H. (1969). Flow through a collapsible tube: experimental analysis and mathematical model. *Biophys. J.*, 9(10):1261–1279.

Kececioglu, I., Mcclurken, M. E., Kamm, R. D., and Shapiro, A. H. (1981). Steady, supercritical flow in collapsible tubes. Part 1. Experimental observations. *J. Fluid Mech.*, 109:367–389.

Knowlton, F. and Starling, E. (1912). The influence of variations in temperature and blood-pressure on the performance of the isolated mammalian heart. *J. Physiol*, 44(3):206–219.

Kress, R., Maz'ya, V., and Kozlov, V. (1989). *Linear integral equations*. Springer.

Ku, D. N. (1997). Blood flow in arteries. *Annu. Rev. Fluid Mech.*, 29(1):399–434.

Liu, H., Luo, X., Cai, Z., and Pedley, T. (2009). Sensitivity of unsteady collapsible channel flows to modelling assumptions. *Commun. Numer. Methods Eng.*, 25(5):483–504.

Lokossou, A., Metanbou, S., Gondry-Jouet, C., and Balédent, O. (2020). Extracranial versus intracranial hydro-hemodynamics during aging: a pc-mri pilot cross-sectional study. *Fluids Barriers CNS.*, 17:1–11.

Love, A. E. H. (1888). XVI. The Small Free Vibrations and Deformation of a Thin Elastic Shell. *Phil. Trans. Roy. Soc. London*, 179:491–546.

Luo, X., Cai, Z., Li, W., and Pedley, T. (2008). The cascade structure of linear instability in collapsible channel flows. *J. Fluid Mech.*, 600:45–76.

Luo, X. and Pedley, T. (1995). A numerical simulation of steady flow in a 2-D collapsible channel. *J. Fluids Struct.*, 9(2):149–174.

Luo, X. and Pedley, T. (1996). A numerical simulation of unsteady flow in a two-dimensional collapsible channel. *J. Fluid Mech.*, 314:191–225.

Luo, X. and Pedley, T. (2000). Multiple solutions and flow limitation in collapsible channel flows. *J. Fluid Mech.*, 420:301–324.

Macklem, P. T. (1971). Airway obstruction and collateral ventilation. *Physiol. Rev.*, 51(2):368–436.

Macklem, P. T., Proctor, D. F., and Hogg, J. C. (1970). The stability of peripheral airways. *Respir. Physiol.*, 8(2):191–203.

Matsuzaki, Y., Ikeda, T., Kitagawa, T., and Sakata, S. (1994). Analysis of flow in a two-dimensional collapsible channel using universal "tube" law. *J. Biomech. Engr*, 116(4):469–476.

Mcclurken, M. E., Kececioglu, I., Kamm, R. D., and Shapiro, A. H. (1981). Steady, supercritical flow in collapsible tubes. Part 2. Theoretical studies. *J. Fluid Mech.*, 109:391–415.

Moreno, A. H., KATZ, A. I., GOLD, L. D., and Reddy, R. (1970). Mechanics of distension of dog veins and other very thin-walled tubular structures. *Circulation research*, 27(6):1069–1080.

Netherwood, D. J. and Whittaker, R. J. (2023). A new solution for the deformations of an initially elliptical elastic-walled tube. *Q. J. Mech. Appl. Math.*, 76(1):49–77.

Pedley, T. and Luo, X. (1998). Modelling flow and oscillations in collapsible tubes. *Theoret. Comp. Fluid Dyn.*, 10(1):277–294.

Pedley, T. J. (1980). *The Fluid Mechanics of Large Blood Vessels*. Cambridge Monographs on Mechanics. Cambridge University Press.

Pedley, T. J. (1992). Longitudinal Tension Variation in Collapsible Channels: A New Mechanism for the Breakdown of Steady Flow. *J. Biomech. Engr*, 114(1):60–67.

Pride, N. B. and Milic-Emili, J. (1995). *Lung Mechanics*, pages 135–160. Springer US, Boston, MA.

Rafieian-Kopaei, M., Setorki, M., Doudi, M., Baradaran, A., and Nasri, H. (2014). Atherosclerosis: process, indicators, risk factors and new hopes. *International journal of preventive medicine*, 5(8):927.

Rast, M. P. (1994). Simultaneous solution of the Navier–Stokes and elastic membrane equations by a finite element method. *Int. J. Numer. Meth. FL.*, 19(12):1115–1135.

Reyn, J. (1987). Multiple solutions and flow limitation for steady flow through a collapsible tube held open at the ends. *J. Fluid Mech.*, 174:467–493.

Rodbard, S. (1966). A hydrodynamic mechanism for autoregulation of flow. *Cardiologia*, 48(6):532–535.

Rodbard, S. and Takacs, L. (1966). Hydrodynamics of autoregulation. *Cardiologia*, 48(5):433–440.

Shapiro, A. H. (1977). Steady Flow in Collapsible Tubes. *J. Biomech. Engr*, 99(3):126–147.

Skalak, R., Ozkaya, N., and Skalak, T. C. (1989). Biofluid mechanics. *Annu. Rev. Fluid Mech.*, 21(1):167–200.

Stewart, P. S., Waters, S. L., and Jensen, O. E. (2009). Local and global instabilities of flow in a flexible-walled channel. *Eur. J. Mech. B/Fluids*, 28(4):541–557.

Trost, J. C. and Hillis, L. D. (2006). Intra-aortic balloon counterpulsation. *Am. J. Cardiol.*, 97(9):1391–1398.

Ur, A. and Gordon, M. (1970). Origin of korotkoff sounds. *Am. J. Physiol.*, 218(2):524–529.

Walters, M. C., Heil, M., and Whittaker, R. J. (2018). The effect of wall inertia on high-frequency instabilities of flow through an elastic-walled tube. *Q. J. Mech. Appl. Math.*, 71(1):47–77.

Walters, M. C., Heil, M., and Whittaker, R. J. (2023). Bending boundary layers near the clamped end of an elastic-walled tube. In prep.

White, J. P. and Heil, M. (2005). Three-dimensional instabilities of liquid-lined elastic tubes: A thin-film fluid-structure interaction model. *Phys. Fluids*, 17(3).

Whittaker, R. J. (2015). A shear-relaxation boundary layer near the pinned ends of a buckled elastic-walled tube. *IMA J. Appl. Math.*, 80(6):1932–1967.

Whittaker, R. J., Heil, M., Boyle, J., Jensen, O. E., and Waters, S. L. (2010a). The energetics of flow through a rapidly oscillating tube. Part 2. Application to an elliptical tube. *J. Fluid Mech.*, 648:123–153.

Whittaker, R. J., Heil, M., Jensen, O. E., and Waters, S. L. (2010b). A rational derivation of a tube law from Shell theory. *Q. J. Mech. Appl. Math.*, 63(4):465–496.

Whittaker, R. J., Heil, M., Jensen, O. E., and Waters, S. L. (2010c). Predicting the onset of high-frequency self-excited oscillations in elastic-walled tubes. *Proc. R. Soc. A*, 466(2124):3635–3657.

Whittaker, R. J., Heil, M., and Waters, S. L. (2011). The energetics of flow through a rapidly oscillating tube with slowly varying amplitude. *Phil. Trans. R. Soc. A*, 369(1947):2989–3006.

Whittaker, R. J., Waters, S. L., Jensen, O. E., Boyle, J., and Heil, M. (2010d). The energetics of flow through a rapidly oscillating tube. Part 1. General theory. *J. Fluid Mech.*, 648:83–121.

Wild, R., Pedley, T., and Riley, D. (1977). Viscous flow in collapsible tubes of slowly varying elliptical cross-section. *J. Fluid Mech.*, 81(2):273–294.

Zhang, S., Luo, X., and Cai, Z. (2018). Three-dimensional flows in a hyperelastic vessel under external pressure. *Biomechanics and modeling in mechanobiology*, 17:1187–1207.